Warwick Manufacturing Group
University of Warwick

Degradation Diagnostics of Lithium-ion Batteries for Automotive Applications

Innovation Report

Submitted in Partial Fulfillment of the Requirements of the Academic Degree

Doctor of Engineering International - EngD (Int.)

Author: M.Sc. Carlos Pastor-Fernández

Registration Number: 1465581

Academic supervisors: Dr. James Marco and Dr. W. Dhammika Widanage
Industrial supervisors: Dr. Tung Fai Yu
Jaguar Land Rover Ltd.

Coventry (United Kingdom), April 24, 2019

Declaration of Academic Honesty

I hereby declare that all information in this document has been obtained and presented in accordance with academic rules and ethical conduct and that this submission is my own work. I also declare that, as required by these rules and conduct, I have fully cited and referenced all material and results that are not original to this work.

April 24, 2019

Carlos Pastor Fernández

Abstract

Motivated by political, social and economic factors, automotive original equipment manufacturers have adopted vehicle electrification as a technology to either reduce or eliminate tailpipe emissions. However, the design and development of Battery Electric Vehicles (BEVs) are facing significant challenges to achieving full market penetration. Some of these challenges are to ensure specific battery performance, range, safety, charging time and lifetime. Battery degradation affects each of these factors negatively. To mitigate this negative impact, researchers agree that battery degradation needs to be better understood. For this, it is essential to develop non-invasive battery health diagnostic techniques that can be applied in real-world operating conditions.

This Innovation Report presents the findings from an International Engineering Doctorate (EngD (Int.)). This Innovation Report investigates factors influencing the degradation of Lithium-ion Batteries (LIB) in BEV applications. The contribution of this research is to provide the underpinning knowledge that allows manufacturers to improve the durability and performance of Electric Vehicle battery assemblies concerning degradation.

This contribution has been achieved through four related studies within two primary areas of investigation. Firstly, the research focuses on evaluating Cell-to-Cell Variabilities (CtCV) in LIB packs in Study 1 and their implications for the monitoring of the State of Health (SoH) in Study 2. Study 1 proposes a systematic procedure to quantify the amount and the origin of CtCV in battery packs. Study 2 quantifies CtCV experimentally with respect to SoH for a scenario equivalent to a typical BEV life (10 years) or customer mileage (100,000 miles). Further, Study 2 suggests a non-invasive methodology to monitor SoH in a vehicle. These results can be employed by academics and engineers to quantify battery degradation in imbalance scenarios. The second avenue of investigation was to improve the current SoH definition employed in the automotive industry. After conducting a critical and extensive review of the most pertinent literature in Study 3, Study 4 suggests a step-by-step methodology to quantify the most pertinent degradation modes. This non-invasive diagnosis methodology can be applied in the context of on-board and off-board vehicle applications. The application of this methodology can be further used by academia and industry to improve lifetime control strategies and future battery designs.

In conclusion, the impact of this thesis is to define diagnosis techniques that can be further employed by engineers to reduce the negative consequences of battery degradation into battery performance, autonomy and lifetime.

Acknowledgements

There are many people who have contributed to my work in various ways, and who deserve my deepest gratitude. Firstly, I would like to acknowledge my academic supervisors from WMG: Dr. James Marco, Dr. W. Dhammika Widanage and Dr. Kotub Uddin. Secondly, I would like to thank you my industrial supervisors from Jaguar Land Rover: Dr. (Nixon) Tung Fai Yu, Dr. Gael H. Chouchelamane and Dr. Miguel Ángel Gama-Valdez.

At WMG I would like also to thank Dr. Yue Guo, Dr. Anup Barai, Dr. James Taylor, Dr. Ravichandra Tangirala and John Palmer for their expertise and advice on conducting my experimental research in a safe and professional manner. Useful feedback was received from Dr. Thomas Gradjean, Dr. Jakobus Groenewald, Dr. Ashwin Radja, Dr. Bostjan Hari and Dr. Satya Dubey. I would also like to thank fellow researchers Thomas Bruen, Dr. James Hooper, Dr. Limhi Somerville, Ronny Genieser, Quirin Kellner, Yashraj Tripathy, Upender Rao Koleti, Daniel Worwood, Dr. Ahmed Abaza, Dr. Prasun Chokshi, and Romeo Malik for the productive discussions regarding different topics covered in this thesis. Specially, I would like to thank Thomas Bruen for allowing me to collaborate with him in my first study (refer to Chapter 4).

I would like to recognise the support of the sponsoring company, Jaguar Land Rover, and the people behind it. Specially, I appreciate the technical advice from Paul Haney, Dr. Sue Slater, Dr. Ivan Zajic, David Gomez, Radhouen Foudhaili, Prakash Kulkarni, Mitesh Shah, Jason Page, Navneesh Philip, Dr. Hin Kwan Wong, Dr. Song Lin, Dr. Krishna Muthukumaran, Dr. Christopher Lyness, Krzysztof Slosarczyk and Julie Chevalier. Tata Motors European Technical Centre provided help in the development of my research. In particular, I truly appreciate feedback in Study 2 and 4 (refer to Chapter 4 and Chapter 6) provided by Dr. Mark Tucker.

I am thankful for the opportunity to work with Dr. Matthieu Dubarry at Hawai'i Natural Energy Institute (HNEI), University of Hawai'i. This collaboration resulted in the last study (refer to Chapter 3) undertaken during the EngD.

I am grateful to be involved in testing a prototype wireless BMS provided by Dukosi Ltd. In particular, many thanks to Adrian Jones and George Paterson for guiding me in using this equipment.

I appreciate the interesting conversations I had with external colleagues I met in conferences or networking events. Specially, I would like to thank you Dr. Christopher Birkl, Dr. David Howey, Dr. Jorge Varela Barreras, Linfeng Zheng and Dr. Lucia Gauchia.

I would like to acknowledge that the research presented within this report was supported by the Engineering and Physical Science Research Council (EPSRC - EP/I01585X/1) through the Engineering Doctoral Centre in High Value, Low Environmental Impact Manufacturing.

Outside my research, I am thankful for the support and advice received from Dr. Antony Allen and Sara Hattersley in my teaching activities. I also want to recognise with gratitude the teachers, supervisors and colleagues from my previous studies and work experiences at Daimler, AVL, Carinthia University of Applied Sciences, Coventry University and Technical University of Madrid. Specially, special thanks to Adnan Nuhic and Dr. Andreja Rojko, supervisors of my master thesis; and Dr. Selim Oleksowicz, supervisor of my bachelor thesis.

I would like to recognise the advice of my friends. Finally but mostly, I would like to thank my sister and my parents for all the love, encouragement and support they have given me over years.

Contents

Abbreviations

AE	Applied Energy
ARPA-E	Advanced Research Projects Agency for Energy
ASME	American Society of Mechanical Engineers
BEV	Battery Electric Vehicle
BMS	Battery Management System
BoL	Begin of Life
C	Capacity
CAL	Calendaric data
CC-CV	Constant Current - Constant Voltage
CF	Capacity Fade
CL	Conductivity Loss
Comb.	Combination
CPE	Constant Phase Element
DC	Direct Current
DMs	Degradation Modes
DoD	Depth of Discharge
DTV	Differential Thermal Voltammetry
ECM	Equivalent Circuit Model
ECS	Journal of Electrochemical Society
EIS	Electrochemical Impedance Spectroscopy
EngD (Int)	Engineering Doctorate (International)
EoL	End of Life
FOI	Feature of Interest
GIC	Graphite Intercalation Compound

HE	High Energy
HEV	Hybrid Electric Vehicle
HIU	Helmholtz-Institut Ulm
HNEI	Hawai'i Natural Energy Institute
HP	High Power
IC-DV	Incremental Capacity - Differential Voltage
ICL	Imperial College London
IEC	International Electrotechnical Commission
IEEE	Institute of Electrical and Electronics Engineers
ISO	International Standard Organisation
JCP	Journal of Cleaner Production
JPS	Journal of Power Sources
L	Long (processing time)
LAM	Loss of Active Material
LCO	Lithium Cobalt Oxide ($LiCoO_2$)
LFP	Lithium iron Phosphate ($LiFePO_4$)
LIB	Lithium-ion Battery
LLI	Loss of Lithium Inventory
LMO	Lithium Manganese Oxide ($LiMn_2O_4$)
LNO	Lithium Nickel Oxide ($LiNiO_2$)
LTO	Lithium-Titanate Oxide ($Li_4Ti_5O_{12}$)
M	Mid (processing time)
Max	Maximum
Min	Minimum
MISRA	Motor Industry Software Research Association
N	No
n.a.	not available
NCA	Nickel Cobalt Aluminum Oxide (LiNixCo1-x-yAlyO2)
NE	Negative Electrode
NEV	Not Evaluated
NMC	Lithium Nickel Manganese Cobalt Oxide (Li[NiMnCo]O_2)

OEM	Original Equipment Manufacturer
Off	Offline
On	Online
ORI	Ohmic Resistance Increase
P	Parallel configuration
PA	Peak Area
PE	Positive Electrode
PF	Power Fade
PHEV	Plug-in Hybrid Electric Vehicle
pOCV	Pseudo Open Circuit Voltage
ppm	Particles per million
RC	Resistance-Capacitor
RDC	Repetitive Drive Cycle
RDF	Rate Degradation Factor
RESS	Rechargeable Energy Storage System
RMS	Root Mean Square value
RMSE	Root Mean Square Error
RS	Repetitive Synthetic data
S	Series configuration
SC	Single Cell
SE	Standard Error
SEI	Solid Electrolyte Interphase
SH	Short (processing time)
SK	Skewed
SoC	State of Charge
SoH	State of Health
SoH_E	State of Health based on capacity
SoH_P	State of Health based on resistance
SPI	Solid Permeable Interphase
SRCV	Slow Rate Cyclic Voltammetry
T	Temperature
UK	United Kingdom
Univ.	University
USABC	United States Advanced Battery Consortium

VIT	Voltage, Current, Temperature
V2G	Vehicle to Grid
WMG	Warwick Manufacturing Group
Y	Yes
ZSW	Zentrum für Sonnenenergie und Wasserstoff-Forschung

Symbols and Indices

Latin symbols

Symbol	Description	Unit
abs	Absolute value	[-]
AhT	Charge-throughput	[Ah]
$argmin$	Minimum argument	[-]
C	Capacitance	[F]
(Number)C	C-rate	[A]
cht	Characterisation test	[-]
C_n	Nominal capacity	[Ah]
C_{pn}	Normalized capacity of the pack	[Ah]
CO_2	Carbon Dioxide	[-]
$Cont_E$	Contribution to SoH_E convergence	[%]
$Cont_P$	Contribution to SoH_P convergence	[%]
cov	Covariance	[-]
D	Average value of the diffusion coefficients	[-]
E_{th}	Thermal Energy	[J]
E_o	Energy released by the battery	[J]
f	Frequency	[Hz]
G	Growth	[%]
h	Equal increment (sampling) of IC	[Ah/V] (IC)
	and DV pack curve	[V/Ah] (DV)
I	Current	[A]
I_a	Current amplitude signal	[A]
I_t	Potentiostatic current signal	[A]
I_{RMS}	Root Mean Square Current	[A]
ΔI	Difference in current between	
	beginning and end of discharge	[A]
L	Specific diffusion thickness	[mm]

Symbol	Description	Unit
m	Cells connected in parallel	[-]
m^{PE}	Parameter equivalent to $\mathrm{LAM}^{\mathrm{PE}}$	[-]
	(Group 2, pOCV diagnosis method)	
m^{NE}	Parameter equivalent to $\mathrm{LAM}^{\mathrm{NE}}$	[-]
	(Group 2, pOCV diagnosis method)	
N	Number of total values simulated	[-]
n_{cyc}	Number of cycles	[-]
n	Cells connected in series	[-]
P	Parallel	[-]
Ph	Phase angle between the current	
	and the applied voltage	[rad]
p	p-value	[-]
$pOCV$	Pseudo Open Circuit Voltage	[V]
$pOCV_{pn}$	Normalised pack pOCV	[V]
Q	Charge	[Ah]
Q_c	Charge of a cell	[Ah]
Q_r	Capacity ration	[Ah/%]
Q_p	Charge of a pack	[Ah]
ΔQ	Differential in charge	[Ah]
r	Pearson correlation coefficient	[-]
R	Resistance	[Ω]
randn	Random	[-]
RC	Rate Capability	[-]
R_o	Ohmic resistance	[Ω]
R_{BMS}	BMS resistance	[Ω]
R_{ct}	Charge-transfer resistance	[Ω]
R_{int}	Internal resistance	[Ω]
R_s	Shunt resistor	[Ω]
R_W	Warburg resistance	[Ω]
S	Series	[-]
sf	Scaling factor	[-]
SoC	State of charge	[%]
$\mathrm{SoH_E}$	State of Health based on capacity	[%]
$\mathrm{SoH_P}$	State of Health based on resistance	[%]
ΔSoH_E	Change of State of Health based on capacity	[%]
ΔSoH_P	Change of State of Health based on resistance	[%]
SoI_E	State of Imbalance due to SoH_E	[%]

Symbol	Description	Unit
SoI_P	State of Imbalance due to SoH_P	[%]
tf	Translation factor	[-]
T	Temperature	[℃]
T_s	Temperature measured by the thermocouples	[℃]
Te	Period	[s]
t	Time	[s]
t_{samp}	Sampling time	[s]
t_v	t-value (t-test)	[-]
V	Voltage	[V]
V_c	Cell voltage	[V]
V_t	Terminal voltage	[V]
V_{oc}	Open Circuit Voltage	[V]
V_R	Voltage across resistance R	[V]
V_o	Voltage across ohmic resistance R	[V]
V_a	Voltage amplitude	[V]
V_P	Voltage of the whole parallel stack	[V]
ss	Sample size	[-]
Z	Impedance	[Ω]
Z_a	Amplitude of the impedance	[Ω]
$Z^{'}$	Real part of the impedance	[Ω]
$Z^{''}$	Imaginary part of the impedance	[Ω]

Greek symbols

Symbol	Description	Unit
δ	Error	[-]
δ^{NE}	Parameter to quantify $\mathrm{LLI}^{\mathrm{NE}}$ (Group 2, pOCV diagnosis method)	[-]
δ^{PE}	Parameter to quantify $\mathrm{LLI}^{\mathrm{PE}}$ (Group 2, pOCV diagnosis method)	[-]
Δ	Difference	[-]
ϵ	Predefined threshold error	[-]
λ	Hypothesis of the origin and the amount of CtCV	[-]
ϕ	Angle between voltage and current	[°]
ψ	Duty cycle step	[s]
ω	Radial frequency	[rad/s]

Symbol	Description	Unit
σ	Standard deviation	[-]
θ	Vector of DMs	[-]

Other symbols

Indice	Description
#	Number of

Indices

Indice	Description
0	Initial (i.e. time=0)
a	FOI number
b	Amount of CtCV
c	Cell
BMS	Battery Management System
BoL	Value at Begin of Life
$c2p$	Cell-to-pack
chg	Charge
ct	Charge-transfer
cyc	Cycling
d	Simulation number
de	Delithiated
$dchg$	Discharge
dl	Double layer
e	End
EIS	Electrochemical Impedance Spectroscopy
eq	Equivalent
EoL	Value at End Of Life
exp	Experimental
f	Final
FC	Full Cell
h	Equal increment cell-to-pack curve
i	Initial
ind	Individual
is	First sample point

Indice	Description
k	Characterisation test
LAM	Loss of Active Material
li	Lithiated
LLI	Loss of Lithium Inventory
max	Maximum
$meas$	Measurement
min	Minimum
Mod	Module
n	Normal value
NE	Negative Electrode
now	Present value
ns	Last sample point
oc	Open circuit value (voltage)
P	Power
p	Pack
PE	Positive Electrode
poc	Pseudo open circuit value (voltage)
pol	Polarisation
q	SoC value (low, mid or high)
r	Ration
rt	Ratio
SEI	Solid Electrolyte Interphase
sim	Simulation
sp	Specific
Topo	Topology
th	Thermal
u	Cell number

List of Figures

List of Tables

1. Introduction

1.1 Motivation for the research

Political, social and economic factors are putting pressure on the automotive original equipment manufacturers (OEMs) to design and develop powertrain systems with a high level of performance while exhaust emissions are reduced [1]. At European level, regulation 443/2009 states that the fleet average exhaust emissions of carbon dioxide (CO_2) for all passenger vehicles sold within the European Union must be at or below 95g/km by 2021 [2]. Following on from this, the British Automotive Council has published roadmaps to promote the development of the technologies which will reduce these exhaust emissions [1]. The fleet average exhaust emissions of CO_2 for Jaguar Land Rover in 2015 was 164 $g{\cdot}km^{-1}$ [3]. If this is unchanged, companies with CO_2 emissions like Jaguar Land Rover will be subject to financial penalties. Ultimately this can make their business strategy economically unfeasible. Therefore, automotive OEMs need to reduce their exhaust CO_2 emissions.

Jaguar Land Rover and its competitors, such as BMW or Mercedes-Benz, have chosen to reduce their fleet CO_2 emissions by introducing a range of Battery Electric Vehicle (BEV) and Hybrid Electric Vehicle (HEV) powertrains [1]. These two approaches are fully or partially powered by an on-board rechargeable energy storage system (RESS). The RESS is comprised of Lithium-ion Battery (LIB) cells due to its high cell voltage window (2.5 – 4.2 V) [4], high usable discharge capacity (110 - 155 mAh/g) [4], high cycle lifetime

(500 - 1500 cycles) [4] and reduced costs ($190/kWh at pack level - Tesla Model 3, 2018 model [5]). These characteristics are more advantageous than other technologies such as lead-acid or nickel-metal hydride [4, 6]. To meet vehicle energy and power requirements, vehicle battery packs are typically equipped with a high number of cells connected electrically in series and parallel. For instance, the battery pack of the Jaguar I-Pace 2018 model comprises 36 modules of 3S4P configuration summing to 432 LIB pouch cells [7]. 3S4P means that four cells are connected in parallel and then this parallel stack is connected three times in series.

From a customer viewpoint, the most important aspects that are considered to purchase a BEV or HEV are vehicle price, running costs, available financing options, regulatory incentives/constraints and technical characteristics of the vehicle [8]. Regarding the technical characteristics, the key performance indicators that customers pay more attention to are: vehicle performance, range, safety, charging time and lifetime [8]. Battery degradation affects each of these key performance indicators negatively. Capacity fade and resistance rise are the two metrics commonly used in the automotive industry to quantify battery degradation. Capacity, as known as the maximum energy that a battery can store and release, determines maximum vehicle's range. Resistance rise increases thermal losses as $P_{bat} = I^2 \cdot R$, and thus, reduces battery performance.

An example where battery degradation can be a serious problem in automotive applications is given by Myall et al. [9] and further reported in [10,11]. The authors in [9] revealed that the lifetime of the 30kWh Nissan Leaf battery pack, manufactured between 2011 and 2017, reduces 75% after 2.1 years due to poor thermal management. This decrease in battery lifetime reduces the range by 29 km on average over 2.3 years. Taking into account that the warranty period of the Nissan Leaf is 5 years, the reported range reduction is leading to recalls from Nissan's customers [10]. Having in consideration that the price of a battery pack for a BEV may be as high as £10,000 each [12], Nissan may need to face significant costs to resolve their customer's recalls. Therefore, mitigating costly failures

within the warranty period is vital for automotive OEMs to ensure a commercially viable business strategy.

Aside from the reduction of vehicle performance, range and lifetime, battery degradation can eventually lead to catastrophic failures after ageing mechanisms are triggered by particular operating conditions. For instance, lithium plating is a well-known ageing mechanism produced at temperatures lower than 5 ℃ and C-rates larger than 2C. Lithium plating leads to dendrite growth on the anode surface that can puncture the separator. If dendrites puncture the separator, the battery will short-circuit (catastrophic failure) [13]. To the best of our knowledge, there has not been reported a battery catastrophic failure in the automotive industry due to a degradation event. The majority of the battery catastrophic failures reported [14] occur due to crash events.

Based on the example reported in [9], it can be concluded that understanding battery degradation is essential to minimise its adverse effects on battery performance, range, safety and lifetime. In line with this, the scope of this research is to study the topic of battery health diagnosis with the aim of improving the technical key performance indicators of a future BEV and HEV.

1.2 Research objective and aims

The research objective of this Innovation Report is to derive the most appropriate definition of battery State of Health (SoH) and to define how, within the context of a real-time embedded control application such as a Battery Management System (BMS), SoH diagnosis may be meaningfully employed to improve the performance of future BEV and HEV. Next, this research aims to reduce the negative implications of battery degradation in future BEV and HEV. This investigation will ultimately bring a positive impact to key performance indicators such as vehicle performance, range and battery lifetime. Following on from the literature review conducted in Chapter 2 and the challenges faced by the

sponsoring company (refer to Section 1.3), battery health diagnosis is studied within two research areas:

1. **Cell-to-cell Variabilities (CtCV) and implications for SoH:** motivated either by intrinsic factors such as inconsistencies in the manufacturing processes, and/or extrinsic factors such as non-uniform temperature distribution over a battery pack, CtCV always exist in LIB packs. As it will be explained in Section 2.2.1, CtCV contribute to battery degradation, and hence, the diagnosis of CtCV is essential to ensure appropriate performance, range, safety and lifetime levels in LIB packs. This research area includes two studies: Study 1 and Study 2.

2. **Improvement of SoH definition:** currently the BMS quantifies battery SoH based on the decrease in capacity, SoH_E, and increase in resistance, SoH_P [15]. This mathematical definition does not include an indication of the underpinning ageing mechanisms causing the degradation. Understanding the root causes of battery degradation is key to improve battery lifetime control strategies and to support future battery designs. This understanding ultimately will have a positive impact on the mentioned key performance indicators of LIBs. This research area includes two studies: Study 3 and Study 4.

1.3 The sponsoring company and their relevance to the direction of the research

The direction of the research was considered from the perspective of Jaguar Land Rover, the sponsoring company. Jaguar Land Rover is a subsidiary of the Indian automotive company, Tata Motors. For the third consecutive year, Jaguar Land Rover is in 2018 the largest automotive manufacturer in the United Kingdom (UK) [16]. Jaguar Land Rover focuses on the design, development, manufacture and sale of luxury cars, sport utility vehicles and sport cars. Jaguar Land Rover products accounted for more than 30% of

all domestic car production in 2016, and their product lines are among the top ten best-selling British manufactured vehicles in 2017 [16, 17].

Like many of their competitors such as BMW or Mercedes-Benz, Jaguar Land Rover has been adopting a vehicle electrification strategy to meet automotive regulations such as European regulation 443/2009 [2]. Jaguar Land Rover has launched HEV variants of their Range Rover model in 2014 [18], and the BEV Jaguar I-Pace in 2018 [19]. Jaguar Land Rover has to ensure that every new product is fit for purpose and operates reliably and safely in the marketplace. When Jaguar Land Rover initially commissioned this doctoral study in 2014, they had limited documentation regarding battery health diagnosis under real-world operating conditions. Jaguar Land Rover outsourced the whole battery design of its Range Rover HEV. During the designing phase of the Range Rover HEV in 2012-2014, Jaguar Land Rover realised the importance of battery technology for the development of HEVs and BEVs [20]. From this point, Jaguar Land Rover changed their strategy by focusing on the in-house development of battery technology. In particular, when this doctorate was commissioned in 2014, Jaguar Land Rover aimed to improve their knowledge and expertise in the following topics:

1. Impact of CtCV on battery pack performance and lifetime.
2. Detection and minimise in-market warranty faults.
3. Description of contingency plan after battery pack failure, e.g., in swapping modules or pack replacement.
4. Assessment of balancing strategies.
5. Accurate SoH estimation.
6. Non-invasive SoH diagnostic techniques.

Based on a battery pack simulation model, Study 1 proposes a systematic procedure to quantify the amount and the origin of CtCV for different pack topologies and cell

chemistries. This procedure and the further application of the simulation model aim to contribute from the first to the fourth challenge identified by Jaguar Land Rover.
Regarding the topic of accurate SoH estimation described in the fifth point, the contribution of this thesis is twofold. Firstly, cell-to-cell SoH for an imbalance scenario is quantified experimentally in Study 2. Secondly, a robust and effective methodology to monitor SoH at battery module/pack level for the same imbalance scenario is also presented in Study 2.
The second research area of this thesis focuses on the evaluation of non-invasive SoH diagnostic techniques, see sixth Jaguar Land Rover challenge. In order to select the most appropriate diagnostic technique to improve the definiton of SoH, an extensive review of the literature was conducted in Study 3. Following on from the outcomes of this review, Study 4 proposes a step-by-step methodology to quantify the most pertinent degradation modes (DMs) based on full-cell measurements. Additional detail regarding the impact of this research into Jaguar Land Rover activities is given in Chapter 7. The results are also applicable to other organisations developing BEVs and HEVs. As evidence, part of the work performed here has been recognised through index conference and journal publications [21–24].

1.4 Scope of the thesis

The scope of this thesis is to provide knowledge of battery health diagnosis and understanding battery degradation within on-board and off-board vehicle applications. On-board and off-board applications are also named as real-world vehicle applications within this thesis. On-board processes take place uniquely inside the vehicle through, e.g., a microcontroller system. Off-board operations require the use of external equipment to measure and process the parameters. On-board and off-board are different terms than online and offline. On-board and off-board determine whether data is measured and processed internally or externally with respect to the vehicle. Online and offline denote when data is being processed. Offline processing is when a method is applied retroactively, on

data which has been previously acquired. Online processing is when a method is applied in real time, as soon as the data is being acquired. There is also a combination of offline and online options, called hybrid option. The hybrid option is characteristic when some parameters are processed offline and others online. Based on this, Table 1.1 shows the different possibilities for an on-board and off-board process. The diagnostic methods studied in this Innovation Report falls into the first possibility. The development of the other possibilities is evaluated in Section 7.5.

Table 1.1: Possibilities for on-board and off-board process.

Possibility	Process	Data processing
1		Offline
2	Off-board	Online
3		Hybrid
4		Offline
5	On-board	Online
6		Hybrid

The author argues that the outcomes of this research would ultimately bring a positive impact to vehicle key performance indicators such as performance, range, and battery lifetime. LIB research and development is a multidisciplinary field driven by many disciplines such as physics, chemistry or engineering. Each of these disciplines is interlinked and hence, knowledge and experience in each of them are required. The research undertaken in this doctorate is focused on the engineering side of battery health diagnosis. Therefore, it is beyond the scope of this thesis to understand, identify and quantify ageing mechanisms at the material, physical and chemical level. Physicochemical and electrochemical invasive techniques such as Scanning Electron Microscopy, Energy Dispersive Spectrometry or X-Ray Diffractometry are commonly used to analyse ageing mechanisms at such level.

Within the field of engineering, this Innovation Report has distinguished different research levels. These research levels are defined as proof of concept, validation and implementation. Proof of concept is defined as the demonstration of an idea that has practical

potential [25]. Proof of concept is usually small and may not be complete [25]. Validation is the group of procedures that are used together to ensure that a product, service, or system meets requirements so that it fulfills its intended purpose [26]. For instance, the validation of a battery simulation model comprises to check the output of the model is the same as the output of the physical system such a battery measurement, within a predefined error threshold. Implementation is the realisation of a technical specification or concept. For example, the implementation of a battery model consists of transferring the concept into a software and hardware environment so that the concept can be applied in reality. As it will be explained in Section 7.5, this research covers different aspects in terms of proof of concept. In particular, it is beyond the scope of this study to:

- Understand and analyse the simulation model provided by Hawai'i Natural Energy Institute (HNEI), described in Chapter 3. Likewise, it is beyond the scope of this study the improvement, validation and potential software and hardware implementation of this model. This model was employed with the aim of developing a systematic procedure to quantify the amount and the origin of CtCV for different pack topologies and cell chemistries.

- Describe the validation and implementation of the proposed non-invasive diagnostic techniques extensively. Such a description needs to define software and hardware requirements for cell, modules and battery packs. An example of such descriptions would be to determine the requirements to perform an Electrochemical Impedance Spectroscopy (EIS) measurement at battery pack level on-board in a vehicle.

Additional information regarding areas of further work within the scope of this thesis is given for each respective study and is discussed in Section 7.5.

1.5 Structure of the portfolio

This Innovation Report is derived from a series of research Submissions based on investigations conducted during the tenure of the Engineering Doctorate (EngD) International (Int.). The portfolio structure is presented in Figure 1.1. The chronological order of the Submissions is not reflective of the structure of this Innovation Report. Therefore, it is recommended that the portfolio supporting this Innovation Report be reviewed in the order defined in Figure 1.1.

As described in Section 1.2, the research within this EngD focused on two key subject areas to understand battery degradation in real-world vehicle scenarios. A definition of the problem and a critical review of the current research is presented within the introductory Chapters of Submissions 4 and 1 for research area 1, and Submissions 3 and 2 for research area 2. Figure 1.1 illustrates that each Submission corresponds to a different study, or Chapter, in this Innovation Report. Submission 4, presented in Chapter 3, represents the work undertaken at HNEI, and hence, experimental data and models are independent to Submission 1, presented in Chapter 4. However, both Submissions belong to the topic of CtCV in a module/battery pack, and thus, they are presented along with research area 1. Submission 2, presented in Chapter 6, uses the conclusions from Submission 3, presented in Chapter 5, and both define research area 2. Submissions 2 and 3 were written simultaneously, explaining why Submission 2 uses the conclusions of Submission 3. Submission 2 was reported earlier than Submission 3 in order to arrange the publication of [24] more rapidly. Submission 3 is an extensive literature review and thus it can be unusual to have it in Chapter 5 of the Innovation Report. However, this Innovation Report has differentiated clearly two research areas and Submission 3 is reported at the beginning of the second research area.

The experimental data gathered in Submission 1 is further used in Submission 2. This relationship shows that although each research area covers a different topic, they are still

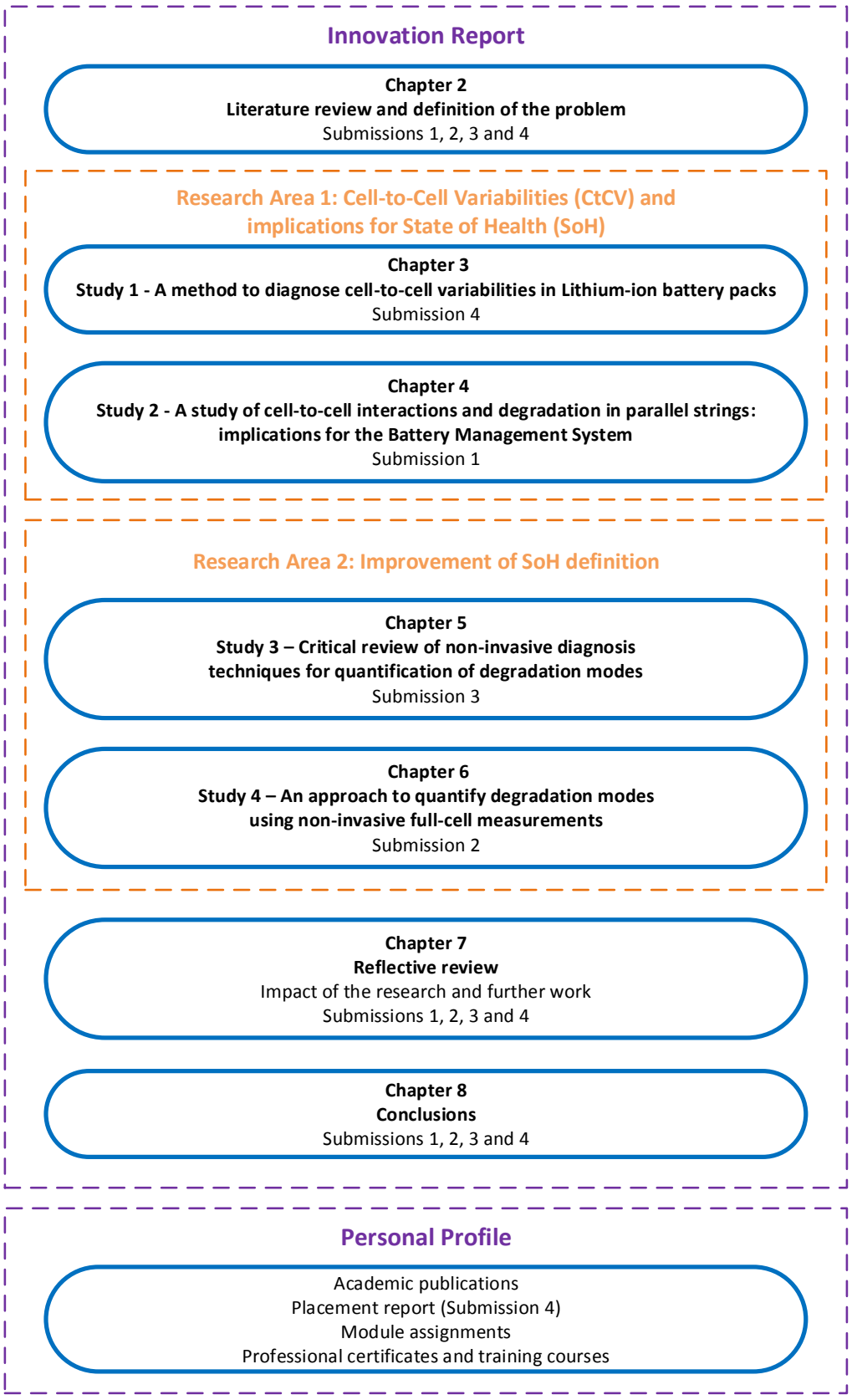

Figure 1.1: Portfolio structure

related to one another under the theme of battery health degradation in real-world vehicle applications.

Other Submissions to the portfolio include all assignments from the four MSc modules undertaken, published journal and conference papers from this research project [21–24], the international placement report, presented as part of Submission 4, and copies of certificates from training courses and professional accreditation. A summary of the primary competencies developed or enhanced through the activities and research completed with the EngD (Int.) is presented in the personal profile.

1.6 Structure of the Innovation Report

This Innovation Report defines the research undertaken and demonstrates the connection between projects that have all contributed to the requirements of the EngD (Int.).

Chapter 2 critically reviews the current state of the art concerning previous studies that have investigated two research areas: 1. CtCV and implications for SoH; and 2. Improvement of SoH definition. After identifying the main findings and knowledge gaps in each research area, research objectives are defined. Each of these objectives led to the research work undertaken within this doctorate.

Chapter 3 investigates a procedure to quantify the amount and the origin of CtCV for different pack topologies and cell chemistries. For this, a battery pack model developed by HNEI was employed. Using battery pack voltage response, Incremental Capacity (IC) analysis is applied to quantify in-situ the amount and the source of CtCV through predefined Features of Interests (FOIs).

Chapter 4 analyses the cell-to-cell SoH variation of four commercial 18650 Li-ion cells con-

nected in parallel. Using the experimental data gathered in this test, Chapter 4 identifies a linear relationship between resistance and capacity measurements for battery modules comprised of cells at different ageing states.

Chapter 5 reviews the non-invasive diagnostic methods employed to quantify DMs. To provide a tangible benefit to Jaguar Land Rover, this review is conducted based on the requirements that these techniques need to fulfill in real-world scenarios. Taking into consideration the conclusions made in Chapter 5, Chapter 6 proposes a step-by-step methodology to identify and quantify DMs based on full-cell measurements. For this, Incremental Capacity-Differential Voltage (IC-DV) and EIS techniques are employed with the aim of considering different ageing indicators, i.e., IC-DV considers voltage and capacity, and EIS considers impedance. The results obtained with each technique are critically evaluated and compared within the context of BMS implementation. To analyse these techniques close to a real application, this study considers the experimental data set gathered in Study 2.

The outcomes of this research have resulted in four innovations. Innovation is defined as the successful exploitation of an idea [27]. For each innovation, the contribution to academia and the impact to the sponsoring company are described in Chapter 7. The contribution to academia is reflected by the first author publication of 3 Q1 Journal papers [21, 24, 28] and 2 index IEEE conference papers [22, 23]. Two Q1 journal articles as second author were also published [29, 30]. The impact into the sponsoring company is evidenced by the significant contribution to the main research areas regarding battery health degradation, shown in Section 1.3. Chapter 7 also discusses the limitations and areas of further work concerning the proof of concept, validation and implementation of the innovations presented in this thesis. Finally, Chapter 8 presents a summary and the overall conclusions of this research.

2. Literature Review

2.1 Introduction

Chapter 1 places this thesis into context, highlighting the key research challenges that academia and industry are facing regarding the diagnosis of LIBs for BEV applications. This chapter aims to translate the research challenges in each of these areas into research questions. For each research question, the most relevant literature is reviewed. Additional details of this review can be found in individual submissions to the portfolio [31–34] and publications [21–24]. After identifying the main findings and knowledge gaps in each research area, research objectives are defined. Each of these objectives leads to the research work undertaken within this doctorate. Table 2.1 relates each research area and research question with the objective and the Chapter where the objective is addressed. In addition, Table 2.1 shows in which submission and publication each research question is investigated in greater depth.

Table 2.1: List of research questions and objectives.

Research Area	Research Question	Main Research Objective	Chapter	Studied in	Published in
CtCV and implications for SoH	1) Can the amount and origin of CtCV be quantified?	Investigate a systematic procedure to quantify the amount and origin of CtCV.	3	Submission 4	[29, 30]
	2) How valid is the SoH as a measure of ageing when cells are connected in parallel?	Experimentally quantify the cell-to-cell SoH for a scenario when each initial cell SoH is different.	4	Submission 1	[21]
	3) Is there a time efficient methodology to monitor SoH?	Evaluate a time efficient methodology to monitor SoH at battery module/pack level comprised of inhomogeneous aged cells.	4	Submission 1	[21]
Improvement of SoH definition	4) Which are the most advantageous non-invasive diagnostic techniques to quantify DMs?	Conduct a critical review to select the most appropriate non-invasive diagnostic technique.	5	Submission 3	[28]
	5) How DMs can be quantified using an automated methodology based on non-invasive full-cell measurements?	Derive an automated methodology to quantify the most pertinent DMs based on non-invasive full-cell measurements.	6	Submission 2	[22–24]

2.2 Research Area 1: Cell-to-cell variabilities (CtCV) and implications for State of Health (SoH)

2.2.1 Research question 1

Cell properties within a single battery pack can vary due to intrinsic and extrinsic factors [35]. Intrinsic factors are defined as inconsistencies in the materials used and manufacturing processes within a battery pack [36]. Intrinsic factors are currently mitigated by improving battery designs and manufacturing and quality control processes [36]. For example, calendric, pasting and coating manufacturing processes in commercial LIBs limit ageing mechanisms related to conductivity losses [37]. These ageing mechanisms can be copper dissolution or aluminum corrosion [38]. Extrinsic factors include those caused by the process environment, e.g., non-uniform current or temperature distribution within the complete battery pack [35]. As reported by Bruen et al. in [35], non-uniform current distribution causes an energy imbalance within the cells and therefore a change in cell internal resistance. The BMS mitigates the impact of extrinsic factors by regulating a number of parameters that include, but are not constrained to, the level of charge or discharge power, the allowable Depth of Discharge (DoD) of the battery or the temperature range that the battery operates over. For instance, according to Worwood et al. [39], a number of studies agree that the absolute operating temperature of LIBs should be kept within a range of circa 15-25 ℃ regardless of the ambient temperature and an absolute temperature gradient between cells not exceeding 5 ℃.

Although the negative impact of intrinsic and extrinsic factors are counteracted, CtCV cannot be eliminated and always exist. For example, differences in commercial cells from initial manufacture and integration (intrinsic variability) may be circa 9% for capacity [40] and 25% for resistance [41]. Furthermore, Jiang et al. [42] illustrated that a maximum of 7% CtCV of initial SoC during battery operation (extrinsic variability) reduces the

maximum available capacity of the pack by 25%. Therefore, to ensure the level of ageing and performance, CtCV within a pack need to be diagnosed along with battery operation. From this, a clear research question is formulated:

Research Question 1: Can the amount and origin of CtCV be quantified?

According to Rumpf et al. [36], the majority of the literature analyses variations of individual cells within a batch. Only a few studies [42–46] evaluate CtCV within battery modules and packs. These studies are reviewed here.

Miyatake et al. [43] have experimentally evaluated the influence of CtCV on the discharge capacity of different battery module topologies composed up to 12 18650 Nickel Cobalt Aluminium (NCA) oxide cells. The results showed that when cells are connected in series, the module capacity is affected by the cell with the smallest capacity. When cells are connected in parallel, the capacities of the single cells add up to the module capacity. When cells are connected in series and parallel, the module capacity depends on the module configuration.

Jiang et al. [42] measured cell variations of a 95S5P 18.5 kWh Lithium-iron Phosphate (LFP) battery pack. This pack was disposed after using over three years, equivalent to 32500 km, from a typical electric passenger car. Jiang et al. [42] show a maximum of 7% CtCV of initial SoC during battery operation reduces the maximum available capacity of the pack by 25%. Furthermore, they evaluate the ageing mechanisms due to CtCV using IC curves. IC analysis is discussed in Section 3.4.4.

Paul et al. [44] study ageing inhomogeneities due to temperature gradients and cell-to-cell variations. In agreement with Jiang et al. [42], the results highlight that temperature and SoC CtCV are the main causes of discrepancies in cell ageing.

Quantifying the mean and the standard deviation, Zhang et al. [45] analysed the influence of CtCV due to variations in capacity and SoC. In agreement with Jiang et al. [42], the

results show that SoC variation has more significant impact into CtCV. This impact is because SoC imbalance is the dominating factor in the reduction of capacity.

Zhou et al. [46] developed a 96S1P LFP battery pack model to evaluate the impact of CtCV. The results revealed that CtCV are mainly affected by coulombic efficiency, self-discharge rate, and temperature. Coulombic efficiency represents the fraction of the electrical charge stored during charging that is recovered during discharging [47]. For LIBs coulombic efficiency varies between 0.85 and 0.95 [47]. Zhou et al. [46] claimed that initial capacity, initial SoC, initial resistance, capacity fade and resistance growth have little effect on CtCV. This finding disagrees with the previously reviewed studies [42, 44]. These studies showed that initial capacity [45], internal resistance [45] and initial SoC [42,44,45] have an impact on CtCV. Validation of Zhou's et al. [46] model with experimental data is not provided in this study. The lack of validation may explain potential inaccuracies in the results obtained in [46] and thus, the disagreement with [42, 44, 45].

Through experiments or simulations and further statistical analysis, the studies highlighted above quantify the impact of CtCV in battery packs due to differences in temperature, SoC, resistance, capacity and coulombic efficiency. However, none of these studies suggests a systematic methodology to evaluate the amount and the cause of CtCV within battery packs, independent of cell chemistry and battery pack topology. From this, the following research objective is defined:

Research Objective 1: Investigate a systematic procedure to quantify the amount and origin of CtCV.

2.2.2 Research questions 2 and 3

If CtCV exceeds the limits recommended by an OEM to ensure appropriate operation of the pack, then the OEM, before mounting the pack in the vehicle, or the BMS, during battery operation, would need to countermeasure it. For instance, Paul et al. [44] suggest that CtCV from intrinsic factors in terms of capacity should be lower than 4% in automotive applications. If CtCV exceeds this limit, then a possible countermeasure would be to replace the modules affected by new modules.

A common effect of CtCV during operation is inhomogeneous degradation within a battery module or pack. An example of inhomogeneous ageing is shown by Paul et al. in [44] where initial CtCV of 4.5% in capacity leads to a maximum cell-to-cell capacity spread of 10.5%. In this study, batteries are aged using a HEV customer's driving profile. Further details of this study can be found in [44]. From Kirchhoff's law, it is known that cells connected in series share the same current, whereas the current is spread through different cells when they are connected in parallel. In the latter case, the current circulated in each cell may be different due to the properties of each cell are not the same (CtCV) and due to variations in interconnection resistance. For example, Gong et al. [48] showed that when two cells with a 20% impedance difference are connected in parallel, the peak current experienced was 40% higher than if the cells were identical.

For the case when cells are connected in parallel, the BMS commonly does not monitor the SoH of each individual cell because the installation of individual current and temperature cell sensors would increase the cost of the battery pack. According to the U.S. government's Advanced Research Projects Agency for Energy (ARPA-E) [49], the cost of sensors accounts for 20-30% of the total cost of a battery pack. Conversely, the absence of current and temperature sensors makes it difficult to determine capacity and power fade at a cell level when cells are connected in parallel. For instance, Coulomb counting, the

most common method to determine capacity in the automotive industry [50], determines capacity based on the integration of current over time. Therefore, the measurement of the current is essential to determine battery capacity. As a solution, the BMS typically approximates the SoH as a single equivalent value for the whole battery module when cells are connected in parallel [51]. This approximation is based on the assumption that the SoH of cells connected in parallel are the same since they have equal terminal voltages. This assumption is however no longer valid when cell properties change over ageing due to intrinsic or extrinsic factors. The lack of experimental data proving or disproving this assumption leads to the following research question:

Research Question 2: How valid is the SoH as a measure of ageing when cells are connected in parallel?

According to Bruen et al. [35], the presence of different resistance paths will underpin an uneven current distribution within the battery system. This scenario represents an example where it may not be beneficial to approximate the SoH as a single equivalent value for the whole battery stack. Such as scenario has been previously examined in [41, 48, 52, 53], and hence, these studies are reviewed.

Gogoana et al. [41] cycled two cylindrical LFP cells connected in parallel to evaluate the degradation of each cell over time. They identified that an initial 20% discrepancy in internal resistance between cells in a parallel string results in a 40% reduction of the total cycle life. They attributed this result to the uneven high currents experienced by each cell.

Gong et al. [48] cycled four groups of Li-ion cells. Similar to Gogoana et al. [41], each group of cells comprised of two cells with different degradation levels. They showed that when two cells with a 20% impedance difference were connected in parallel, the peak current experienced was 40% higher than if the cells had the same impedance.

Unlike Gogoana et al. [41] and Gong et al. [48] where the temperature was kept constant, Zhang et al. [52] cycled two 26650 LFP cells connected in parallel, with each cell

at 5℃ and 25℃, respectively. Based on a simplified thermal-electrochemical model, it was shown that temperature differences between the cells make self-balancing difficult. Consequently, this situation leads to accelerating battery degradation [52].

Shi et al. [53] cycled two groups of LFP batteries, each one comprised of two cells, for life and performance analysis. The first group was tested at 25℃, whereas the second group was tested at 25℃ and 50℃ to evaluate the effect of high temperature. In agreement with Zhang et al. [52], they concluded that imbalanced currents directly affect the rate of capacity fade of cells connected in parallel.

These studies highlight that when cells are connected in parallel, they will age differently if the SoH of each individual cell is not the same. However, none of these studies quantifies the SoH in an ageing scenario. From this, the second research objective is defined as:

Research Objective 2: Experimentally quantify the cell-to-cell SoH for a scenario when each initial cell SoH is different.

Following on from [6,15], SoH_{E} and SoH_{P} are calculated as a percentage with respect to the difference between Begin of Life (BoL) and EoL in either capacity or resistance, as shown Equation 2.1 and Equation 2.2, respectively.

$$SoH_E = \frac{C_{now} - C_{EoL}}{C_{BoL} - C_{EoL}} \cdot 100 = \frac{C_{now} - 0.8 \cdot C_{BoL}}{C_{BoL} - 0.8 \cdot C_{BoL}} \cdot 100 = \frac{C_{now} - 0.8 \cdot C_{BoL}}{0.2 \cdot C_{BoL}} \cdot 100 \tag{2.1}$$

$$SoH_P = \frac{R_{now} - R_{EoL}}{R_{BoL} - R_{EoL}} \cdot 100 = \frac{R_{now} - 2 \cdot R_{BoL}}{R_{BoL} - 2 \cdot R_{BoL}} \cdot 100 = \left(2 - \frac{R_{now}}{R_{BoL}}\right) \cdot 100 \tag{2.2}$$

An upper and a lower limit bounds the calculation of SoH: BoL and EoL. BoL, equivalent to SoH = 100%, represents the state when the battery is new. EoL is defined as the

condition when the battery cannot meet the performance specification for the particular application for which it was designed [15]. In essence within many applications, EoL corresponds to the battery end of warranty period. Each automaker sets its own end of warranty period according to different factors such as government incentives, legislation, product costs, performance limits or customer relationship. For instance, Jaguar Land Rover end of warranty is set to 8 years or 100,000 miles, whichever comes first [54]. In relation to capacity and resistance, the EoL values are defined as [6, 15]:

$$C_{EoL} = 0.8 \cdot C_{BoL} \tag{2.3}$$

$$R_{EoL} = 2 \cdot R_{BoL} \tag{2.4}$$

According to standards such as the United States Advanced Battery Consortium (USABC) [55], and test procedures such as CATAPULT [56], measuring capacity or resistance on-board by a BMS can be difficult in automotive applications. According to USABC standard [55], capacity determination requires at least a complete discharge cycle with a current that is less than or equal than 1C. These conditions are difficult to achieve during operation since the battery is loaded with different dynamic profiles [6]. On the other hand, discharging the battery when a vehicle is parked and transfers this energy to the electrical grid, i.e., Vehicle to Grid (V2G) scenario, could be a possibility as reported by Uddin et al. [57]. However, V2G technology is still under development and full commercialisation of this concept has not been proved [57].

Regarding the measurement of the cell resistance, this is either performed in the time domain using the pulse power test, or in the frequency domain using the EIS test [58]. As shown by Waag et al. [59], resistance measurements mainly depend on temperature and SoC. A prior SoC adjustment to measure the resistance involves keeping for 3h the cells under no load until they reach their equilibrium state [60]. Similar to the capacity test,

allowing time for the cells to relax makes the pre-conditioning process of the EIS or pulse power test slow. The amount of time required to measure capacity or resistance leads to the following research question:

Research Question 3: Is there a time efficient methodology to monitor SoH?

To answer this question, previous studies [58, 61, 62] have found a linear relationship between the measurement of capacity fade and the resistance raise. This relationship can be employed to estimate capacity based on the measurement of the ohmic resistance. This relationship requires only the measurement of the ohmic resistance and thus, the time required to measure the capacity is saved. As explained in [58], the measurement of the ohmic resistance using the pulse power test is in the order of seconds. The ohmic resistance does not change significantly with respect to the SoC and hence, the measurement of the ohmic resistance does not require to keep the cells relaxed for 3h previous to the measurement. Previous studies [58, 61, 62] which have investigated this relationship are reviewed as follows.

Takeno et al. [61] measure the capacity and the resistance at 1kHz of 800 commercially available Li-ion battery packs for mobile phones, which were degraded at a variety of capacity levels. They calculated a linear regression to estimate the capacity of each battery pack based on the measurement of the resistance. The error in the estimation of the capacity was less than 20% for about 90% of the tested battery packs. Following on from internal communications with Jaguar Land Rover [20], the author states that this error is not admissible for automotive applications. An appropriate value for the error of capacity estimation depends on the particular requirements of each OEM.

Similarly to Takeno et al. [61], Dong et al. [62] show a linear correlation between capacity measurements and the polarisation resistance of 18650 LIBs. The polarisation resistance is defined as the sum of the ohmic and the charge-transfer resistance. In between constant charge and discharge cycles, the capacity and the polarisation resistance was measured.

The batteries were cycled until their EoL threshold, defined as 70% of the nominal capacity.

Schuster et al. [58] investigate the correlation between capacity and resistance of NMC LIBs. In comparison to Takeno et al. [61] and Dong et al. [62], the investigated cells were aged in different operational conditions: laboratory ageing experiments as well as three years of usage in two identical BEVs. The laboratory ageing tests composed of capacity and EIS tests were subdivided into calendar and cycle life tests. For all the tests studied, the authors found a correlation between capacity and ohmic resistance, and between capacity and polarisation resistance.

The reviewed studies reinforce the concept of a correlation between capacity reduction and resistance rise for individual cell measurements. Only Schuster et al. [58] prove this correlation of cells disassembled from a BEV battery pack. However, this data is related to a specific state of ageing. Thus, the relationship between capacity and resistance may not be valid for different ageing states and therefore may not be useful to implement in cases of inhomogeneous aged cells. In line with this, the third research objective of this doctorate is defined:

Research Objective 3: Evaluate a time efficient methodology to monitor SoH at battery module/pack level comprised of inhomogeneous aged cells.

2.3 Research Area 2: Improvement of SoH definition

2.3.1 Research question 4

Degradation of LIBs is an extremely complex process that depends on a variety of ageing mechanisms. Ageing mechanisms can be caused by parasitic reactions such as SEI or lithium plating; or by mechanical degradation, e.g., reduction of sites, or mechanical

stress, e.g., particle cracking [38]. Parasitic or side reactions are chemical reactions as part of the working processes of batteries, e.g., charge-transfer reactions. These reactions are characteristic of leading to unwanted effects such as the acceleration of degradation [38]. Aside from chemical processes, mechanical processes can lead to degradation as well [38]. For instance, a typical mechanical process in LIBs that leads to battery degradation is the change in electrode particle's structure [38]. As the nature of each ageing mechanism is different, each of them is accelerated by a particular extrinsic or/and intrinsic factors [38]. For instance, SEI growth is caused by parasitic reactions, and it is known to be accelerated at temperatures higher than 35℃ and currents rates larger than 2C [38]. Conversely, particle cracking is a mechanical process motivated at temperatures higher than 35℃, current rates larger than 2C and DoD windows larger than 80% [38].

According to [63, 64], understanding the reasons for battery ageing under real-world operating conditions can be used to:

1. Improve the design of new batteries and manufacturing processes.

2. Improve lifetime control strategies within the BMS.

For instance, an intercalation gradient strain in the active material leads to a volume change within the electrode [65]. A battery design improvement would be to use robust polymeric binders such as alginate binder, for the cases where volume expansion, i.e., mechanical fracture of the electrodes, is pertinent [66]. The BMS can also reduce the impact of extrinsic factors on battery pack degradation. For example, lithium plating is an ageing mechanism characteristic of charging LIBs at temperatures lower than 5℃ [38]. A strategy for the BMS to mitigate lithium plating would be to control the temperature as a function of the amount of lithium plating. In practice, such a strategy can be achieved through efficient thermal management.

Previous studies [64, 66–68] suggest categorising the different ageing mechanisms into DMs named as Conductivity Loss (CL), Loss of Lithium Inventory (LLI) and Loss of Ac-

tive Material (LAM). CL includes the degradation of the electronic parts of the battery such as current collector corrosion or binder decomposition [38]. LLI is attributed to the variation of the number of lithium-ions (Li-ions) that are available for intercalation and de-intercalation processes [38]. LAM is related to structural transformations in the active material (positive or negative electrodes), and non-active material elements (separator and electrolyte) [38]. The definition of the SoH does not quantify the most pertinent ageing mechanisms causing the degradation. Classifying the ageing mechanisms into DMs facilitate the ability of the BMS to indicate the ageing root causes in real-world applications [64].

Internal life assessment of LIBs such as changes in the structure of the materials has been widely studied in the past by applying physicochemical and electrochemical invasive techniques such as Scanning Electron Microscopy, Energy Dispersive Spectrometry or X-Ray Diffractometry [69]. The common disadvantage of these techniques is their inability of applying them in-situ, without opening the cells internally. This limitation makes these techniques unsuitable for SoH diagnosis within BMS applications. Hence, it is beyond the scope of this study to explain the operation of these techniques. From the evaluation of the pertinent literature, the following research question arises.

Research Question 4: Which are the most advantageous non-invasive diagnostic techniques to quantify DMs?

In-situ diagnostic techniques for LIB follow either thermodynamic or kinetic principles [70]. The thermodynamic based diagnostic techniques infer ageing mechanisms based on voltage phase changes [70]. The kinetic based techniques relate ageing mechanisms based on charge-transfer and diffusion reactions [70].

Concerning the capability to identify and quantify DMs, the thermodynamic based diagnostic techniques that are widely reported in the literature are pseudo Open Circuit Voltage (pOCV), IC-DV and Differential Thermal Voltammetry (DTV). On the other hand, EIS is used as a kinetic diagnostic technique. A detailed description, advantages,

and limitations of these techniques can be found in Submission 3 within the doctorate portfolio [33]. Before applying any of these techniques in isolation, it is required to evaluate the benefits and drawbacks of them. To ensure the impact of this research into Jaguar Land Rover, this evaluation was conducted based on the requirements that these techniques need to fulfill as part of real-world applications.

The primary reviews available in the literature focus on studying SoH diagnosis [6, 71–74] or prognosis [75–78] techniques. SoH diagnostic techniques estimate the SoH in the current state whereas SoH prognosis techniques estimate the SoH in a future state. The research area of quantification of DMs is in its early stage, with a limited body of publications. Thus, the fourth research objective of this doctorate is defined as:

Research Objective 4: Conduct a critical review to select the most appropriate non-invasive diagnostic technique.

2.3.2 Research question 5

The literature review conducted as part of Research Objective 4, presented in Chapter 5, evaluates the following non-invasive diagnostic techniques with the aim of quantifying DMs: pOCV, IC-DV, EIS, DTV and the combination (Comb.) of pOCV and EIS techniques. The review highlights that pOCV and IC-DV seem to be more advantageous than EIS, DTV and Comb. techniques because they fulfill a larger number of requirements of the evaluation criteria defined in Section 5.6.2.

The studies of Dubarry et al. [67] and Marongiu et al. [68] for pOCV and Dubarry et al. [67] for IC-DV have a substantial impact on the reviewed literature. Dubarry et al. [67] propose a half-cell and full-cell Equivalent Circuit Model (ECM) to simulate the electrode's response regarding voltage and capacity when the battery is at equilibrium. To emulate the equilibrium state, the cell is charged or discharged at current rates lower than C/10, measuring the charge and the pOCV. This response is connected to DMs through two parameters: the loading ratio and the offset. The loading ratio is the ratio

of the capacity between the Negative Electrode (NE) and Positive Electrode (PE), i.e., loading ratio = Q_{NE}/Q_{PE}. The offset represents the initial irreversible capacity loss of the NE that compensates the SEI formation. Further detail about the description of this model is provided within Submission 3 in Section 5.1.1 [33] and within Submission 4 in Section 2.1.1 and 2.1.2 [34].

The main drawback of the approach presented by Dubarry et al. [67] is the lack of evidence to implement it in real-world applications. This limitation is overcome in the method presented by Marongiu et al. [68]. The authors adapted the method proposed by Dubarry et al. [67] to quantify DMs of an LFP cell cycled by a repetitive dynamic profile at 25 ℃. This study stands out because of the capability to quantify DMs on-board using input data from parking and driving scenarios. Although this method was tested for LFP cells, it can also be applied to other cell chemistries similarly as the method proposed by Dubarry et al. [67].

Aside from quantifying the DMs using half-cell pOCV measurements, Dubarry et al. [67] also introduce the theory to relate the changes of IC and DV curves with DMs. Estimating the DMs based on the pOCV curves, then the changes in the full-cell IC and DV curves are related to these particular DMs. Based on this approach, Dubarry et al. [63] defined specific FOIs to quantify the changes in the IC and DV curves in a more systematic way. For instance, a FOI can be the peak's intensity of the IC curve. Additional detail regarding the determination of FOIs from IC and DV curves can be found in Section 3.4.4.

The working principle of the pOCV and IC-DV studied in [67,68] requires half-cell pOCV measurements. Even under laboratory conditions, half-cell voltage measurements are complex to perform because they need appropriate instrumentation equipment, e.g., reference electrode cell holders, for each specific cell format. Zhang et al. [66] show that for measuring half-voltages of 18650 cylindrical cells, a particular reference electrode was designed. Furthermore, commercial cells employed in real-world applications are two-electrode sys-

tems, i.e., only the potential between the working electrode and counter electrode may be measured. Therefore, half-cell voltage measurements are not possible to perform in real scenarios. To solve this, previous studies such as McTurk et al. [79] propose the installation of an internal cell reference electrode, enabling engineers to measure half-cell voltages in commercial cells. This research area is still in its early stage, and hence, full commercialisation of these cells has not been proved economically [79]. Therefore, pOCV and IC-DV techniques need to be adapted for full-cell measurements so that they can be implemented in real applications in the short-term. From this, the following research question is defined:

Research Question 5: How DMs can be quantified using an automated methodology based on non-invasive full-cell measurements?

Studies such as [42, 80, 81] identify DMs using IC-DV curves based on full-cell voltage measurements. However, none of them propose an automated methodology to quantify DMs. This limitation appears because automating the quantification of DMs involves the risk of performing an inaccurate diagnosis. As can be inferred from [38], ageing mechanisms are processes difficult to diagnose just by analysing voltage, capacity and resistance measurements. This is because ageing mechanisms depend on many other factors that are not considered with those measurements. For instance, SEI depends on electrode porosity.

As discussed in Section 2.2.2, SoH diagnosis involves the measurement of the capacity and the resistance [6]. Therefore, it is argued that considering the resistance as an ageing indicator will be beneficial for SoH diagnostic purposes. Zhang et al. [66] and Aurora et al. [82] employ EIS as a diagnostic technique to identify DMs. Same as the IC-DV related studies [42, 80, 81], neither Zhang et al. [66] nor Aurora et al. [82] propose an automated methodology to quantify DMs. In comparison to these studies, Schindler et al. [83] propose an automated method composed of a half-cell based pOCV model to quantify LAM and LLI; and an EIS based model to quantify the overpotential due to Li-ion kinetics. Despite the EIS sub-model provides useful insights into linking EIS

resistances with DMs, this submodel does not quantify the most pertinent DMs [83]. From the analysis of the literature it can be concluded that a diagnostic technique for quantification of DMs needs to fulfill two requirements:

1. It needs to use non-invasive full-cell measurements.
2. The quantification of DMs needs to follow an automated process.

Meeting these requirements would facilitate the application of a new diagnostic technique in real-world scenarios. From this, the following research objective is defined:

Research Objective 5: Derive an automated methodology to quantify the most pertinent DMs based on non-invasive full-cell measurements.

The term "most pertinent" means that the DMs quantified are an approximation of the DMs that can be inferred by applying physicochemical and electrochemical invasive methods such as Scanning Electron Microscopy. To quantify the level of approximation of this approach, the results obtained with non-invasive techniques, e.g., IC-DV, would need to be compared against the results derived by applying invasive methods in the future. Such a comparison requires to perform post-mortem analysis and hence, it is beyond the scope of this EngD.

After deriving automated methods to quantify DMs using IC-DV and EIS techniques, a question to answer would be whether both methods provide similar results. Answering this question shows whether employing different ageing indicators, full-voltage and capacity for IC-DV and impedance for EIS, would reveal different DMs. Following on from the literature review conducted in Submission 3, different studies identify DMs using IC-DV [42,80,81] and EIS [66,82,83] diagnostic techniques. As these studies focus independently either on IC-DV or EIS, none of them compare the results obtained between each of the techniques for the same scenario. In cases that both techniques provide similar results, then it would not be necessary to apply both in a particular scenario. This advantage is

extremely beneficial since using a single technique would ultimately reduce the time of the diagnostic task. This comparison is further evaluated in Chapter 6.

2.4 Conclusions

Battery health diagnosis in LIBs represents a key research area for industry and academia because battery degradation has a direct impact on vehicle performance, range and lifetime of BEVs. From this, the scope of this thesis is focused on two research areas: 1. CtCV and its implications for the diagnosis of SoH; and 2. Improvement of SoH definition. For each research area, this Chapter has formulated five research questions. For each research question, the most relevant literature is reviewed leading to five research objectives. The relationship between research questions and objectives is defined in Figure 2.1.

This review has shown that the presence of CtCV impacts negatively on the ageing, performance, and safety of battery modules and packs. To minimise the negative impact of CtCV it is essential to quantify the amount and the origin of CtCV. From this, researchers have reported the causes of CtCV so that the negative impact of CtCV into capacity fade within a battery pack can be controlled. None of the reviewed studies suggests a systematic methodology to evaluate the amount and the cause of CtCV within battery packs, independent of cell chemistry and battery pack topology. Instead, the reviewed studies [42, 44, 45] highlight via experiments or simulations the impact of CtCV in battery packs due to temperature, SoC, resistance, capacity and coulombic efficiency. From this, the first research objective is to investigate a systematic procedure to quantify the amount and origin of CtCV to reduce their negative impact within battery packs.

CtCV in, e.g., capacity or resistance, leads to inhomogeneous ageing through battery operation [35]. For the case when cells are connected in parallel, the BMS approximates the SoH as that of a single equivalent value for the whole battery stack. This approxima-

tion is based on the assumption that the SoH of cells connected in parallel are the same since they have equal terminal voltages. Previous studies [35, 41, 48, 52, 53] questioned that this assumption is no longer valid when cell properties change due to intrinsic or extrinsic factors. However, none of these studies prove this assumption under an ageing scenario. From this, the second research objective of this Innovation Report is to prove this assumption experimentally.

According to automotive standards such as USABC [55] and test procedures such as CATAPULT protocols [56], measuring capacity or resistance on-board by a BMS is time-consuming. Previous studies [58, 61, 62] have proved a correlation between the capacity reduction and the ohmic resistance rise in individual cells. This correlation enables to estimate the capacity based on the value of the ohmic resistance. This correlation requires only to measure the ohmic resistance and thus, the time required to measure the capacity is spared. In view of a potential implementation of this approach where a number of cells are connected resulting in battery modules and packs, this correlation needs to be tested. To answer this question, the third research objective is to prove that this correlation is valid when cells connected in parallel have different ageing states.

The common definition of SoH in BMS vehicle applications, used in Chapter 3, Chapter 4 and Chapter 5, does not indicate the ageing mechanisms which cause battery degradation. Previous studies [64,66–68] suggest categorising the different ageing mechanisms into DMs called CL, LLI, and LAM. Quantifying DMs under real operating conditions can be used to improve lifetime control strategies within the BMS and to improve the design of new batteries and manufacturing processes. In the aim of this, before selecting a diagnosis technique is required to investigate the advantages and drawbacks of them. In line with this, the fourth research objective is to conduct a review regarding the non-invasive SoH diagnostic techniques available in the scientific literature. Following on from the outcomes of this review, the fifth research objective is to develop a framework to quantify the DMs

using non-invasive diagnostic techniques based on full-cell measurements. IC-DV and EIS techniques were used for this purpose. The results obtained from each technique were compared to evaluate if the change in voltage/capacity, IC-DV, and resistance, EIS, leads to common DMs.

In summary, the literature review conducted in this Chapter has highlighted key areas which require attention in terms of battery health diagnosis of LIBs for BEV applications. The research questions and objectives formulated in this Chapter drives the entire direction of the rest of this report.

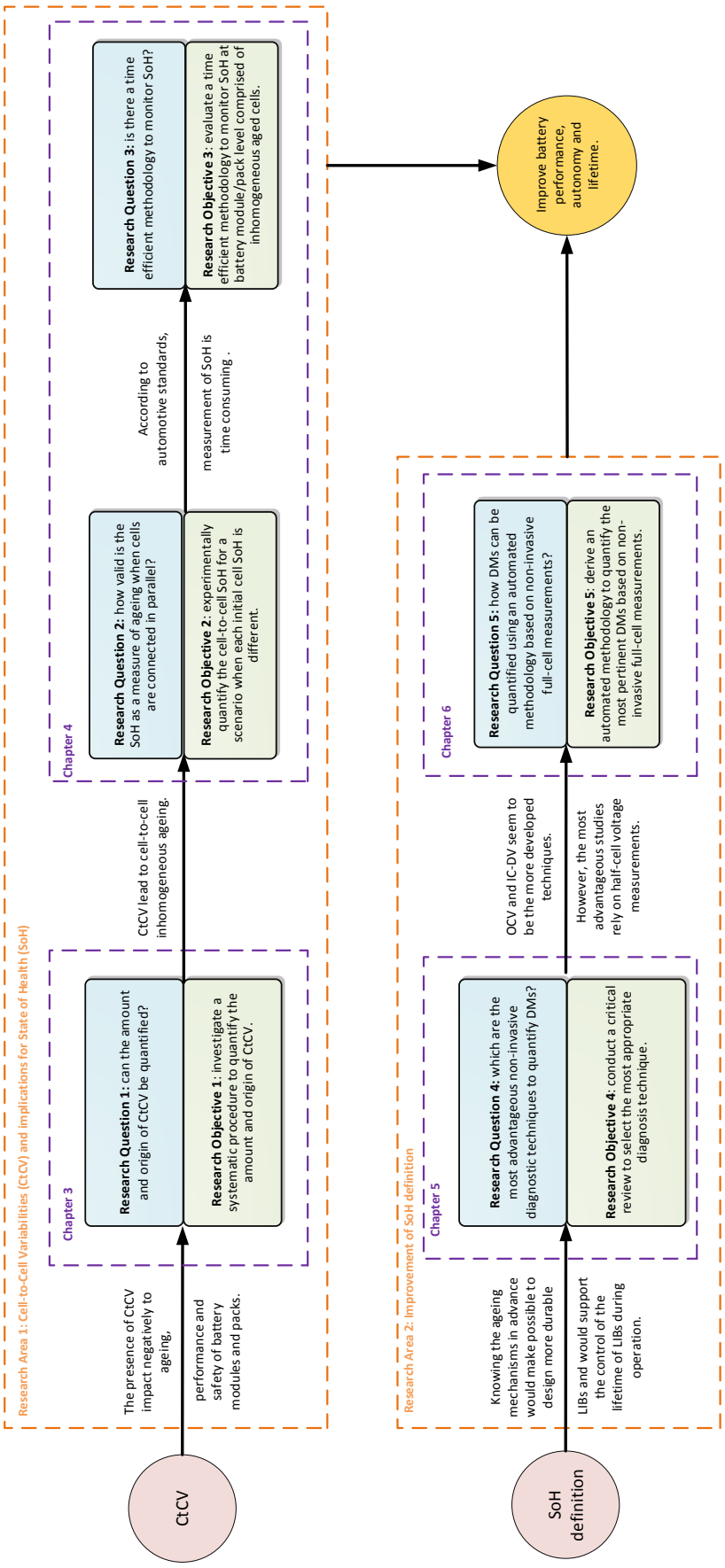

Figure 2.1: Relationship between different research questions/objectives

3. Study 1 - A method to diagnose CtCV in Lithium-ion battery packs

3.1 Introduction

To ensure an appropriate level of longevity, performance and safety, CtCV within a pack need to be diagnosed along with battery operation. Using experiments or simulations and further statistical analysis, the studies reviewed in Chapter 2 quantify the impact of CtCV in battery packs due to differences in temperature, SoC, resistance, capacity and coulombic efficiency. However, none of these studies suggest a systematic methodology to evaluate the amount and the cause of CtCV within battery packs, independent of cell chemistry and battery pack topology. To fill this knowledge gap, this study investigates a universal procedure to quantify the amount and the origin of CtCV in battery packs. For this, a battery pack model developed at HNEI was employed. Using battery pack voltage response, IC analysis is applied to quantify in-situ the amount and the source of CtCV through predefined FOIs. This study focuses on CtCV that are pertinent when the battery pack is new before mounting it into a vehicle. These can be intrinsic to the battery, e.g., CtCV due to manufacturing tolerances or differences in the amount of electrode material used [21, 36]; or extrinsic to the battery, e.g., variations in battery shipping or storage conditions [36]. CtCV which typically appear during battery cycling, such as non-uniform current or temperature distribution, are not considered in this study. As described in Section 3.7, such a study represents further work.

The structure of this Chapter is divided as follows: Section 3.2 defines the main objective of this study. Section 3.3 introduces the battery pack model used and its corresponding sub-models. Section 3.4 describes step-by-step the proposed diagnostic procedure to quantify the amount and the origin of CtCV. In order to meet the objectives defined in Section 3.2, the diagnostic procedure is applied to a range of test scenarios. The results are discussed in Section 3.5. Section 3.6 outlines the implications of the proposed diagnostic procedure for a BMS. To understand the further application of this diagnostic procedure, Section 3.6.3 suggests an approach to implement this methodology within the context of BMSs. The limitations of this study and further work are stated in Section 3.7. Finally, Section 3.8 presents the main conclusions of this study.

3.2 Objectives of this study

In agreement with Table 2.1, the main objective of Study 1 is to investigate a systematic procedure to quantify the amount and origin of CtCV to reduce its negative impact within battery packs.

3.3 Battery pack model description

Battery pack modelling for automotive applications is especially complex because of the number of different parameters to consider. Modelling single cells (SCs) needs to consider the small manufacturing and ageing differences described in Chapter 2. All single cell models should, therefore, be considered independently while modelling the full system. Even with a perfect replication of the single cells, there are other parameters to consider with, among others, the topology, the temperature distribution and the overall control scheme.

From the analysis of the literature is seen that the majority of the models which describe internal degradation processes are based on Newman electrochemical [84–86] or stochastic

approaches [87, 88]. Although accurate, and despite recent work on reduced ordered models [89], they are not suitable to scale up to the pack level because of the involved numerical requirements, such as series of differential equations, for modelling every single cell individually. To reduce this complexity, most battery pack models are using multiple equivalent circuit models connected in series or parallel [35, 90].

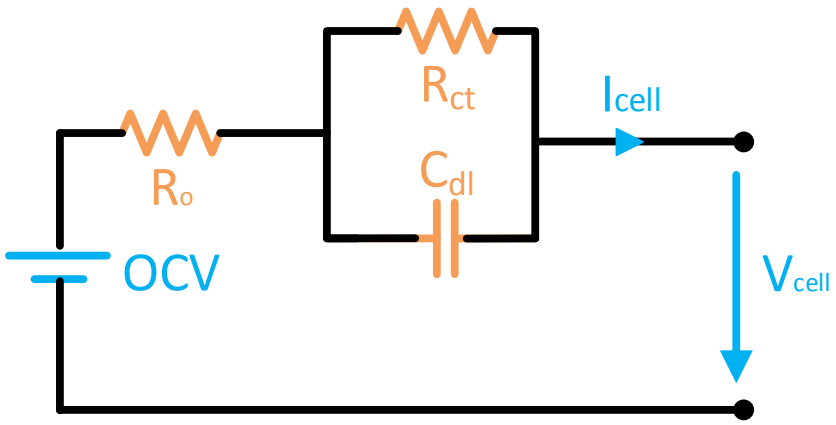

Figure 3.1: Example of a common Randles battery ECM.

Figure 3.1 shows a Randles ECM. This ECM is composed by the open circuit voltage V_{oc} source connected with the ohmic resistance, R_o, in series, and the charge-transfer resistance, R_{ct}, and double-layer capacitance, C_{dl}, in parallel [51]. Depending on the accuracy of the response required, additional RC pairs could be added in series [51]. To reduce numerical complexity in the simulations only one RC pair is used. Taken an ECM as the single cell unit model, Dubarry et al. [29] have developed a new modular methodology for battery pack modelling. This battery pack model is fit for this study because it emulates single cell variations, both intrinsic and ageing induced, without adding significant calculation time. This model is employed to simulate different battery pack topologies and cell chemistries. Conducting such a test based on experimental measurements would be time prohibitive due to the different variables involved: amount and origin of cell variations, cell chemistries and pack topologies. Hence, the approach proposed in this study is purely based on simulations. The simulation model was named Hanalike after the Hawaiian word for "all together" because it is unifying various models proposed and validated in recent years at HNEI. The verification of each of these models uses synthetic

data, i.e., data acquired under laboratory conditions, and hence, none of the models have been validated under real-world scenarios. Table 3.1 summarises the functionality of each Hanalike submodels and Figure 3.2 illustrates graphically the interactions between them.

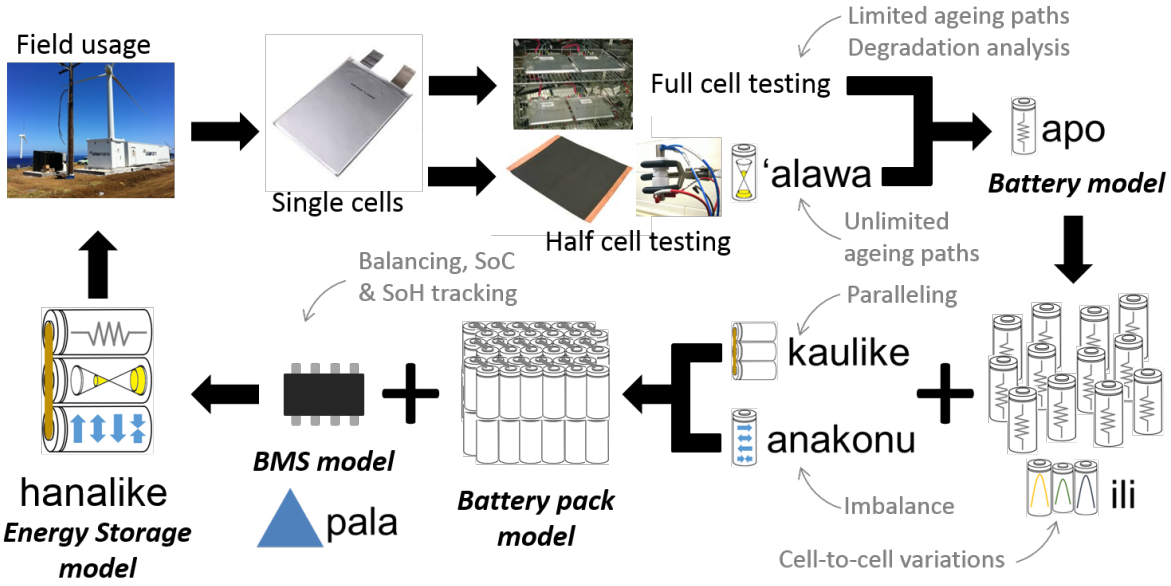

Figure 3.2: Schematic view of the Hanalike model based on previously published submodels: 'Alawa [67], Apo [91], ili [92], Kaulike [94], Anakonu [93] and Pala [63].

Figure 3.3 presents the modelling flow diagram of Hanalike. A detailed explanation of the operating principles and limitations of the models developed by HNEI was given in Section 3 of Submission 4 and in the publications listed in Table 3.1.As stated in Section 1.4, it is beyond the scope of this thesis to report in detail the working principle of each of the sub-models of Hanalike. However, the analysis conducted in Submission 4 and the publication of these models in high-impact journals [63, 67, 91–94] gave to the author sufficient confidence that the Hanalike sub-models were applied appropriately to meet the objectives of this Chapter. An overall description of the working principle of the Hanalike model as a whole is given subsequently:

The simulation starts with the first step of the requested duty cycle at a time t. The single cell engine first calculates the single cells full-cell voltage response based on their initial parameters and their SoH. This procedure will be repeated for each step of the duty cycle if the SoH, capacity based, is changing.

Table 3.1: Summary of the Hanalike submodels.

Model's name (Hawaiian)	**Model battery's level**	**Model's formulation and validation**	**Year published**	**Model's functionality**
Apo (English translation: circuit)	Cell	[91]	2007	Calculate the cell voltage response based on the input current. A common Randles ECM model is used. Parametrisation data is gathered either from experimental testing or generated from 'Alawa simulations [67].
'Alawa (English translation: diagnosis)	Cell	[67]	2012	Update the cell voltage response from the Apo model considering LLI, LAM and kinetics.
ili (English translation: distribution)	Module	[92]	2009	Calculate the voltage response of a group of cells models (module). This calculation considers cell-to-cell variations due to capacity ration (Qr), the ohmic resistance (R1), the rate capability (RC), and the initial SoH (SoH_i).
Anakonu (English translation: equilibrium)	Module	[93]	2015	Calculate the pack voltage response when single cells or modules connected in series are imbalance.
Kaulike (English translation: parallel)	Module	[94]	2016	Calculate the pack voltage response when single cells or modules connected in parallel are imbalance.
Pala (short form for palapala'aina). (English translation: map)	Cell, module and pack	[63]	2017	Determines cell, module and battery pack state functions (SoC and SoH) and the need for potential balancing and protection.

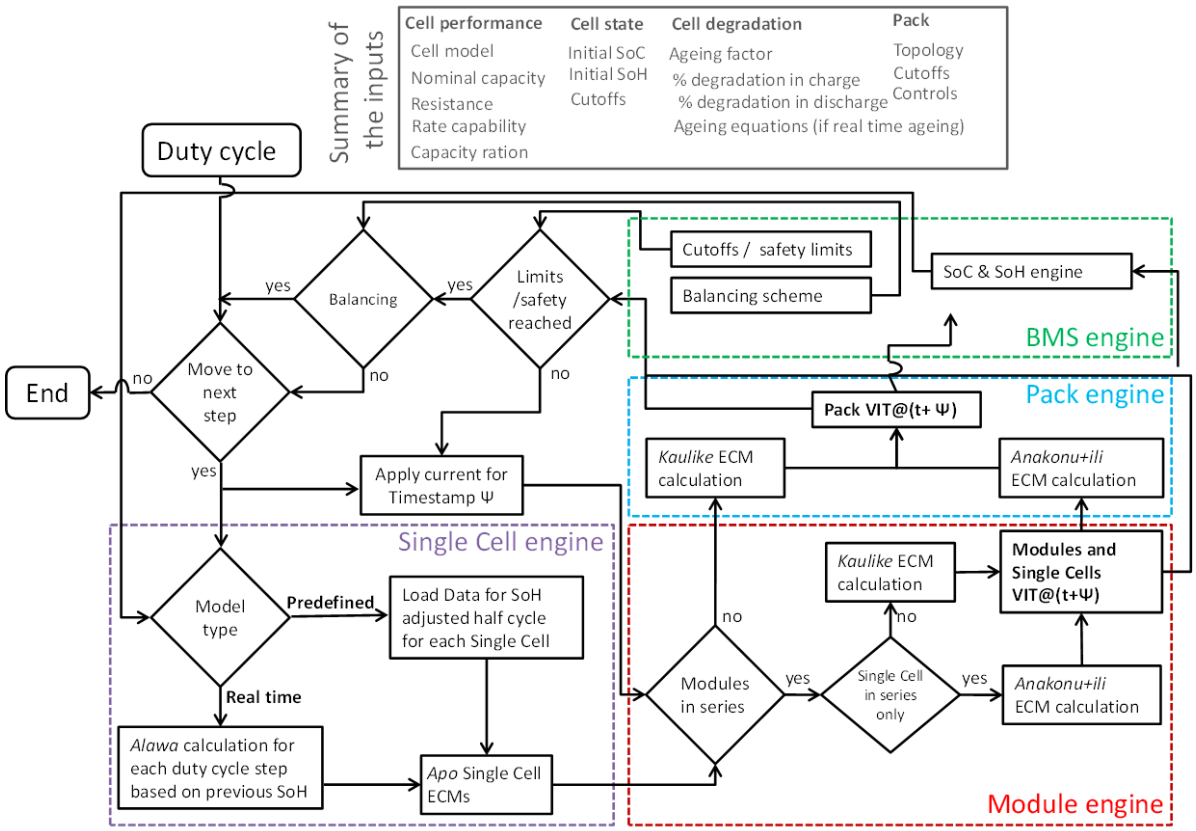

Figure 3.3: Hanalike flow diagram highlighting the different calculation engines for single cells, modules, full pack and BMS.

Each of the single cell ECM can be parametrised offline or online. For the offline case, predefined data can be generated in two different ways:

1. From full-cell experimental data.

2. From half-cell data using the 'Alawa model [67].

Comparing 1 and 2, the level of accuracy and precision of 1 is larger than of 2. 2 needs to account for experimental errors plus errors in the modelling whereas 1 only needs to consider experimental errors. However, the data obtained from full-cell measurements is limited to the conditions of an experiment, whereas half-cell data generated with 'Alawa model can replicate any experimental condition. As the objective of this study is to develop a universal procedure to diagnose CtCV, then half-cell data generated with the 'Alawa model is used.

As mentioned in Chapter 2, DMs are connected to the loading ratio and offset parameters. These parameters are calculated in the 'Alawa submodel for each step of the duty cycle online instead of being calculated in advance offline. The 'Alawa model is parametrised offline in this study because this model requires less computation than parametrising it online.

Once the loading ratio and offset of the single cell model are defined, the model establishes the pack voltage, current and temperature (VIT) for each time-step ψ, which is in the order of 500 points per full discharge. Taking the example that a full discharge last 1h, then the sampling time results in 7.2s. 7.2s is the result of dividing 3600s (1h) over 500 points. This sampling time may have negative implications to capture the kinetics in BMS applications. Ideally, the sampling time for BMS applications should be in the order of a second as suggested by Zhi et al. [95]. Anakonu [93] and Kaulike [94] models simulate the imbalance in terms of SoC, SoH or Qr for cells connected in series and in parallel, respectively. The parameters used to emulate the imbalance in each of these models are the scaling and translation factors. As explained in Submission 4 [34], the module and pack engine calculate these factors using the SoC and capacity ration, Q_r. The capacity ration, in mAh/%SoC, is defined as the ratio between capacity and SoC. Q_r is defined to account for CtCV when cells have a different capacity at the same ageing state. A typical example of this scenarios is when cells of different sizes or manufacturers are interconnected.

$$Q_r = \frac{C_n}{\Delta SoC} \tag{3.1}$$

The final phase of each time-step corresponds to the control of the battery dictated by the BMS model. If VIT at time t+ψ reached a cutoff or safety limit, the step is terminated. If VIT lie within cutoff safety limits, the duty cycle would be modified to take balancing into account before the next step starts. The balancing capability was not developed in the model used in this study. Hence, developing such a balancing strategy represents an

area of further work as described in Section 3.7.

The process depicted in Figure 3.3 is repeated until all the duty cycle steps are simulated. The choice of duration of the time step ψ is a balance between accuracy and calculation time.

3.4 Diagnostic procedure to evaluate CtCV through Incremental Capacity (IC) and Differential Voltage (DV) curves

This section aims to present the procedure that has been followed to develop a universal diagnostic method. This diagnostic method quantifies the amount and the origin of CtCV through IC and DV curves. Figure 3.4 shows the steps taken into this process. A subscript "*" is added to differentiate the steps between theoretical and real scenarios.

- **Step 1 and 1*:** different scenarios as a function of cell chemistry, amount and origin of CtCV, and battery pack topology are proposed.
- **Step 2 and 2*:** the Hanalike submodels described in Section 3.3 are parametrised according to the conditions defined in step 1.
- **Step 3 and 3*:** a constant current discharge at C/25 of the battery pack is simulated using the Hanalike model.
- **Step 4 and 4*:** current, Hanalike's input, and voltage, Hanalike's output, of cell, module and pack are used to compute IC and DV curves. Subsequently, the FOIs are visually identified from IC and DV curves.
- **Step 5 and 5*:** the change of the uniquely observable FOIs, inferred in step 4 and 4*, is quantified for theoretical and real scenarios.

- **Step 6 and 6*:** identifies which theoretical FOIs are uniquely observable with respect to the real FOIs.

Each of these steps is further described in the following subsections.

3.4.1 Step 1 and 1*: definition of initial conditions

The conditions of the scenarios tested are defined as a function of:

- **Pack topology:** 49S1P, 1S49P, 7(1)S1P and 7S7P.
- **Cell chemistry:** Lithium Manganese Oxide (LMO), NCA and LFP.
- **Origin of CtCV:** initial SoC, SoC_i; initial SoH, SoH_i; initial Q_r, Q_{ri}; and initial resistance, R_i. The variation of cell-to-cell SoC_i, SoH_i and R_i is pertinent in automotive applications in scenarios when, e.g., cells experience thermal gradients within a battery pack due to incorrect thermal management [35]. In such scenario the current flowing through the cells might be different, discharging or charging them at a different rate, leading the cells to have different SoCs and experience an inhomogeneous degradation (differences in SoH and R). The variation of Q_{ri} can be also pertinent when battery packs are manufactured using cells from different suppliers as part e.g., of a second-life recycling strategy [96].
- **Amount of CtCV:**

  [0%, ±2.5%, ±5%, ±7.5%, ±10%] for SoC_i, SoH_i and Q_{ri}. Reference point is 90% for SoC_i and 100% for SoH_i and Q_{ri}.

  [0%, ±10%, ±20%, ±30%, ±40%] for R_i.

- **Input distribution:**

  Normal distributed.

  Skewed distributed (1/4 skew factor).

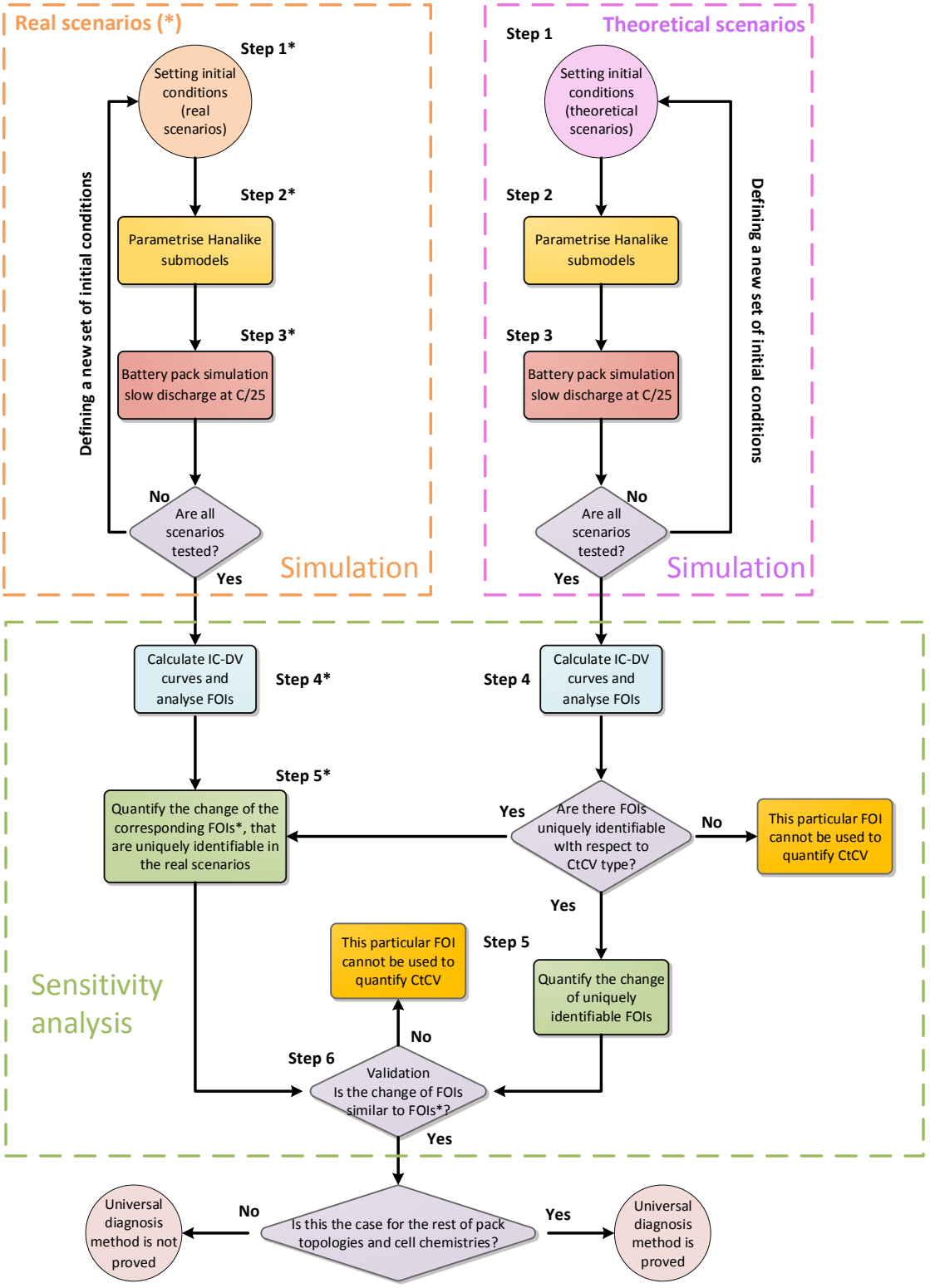

Figure 3.4: Steps taken to develop a universal diagnostic method to quantify CtCV through IC and DV curves.

Subsequently, a short explanation of the reasons for selecting of these conditions is given.

Pack Topology

Figure 3.5 illustrates the battery pack topologies that the Hanalike model can handle. The topologies are:

- **nS1P:** n cells connected in series and 1 cell connected in parallel. This configuration is typically used in high power applications where the voltage is high and capacity low. Energy storage systems for photovoltaic applications commonly use this type of battery topology [97] because its operation involves large voltage levels, e.g., 220V.

- **1SmP:** 1 cell connected in series and m cells connected in parallel. This configuration is usually used in high energy applications where the voltage is low and capacity is high. Examples of applications of this pack topology are batteries used in laptops or notebooks [98], which operates at low voltage levels, e.g., 11V in 3S1P [99].

- **n(1)SmP:** n cells connected in series and parallel. This pack configuration optimizes energy and power output. As some cells are connected in series, this topology has the disadvantage that if one cell fails, then the whole cell string cannot be longer used. This configuration is usually employed in applications where the failure of one cell is not critical in terms of performance and safety. For instance, batteries used in photovoltaic systems can have this configuration as shown in [100].

- **nSmP:** m cells connected in parallel forming a battery module which is n times connected in series. Similarly as to the n(1)SmP configuration, this topology optimizes output energy and power. As cells are not connected in series, the pack can be used even if one cell fails. This advantage makes n(m)S1P the preferred topology for automotive applications. For instance, the Tesla S Roadster model 2008 comprises a 6S74P battery pack [101].

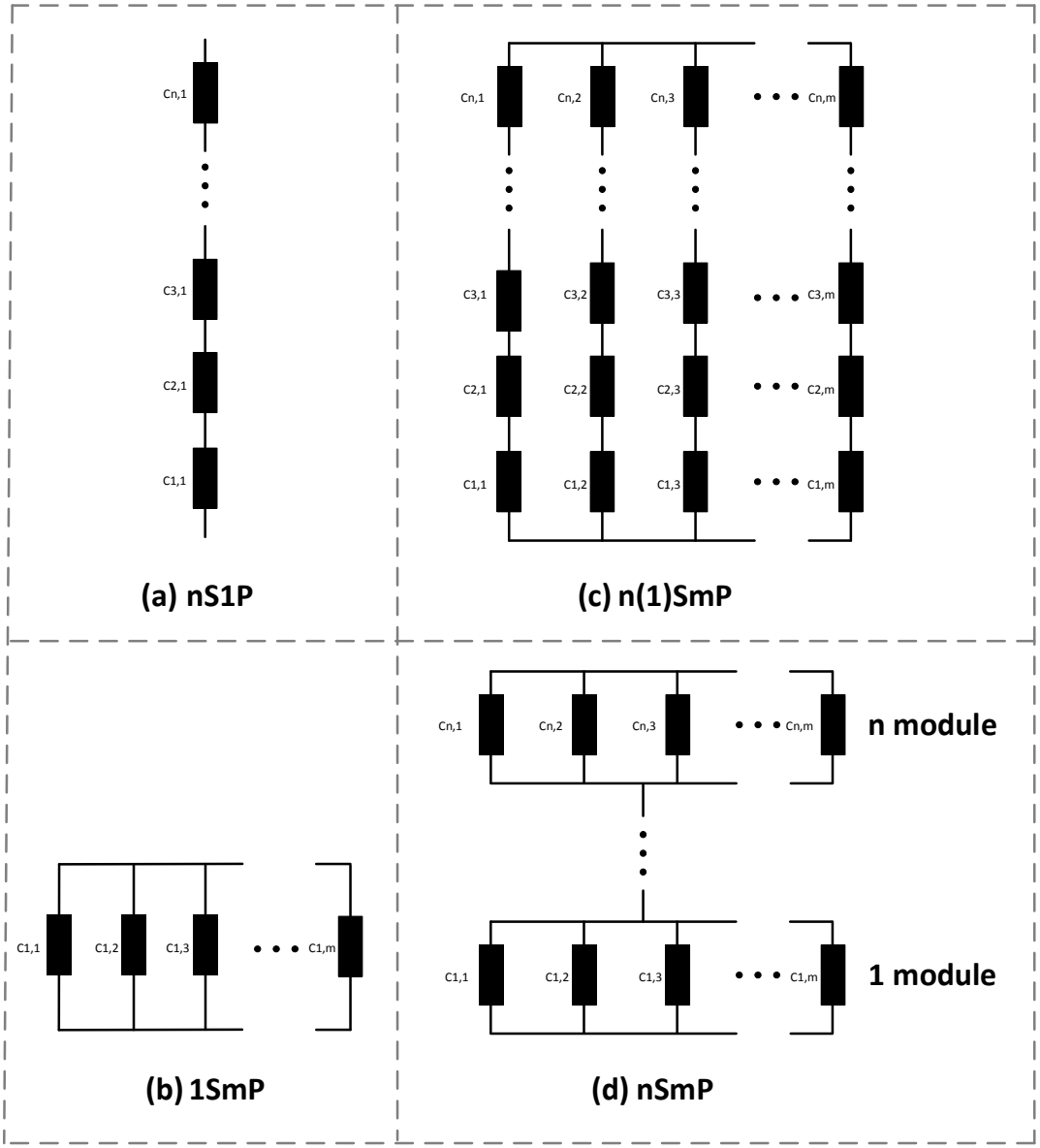

Figure 3.5: Battery pack topologies tested in this study.

Each of these four topologies was simulated to test the feasibility of the proposed diagnostic procedure in different applications. A battery pack composed with a total of 49 cells was selected. For the scenario tested in this study, which is a single slow discharge cycle, a 49 cells battery pack does not involve an excessive computation time (approximately 40min/cycle) at the same time that such a pack is representative in automotive applications. For instance, the Mild-Hybrid Mercedes-Benz S-400 2009 model is powered by a 35S1P Lithium-ion battery pack [102].

Cell chemistry

LMO, NCA and LFP cell chemistries are tested in this study. They were selected because they are commonly used in automotive applications [103]. Table 3.2 summarises the characteristics of each of them.

Table 3.2: Specifications of the cell chemistries used.

Cathode material	**LMO**	**NCA**	**LFP**
Anode material	GIC	GIC	GIC
Cell type*	HP	HP	HP
Nominal capacity	1.2 Ah	3.03 Ah	60 Ah
Nominal voltage	3.5 V	3.35 V	3.075 V
Charge cutoff voltage	4.2 V	4.2 V	3.65 V
Discharge cutoff voltage	2.8 V	2.5 V	2.5 V
Nominal energy	4.2 Wh	10.15 Wh	184.5 Wh

* HP: High Power; HE: High Energy.

Origin of CtCV

As described in Section 2.2.1, CtCV can be caused by differences in internal cell capacity, cell resistance, temperature gradient and coulombic efficiency. Because the Hanalike model does not consider temperature gradients and coulombic efficiencies, these CtCV have not been considered in this study. As it will be explained in Section 3.7, the improvement of Hanalike in this regard represents further work. Based on this, Figure 3.6 illustrates the CtCV cases here considered:

- **SoC$_i$ CtCV:** cell-to-cell SoC$_i$ is different. SoC is defined as the ratio between the current energy of the battery with respect to the total energy the battery can store.
- **SoH$_i$ CtCV:** cell-to-cell SoH$_i$, capacity based, is different. In this case Q_{ri} changes because, as specified in Equation 3.1, Q_{ri} is proportional to the capacity, SoH$_i$. As this study only considers CtCV from initial manufacture and integration rather than from actual battery operation, SoH$_i$ CtCV are mainly caused by calendar ageing. According to [104,105], calendar ageing is primarily mainly driven by LLI because of the occurrence of side reactions at the anode, e.g., solvent decomposition leading to

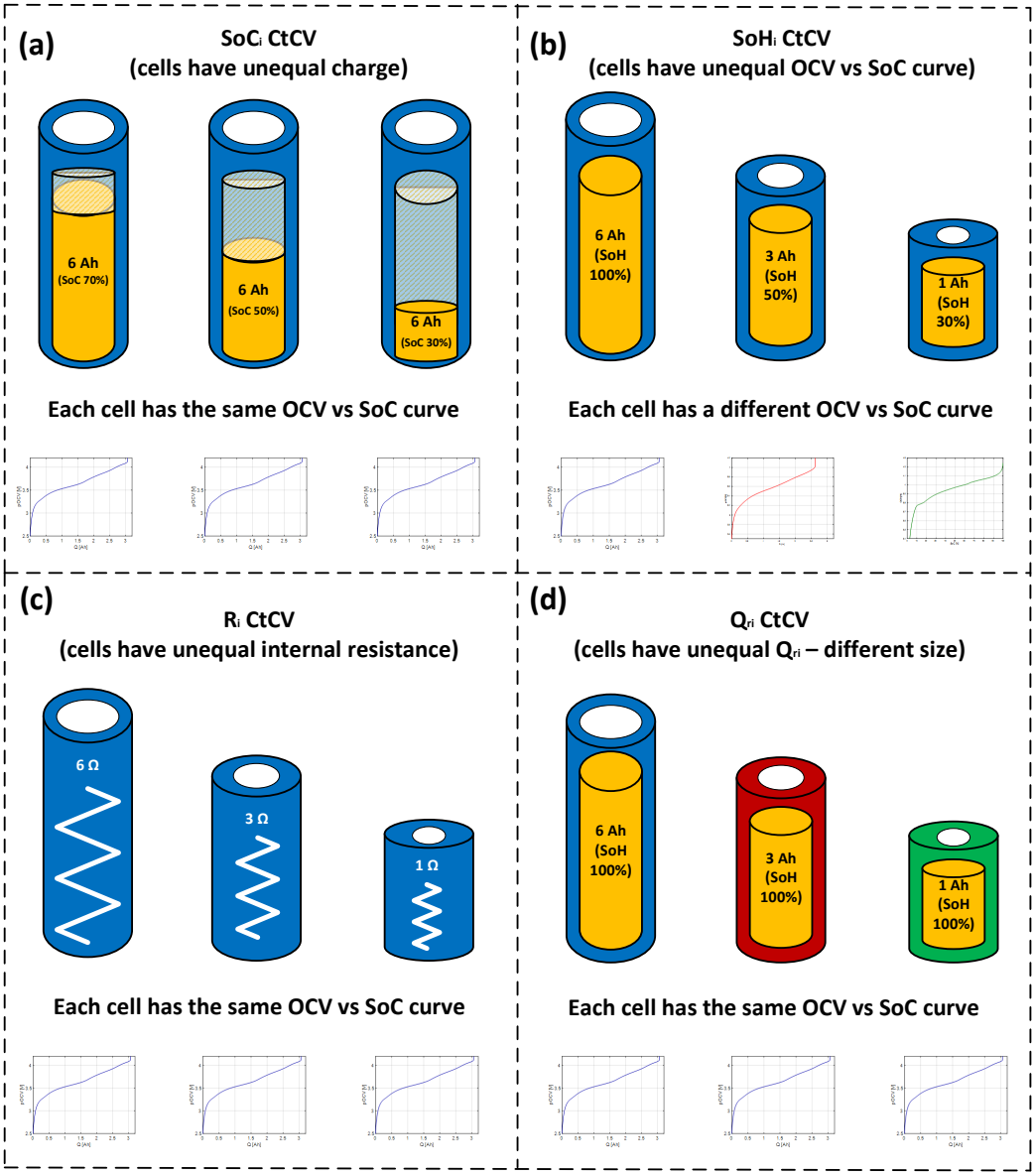

Figure 3.6: CtCV cases considered: (a) SoC_i, (b) SoH_i, (c) R_i and (d) Q_{ri}.

the growth of the SEI. Kassem et al. [104] made this conclusion for Graphite/LFP commercial cells stored at 30 ℃, 45 ℃, and 60 ℃, and SoC 30%, 65%, and 100% during 8 months. Eddatech et al. [105] studied the effects of calendar ageing in LMO, NCA, NMC and LFP cells when they are stored during 600 days at 30 ℃, 45 ℃ and 60 ℃, and SoCs 30%, 65% and 100% for each temperature. They concluded that LAM and LLI are pertinent for LMO and NMC chemistries when the cells are stored at temperatures higher than 45 ℃. For the case of LFP and NCA, they showed that they present higher stability through ageing. As the effect of temperature has not

been considered in our study and consistency among the chemistries was desired, then it was decided to assign a low value of LLI, 1% per cycle, for each of the chemistries tested. To emulate the amount of LLI in the single cells of the battery pack, the 'Alawa submodel is used.

- **R_i CtCV:** cell-to-cell R_i is different.
- **Q_{ri} CtCV:** cell-to-cell Q_{ri} is different. Q_{ri} is for the first time introduced in the literature as a parameter to account for CtCV. Comparing this to the variation of SoH_i, the change of Q_{ri} does not involve changes in the OCV vs SoC relationship, whereas the variation of SoH_i does.

Amount of CtCV

Previous studies [40,41] claimed that differences in cell properties from initial manufacture and integration may be circa 9% for capacity and 25% for resistance. According to these studies the range of CtCV is defined as follows:

- **SoC_i, SoH_i and Q_{ri}:** the range of variation is defined from 0% to a maximum of 10% with intervals of 2.5%, i.e. [0%, ±2.5%, ±5%, ±7.5%, ±10%]. For SoC_i, the reference point, 0% no variation, is set to 90% to avoid that the battery pack is overcharged (SoC_i>100%). For SoH_i and Q_{ri} the reference point is set to 100% because in reality SoH_i and Q_{ri} can vary more than 100% and less than 100%. For the case of LMO 49S1P, Figure 3.7 (a) and (b) illustrates an example of SoH_i ±10% variation following normal and skewed distribution.
- **R_i:** the range of variation is defined from 0% (no variation) to a maximum of 40% with intervals of 10%, i.e. [0%, ±10%, ±20%, ±30%, ±40%].

Distribution of CtCV

Previous studies have shown that CtCV in Li-ion battery cells follow a centred normal distribution and a skewed distribution [42, 45, 46, 106, 107]. Skewed normal distribution is predominant when cells have been aged [42, 58]. Distribution of fresh cells is also skewed

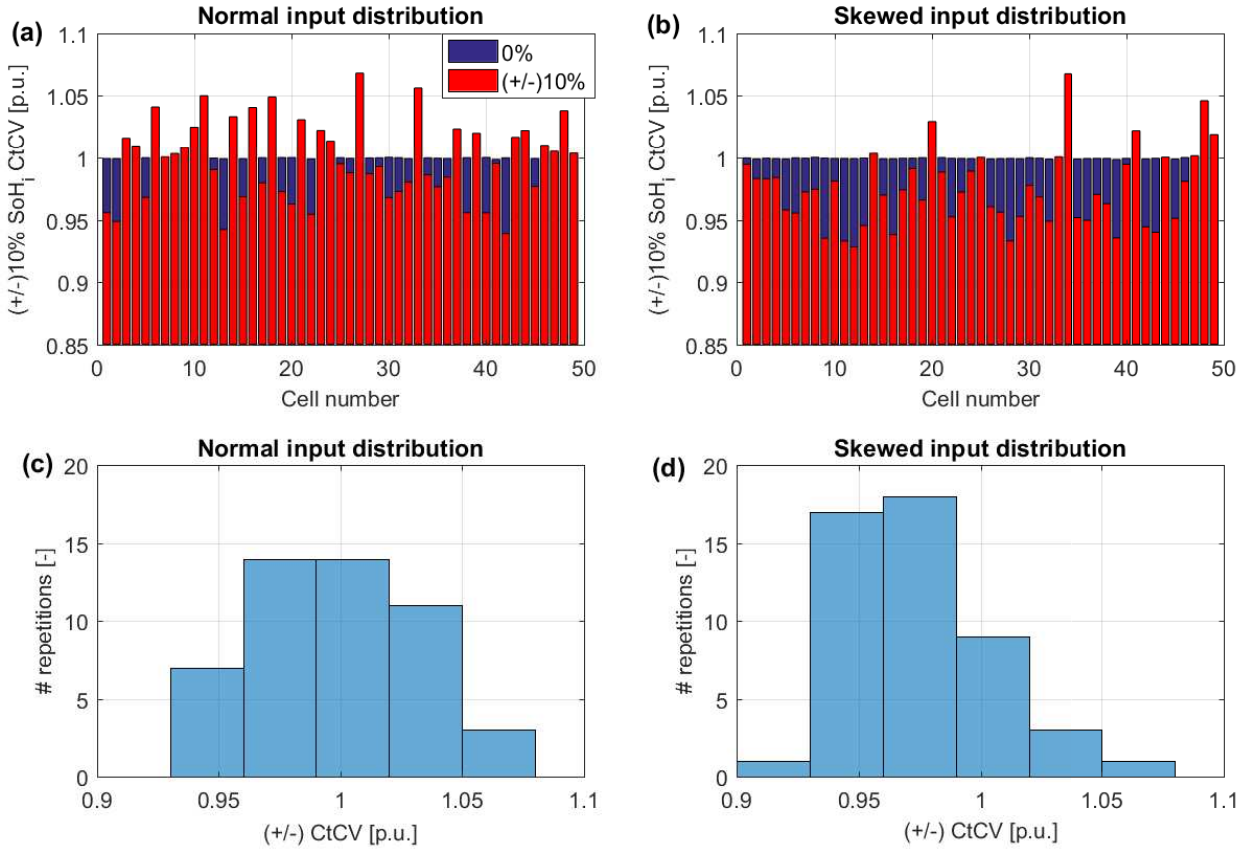

Figure 3.7: (a) Cell SoH_i LMO 49S1P ±10% variation for normal distributed input data; (b) Cell SoH_i LMO 49S1P ±10% variation for skewed distributed input data; (c) Histogram of cell SoH_i LMO 49S1P ±10% variation for normal distributed input data; (d) Histogram of cell SoH_i LMO 49S1P ±10% variation for skewed distributed input data.

but at a lower level than the aged cells [36]. Following on from this, this study defines the variation of SoC_i, SoH_i, Q_{ri} and R_i according to a normal distribution and a skewed distribution. Both distributions are generated in MATLAB using *randn* for normal input distribution and *pearsrnd* for skewed input distribution [108]. Figure 3.7 (c) and (d) show normal and skewed distribution for the case of SoH_i.

Theoretical and real scenarios

Theoretical scenarios are defined when SoC_i, SoH_i, Q_{ri} and R_i change individually. However, in practical cases, more than a single CtCV parameter can vary and hence, an additional set of scenarios where the change of all parameters change simultaneously is considered. These are named real scenarios.

For normalized input distribution, LMO 49S1P case, 0% and ±10% variation, Figure 3.8 illustrate the theoretical case for SoC_i (a)-(d), SoH_i (e)-(h), Q_{ri} (i)-(l) and R_i (m)-(p). As mentioned in "Origin of CtCV", when SoH_i varies, Q_{ri} also changes because, as specified in Equation 3.1, Q_{ri} is a function of the capacity (SoH_i). This is not the case for the SoC_i, Q_{ri} and R_i as shows Figure 3.8 (a)-(d), (i)-(l) and (m)-(p) in which only SoC_i and Q_{ri} change. Figure 3.8 (q) illustrates the real scenario where SoC_i, SoH_i and Q_{ri} vary simultaneously.

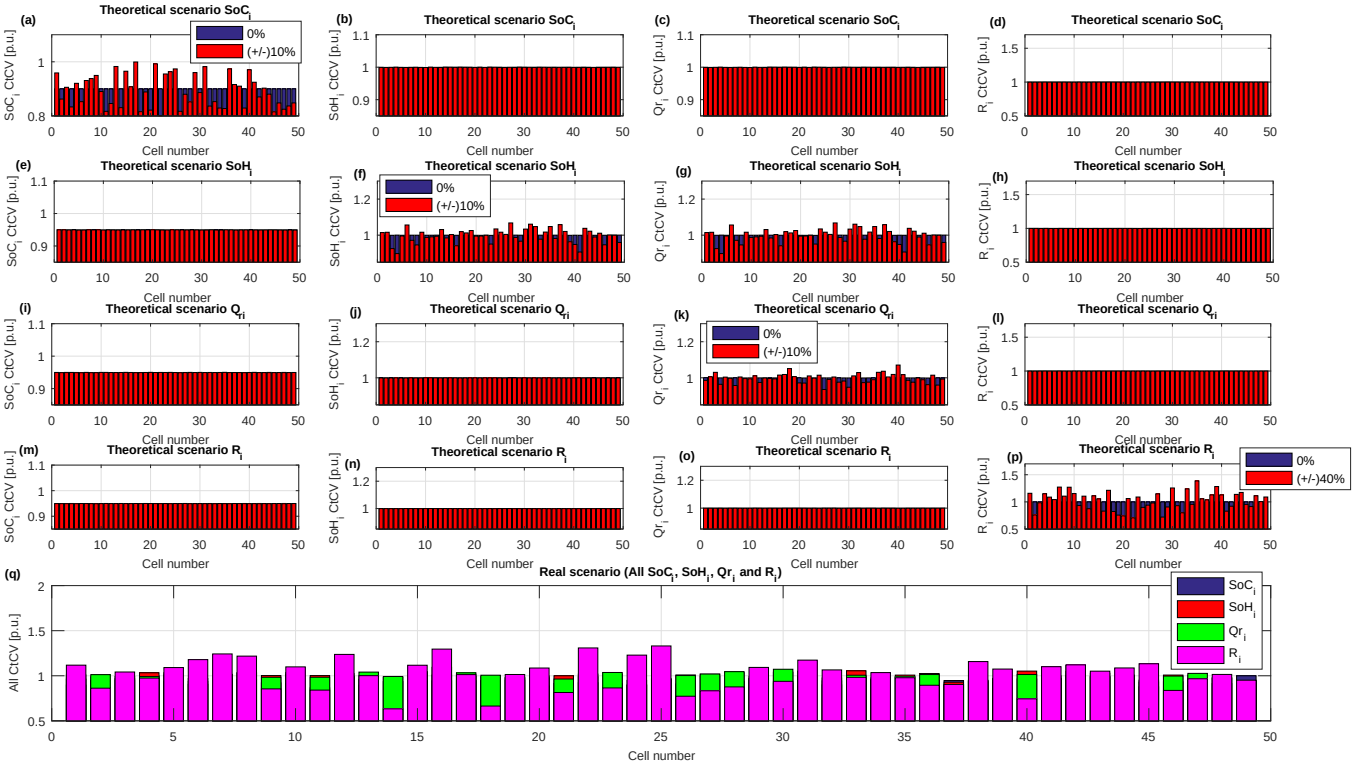

Figure 3.8: LMO 49S1P 0% and ±10%: (a)-(d) CtCV for each parameter (SoC_i, SoH_i, Q_{ri} and R_i) for the SoC_i theoretical case; (e)-(h) CtCV for each parameter (SoC_i, SoH_i, Q_{ri} and R_i) for the SoH_i theoretical case; (i)-(l) CtCV for each parameter (SoC_i, SoH_i, Q_{ri} and R_i) for the Q_{ri} theoretical case; (m)-(p) CtCV for each parameter (SoC_i, SoH_i, Q_{ri} and R_i) for the R_i theoretical case; (q) CtCV real scenario. All SoC_i, SoH_i, Q_{ri} and R_i vary simultaneously.

In order to distinguish each simulation, the scenarios tested in this study are named according to the following nomenclature:

(Chemistry)_(CtCV parameter)_(Pack Topology)_(Distribution and amount of CtCV) (3.2)

For instance, the LFP_SoH_7S7P_±5% scenario is the one in which there is a maximum initial CtCV of ±5% SoH_i in a 7S7P LFP battery pack. For the cases when the data is skewed distributed, an "SK" is added before the ±, so it would be LFP_SoH_7S7P_SK±5%.

Table 3.3 illustrates the possibilities for each entry in the nomenclature:

Table 3.3: Possible entries of the nomenclature to define the test scenarios.

Cell Cathode material	LMO	NCA	LFP		
CtCV parameter	SoC_i	SoH_i	Q_{ri}	R_i	"All" (real scenario)
Pack topology	49S1P	1S49P	7(1)S7P	7S7P	
Input data distribution	"SK" if it is skewed distributed				
Amount of CtCV for SoC_i, SoH_i & Q_{ri}	0	2.5%	5%	7.5%	10%
Amount of CtCV for R_i	0	10%	20%	30%	40%

All the possible combinations were simulated except for the cases of R_i and skewed distribution. The case of R_i was not simulated because, as shown in Figure 3.16, it is not possible to quantify CtCV due to R_i using IC curves. The skewed scenario was neither entirely evaluated because the scope of this study was to outline the data distribution type affects the number of FOIs that can be used. Considering these exceptions, the number of simulations were reduced from 455 to 285 simulations. From this 285 simulations, 180 are theoretical and 60 real scenarios. CtCV due to R_i were simulated for theoretical and real scenarios for the case of LMO, 49S1P and normal distributed data. These scenarios were enough to prove that IC curves are not suitable to quantify CtCV due to R_i as it will be explained in Section 3.4.4. The skewed distributed data was only tested for theoretical and real scenarios for the case of LMO, 49S1P, [0%, ±2.5%, ±5%, ±7.5%, ±10%]. This test was sufficient to prove that the data distribution type affects the number of FOIs that can be used. This is further explained in Section 3.5.2.

3.4.2 Step 2 and 2*: model parametrisation

After defining the initial conditions, the Hanalike submodels listed in Table 3.1 are parametrised. The parametrisation of the parameters included in the Hanalike submodels is summarised in Table 3.4 as a function of the cell chemistry. From Table 3.4, all the parameters have been defined in this thesis, or are widely known except the Ohmic Resistance Increase (ORI) and Rate Degradation Factor (RDF). These parameters belong to the 'Alawa submodel [67] and account for modelling changes of ohmic resistance (ORI) and changes of the electrode kinetics (RDF). As this study emulates a C/25 slow discharge

where no cycling is involved, there are ageing related parameters such as RDF_{PE}/RDF_{NE}, ΔSoH, $\%deg_{cha}$ and $\%deg_{dch}$ that have not been used in this study.

Table 3.4: Parametrisation of the battery pack submodels for this particular study.

Single cell engine model ('Alawa option considered)				
Parameter	**Unit**	**LMO**	**NCA**	**LFP**
C	F	0.04	0.04	0.04
V_{PE} vs. SoC	V vs %	Not available. Property of HNEI		
V_{NE} vs. SoC	V vs %	Not available. Property of HNEI		
Loading ratio	-	1	1.05	0.98
Offset	%	17	2.5	9
ORI_{PE}/ORI_{NE}	-	0.07	0.3	0
RDF_{PE}/RDF_{NE}	%	Not considered in this study		
Single cell engine model for module and pack parametrisation				
Loading ratio	V vs %	1	1.05	0.98
Offset	%	17	2.5	9
ORI_{PE}/ORI_{NE}	-	0.07	0.3	0
RDF_{PE}/RDF_{NE}	-	Not considered in this study		
$Topology_{Mod}$	-	Given by initial conditions		
$Topology_{Pack}$	-	Given by initial conditions		
BMS engine model				
Parameter	**Unit**	**LMO**	**NCA**	**LFP**
$Cutoffs_{SC}$ (V/I/T)	V/A/°C	4.25V - 2.8V	4.25V - 2.8V	3.6V - 2.5V
$Cutoffs_{Mod}$ (V/I/T)	V/A/°C	4.15V*nSm - 3V*nSm^2	4.2V*nSm - 3V*nSm^2	3.55V*nSm - 2.5V*nSm^2
$Cutoffs_{Pack}$ (V/I/T)	V/A/°C	4.15V*nSp - 3V*nSp^3	4.2V*nSp - 3V*nSp^3	3.55V*nSp - 2.5V*nSp^3
$Cutoffs_{cond}$ (V/I/T)	V/A/°C	Not considered in this study because battery is not cycled		
$Safety_{SC}$ (V/I/T)	V/A/°C	Not considered in this study because battery is not cycled		
$Safety_{Mod}$ (V/I/T)	V/A/°C	Not considered in this study because battery is not cycled		
$Safety_{Pack}$ (V/I/T)	V/A/°C	Not considered in this study because battery is not cycled		
ΔSoH	%	Not considered in this study because battery is not cycled		
$\%deg_{cha}$	%	Not considered in this study because battery is not cycled		
$\%deg_{dch}$	%	Not considered in this study because battery is not cycled		

[1] rdm(CtCV): random value of CtCV.
[2] nSm: number of cells connected in series within a module.
[3] nSp: number of cells connected in parallel within the pack.

3.4.3 Step 3 and 3*: battery pack simulation

The battery pack is discharged slowly to limit the contribution from kinetics. This condition is required to derive high quality IC and DV curves from which clear FOIs can be inferred. According to Table 3.2, the constant discharge is performed from the upper cell voltage threshold to the lower cell voltage threshold at C/25. For the cases that cells are imbalance due to CtCV the BMS engine will terminate the discharge when a cell reaches its lower voltage threshold. This BMS action is taken to avoid cells discharging below their limits. As an example, Figure 3.9 illustrates the output voltage against the SoC for two random cells in the LMO_SoC_49S1P_5% scenario. It is clearly seen that each cell has different SoC at the beginning of the discharge. As explained, the BMS ensures that the end of the discharge is limited by the lower cutoff voltage. The lower cutoff voltage of 2.951V does not match exactly with the value of 2.8V specified in Table 3.4. This difference can be due to two reasons. Firstly, the cutoff voltage is measured right after the discharge finishes without letting the cells to relax. It needs to be considered that the values specified in Table 3.4 are measured after cells are relaxed. Secondly, the accuracy of the model is not sufficient to match the cutoff voltage specified in Table 3.4.

3.4.4 Step 4 and 4*: calculation of IC-DV curves and analysis of Features of Interests (FOIs)

The IC-DV technique is widely used to evaluate changes in the electrochemical properties of cell, modules and packs [67, 109, 110] when the cell is assumed to be at equilibrium. Recently, IC has been employed as a technique to diagnose CtCV in battery packs [42] as well. The principle of this technique is that at equilibrium, two or more phases with different lithium concentrations at the same chemical potential coexist. This characteristic enables the researcher to infer changes in the electrochemical properties that physically can be measured through changes in charge and pOCV. An approximate equilibrium state is achieved if the cell is typically charged or discharged at current rates lower than C/25

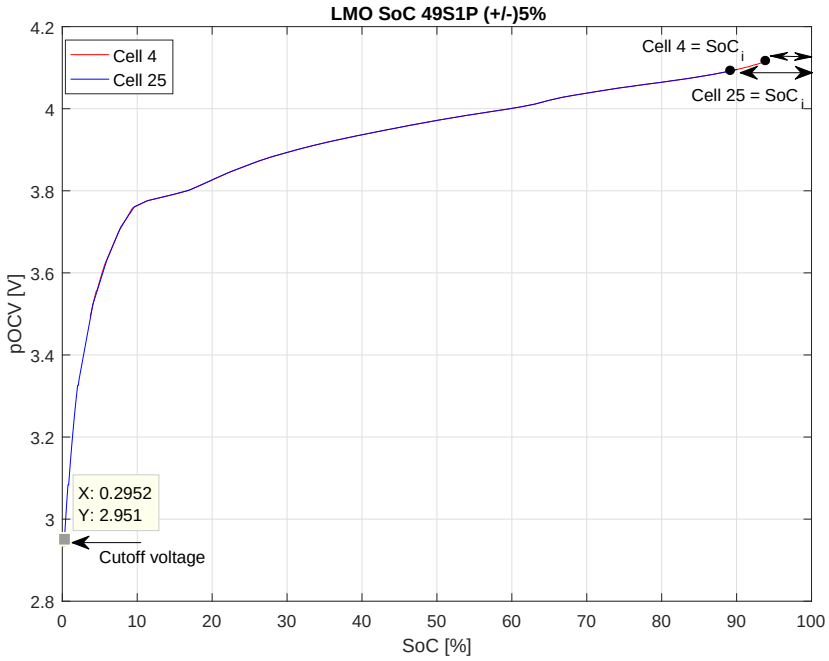

Figure 3.9: Slow discharge for two random cells (cell 4 and 25) in the LMO_SoC_49S1P_5% scenario

while measuring the Q and the pOCV [67]. However, charging and discharging the cell at such low currents is challenging to perform in a real application since the time required would be prohibitive [109]. This scenario represents a compromise between a true state of equilibrium measurement and a pragmatic solution that may be feasibly employed within a BMS. High definition of the IC-DV curves is key in this case to prove the validity of the diagnostic method and hence, as suggested in [67], a current rate of C/25 is used.

Figure 3.10 and Figure 3.11 show the relationship between pOCV and IC and DV curves. The IC curve is computed as the gradient of Q with respect to $pOCV$ using Equation 3.3. The *gradient* function in MATLAB is employed to perform this calculation [108].

$$\frac{dQ}{d(pOCV)} \approx \frac{\Delta Q}{\Delta(pOCV)} \tag{3.3}$$

Calculating the inverse of the IC curve yields the DV curve. Mathematically, the DV curve is derived as the gradient of $pOCV$ with respect to Q using Equation 3.4.

$$\frac{d(pOCV)}{dQ} \approx \frac{\Delta(pOCV)}{\Delta Q} \tag{3.4}$$

IC and DV curves offer different insights into the rate and nature of the degradation within the cell. This feature is because IC and DV curves are plotted against different parameters: IC is dQ/dV against the voltage; and DV is dV/dQ against the charge. The magnitude of the peaks or valleys changes with respect to voltage for IC, or capacity for DV, depending on the cell chemistry and operating conditions, e.g., average temperature, C-rate, average SoC and ΔDoD [111].

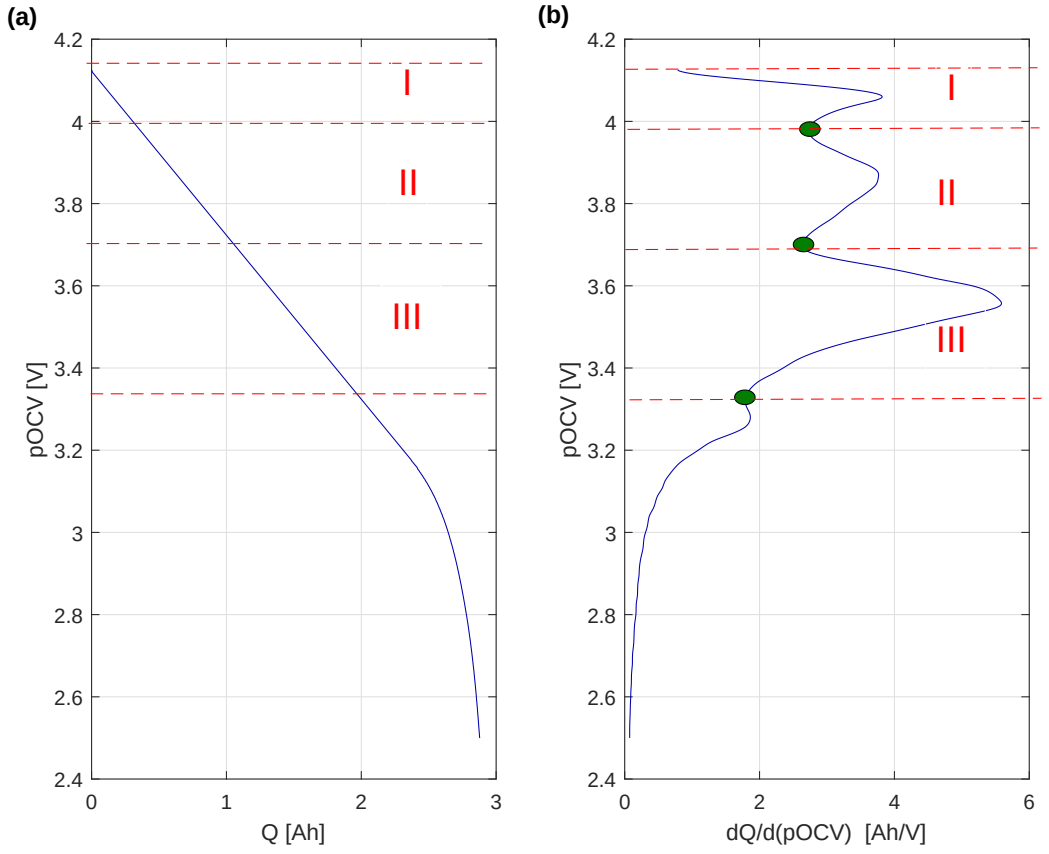

Figure 3.10: Relationship between (a) constant gradient pOCV regions and (b) peaks in the IC curve.

Figure 3.12 (a) and (c) illustrates that the measurements of the capacity Q and the pOCV are disturbed by noise. To filter the amount of noise in the measurements the IC and DV curves are smoothed before the derivatives are computed as illustrated in Figure 3.12

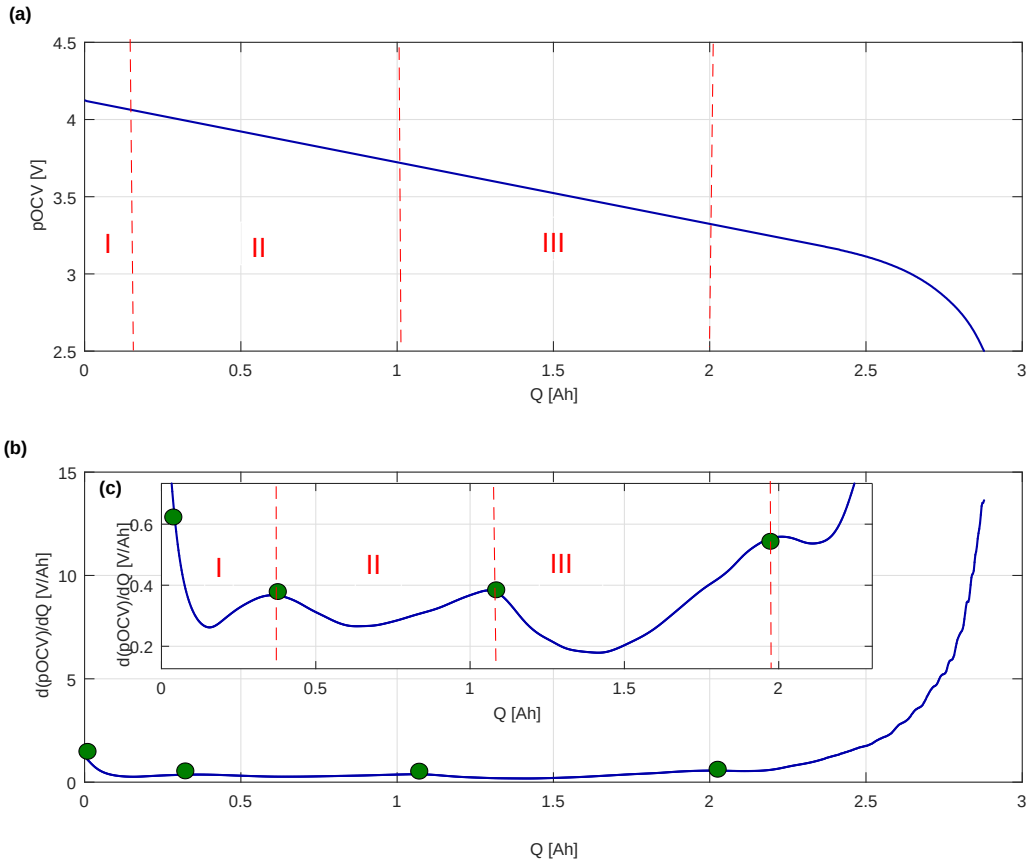

Figure 3.11: Relationship between (a) constant gradient pseudo-OCV regions, (b) valleys in the DV curve and (c) valleys of DV curve zoomed.

(b) and (d). The filtering procedure firstly consists of averaging pOCV values which are related to any repeated charge measurements. Secondly, the remaining data points are linearly interpolated so that pOCV values exist at equally spaced Q values. The smoothed data was compared to the original data set to evaluate whether the smoothed data follow the original data accurately. This was done by ensuring that the median of the absolute deviations of the recorded dataset about the smoothed line is below 2%. As it is shown in this section, this difference enables us to infer FOIs clearly and therefore it is suitable for the object of this study.

In the context of automotive applications, deriving the pOCV curve during operation is easier during charging than during discharging. This is because the discharging process cannot be controlled as it depends on driving conditions. However, the IC-DV curves can

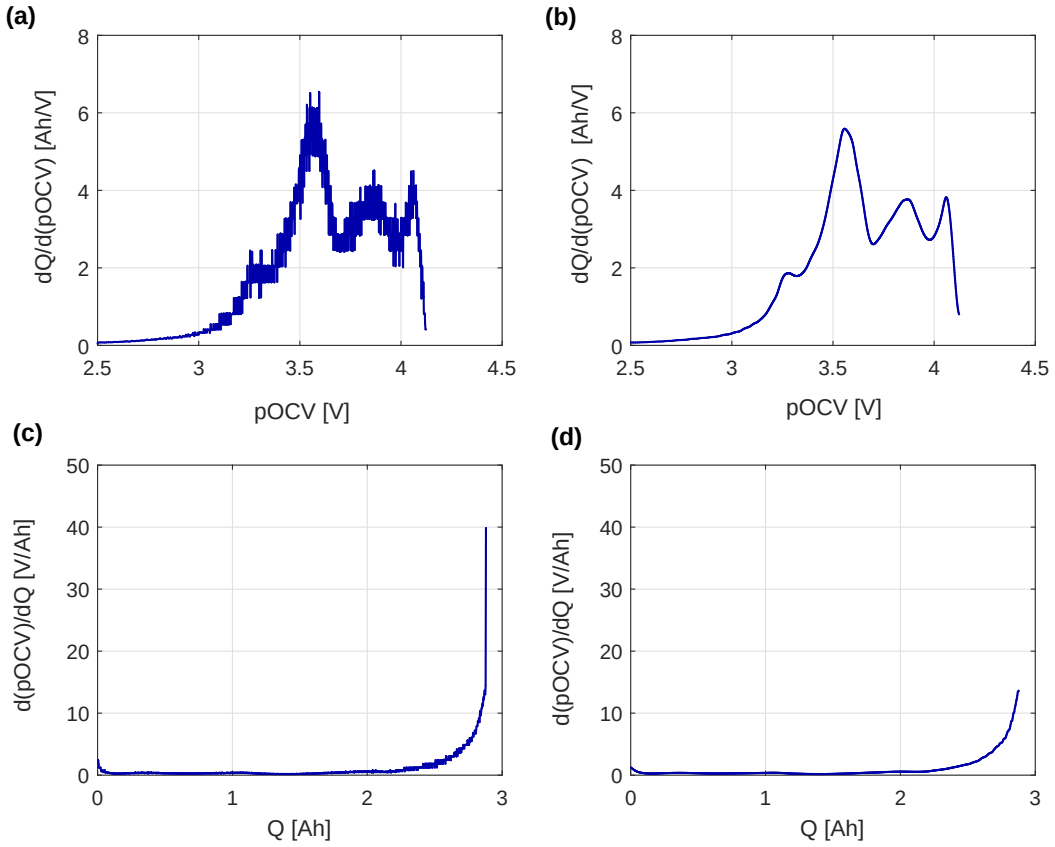

Figure 3.12: (a) and (b) IC and (c) and (d) DV curves before smoothing (left) and after smoothing (right).

be slightly different between charge and discharge measurements due to hysteresis effects. For instance, for a NMC 2.2 Ah cell Barai et al. [112] shows that pOCV measurements have a maximum difference of 20 mV between charge and discharge. In this study only discharge pOCV measurements were used. However, further work includes to calculate IC-DV curves based on charge measurements and evaluate the differences with respect to the curves generated using discharge measurements.

Regarding the analysis of IC and DV curves, Dubarry et al. [63, 113] suggested the use of FOIs. FOIs have been employed in this study to quantify the changes in IC-DV curves due to CtCV. Hence, FOIs represent an indirect measure of CtCV and are therefore considered in the proposed diagnostic procedure. Figure 3.13 illustrates examples of FOIs for IC and DV curves. These FOIs can be categorised as:

- **Voltage (IC) and capacity (DV) based:** peak or valley position, length of front or back tail, peak or valley half-width, voltage variation (IC), capacity variation (DV) and resistance increase.
- **Intensity based:** peak or valley intensity, intensity at front or back tail and intensity variation.
- **Area based:** area (capacity) under the curves.
- **Derivative based:** slope of peak or valley.

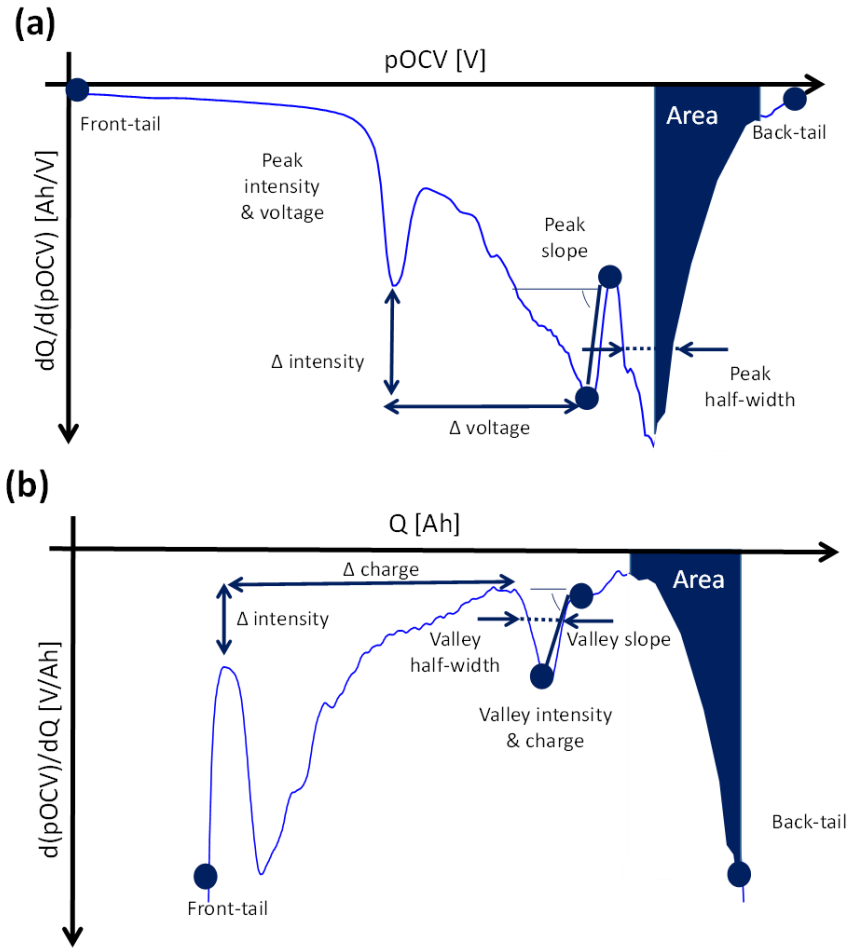

Figure 3.13: Schematic representation of possible FOIs on an (a) IC and (b) DV curve.

The sensitivity analysis of CtCV through FOIs using IC-DV curves is here explained for the example of LMO chemistry, 49S1P pack topology and normal input distribution. The results for the rest of the test scenarios are described in Section 3.5, or contained within

the Appendix A. Figure 3.14 and Figure 3.15 illustrate the resulting IC and DV pack curves for when SoC_i, SoH_i and Q_{ri} vary individually, known as theoretical scenarios, and for when all three CtCV parameters vary simultaneously, known as real scenario. For these scenarios the following FOIs have been defined:

- FOI 1: minimum voltage (front tail point).
- FOI 2: intensity of the first peak.
- FOI 3: intensity of the second peak.
- FOI 4: intensity of the third peak.
- FOI 5: intensity of the fourth peak.
- FOI 6: maximum voltage (back tail point).

These FOIs have been quantified for test scenarios evaluated in this study because they can be visually distinguished for different amounts of CtCV through IC and DV curves. For other test scenarios and cell chemistries, the number and type of FOIs can be different. As IC-DV curves are calculated from a slow discharge, the FOIs follow an ascend numeration from high SoCs (right) to low SoCs (left). Following on from the notation used in Figure 3.4 to separate between theoretical and real scenarios, here is also used a superscript '*' to distinguish between FOIs derived from a theoretical or a real scenario.

Comparing IC against DV, the DV curves need to be zoomed significantly to appreciate the differences in the FOIs at an appropriate resolution as illustrated in Figure 3.15 (b). Apart from this, DV curves are plotted against capacity in the abscissa axis. The capacity changes with ageing, and thus, it does not represent a fix reference point. By comparing IC and DV curves, it seems that the use of IC curves is more advantageous than the use of DV curves and therefore IC curves are here employed.

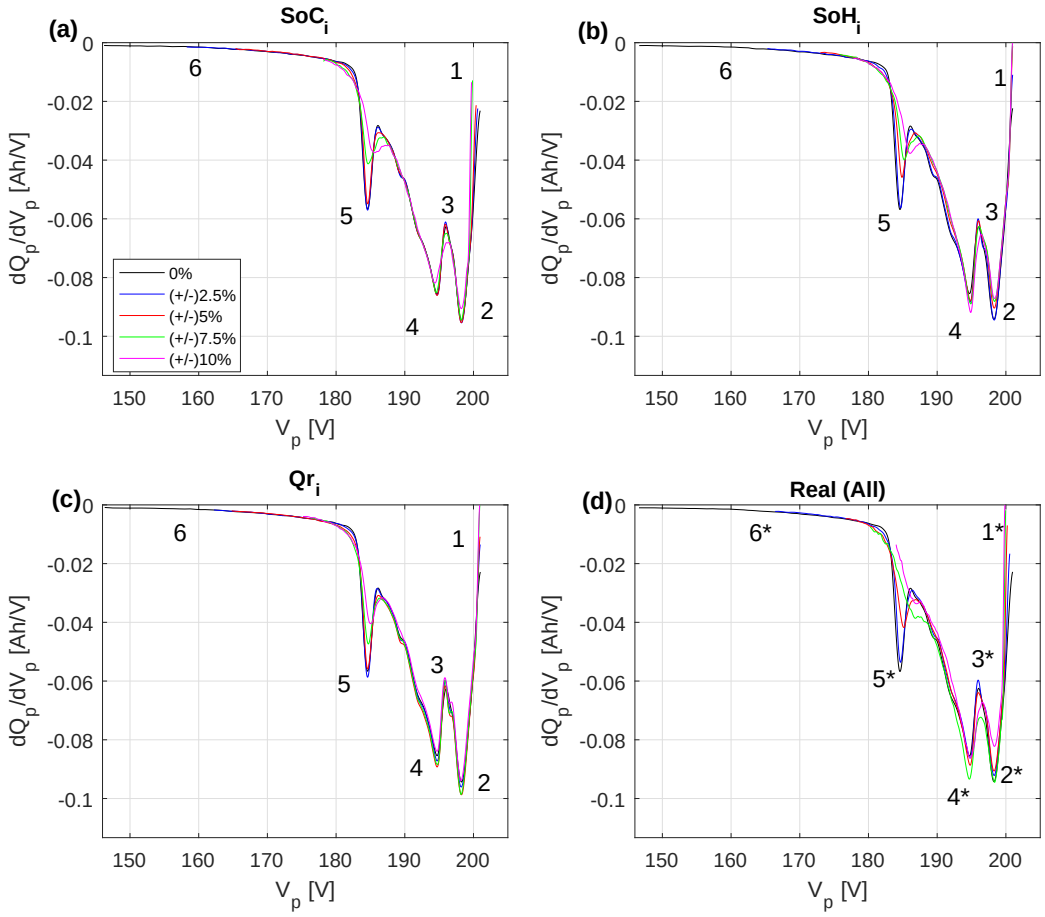

Figure 3.14: LMO 49S1P normal input variation IC pack curves: (a) - (c) individual variation (theoretical case) of CtCV(SoC$_i$, SoH$_i$ and Q$_{ri}$); (d) simultaneous variation (real case) of CtCV (SoC$_i$, SoH$_i$ and Q$_{ri}$)

Similarly to Figure 3.14, Figure 3.16 illustrates the IC response of the battery pack for when variations in initial resistance are considered. The battery pack was discharged at C/2 in order to account for kinetic effects i.e. variation of cell resistance. The higher C-rate reduces the resolution of the IC curves. In comparison to Figure 3.14, FOI 2 and 3 are in this case more difficult to visualize. In addition, CtCV due to initial resistance do not cause significant changes in the IC pack response as shown in Figure 3.16 (d). From this result is concluded that the use of IC curves with the aim of quantifying R$_i$ CtCV is then not suitable.

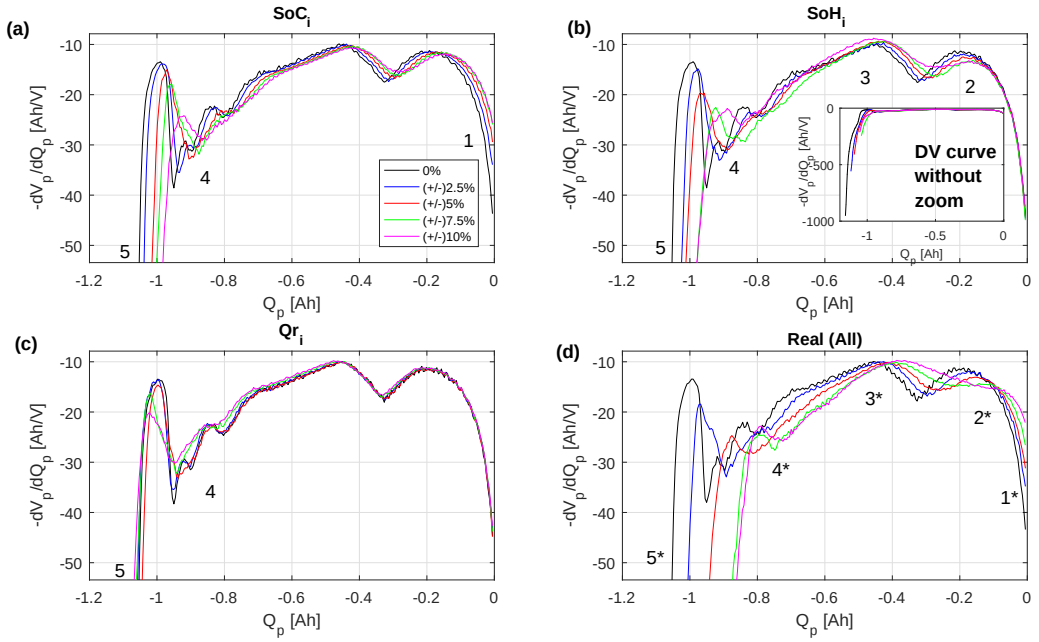

Figure 3.15: LMO 49S1P normal input variation - DV pack curves: (a) - (c) individual variation (theoretical case) of CtCV (SoC$_i$, SoH$_i$ and Q$_{ri}$); (d) simultaneous variation (real case) of CtCV (SoC$_i$, SoH$_i$ and Q$_{ri}$)

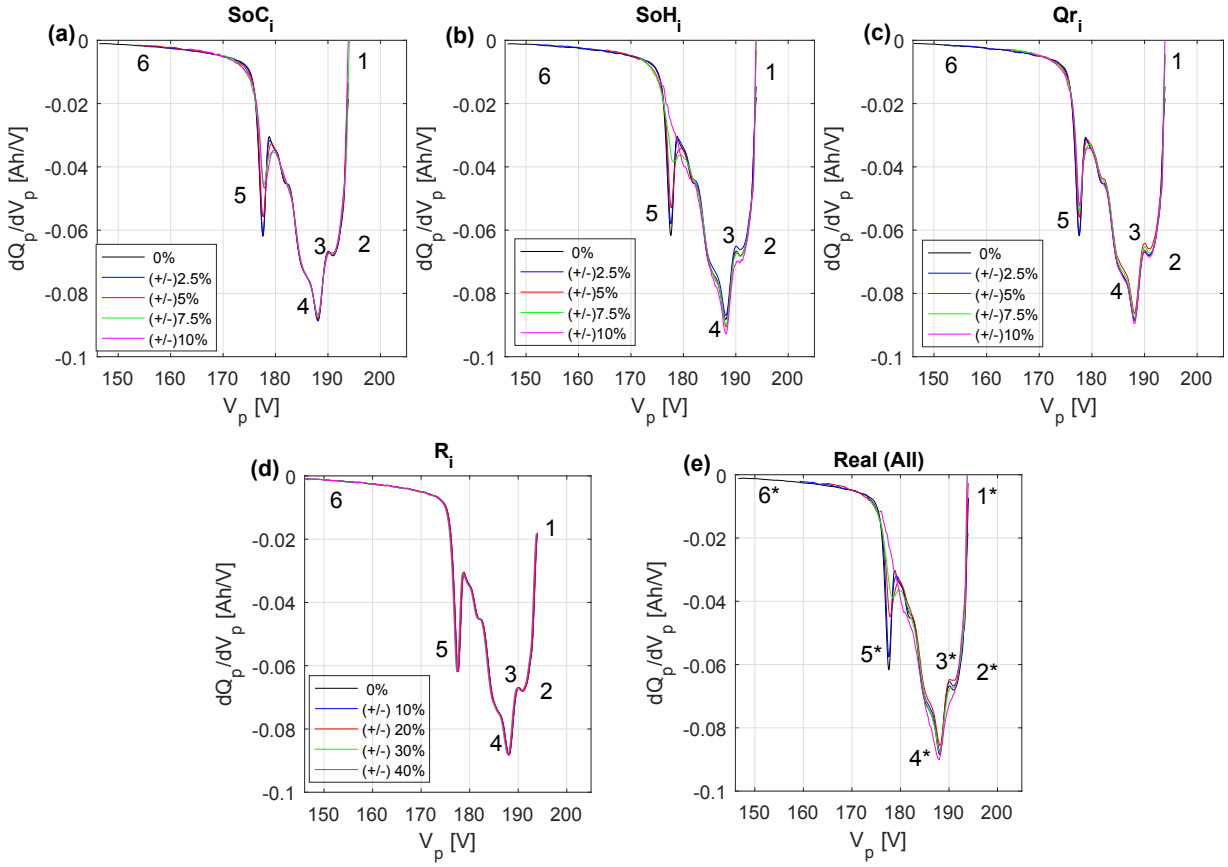

Figure 3.16: LMO 49S1P normal input variation - IC pack curves considering R$_i$ variation: (a) - (d) individual variation (theoretical case) of CtCV (SoC$_i$, SoH$_i$, Q$_{ri}$ and R$_i$); (e) simultaneous variation (real case) of CtCV (SoC$_i$, SoH$_i$, Q$_{ri}$ and R$_i$)

3.4.5 Step 5, 5* and 6: quantification and validation of FOIs from IC curves

Once the FOIs have been identified, the next step is to identify which FOIs are uniquely observable, i.e., which FOIs can be used to quantify the amount and the origin of CtCV. The growth in percentage (G_{FOI}) is the metric used for this. The G_{FOI} is selected because its calculation is simple, fast and can be applied to any type of FOI. For a given simulation, the G_{FOI} is computed for each FOI a and each amount of CtCV b using Equation 3.5.

$$G_{FOI} = \frac{FOI_{a,b\%} - FOI_{a,0\%}}{FOI_{a,0\%}} \cdot 100 \tag{3.5}$$

Where a = [1,2, ... ,5], and b = [0, ±2.5%, ±5%, ±7.5%, ±10%]

For the case here studied, LMO 49S1P normal input variation, G_{FOI} is calculated based on dQ/dV peak's intensity for FOI 2, 3, 4 and 5; and voltage for FOI 1 and 6.

According to the theory of Design of Experiments [114], simulations need to be repeated a minimum number of times in order to ensure precision in the results. 10 repetitions was the minimum number chosen to calculate the impact of the randomness in the quantification of FOIs. Further details regarding this choice are given in Appendix A.1.1.

For 10 repetitions, the mean value of G_{FOI}, $\overline{G}_{FOI}$, is calculated. Figure 3.17 compares the change of $\overline{G}_{FOI}$ for each FOI with respect to the amount of CtCV due to SoC_i, SoH_i, Q_{ri} in the theoretical and real scenarios. For the 10 repetitions considered, the Standard Error (SE) is depicted in Figure 3.17. The calculation of the SE is explained in Appendix A.1.1. In order to validate a FOI to quantify CtCV, the next two requirements need to be fulfilled:

1. For a specific scenario, a theoretical FOI is uniquely observable with respect to the real FOI. This statement means that only a theoretical FOI due to a single CtCV

parameter (SoC_i, SoH_i or Q_{ri}) change in the same way as the real FOI. The rest of the theoretical FOIs related to the other CtCV parameters (SoC_i, SoH_i or Q_{ri}) do not contribute to the change of the real FOI.

2. For a specific scenario, the difference between the uniquely observable FOI and the real FOI is not larger than 50%. This value has been chosen because for the cases tested in this work this is the maximum difference that has been obtained. Further work includes selecting this error following a less empirical procedure.

From Figure 3.17 it is seen that FOI 1 for SoC_i and FOI 5 for SoH_i fulfill these requirements because:

1. $\overline{G}_{FOI1}$ and $\overline{G}_{FOI5}$ are unique observable. $\overline{G}_{FOI1}$ only changes for the case of the SoC_i whereas $\overline{G}_{FOI1}$ does not vary for the cases of SoH_i and Q_{ri}. Similarly occurs for the $\overline{G}_{FOI5}$. $\overline{G}_{FOI5}$ only changes for the case of SoH_i whereas for the SoC_i and Q_{ri} cases remains approximately constant.

2. $\overline{G}_{FOI1}$ and $\overline{G}_{FOI5}$ follows the same trend as the real scenarios, $\overline{G}^*_{FOI1}$ and $\overline{G}^*_{FOI5}$.

For the case studied in this example, LMO 49S1P normal input distribution, it is observed that CtCV due to SoC_i and SoH_i can be quantified using FOI 1 and 5. Quantifying two out of the three causes of CtCV makes the proposed diagnostic procedure viable to implement in real applications. Further details regarding the implementation of this procedure are given in Section 3.6.3.

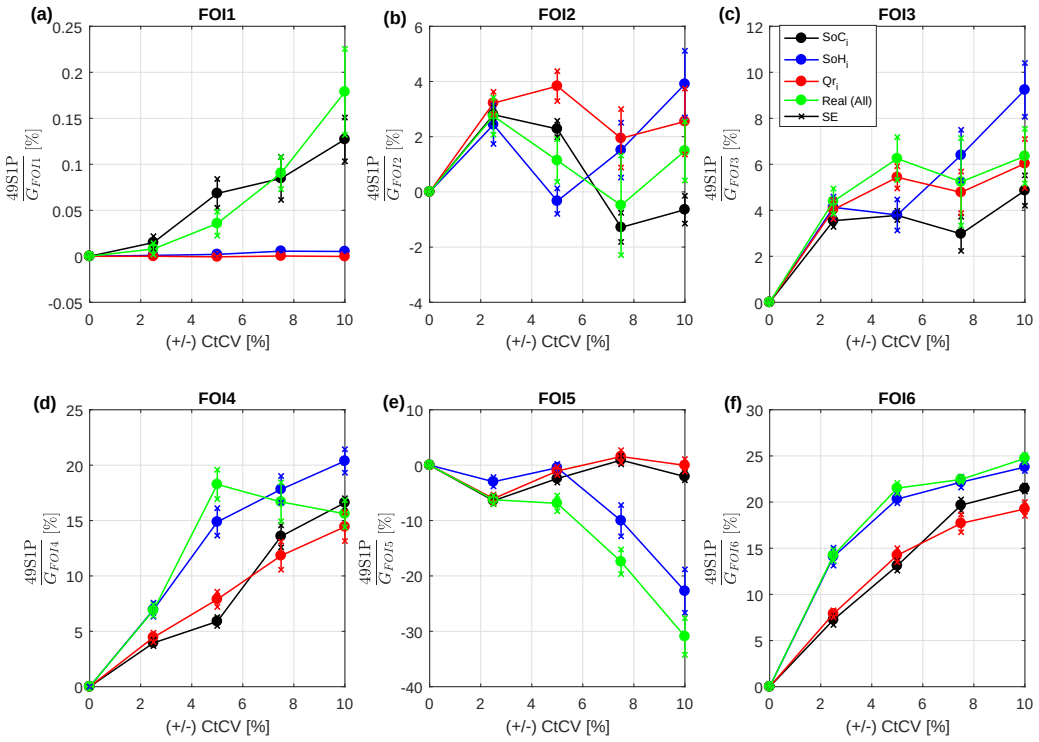

Figure 3.17: Quantification of FOIs with respect to CtCV parameter for LMO 49S1P normal input distribution.

3.5 Results and discussion

3.5.1 Pack topology dependency

Figure 3.18 illustrates the change of the FOIs for the LMO 49S1P normal input distribution with respect to the pack topology. It is said that a FOI is independent on the pack topology when this FOI changes in a similar way for each pack topology. Figure 3.18 shows FOI 1 is independent of the pack topology, whereas FOIs 2, 3 and 4 are dependent.

In contrast, FOI 5 changes independently for the 49S1P, 7(1)S7P and 1S49P topologies. This result can also be seen for FOI 6 which changes independently for 1S49P, 7(1)S7P and 7S7P topologies. It is noteworthy that the change of FOI 4 and 6 for the 49S1P topology is significantly larger than for the rest of the topologies. A possible explanation for this would be that cells connected in series such in the 49S1P topology are prone to

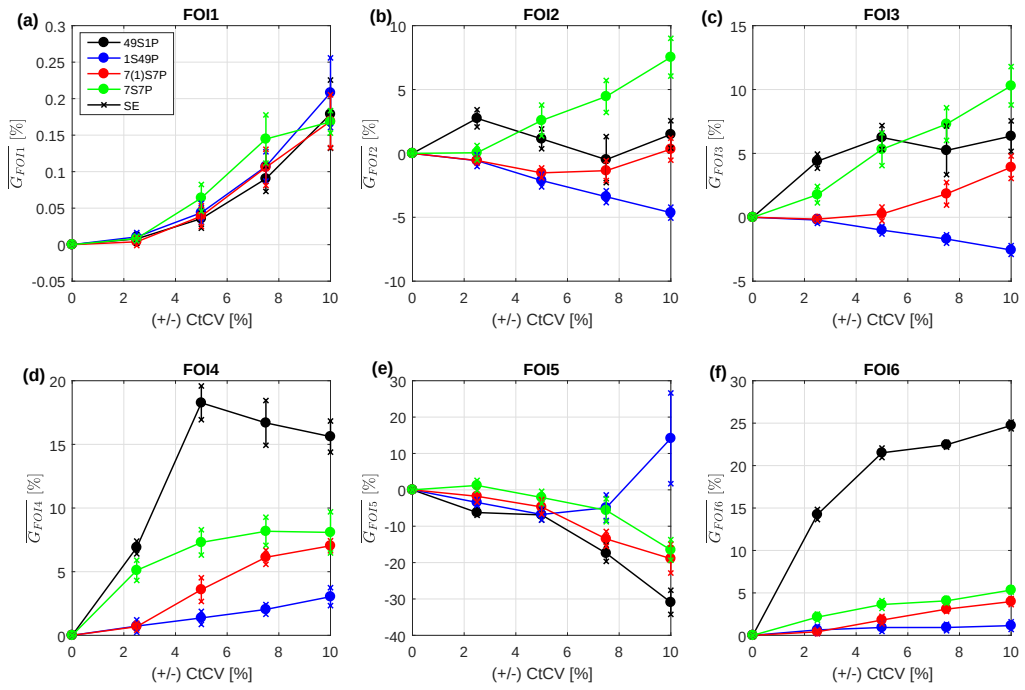

Figure 3.18: Quantification of FOIs for LMO 49S1P normal input distribution with respect to each pack topology.

voltage imbalance more than cells connected in parallel such in 1S49P, 7(1)S7P and 7S7P topologies [35].

The results for the cases of the NCA and LFP chemistries keeping the same conditions as the previous example are shown through Figure A.2 and Figure A.3 in the Appendix A. Figure A.2, NCA case, shows the change of FOI 1 is independent on the pack topology. The change of FOIs 2 and 3 is different for the case of 49S1P whereas the rest of the topologies change similarly. The FOIs 4, 5, 6 and 7 change differently for the 1S49P whereas for the rest of the topologies follow a similar trend.

Figure A.3, LFP case, illustrates the change of FOI 1 follows a trend for the 49S1P and 7(1)S7P and a different trend for the 1S49P and 7S7P. The change of FOI 2 is different for 49S1P and 7S7P whereas for 1S49P and 7(1)S7P follows the same trend except for the point of $\pm$ 10% variation. The FOIs 3, 4, 5 and 6 change differently for the 49S1P whereas for the rest of the topologies follow a similar change. In fact, the change of FOI 2 to 6 for

the 49S1P is significantly larger with respect to the other topologies. This result is the same as for FOI 4 and 6 in the LMO case as illustrated in Figure 3.18. As suggested in the LMO case, this result may occur because cells connected in series such in the 49S1P topology are prone to imbalance more than cells connected in parallel such in the 1S49P, 7(1)S7P and 7S7P topologies.

Table 3.5: Summary of the pack topology dependencies with respect to FOIs and cell chemistry.

FOI	LMO	NCA	LFP
FOI 1	Independent for all topologies	Independent for all topologies	Independent for 49S1P-7(1)S7P and 1S49P-7S7P
FOI 2	Dependent	Independent for all topologies except 49S1P	Independent for 1S49P-7(1)S7P
FOI 3	Dependent	Independent for all topologies except 49S1P	Independent for all topologies except 49S1P
FOI 4	Dependent	Independent for all topologies except 1S49P	Independent for all topologies except 49S1P
FOI 5	Independent for all topologies except 7S7P	Independent for all topologies except 1S49P	Independent for all topologies except 49S1P
FOI 6	Independent for all topologies except 49S1P	Independent for all topologies except 1S49P	Independent for all topologies except 49S1P

Table 3.5 summarises pack topology dependencies with respect to FOIs and cell chemistry. It can be concluded that LMO and LFP hold similar pack topology dependency, i.e., FOIs are independent for the 49S1P case. In practice, this result means that the same FOI, e.g., FOI 1 for the LMO case, can be used independently for each pack topology to quantify CtCV.

3.5.2 Input variability dependency

Following the same example as in Section 3.4.4, this subsection aims to identify the FOIs that can be further used to quantify the amount and the origin of CtCV for skewed input distribution. Instead of explaining each step in detail as in Section 3.4, here the diagnostic procedure is directly applied. Figure 3.19 illustrates the IC pack response for this test scenario and Figure 3.20 the corresponding quantification of FOIs. In comparison to the case depicted in Figure 3.14, it is seen that only FOI 1 can be used to quantify CtCV due to SoC_i because FOI 1 fulfills the requirements described in Section 3.4.5. This result highlights that the input distribution of CtCV affects which FOIs can be used.

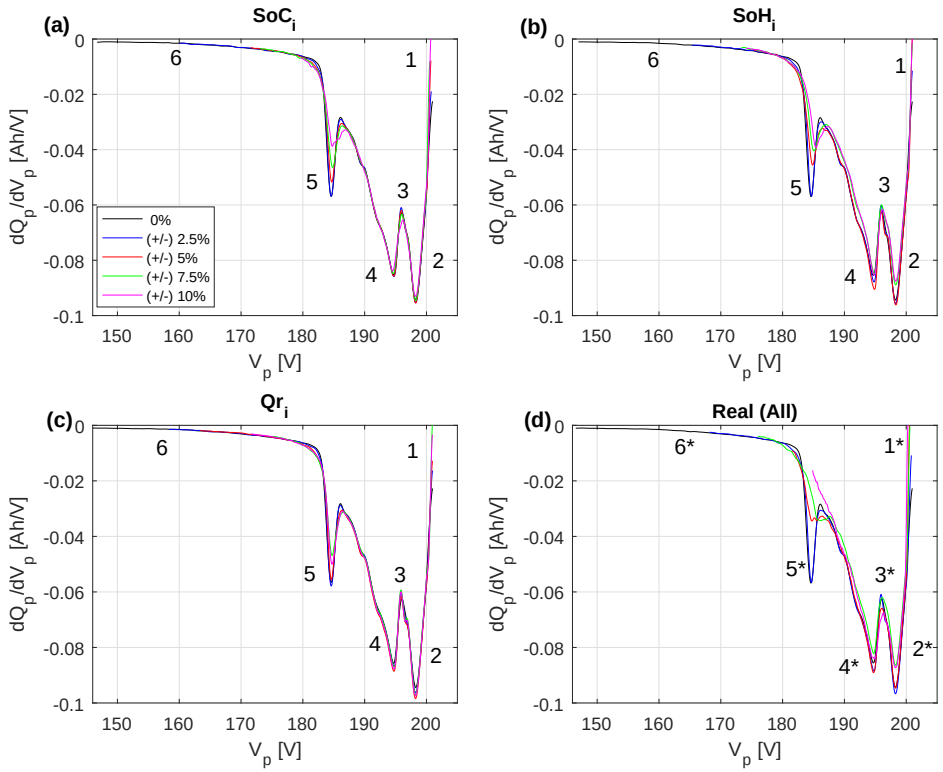

Figure 3.19: LMO 49S1P skewed input distribution - IC pack curves: (a) - (c) CtCV theoretical case; (d) CtCV real case.

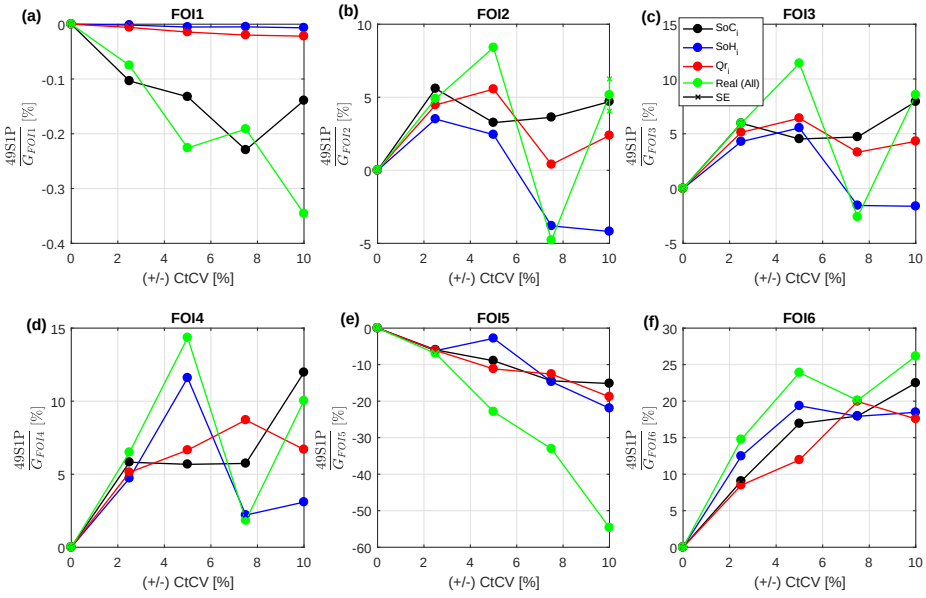

Figure 3.20: Quantification of FOIs with respect to CtCV parameter for LMO 49S1P skewed input distribution.

3.5.3 Analysis of the rest of simulation scenarios for normal input distribution

Table 3.6 summarises the FOIs that can be used to quantify the amount and the origin of CtCV for each cell chemistry and pack topology for normal CtCV distribution. It is often seen that FOI 1 and 3 can be used to quantify CtCV due to SoC_i and FOI 2 can be used to quantify CtCV due to SoH_i. For the case of NCA 1S49P, FOI 7 can also be used to quantify CtCV due to SoH_i. From here it is possible to conclude that for the conditions analysed in this study none of the FOIs can be used to quantify CtCV due to Q_{ri}. Further work with this respect is needed.

It is beyond the scope of this study to conduct a similar evaluation for the results derived by applying a skewed input distribution. Skewed input distribution was used to highlight the sensitivity of the proposed procedure with respect to the input data. As shown in Section 3.5.2, the FOIs used to quantify CtCV for the LMO 49S1P scenario depends on how CtCV are distributed. From this, further work includes studying the minimum level of skewness of the input data until which is possible to consider the same FOIs as when CtCV are normally distributed.

Table 3.6: FOIs that can be used to quantify amount and origin of normal CtCV distribution for LMO, NCA and LFP cell chemistries, and 49S1P, 1S49P, 7(1)S7P and 7S7P pack topologies.

	LMO		**NCA**		**LFP**	
Topology	**FOI**	**CtCV**	**FOI**	**CtCV**	**FOI**	**CtCV**
49S1P	1	SoC_i	1	SoC_i	1	SoC_i
	5	SoH_i	2	SoH_i	-	-
1S49P	1	SoC_i	7	SoH_i	1	SoC_i
	3	SoC_i	-	-	3	SoC_i
7(1)S7P	1	SoC_i	1	SoC_i	1	SoC_i
	-	-	-	-	3	SoC_i
7S7P	1	SoC_i	1	SoC_i	1	SoC_i

3.6 Implications for Battery Management Systems (BMSs)

3.6.1 Battery pack performance

Given normal input distribution, Figure 3.21 illustrates the corresponding normalised pack capacity fade, $C_{p\,n}$, of the LMO chemistry for each CtCV type and pack topology. Looking at the capacity reduction for the real scenarios it is seen that for a maximum of ±10% CtCV, the capacity can decrease up to 15% for 49S1P and 10% for 7(1)S7P and 7S7P topologies. The capacity only reduces up to 2.5% for the case of 1S49P because cells connected in parallel tend to self-balance as explained in Section 3.5.1. The significant reduction in capacity for the 49S1P, 7(1)S7P and 7S7P cases highlights that CtCV contribute significantly to meet the end of warranty limit of automotive battery packs. This result suggests that it is essential to minimise CtCV.

CtCV due to SoH_i leads to a larger pack capacity reduction than CtCV due to SoC_i and Q_{ri}. This result highlights that changes in the SoH_i are mainly driven by changes in OCV vs. SoC (internal capacity). This is realistic for this case as the battery pack has been discharged at C-rate of C/25 before putting it in operation and hence, kinetics effects are not pertinent. On the opposite, CtCV due to SoC_i and Q_{ri} have a lower impact on the reduction of capacity because their definition is not directly dependent on the capacity. Figure A.21 and Figure A.22 show that this result is consistent for the NCA and LFP cell chemistries. However, there is an exception for the case of LMO 7S7P ±5% variation where the capacity fade due to Q_{ri} is larger than the capacity fade due to SoH_i. Further work is needed to explain this result. For all the cases analysed, the resulting capacity fade for real scenarios is larger than for the theoretical scenarios. From Figure 3.21 can be inferred that the effects of each CtCV type are additive producing a large reduction in the capacity in the real scenario case.

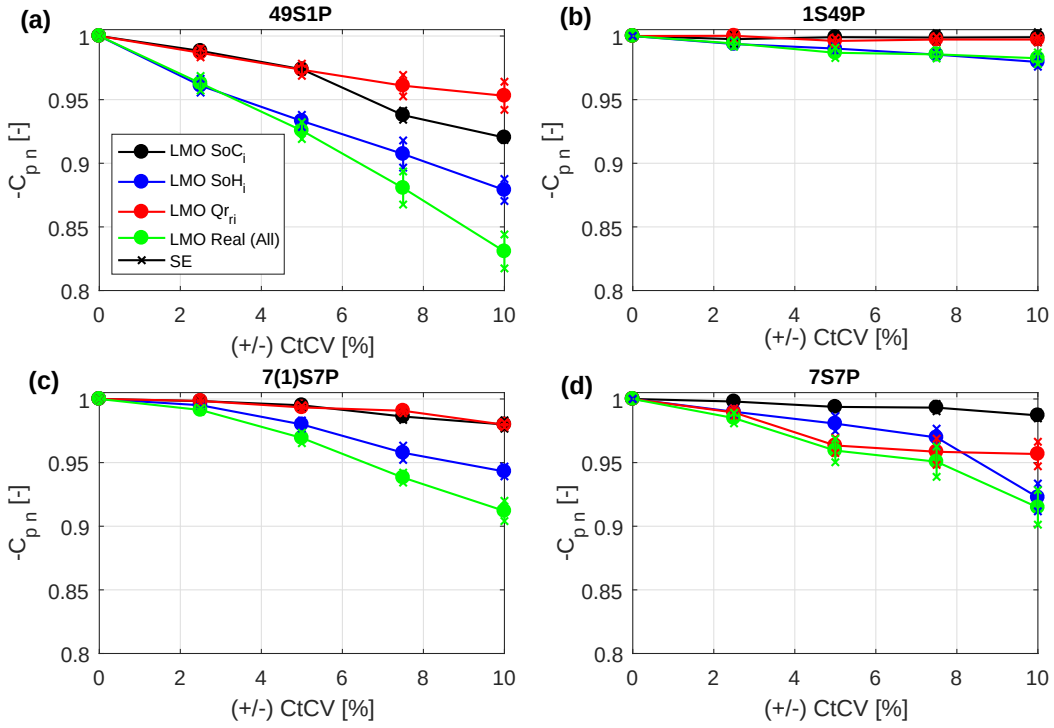

Figure 3.21: LMO normalised pack capacity fade for each pack topology for CtCV theoretical and real scenarios.

Figure 3.22 illustrates that the capacity decrease for each chemistry is very similar for every pack topology except for 7(1)S7P. Figure 3.22 shows that for the NCA 7(1)S7P the reduction in capacity is larger, following by the LMO and LFP chemistries. It is believed that the different shape of the OCV vs. SoC curves for each chemistry explains this result as illustrated in Figure 3.23. NCA OCV vs SoC curve is less flat than LFP and LMO and hence, the lower cutoff voltage, represented by a dashed line in Figure 3.23, is more likely to remove more capacity than for the case where the voltage drop is steeper seen in the LMO and LFP cases.

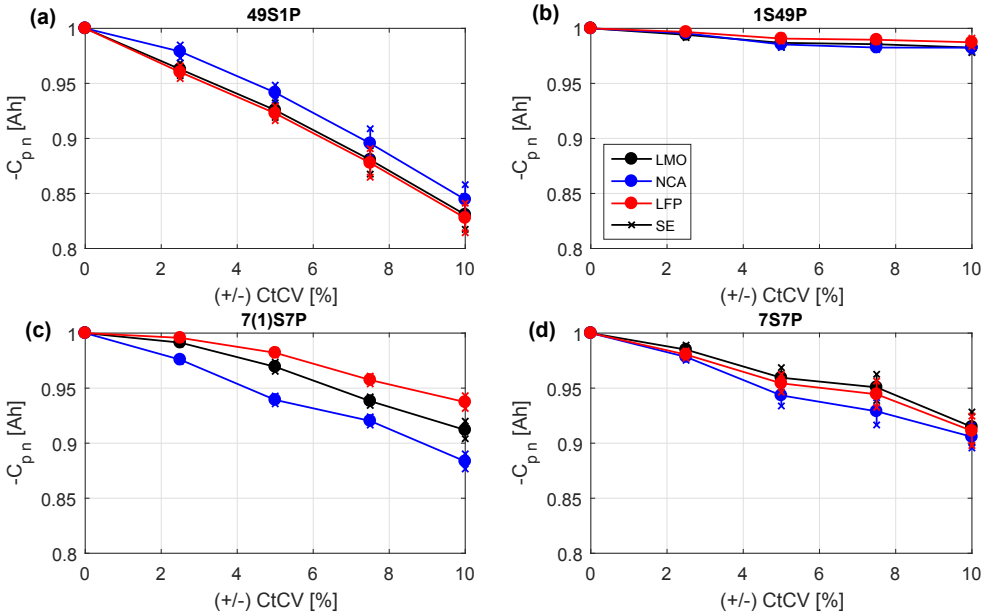

Figure 3.22: Normalised capacity fade for each pack topology and cell chemistry for CtCV real scenario.

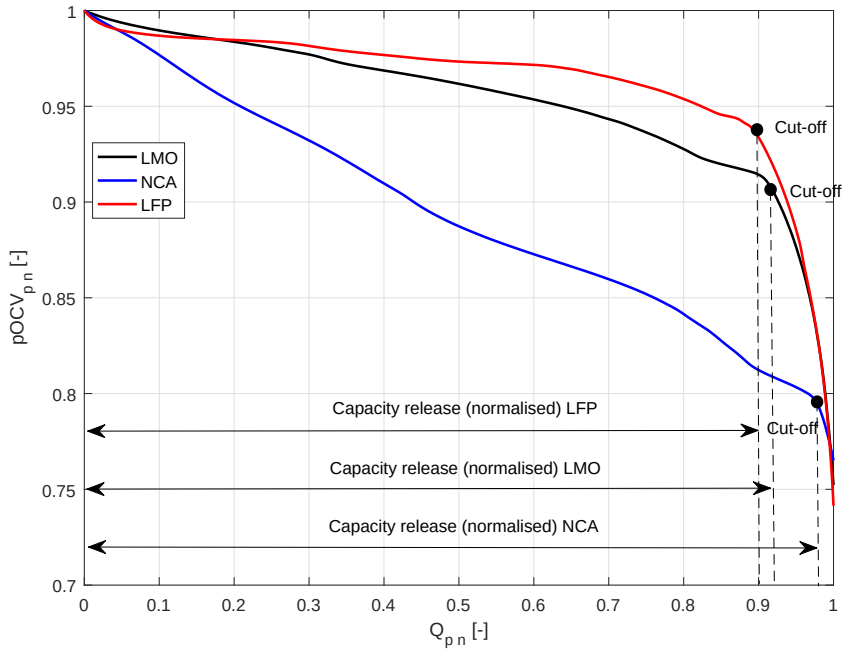

Figure 3.23: Normalised battery pack pOCV vs Q for LMO, NCA and LFP cell chemistries.

3.6.2 Analysis of CtCV from pack to cell level

This section aims to relate the changes of the IC curves at battery pack level with changes of the IC curves at cell level.

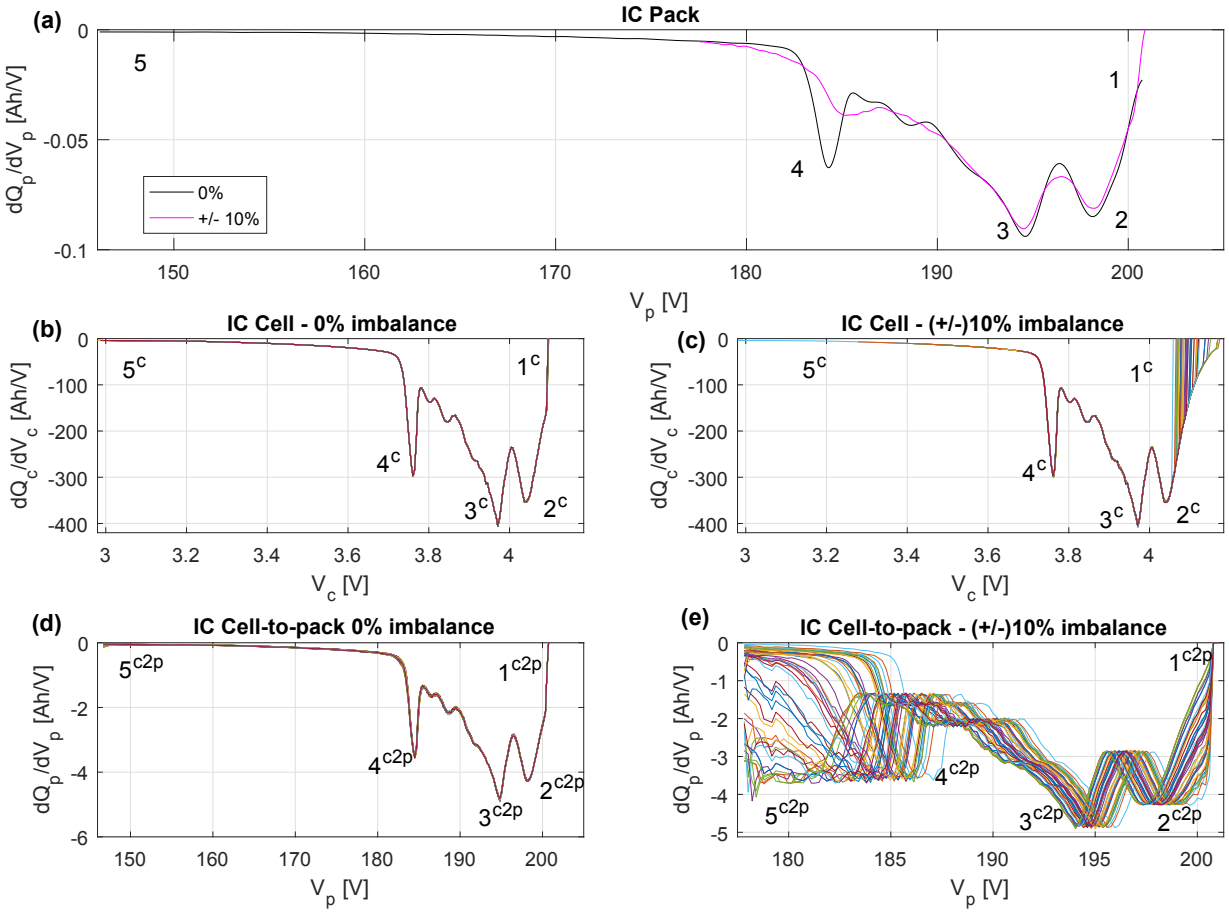

Figure 3.24: Example of 49S1P (a) IC pack, (b) - (c) IC cell and, (d) - (e) IC cell-to-pack curves for 0% and ±10% SoC_i CtCV

Figure 3.24 (a) illustrates the corresponding IC pack signatures for the LMO_SoC_49S1P_0% and LMO_SoC_49S1P_±10% scenarios, similar as was shown in Figure 3.17. Figure 3.24 (b) and (c) depict the corresponding IC signatures for each of the 49 cells for the CtCV 0% scenario and ±10%, respectively. To differentiate with the enumeration of the FOIs of the pack signatures, the FOIs of the IC cell signatures includes a superscript "c". Figure 3.24 (b) illustrates that for the case of CtCV 0% the IC cell curves overlap since they are not

subject to any variability. Figure 3.24 (c) depicts differences in FOIs 1 and 6 for the case of CtCV ±10%. The variability of SoC_i is translated into differences in the initial and end voltages (cell SoC) of the IC curves. However, from the IC cell responses is not possible to explain the changes of the decrease in intensity of the FOIs 2, 3, 4 and 5. This result outlines that individual cell IC curves do not provide enough insights to infer the CtCV at battery pack's level. To solve this, cell-to-pack IC curves are calculated as explained in Appendix A.1.5. Figure 3.24 (d) and (e) illustrates that cell-to-pack IC curves have the shape of single cell IC curves outlining the differences seen in IC pack curves.

The FOIs in Figure 3.24 (d) and (e) include a superscript "c2p" to differentiate with the enumeration of the FOIs of the pack and cell signatures. As expected, Figure 3.24 (d) does not show any difference between the cell-to-pack IC curves because the simulation does not consider any CtCV. For the case that there is ±10% CtCV, Figure 3.24 (e) illustrates that at high voltage (FOI 1^{c2p}), the capacity usage in each single cell appears shifted depending on the initial SoC, which was expected based on Figure 3.24 (c) (FOI 1). The most noticeable changes, however, are at low voltage (FOI 5^{c2p}), where the last peak appears extremely broad for some cells. This result can be explained by the fact that at this stage, the cells that started at lower SoCs are already fully discharged, i.e., a peak is completed, whereas the cells that started at higher SoCs still have some capacity. At the pack level, most cells finished the peak in FOI 5 and thus have their voltage dropping sharply. As a result, there is a large dV difference for a small dQ difference, and hence, the peak at the cell-to-pack (FOI 5^{c2p}) appears broader. This new graphical visualization tool for IC or DV curves can be used further to quantify changes in pack voltage signature upon ageing, e.g., analysis of degradation modes, evaluate balancing strategies or outline differences between cells throughout a pack. These areas of further work are discussed in Section 3.7.

3.6.3 Practical implementation

The diagnostic procedure here presented quantifies the amount and the origin of CtCV in battery packs through the analysis of IC curves. In particular, CtCV is here defined as a metric which quantifies the amount of initial SoC, SoH and Qr cell-to-cell differences. Quantifying CtCV can mitigate the negative effects of extrinsic and intrinsic factors described in Section 2.2.1. The framework of a hypothetical implementation of this diagnostic method by an automotive OEM is shown in Figure 3.25. This framework is composed of eight steps that are described below:

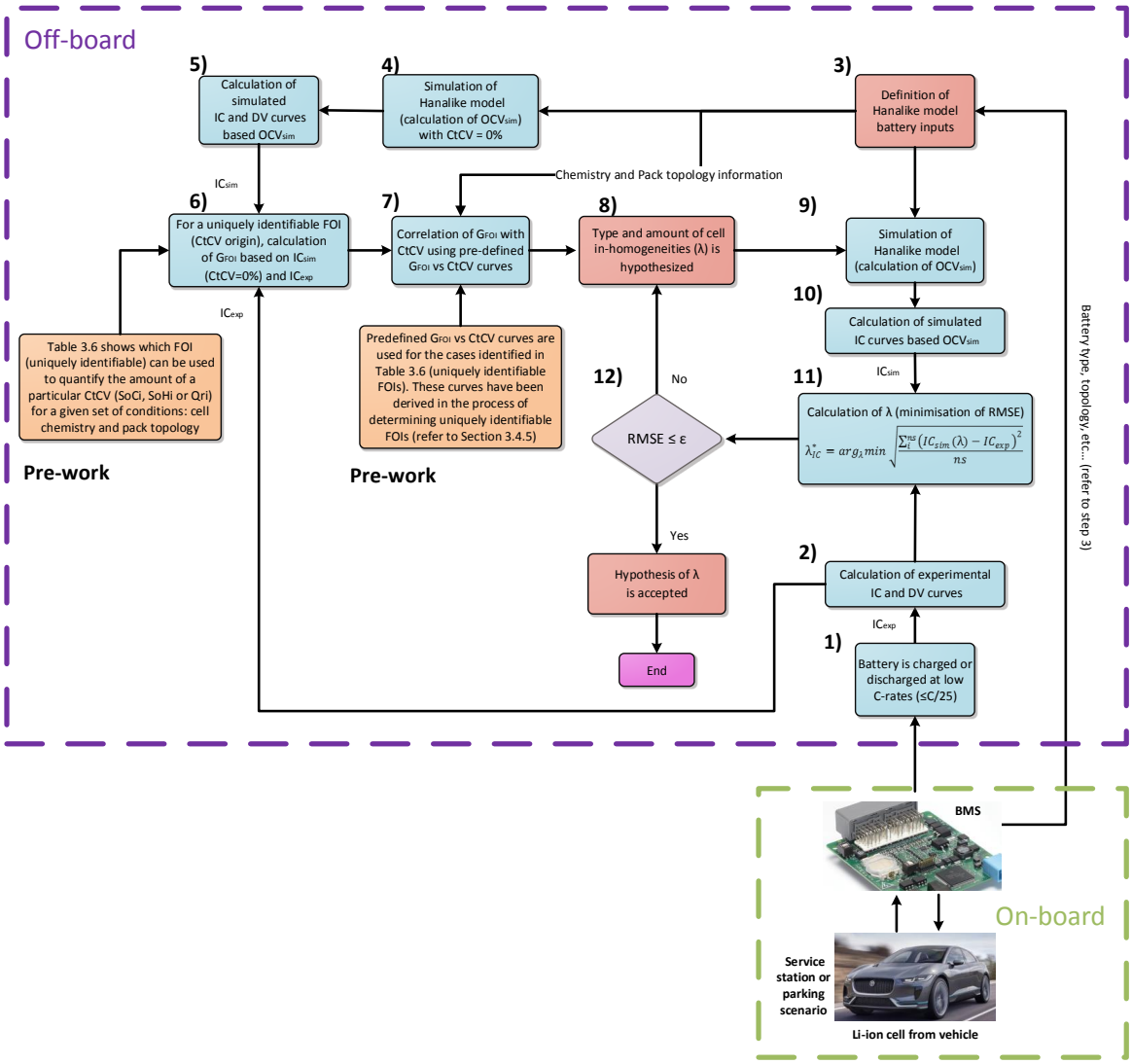

Figure 3.25: Suggested framework to implement the proposed diagnostic method.

- **Step 1:** the battery pack is charged or discharged at a constant C-rate lower than C/25 to generate the required full-cell OCV data. This test can be performed using an automated battery pack tester, commonly used in the laboratory. An example of this tester including its specifications such as accuracy and precision levels can be found in [115].

- **Step 2:** the gathered charge and discharge full-cell OCV data is employed to calculate the corresponding experimental IC and DV curves known as IC_{exp} and DV_{exp}.

- **Step 3:** the inputs of the Hanalike model are defined according to the specific battery that needs to be diagnosed. These inputs are:

  - Cell chemistry.
  - Battery pack topology.
  - Cell, module and pack cutoff voltage, temperature and current values.
  - Constant current charge or discharge profile at constant C-rate lower than C/25 in order to generate the required full-cell OCV data. This data is used to calculate the IC and DV curves.

- **Step 4:** a slow charge or discharge at a constant C-rate lower than C/25 considering 0% CtCV is simulated in the Hanalike model. This simulation considers the chemistry and topology of the pack that needs to be diagnosed.

- **Step 5:** the gathered charge or discharge full-cell OCV data from Step 4 is employed to calculate the corresponding simulated IC and DV curves, known as IC_{sim} and DV_{sim}.

- **Step 6:** for a particular cell chemistry and pack topology, the FOIs that can be used to determine the origin and the amount of CtCV are shown in Table 3.6. For instance, for the case of LMO 49S1P battery pack, FOI 1 can be used to quantify the amount of CtCV due to SoC_i. Then, the simulated (refer to Step 5) and the experimental (refer to Step 2) IC curves are considered to determine G_{FOI} according

to Equation 3.5. For instance, to know the amount of CtCV due to SoC_i for the case of LMO 49S1P battery pack normal input data, $G_{FOI\,1}$ would be calculated as illustrated in Figure 3.26 (a).

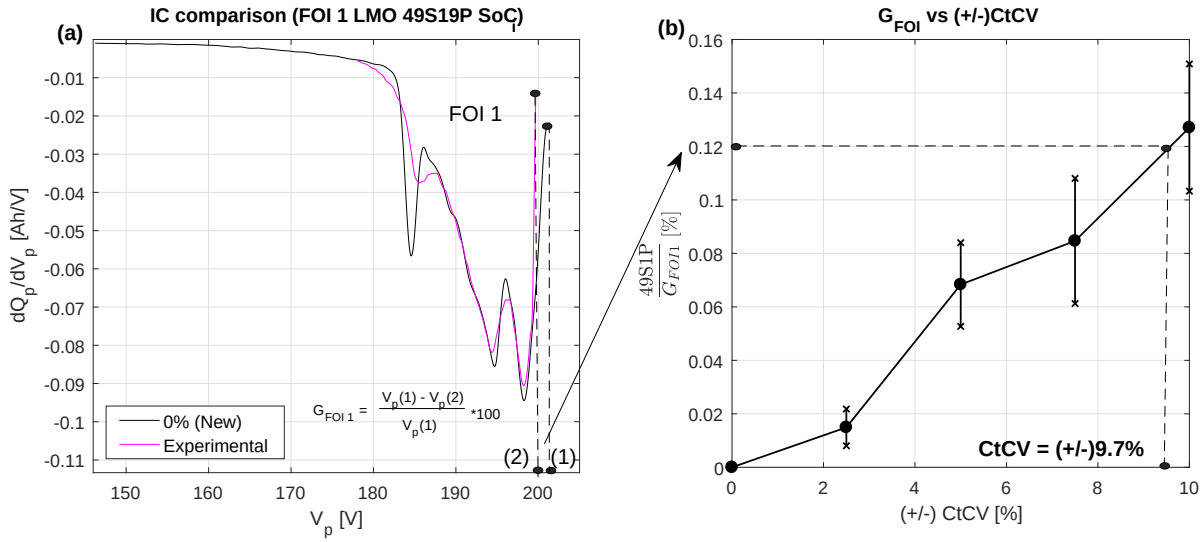

Figure 3.26: FOI 1 LMO 49S1P CtCV due to SoC_i case: (a) Graphical illustration of calculation of $G_{FOI\,1}$; (b) Correlation of $G_{FOI\,1}$ value with CtCV. This correlation is previously calculated according to the explanation in Section 3.4.5.

- **Step 7:** once the value of G_{FOI} from step 6 is calculated, this is used as an input to derive the amount of CtCV. For this, the G_{FOI} vs CtCV curves previously validated in Section 3.4.5 are considered. For the example of $G_{FOI\,1}$ LMO 49S1P, the black curve in Figure 3.17 (a) would be used. Entering the value of G_{FOI} for a particular FOI from step 6, the corresponding amount of CtCV is derived. For the example of $G_{FOI\,1}$ LMO 49S1P, the amount of CtCV due to SoC_i (FOI 1) is 9.7% as illustrated in Figure 3.26 (b).

- **Step 8:** a vector λ to hypothesize the origin of CtCV (Step 6) and the amount of CtCV (Step 7) is defined.

- **Step 9:** based on the battery pack inputs from step 3 and the hypothesized CtCV from step 8, the Hanalike model is run again to calculate the output voltage, OCV. This simulation will calculate the loading ratio and offset 'Alawa parameters for each duty cycle step as a function of the previous SoH. This simulation would be

performed online as shown in Figure 3.3. Loading ratio and offset are used to quantify the linear increase of LLI due to calendar ageing as explained in "Origin of CtCV", see Section 3.4.1.

- **Step 10:** the OCV and charge from step 6 are used to compute the corresponding IC_{sim} and DV_{sim} curves.
- **Step 11:** IC_{sim} and DV_{sim} are compared against the IC_{exp} and DV_{exp} calculated in step 2 by means of the root mean square error (RMSE) as shows Equation 3.6 for the IC, and Equation 3.7 for the DV.

$$RMSE(IC) = \sqrt{\frac{\sum_{is}^{ns} \left(IC_{sim}(\lambda) - IC_{exp}\right)^2}{ns}} \tag{3.6}$$

$$RMSE(DV) = \sqrt{\frac{\sum_{is}^{ns} \left(DV_{sim}(\lambda) - DV_{exp}\right)^2}{ns}} \tag{3.7}$$

Equation 3.6 and Equation 3.7 assume that the charge or discharge process takes from the first, is, to the last, ns, sampled points. Equation 3.8 and Equation 3.9 are used to minimise the RMSE using an optimisation algorithm such as genetic algorithm [111] or particle swarm optimisation (PSO) [116] so that λ can be determined.

$$\lambda_{IC}^{*} = arg_{\lambda} min \sqrt{\frac{\sum_{is}^{ns} \left(IC_{sim}(\lambda) - IC_{exp}\right)^2}{ns}} \tag{3.8}$$

$$\lambda_{DV}^{*} = arg_{\lambda} min \sqrt{\frac{\sum_{is}^{ns} \left(DV_{sim}(\lambda) - DV_{exp}\right)^2}{ns}} \tag{3.9}$$

- **Step 12:** the RMSE is compared to a defined threshold error called ϵ. The numerical value of ϵ is defined according to the requirements of each particular application. If the RMSE is smaller or equal to ϵ, then the hypothesized λ is accepted. Otherwise λ is rejected and steps 4 to 8 are repeated iteratively until the RMSE is smaller or

equal to ϵ. According to [68], where a similar approach is applied using OCV instead of IC and DV as variables, ϵ should be less than 8%. The approach presented in [68] aimed to quantify DMs.

This method can be implemented on-board and off-board. The advantage of implementing this method on-board is that external equipment to perform the required measurements and calculations is not needed. However, the volume, velocity and variety of the data and calculations involved in this method would need to be reviewed with regards to the specifications of a low-cost microcontroller unit [33]. This review is beyond the scope of this study and further work is needed with this respect. Apart from this, the main limitation relies on the applicability of the method itself. For the case of automotive applications, real battery operation is more dynamic than the conditions required to generate the IC and DV curves and therefore, this method is only suitable when the battery is at rest condition. This study used a rate of C/25. However, previous studies [24,109,117] have shown that higher C-rates, e.g., C/10, are enough to capture differences within IC and DV curves. For a potential on-board implementation, the application of this diagnostic procedure is feasible if the customer set the departure time allowing at least 10h of charging. For the off-board case, the customer would need to park the vehicle for at least 10h at a service station or dealership. In both cases, this should be viable since this type of diagnosis does not need to be performed regularly, e.g., twice per year [118].

3.7 Limitations and further work

The Hanalike battery pack model is comprised of sub-models that have been validated individually. However, this model has not been validated as a whole against experimental data and hence, the validation of this model represents a relevant area of further work. Aside from this, the Hanalike model can be improved regarding the following aspects:

- **Thermal component:** the current state of the model does not include any thermal component to consider the changes of temperature in cells based on the applied duty cycle and the undergoing electrochemical reactions in the single cells [119–122].

- **Pack topology:** the pack topology in which modules consisted of cells in series and parallel are themselves connected in series and parallel is not supported by the latest version of the model.

- **BMS submodel:** the current BMS model is quite rudimentary and does not perform some of the classic BMS calculations such as online capacity, SoC or SoH tracking. Work is in progress to implement the same controls that are on a conventional BMS.

- **Computation time:** the calculation of a duty cycle for when cells are connected in parallel (250s/cycle) is approximately 70 times slower than for when cells are connected in series (3.5s/cycle). The difference between both cases is that for cells connected in series only one current needs to be computed, whereas for cells connected in parallel a different current circulates through each cell. Thus, the amount of calculations is larger for the latter. This result is problematic for modelling packs that contain more than 50 cells connected in parallel because the model needs to handle a larger number of calculations. For instance, for the case of a 50S50P comprising a total of 2500 cells, the calculation time is around 40min/cycle. This calculation time is computed for a time-step of 200 points per regime, which is the optimum found in terms of accuracy and resolution [123, 124]. Optimising the code by, e.g., taking advantage of parallel computing could be investigated in the future to solve this problem.

Aside from improving the Hanalike model itself, three topics can be the subject of further investigations: assessment of balancing techniques, impact of CtCV in battery packs under different operating conditions and study the feasibility of the IC-DV technique in battery packs.

The battery pack model described in this work is flexible enough to assess the influence of different balancing techniques such as active balancing under different operating conditions. In addition, the accuracy and feasibility of SoC and SoH estimation techniques, e.g., Kalman filter for SoC estimation, under CtCV scenarios can be further evaluated.

This study investigates a potential procedure to quantify CtCV using IC pack signatures. However, there are many other research areas related to CtCV in battery packs. For instance, further studies include to investigate:

- CtCV under different operating conditions, e.g., considering temperature gradients.
- CtCV under different CtCV distribution, e.g., random distribution instead of a normal distribution.
- Different source of CtCV, e.g., Q_{ri}, coulombic efficiency, self-discharge rate or temperature.
- Grade of the severity of a cell failure, i.e., impact of CtCV of a single cell in isolation.

Concerning the use of IC curves as a diagnostic technique to quantify CtCV, further work can be focused in the following areas. Firstly, the use of alternative FOIs, e.g., area under the IC curves, can be explored to achieve a better quantification of CtCV in battery packs. Secondly, cell-to-pack IC curves can be further used to study the most pertinent DMs due to inhomogeneous ageing. As explained in Appendix A.1.5, further investigation is required to compute cell-to-pack IC curves for the nSmP or n(1)SmP pack topologies.

In view of a potential implementation, the IC technique lacks in different practical aspects that require attention. The C-rate of C/25 used in this study would require to discharge the battery over 25h. This test procedure is excessively long for a potential implementation and therefore, the feasibility of this procedure should be tested using C-rates lower than C/10. Even if the C-rate is larger, methods to avoid a full charge or discharge of the

pack need to be investigated as suggested in [109]. A recommendation would be to search for indexes that can be quickly obtained for battery screening without completing a full charge or discharge. These indexes can be, e.g., the FOIs presented in this study. Likewise, techniques to ensure smoothness of the IC curves at C-rates higher than C/10 need to be studied. These advancements would reduce the experimental time required to charge or discharge a pack fully and hence, would motivate the implementation of this technique in commercially viable applications.

3.8 Conclusions

According to the research objectives defined in Section 3.2, this study proposes a diagnostic procedure to quantify the amount and the source of CtCV in LIBs through IC battery pack signatures. This diagnostic procedure is tested using the Hanalike battery pack model, a model which unifies various models that were proposed and validated in the previous years [67,91–94]. The modular characteristic of the Hanalike model enables us to test the proposed diagnostic procedure into multiple scenarios. These scenarios comprise the simulation of LMO, NCA and LFP cell chemistries and 49S1P, 1S49P, 7(1)S7P and 7S7P pack topologies. This study focuses on CtCV that are pertinent when the battery pack is new before mounting it into a vehicle. In particular, variations in SoC_i, SoH_i, Q_{ri} and R_i were considered following a normal and a skewed distribution.

Based on these scenarios, IC curves were used to quantify the amount and the source of CtCV through predefined FOIs. FOIs were found to quantify CtCV due to SoC_i and SoH_i only for some cases, highlighting that the proposed diagnostic procedure is not universal. The change of the FOIs is analysed with respect to the pack topology. From this, it is seen that FOIs change differently for 49S1P topology since cells connected in series tend to imbalance easier than cells connected in parallel.

The reduction in battery pack capacity due to CtCV for the different simulation scenarios

is quantified. The results revealed that CtCV contribute significantly to meet the end of the warranty period of automotive battery packs for the 49S1P, 7(1)S7P and 7S7P topologies.

Cell-to-pack IC and DV curves are calculated to relate changes from pack to cell level. This new graphical visualization can be used to quantify changes in pack voltage signature upon aging, evaluate balancing strategies and outline differences between cells throughout a pack.

Finally, the aim of this study is ultimately to quantify the amount and origin of CtCV within a BMS automotive application. For this, an automated methodology is proposed to implement this diagnostic procedure as part of a real-time BMS. Off-board and on-board applications of this diagnostic method seem to be feasible in practice because CtCV are not necessary to be quantified on a short-term basis. It is believed that under normal operation, CtCV can be quantified twice per year. With the aim of improving battery pack performance, longevity and safety, it is argued that the implementation of this diagnostic approach would support lifetime control strategies within the BMS and the improvement of manufacturing and design processes of future LIBs.

4. Study 2 - A study of cell-to-cell interactions and degradation in parallel strings: implications for the BMS

4.1 Introduction

The self-balancing characteristic of parallel cells allows a BMS to approximate the cells as one equivalent cell with a single SoH value. As shown with [35], a single SoH value is however not applicable if the initial SoH of each cell is different, which can occur when cell properties change due to inconsistent manufacturing processes or in-homogeneous operating environments. As described in Section 2.2.2, previous studies [41, 48, 52, 53] highlight that cells connected in parallel will age differently when the SoH of each cell is not the same. However, none of these studies show the quantification of SoH over ageing. As such, this work quantifies SoH_E and SoH_P when initial cell-to-cell SoH is different. Four commercial 3Ah NCA 18650 cells connected in parallel at 25℃ are aged for 500 cycles, depth of discharge 100%. Each of the cells was initially aged to a different amount: cell 1, 0 cycles, cell 2, 50 cycles, cell 3, 100 cycles and cell 4, 150 cycles. Extrapolating this test to the Tesla Roadster 2008 model battery pack, the duration of the test is representative of 100,000 miles / 10 years BEV service. Further details of this extrapolation are given in Appendix A.2.3.

As explained in Section 2.2.2, the measurement of capacity is in the order of hours whereas the measurement of the resistance is in the order of minutes. However, according to Section 2.2.2, both capacity, and resistance are necessary metrics to calculate the SoH because each of these is related to different vehicle attributes: capacity to driving range and resistance to vehicle performance. To reduce the time in measuring capacity, previous studies have proved a correlation between capacity and resistance for individual cells [61,62] and packs [58]. This correlation enables us to calculate the capacity by just measuring the resistance, saving consequently time and money, e.g., in instrumentation equipment. However, none of these studies [58,61,62] prove this correlation when cells forming a module have different ageing states. Such a scenario can be equally pertinent in real applications as the ones previously studied. Undertaking the data gathered in the first part of this Chapter, the second part aims to prove the validity of the correlation between resistance and capacity for the case when a battery module is composed of cells with different ageing states.

The structure of this Chapter is divided as follows: Section 4.2 defines the main objectives of this study. Section 4.3 summarises the experiment where four cells connected in parallel were aged by 500 cycles. The obtained results are explained in Section 4.4. To understand the reasons behind the change in SoH, the distribution of the SoC, current, temperature, charge-throughput and thermal energy were studied in Section 4.4. Section 4.5 evaluates the correlation between capacity and resistance for the data gathered from Section 4.3. The limitations of this study and further work are outlined in Section 4.6. Finally, the conclusions of this study are presented in Section 4.7.

4.2 Objectives of this study

According to Table 2.1, the main objectives of Study 2 are:

1. Experimentally quantifies the cell-to-cell SoH, until the battery's EoL, for a scenario when each initial cell SoH is different.

2. Evaluate a time efficient methodology to monitor SoH at battery module/pack level comprised of inhomogeneous aged cells.

4.3 Experimental procedure

This study extends the experiment performed in [35], where four 3 Ah NCA 18650 Li-ion cells were pre-aged by 0, 50, 100 and 150 cycles individually. This pre-ageing test gave an initial SoH_E difference of 40% and SoH_P difference of 45% between the least and the most aged cells. These values correspond to a difference in capacity and impedance of circa 8% and 30% respectively. As mentioned in Section 2.2.1, research published highlights that differences in cell properties from initial manufacture and integration may be circa 25% for impedance [41] and 9% for capacity [40], which are in agreement with the initial differences considered in this study. The four cells are then connected in parallel and cycled for a total of 500 cycles. 500 cycles represent the EoL state according to the manufacturer's specifications [125].

Table 4.1 shows the experimental procedure is divided into two phases: cycle ageing and cell characterisation. The following subsections summarise each of these tests. A detailed analysis of the error in the measurements was provided within Section 3.2.4 in Submission 1 [31]. This analysis concluded that the measurements are within the acceptable error defined by the equipment manufacturer. Additional explanation of this test is given in Section 3 of Submission 1 [31] and [35].

4.3.1 Cycle ageing

Figure 4.1 (a) illustrates the cycle used to age the cells. This test involved repeated cycles at constant ambient temperature of 25 ℃ ± 1 ℃ of the following: a 1 C discharge until the lower voltage limit was reached followed by Constant Current-Constant Voltage (CC-

Table 4.1: Experimental test matrix [21].

Cell	Test	# ageing cycles (individual cells) [#cycles]	# test cycles (cells connected in parallel) [#cycles]	# cycles (individual +parallel cells) [#cycles]	Testing procedure	T [°C]	ΔDoD [%]	t_{samp} [s]
1	Cycling	0	500	500	CC-CV chg and 1C dchg	25	100	1
	Characterisation	Every 50 cycles	Every 50 cycles	-	1C dchg, EIS test and pOCV	25	100	1
2	Cycling	50	500	550	CC-CV chg and 1C dchg	25	100	1
	Characterisation	Every 50 cycles	Every 50 cycles	-	1C dchg, EIS test and pOCV	25	100	1
3	Cycling	100	500	600	CC-CV chg and 1C dchg	25	100	1
	Characterisation	Every 50 cycles	Every 50 cycles	-	1C dchg, EIS test and pOCV	25	100	1
4	Cycling	150	500	650	CC-CV chg and 1C dchg	25	100	1
	Characterisation	Every 50 cycles	Every 50 cycles	-	1C dchg, EIS test and pOCV	25	100	1

CV) charging protocol. The CC phase involved charging the cell at C/2 until the end of charge voltage (4.2 V) was reached. The CV phase then consists of charging the cell until the current fell to C/20 (150 mA). This profile was selected to significantly age the cells while not exceeding the manufacturers operating specification. This profile was achieved by cycling the cells with a full DoD without using large currents [35]. A large DoD is conceived to emulate the operation of a typical BEV in which, as discussed within [21], the BMS will control a large variation in SoC to maximise the range of the vehicle.

The Bitrode MCV16-100-5 automated battery tester used in this experiment can control the applied current to the parallel stack, but it is unable to measure the current in each individual cell. Measuring the individual current in each cell was key within this work to understand the cell-to-cell SoH variation over time. For this, the existing test set up developed by Bruen et al. [35] was used. According to Bruen et al. [35], different methods can be used to measure the individual current over each cell. Ideally, the equipment for measuring the current should not be part of the circuit, so that the magnitude of the current does not change. Hall-effect sensors represent a candidate to measure the current in this way. However, according to [35], the resolution and accuracy of Hall-effect sensors were considered insufficient for capturing the low magnitude self-balance currents in this test. An alternative option was to connect a shunt resistor in series with each cell. Measuring the voltage over each resistor, the current circulating in each cell can be computed using Ohm's law. However, connecting the resistors with each cell string changes the total resistance. Hence, the measured current is not exactly the same as the true current that

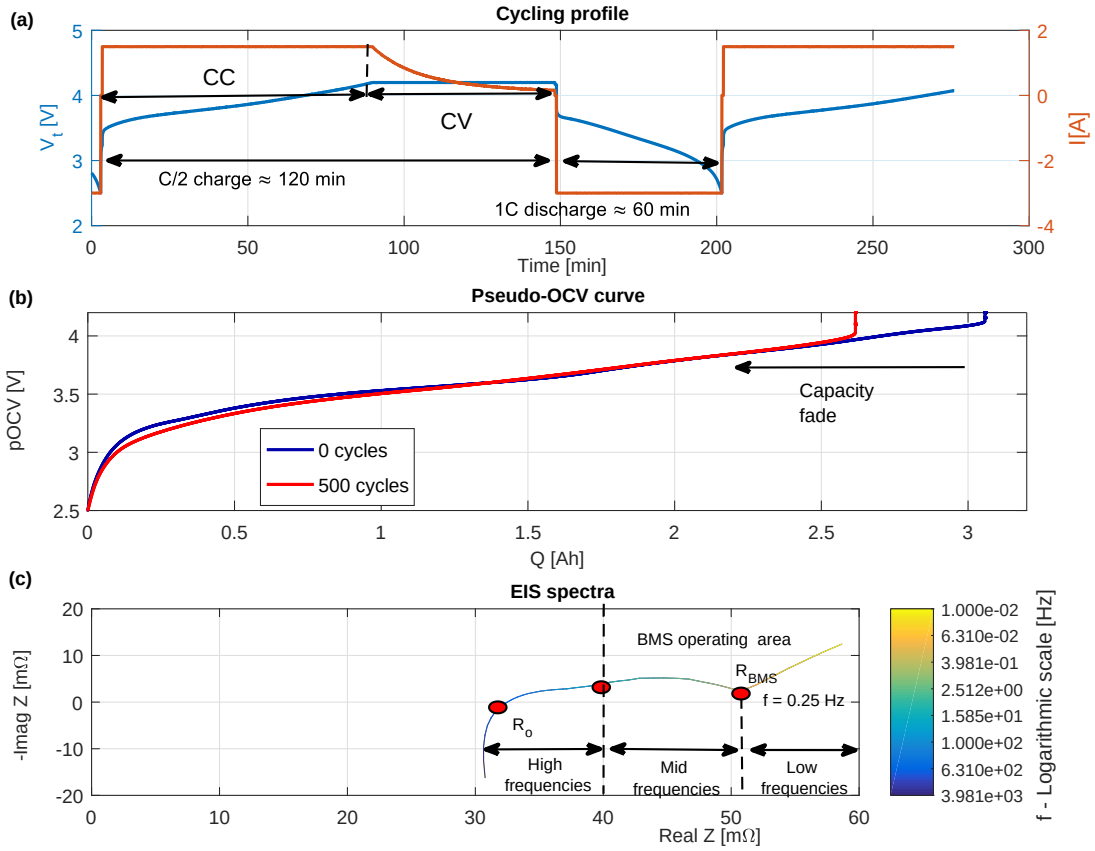

Figure 4.1: (a) Charge-discharge cycling profile employed to age the cells, (b) Pseudo-OCV-SoC curve of cell 1 for 0 and 500 cycles for a discharge event, (c) EIS test with respect to the frequency showing BMS operating area and R_{BMS}.

would circulate without installing the shunt resistors in the circuit. Despite this, Bruen et al. [35] argues that following this procedure the measured current will be proportional to the true current, and therefore, this method was selected. A shunt resistor was connected in series with each cell with a nominal value of 10mΩ with less than 500 ppm K^{-1} thermal sensitivity. Each resistor was calibrated by passing a number of known currents through the resistor and measuring the voltage over the resistor. The current/voltage relationship was obtained through a least squares solution. The results reported in [35] show that the total current estimated from the shunt voltage is less than 0.1% difference to the applied current. In addition to the current, the temperature was also measured during cycling. T type thermocouples were located midway along the length of each cell. Detail specifications of the equipment and the test bench of this experiment can be found

in Appendix A.2.1.

4.3.2 Cell characterisation

Cell characterisation includes three tests: capacity test, pseudo-OCV test, and EIS test. To track the aged state of each cell over time, each of these tests was performed every 50 cycles. In total, each cell was characterised 11 times.

- The capacity test determines the quantity of electric charge that a battery can deliver under specified discharge conditions. Following on from the CC-CV protocol, each cell was charged to the upper voltage limit, 4.2V. Then, each cell was discharged at 1C to the lower voltage limit, 2.5V. The cell's capacity is defined as the charge dissipated over this discharge event.

- The pOCV test comprises measuring the cell terminal voltage using a C-rate of C/10 to emulate equilibrium conditions. The pOCV test was performed by discharging from the cell upper voltage threshold to the cell lower voltage threshold. Figure 4.1 (b) illustrates the measured pOCV against the SoC.

- The EIS test determines the internal cell resistance along a range of frequencies. In comparison to other techniques such as pulse power test, EIS has the advantage of giving a deeper understanding of the cell dynamics [126]. EIS measurement is performed by applying a single frequency voltage or current to the system and measuring the amplitude and phase shift of the resulting current or voltage at that frequency. The mathematical description of the EIS is provided in Appendix A.2.2. The frequency range depends on the range of interest, the limitation of the equipment used and the duration of the test. In order to minimise the effect of battery non-linearities such as large voltage variations under small current amplitudes, a SoC variation lower than 5%, and a current amplitude lower than 250mA are used.

According to [127], these small amplitudes are large enough compared to the measurement noise and so distinguishable from it. The EIS test is performed using the Solartron Modulab system model 2100A in galvanostatic mode, i.e., current is controlled, with a peak current amplitude of 150mA (C/20). The tests were performed between 2mHz and 100kHz at SoC=20%, SoC=50% and SoC=90%. The SoC is adjusted in the automated battery cycle software by setting the appropriated pOCV value obtained from Figure 4.1 (b). The change in pOCV along ageing was not considered, keeping the same pOCV values along the whole experiment. Thus, instead of performing the EIS test at SoC 20%, 50% and 90%; the test was performed between 20% and 30% SoC (low SoC), between 50% and 60% SoC (mid SoC), and between 90% and 100% SoC (high SoC).

Figure 4.1 (c) illustrates the EIS spectra for cell 1 at 0 cycle, covering the frequency range that a BMS typically operates (<100Hz) [35]. According to [112], a relaxation period of 4 hours rest was allowed before performing the EIS test. This rest period avoids changes in the internal impedance after the cells are excited. It is noteworthy the importance of proper connection of the cells to the EIS test system as inaccurate EIS measurements can easily result from poor connections.

EIS results are usually represented by the Nyquist plot as illustrated in Figure 4.1 (c). Figure 4.1 (c) plots the cartesian coordinates of the impedance, imaginary y-axis and real x-axis. Since the main processes in the EIS are capacitive, negative imaginary part, the traditional Nyquist plot is inverted on the y-axis, being the y-axis equal to the negative imaginary part of the impedance. Operation at frequencies larger than 2.5kHz would increase the cost of a BMS hardware substantially because the sampling rate required will be higher [128]. This result explains why a BMS will only operate at mid and low frequencies [128]. As such, the resistance considered for this work is the one that the BMS is capable of measuring. This resistance is here named as a BMS resistance, R_{BMS}, and, it is represented by the mid-frequency

turning point of the EIS plot as illustrated in Figure 4.1 (c). This approach is consistent with other studies reported in the literature [35], [59].

4.4 Results and discussion

4.4.1 Capacity – SoH_E and Resistance – SoH_P

Figure 4.2 (a) and (b) illustrate the degradation of each cell over time based on the measurement of the capacity at 1C and the R_{BMS} at mid SoC.

Figure 4.2 (a) and (b) indicate that R_{BMS} and capacity tends to converge for cells 2, 3 and 4 over cycle number. Since cell 1 represents the least aged cell, cell 1 requires more time to converge to the same level as the rest of the cells. Figure 4.2 (c) and (d) show that the resulting SoH_E and SoH_P trend is similar to the capacity and R_{BMS} trend. It is seen that the SoH_P decreases faster than SoH_E reaching the EoL value between 200 and 350 cycles. This result indicates the lifetime power capability of these cells is shorter than the energy capability. This result is in agreement with the specifications of the cell manufacturer since these cells are designed for high energy applications instead of high power applications [125]. This result also highlights that this cell would not meet the end of the warranty period of 8 years of an automotive OEM in terms of power. This result should not be very critical for an automotive OEM because, according to internal communications with Jaguar Land Rover [20], automotive OEMs do not consider the SoH_P metric when the vehicle is in use. Automotive OEMs only consider the SoH_E in real-world operations to estimate vehicle range and battery lifespan. However, SoH_P needs to be considered in other applications e.g., when batteries are used in second-life applications where the speed of response is more important than the duration of the response [96].

The cell-to-cell maximum difference considered in this study correspond to a difference of capacity and impedance of circa 8% and 30% respectively. Research published highlights

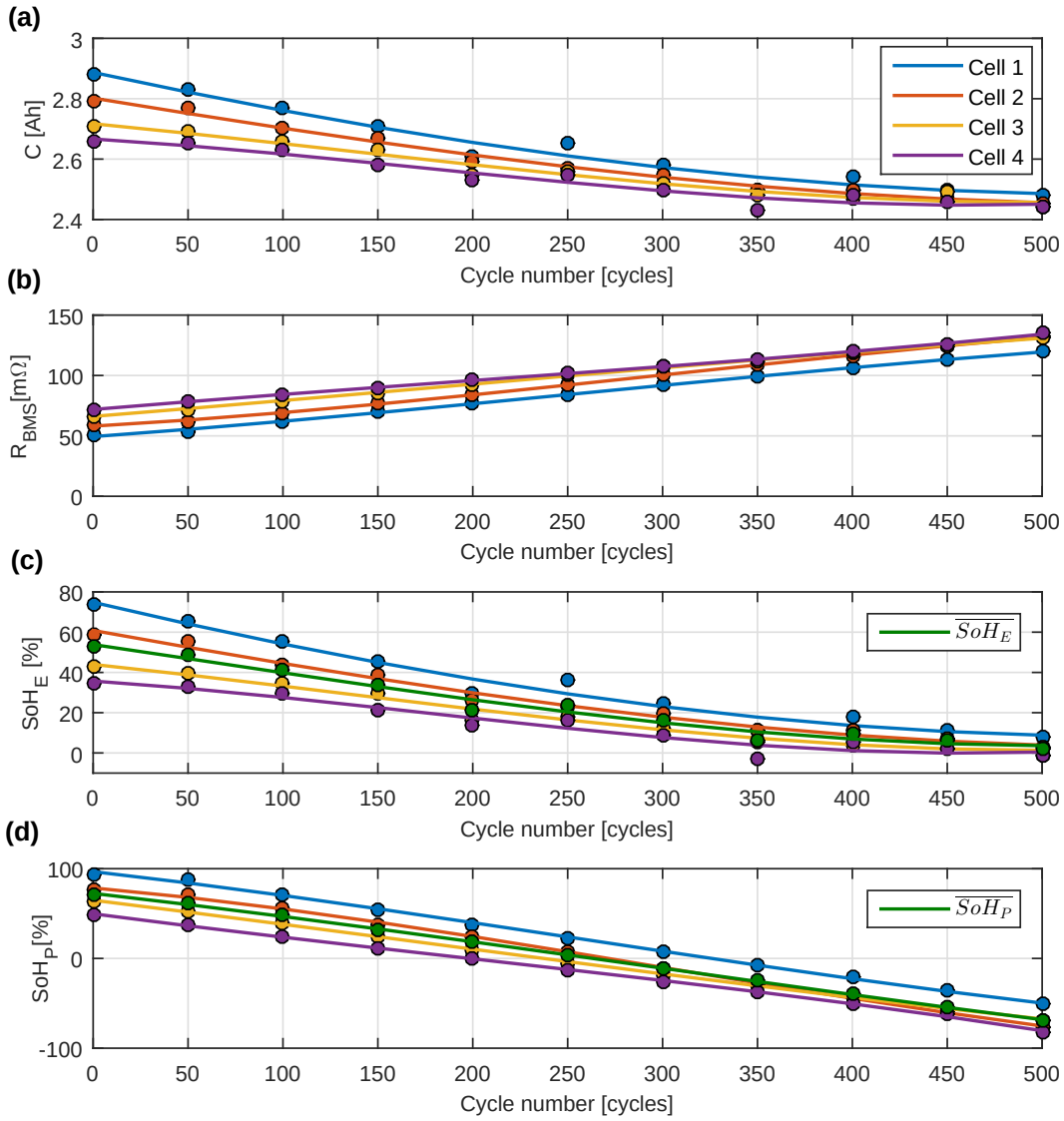

Figure 4.2: (a) Cell capacity over cycle number, (b) Cell R_{BMS} at mid SoC over cycle number, (c) Cell SoH_E and $\overline{SoH_E}$ over cycle number, and (d) Cell SoH_P and $\overline{SoH_P}$ over cycle number.

that differences in cell properties from initial manufacture and integration may be circa 9% for capacity [40] and 25% for impedance [41], which are in agreement with the initial differences considered in this study. However, during vehicle operation, commercial viable BMS used by automotive OEMs keep cells under the same state, avoiding cell-to-cell variations to be larger than 5% [20]. For these scenarios is not only relevant the result that the cell capacity and resistance will converge but also to identify the point when the cells converge so that a balancing strategy can be designed more effectively. Following on

from Section 4.6, such a study is considered as an area of further work.

Represented with $\overline{SoH_E}$ and $\overline{SoH_P}$, Figure 4.2 (c) and (d) also illustrate the SoH value that the BMS would track. This value is representative of the SoH of the four cells connected in parallel. This value is calculated as the mean value of the SoH of the four cells because the capacity and the resistance on the parallelized stack were not measured experimentally. Instead, the cells were individually characterised as explained in Section 4.3. Following on from internal discussions with Jaguar Land Rover [20], using the mean value to quantify the spread of the SoH for this case study is appropriate from a pragmatic viewpoint.

A new metric called State of Imbalance (SoI) is defined to quantify the maximum cell-to-cell SoH difference at each characterisation test k. This metric enables us to analyse the convergence more easily than as shown in Figure 4.2. The SoI is calculated for the case of SoH_E and SoH_P as shown Equation 4.1 and Equation 4.2.

$$SoI_E^k = max(SoH_E^k) - min(SoH_E^k) \tag{4.1}$$

$$k = 1...11$$

$$SoI_P^k = max(SoH_P^k) - min(SoH_P^k) \tag{4.2}$$

$$k = 1...11$$

Figure 4.3 (a) illustrates that for an initial SoI_E of 40%, the SoH_E converges with an SoI_E of 10% at the end of the test. The SoI_P decreases slower than the SoI_E. Numerically, SoI_P is 45% at the beginning of the test and SoI_P is 30% at the end of the test. In order to study which cell contributes more to the convergence, Figure 4.3 (b) and (c) show the difference of each cell SoH_E and SoH_P with respect to the $\overline{SoH_E}$ and $\overline{SoH_P}$

illustrated in Figure 4.2 (c) and (d), respectively. $Cont_E$ and $Cont_P$ of each cell u at each characterisation test k is computed using Equation 4.3 and Equation 4.4.

$$Cont^k_{E\ u} = SoH^k_{E\ u} - \overline{SoH^k_{E\ u}} \tag{4.3}$$

$$Cont^k_{P\ u} = SoH^k_{P\ u} - \overline{SoH^k_{P\ u}} \tag{4.4}$$

$$k = 1...11,\ \ u = 1...4$$

Figure 4.3 (b) and (c) show cell 1, the least aged cell, contributes more to the convergence while cell 4, the most aged cell, contributes the least. The $Cont_E$ and $Cont_P$ decreases with cycle number, outlining the SoH of each cell tends to converge.

4.4.2 Driving factors for SoH convergence

4.4.2.1 Current and charge-throughput distribution

Previous work [35] shows that cells connected in parallel under imbalanced scenarios can undergo significantly different currents, contributing the cells to degrade differently. To understand the variation of the individual cell currents when the cells are connected in parallel, the Randles ECM presented in Figure 3.1 is considered. The RC parallel and R_o is simplified to the cell's internal resistance, R_{int}, to help explain the cell-to-cell SoH variation more easily. Based on this simplified Randles ECM, the individual cell current is derived as in Equation 4.5.

$$V_t = V_{oc} + V_R = V_{oc} + R_{int} \cdot I \rightarrow I = \frac{V_t - V_{oc}}{R_{int}} \tag{4.5}$$

From Equation 4.5 is seen that changes in V_{oc} (capacity) and R_{int} (SoC) will cause variations in cell currents.

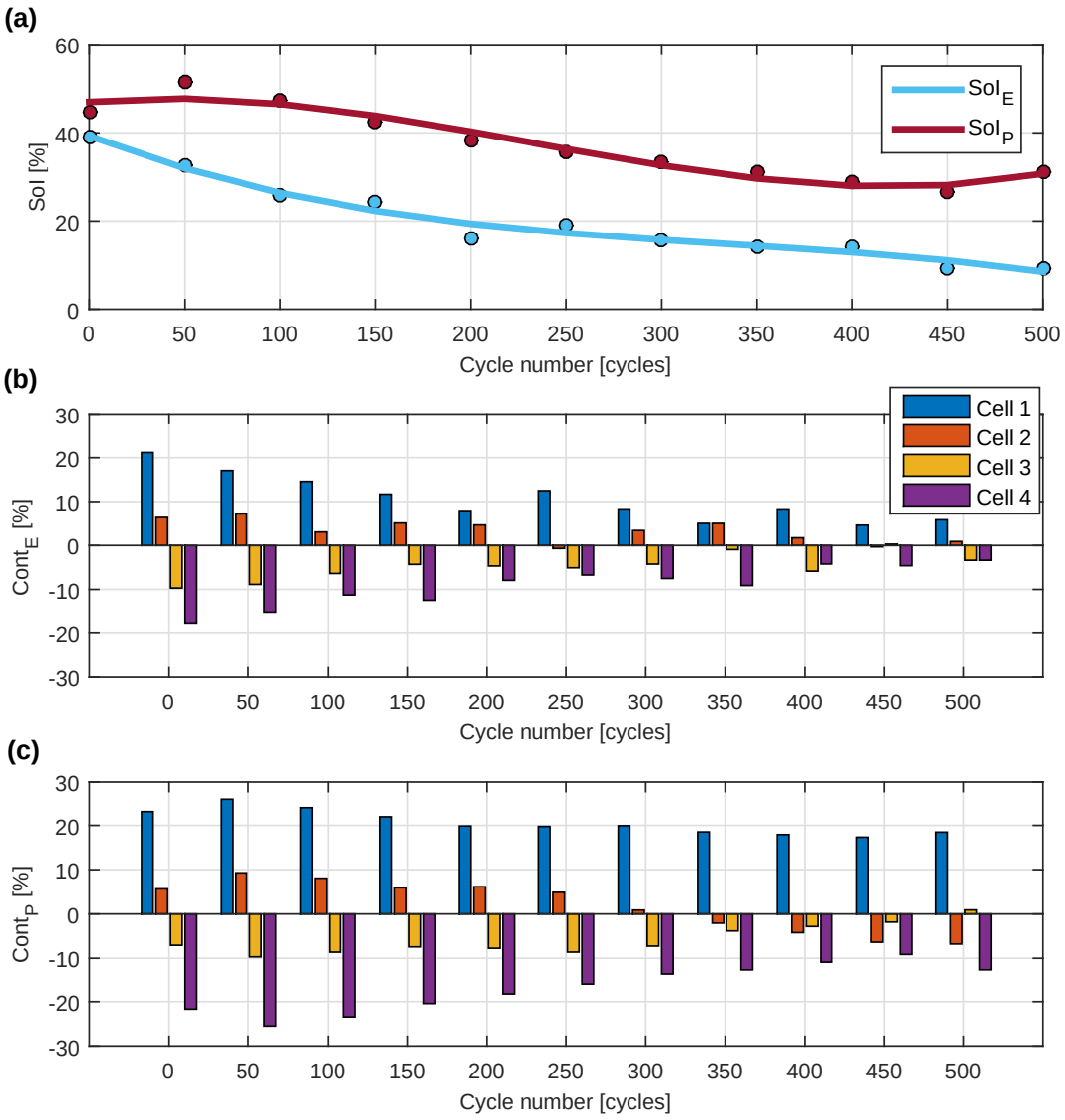

Figure 4.3: (a) SoI_E and SoI_P over cycle number, (b) Cell $Cont_E$ over cycle number and (c) Cell $Cont_P$ over cycle number.

Figure 4.4 (a) and (b), and Figure 4.5 (a) and (b) relate the individual SoC and the individual cell currents of each cell I_1, I_2, I_3 and I_4 for the 35^{th} and the 435^{th} discharge-charge cycle, respectively. These cycles were arbitrarily selected near to the beginning and the end of the test.

The individual current of each cell diverges more for the discharging event than for the charging event because the magnitude of the C-rate is larger for discharging, -1 C, than for charging, +0.5 C. The SoC of the less aged cells decreases during discharging or increases

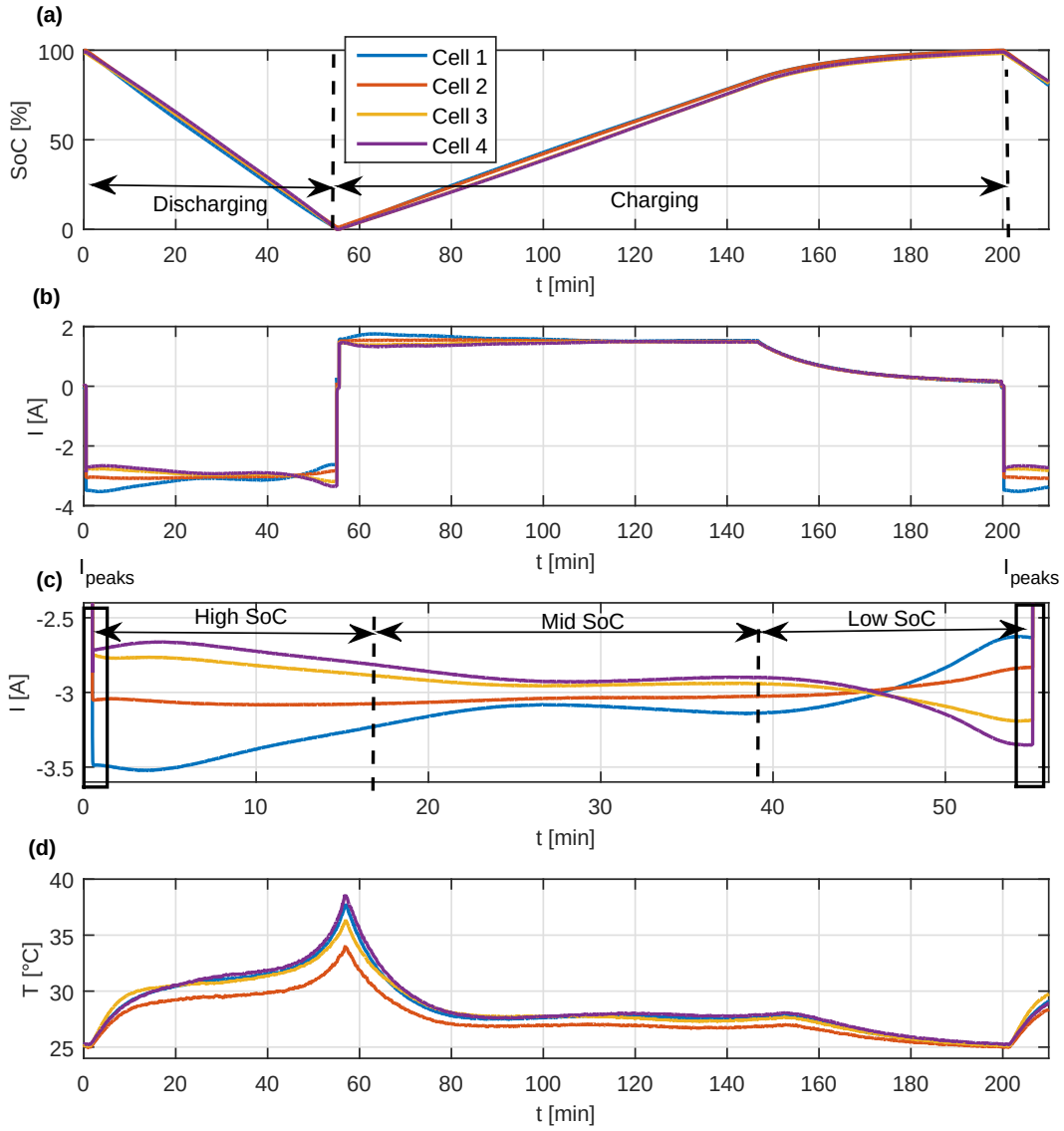

Figure 4.4: (a) Individual SoC of each cell for the 35^{th} cycle, (b) current distribution of each cell for the 35^{th} cycle, (c) detailed view of this current distribution, (d) temperature distribution of each cell for the 35^{th} cycle.

during charging faster than for the more aged cells because the current flow in the less aged cells is higher in magnitude than in the more aged cells. Thus, when the less aged cell has fully discharged or charged, the more aged cells have not discharged or charged entirely yet, which consequently may drive higher currents in these cells.

According to [35], this uneven current distribution during charging and discharging causes peaks in the current which could lead to premature ageing of the cells. Figure 4.4 (c) and Figure 4.5 (c) illustrate the current distribution of each cell during discharge. The

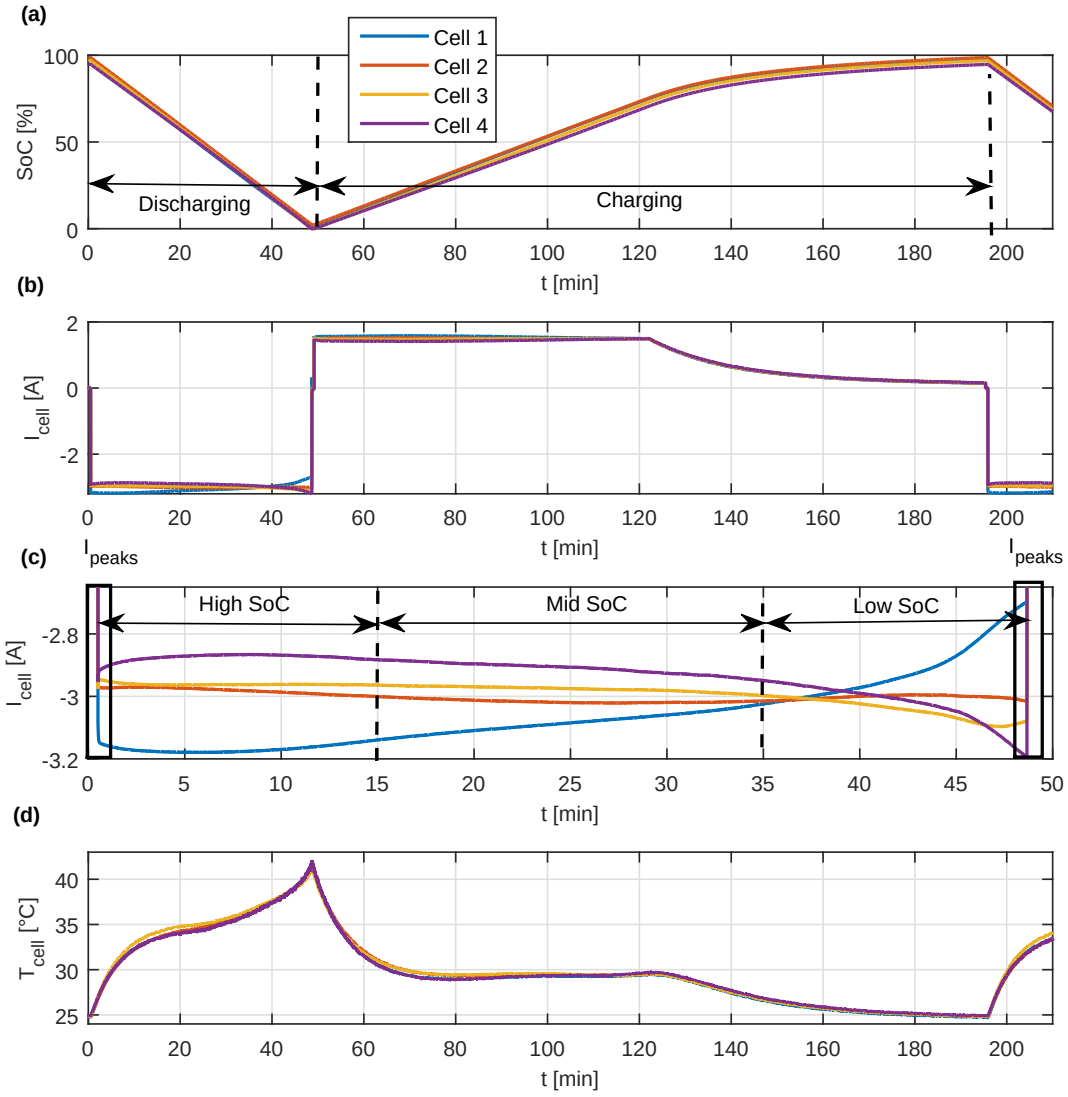

Figure 4.5: (a) Individual SoC of each cell for the 435^{th} cycle, (b) current distribution of each cell for the 435^{th} cycle, (c) detailed view of this current distribution, (d) bulk temperature distribution of each cell for the 435^{th} cycle.

peaks in the current are reached at low and high SoC, as a result of the deepest discharge effects of the pOCV curve as shown in Figure 4.1 (b). The less aged cells release more current at high SoC as their impedance is lower than the impedance of the more aged cells. However, there is a cross-over point at low SoCs where the more aged cells release more current than the less aged cells. This result is counterintuitive since the impedance of the more aged cells is larger than the impedance of the less aged cells. To explain this result is considered the case where two cells are connected in parallel as illustrates

Figure 4.6.

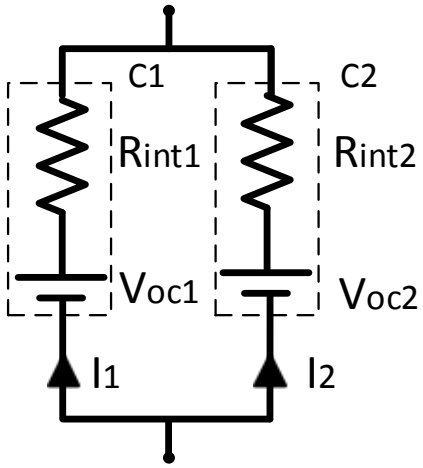

Figure 4.6: Example of two cells connected in parallel.

Cell 1 is new and Cell 2 is old. The voltage V_t over each cell is the same. According to Equation 4.5, Equation 4.6 is written as:

$$V_{oc1} + R_{int1} \cdot I_1 = V_{oc2} + R_{int2} \cdot I_2 \tag{4.6}$$

$R_{int2} > R_{int1}$ and at low SoCs is seen that $I_2 > I_1$. To keep Equation 4.6 balance, $V_{oc1} > V_{oc2}$. This is true at low SoC as shown Figure 4.1 (b). Therefore, the current cross-over is explained due to the change in SoC, impedance and V_{oc}. This result has been previously reported in [35], [41].

Another observation from Figure 4.4 (c) and Figure 4.5 (c) is the peak-to-peak current difference between the 35^{th} and the 435^{th} cycle. The peak-to-peak current difference between the least and the most aged cell is larger at high SoC or low SoC for the 35^{th} cycle (0.75A) than for the 435^{th} cycle (0.5A). This convergence in the peak-to-peak current is explained by the convergence of the individual cell capacity and resistance as illustrated in Figure 4.2 (a) and (b).

The charge-throughput is evaluated to analyse the effect of the current distribution in the longer-term. The charge-throughput is the amount of accumulated current in absolute

value that is stored or released in the battery over time. Using Equation 4.7 the charge-throughput is computed as the integral of the current over the difference between the final, t_f^k, and the initial, t_0^k, time. In this case, as the cycling test is "paused" to characterise the cells, the charge-throughput, AhT, over the test is derived as the monotonic accumulation of the charge-throughput of each characterisation test k and cell u, one after another.

$$AhT_u^k = \sum_{k=1}^{k} \int_{t_0^k}^{t_f^k} \left| I(t)_u^k \right| dt \tag{4.7}$$

$$k = 1...11, \;\; u = 1...4$$

Figure 4.7 (a) illustrates the charge-throughput release over cycle number. Figure 4.7 (a) reveals that the charge-throughput of the less aged cells is larger than for the more aged cells. This result outlines that the current in the less aged cells is in overall larger than in the more aged cells.

To see clearly that the charge-throughput also converges the individual charge-throughput at each characterisation test is computed using Equation 4.8. Equation 4.8 is the same as Equation 4.7 without accumulating the charge-throughput over cycle number.

$$AhT_{u\ ind}^k = \int_{t_0^k}^{t_f^k} \left| I(t)_u^k \right| dt \tag{4.8}$$

$$k = 1...11, \;\; u = 1...4$$

Figure 4.7 (b) illustrates that the individual charge-throughput after each cycling test converges. A cycling test is the number of cycles in between two characterisation tests. The result of Figure 4.7 (b) , in the long-term, together with the convergence of the current, in the short-term, supports the convergence of the SoH_E and SoH_P as depicted in Figure 4.2 (c) and (d).

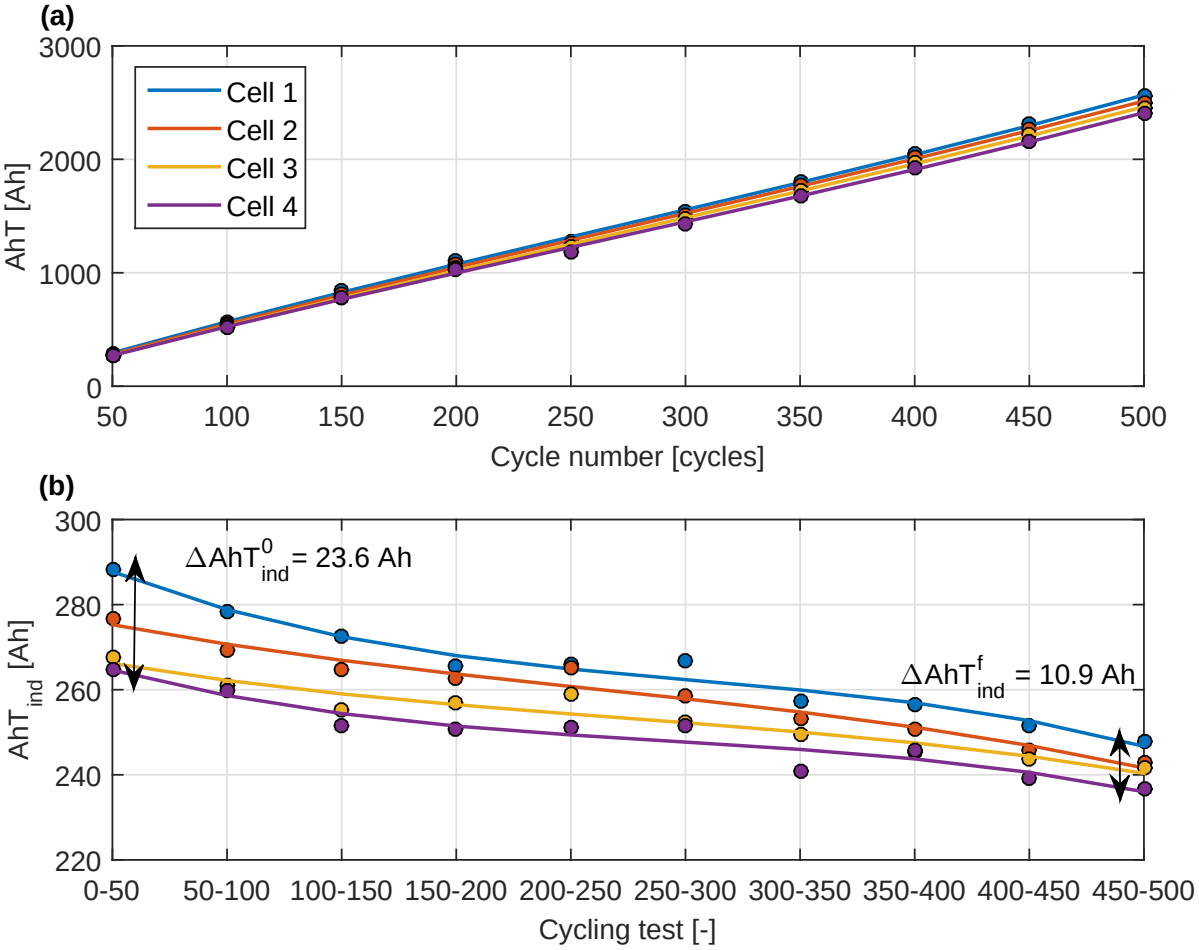

Figure 4.7: (a) Accumulative charge-throughput release by each cell over cycle number, (b) charge-throughput release by each cell over each cycling test.

4.4.2.2 Temperature and thermal-energy distribution

Since cell temperature primarily depends on cell impedance and current, a number of studies correlate these parameters with SoH [35], [52], [53]. Figure 4.4 (d) and Figure 4.5 (d) show the bulk temperature distribution in each cell for the 35^{th} and the 435^{th} charge-discharge cycle, respectively.

Figure 4.4 (d) and Figure 4.5 (d) illustrate that the cell temperature is larger for all the cells at the 435^{th} (43 ℃) than the 35^{th} cycle (38 ℃). The increase in temperature over cycle number is due to the increase of R_{BMS} as depicted in Figure 4.2. This increase of temperature is more significant for low and high SoC with respect to mid SoC due to the divergence of the individual cell currents as shown in Section 4.4.2.1 and larger magnitude

of R_{BMS} [59].

In comparison with the current depicted in Figure 4.4 (d) and Figure 4.5 (d), the variation of the temperature does not follow the initial order of ageing of each cell. Figure 4.4 (d) depicts that the temperature of cell 1, cell 3 and cell 4 is larger than the temperature of cell 2. This result is explained based on the relative values of the impedance of each cell with respect to the current. The difference in current of cell 1, cell 3 and cell 4 (ΔI_1=0.9 A, ΔI_3=0.42 A and ΔI_4=0.65 A) vary significantly from the beginning to the end of the discharge, whereas the difference in current of cell 2 changes less (ΔI_2=0.2 A). In addition, the change of the impedance with respect to the SoC also influences in the variation of cell temperature. For instance, since cell 1 is the least aged cell, cell 1 has the lowest resistance value as illustrated in Figure 4.2 (b). However, the impedance of cell 1 rises at low SoCs due to the significant drop of V_{oc} as shown in Figure 4.1 (b) causing an increase in temperature. The temperature of cell 2 is consistently the lowest temperature because it has a relatively low impedance without undergoing substantial current differences. This result is supported in [35] where cell temperature did not vary concerning the order of ageing.

For the case of the 435^{th} cycle, the temperature is approximately the same for all the cells since the current from the beginning to the end of the discharge changes very little (ΔI_1=0.4 A, ΔI_2=0.04 A, ΔI_3=0.15 A and ΔI_4=0.3 A) and the resistance of each cell tend to converge as illustrated in Figure 4.2 (b). Comparing both Figure 4.4 (d) and Figure 4.5 (d) it is possible to conclude that temperature tend to converge over time.

It can also be seen that the average peak temperature at 435^{th} cycle, 41.5 ℃, is larger than the average peak temperature at 35^{th} cycle, 36 ℃, due to the increase of R_{BMS} with cycle number as shown in Figure 4.2 (b). To evaluate the temperature convergence in the long-term, Equation 4.9 approximates the total thermal energy released in each cell u before each characteristation test, k, as:

$$E^k_{th\ u} = \sum_{k=1}^{k} \int_{t_0^k}^{t_f^k} (I(t)^k_u)^2 \cdot \overline{R^k_{BMS\ i}} dt \tag{4.9}$$

$$k = 1...11,\ \ u = 1...4$$

Where $I(t)_u$ denotes the current flow, and t_0^k and t_f^k the initial and the final time. Equation 4.10 gives $\overline{R_{BMS}}$ as the mean value of the instantaneous R_{BMS} for each characterisation test k and cell u considering the R_{BMS} at each measured SoC.

$$\overline{R^k_{BMS\ u}} = \frac{R^k_{BMS\ u\ \text{Low SoC}} + R^k_{BMS\ u\ \text{Mid SoC}} + R^k_{BMS\ u\ \text{High SoC}}}{3} \tag{4.10}$$

$$k = 1...11,\ u = 1...4$$

The root mean square (RMS) value of the current is employed to simplify Equation 4.9. This was calculated using Equation 4.11 over the charge-discharge cycle period, T_e.

$$I^k_{RMS\ u} = \sqrt{\frac{1}{T^k_e} \int_{t_f^k - Te^k}^{t_f^k} (I(t)^k_u)^2 dt} \tag{4.11}$$

$$k = 1...11,\ \ u = 1...4$$

The thermal energy based on the RMS value of the current is computed using Equation 4.12.

$$E^k_{th\ u} = \sum_{k=1}^{k} (I^k_{RMS\ u})^2 \cdot \overline{R^k_{BMS\ u}} \cdot \left(t^k_f - t^k_0\right) \tag{4.12}$$

$$k = 1...11,\ \ u = 1...4$$

Similarly as with the charge-throughput, the thermal energy was computed as the monotonic accumulation of the thermal energy before each characterisation test, k.
Figure 4.8 (a) demonstrates the thermal energy released by the more aged cells is larger

than the thermal energy released by the less aged cells. The least aged cell typically undergoes the highest current, having the lowest impedance. Likewise, the most aged cell typically undergoes the lowest current, having the highest impedance. Thus, this result indicates the R_{BMS} contributes more to the thermal energy than the I^2_{RMS}. To compare the contribution between R_{BMS} and I^2_{RMS}, the ratio between the R_{BMS} for cell 4 and cell 1, and the ratio between the I^2_{RMS} for cell 1 and cell 4 are derived using Equation 4.13 and Equation 4.14.

$$R^k_{rt\ BMS} = \frac{R^k_{BMS\ u=4}}{R^k_{BMS\ u=1}} \tag{4.13}$$

$$I^k_{rt\ RMS} = \frac{(I^k_{RMS\ u=1})^2}{(I^k_{RMS\ u=4})^2} \tag{4.14}$$

$$k = 1...11$$

Figure 4.8 (b) illustrates $R^k_{rt\ BMS}$ is for the majority of the test larger than $I^k_{rt\ RMS}$ suggesting that thermal energy is more sensitivity to R_{BMS} than to I^2_{RMS}.

To see clearly that the thermal energy also converges over time, the individual thermal energy released after each cycling test is computed using Equation 4.15. Equation 4.15 is the same as Equation 4.12 without accumulating the thermal energy over cycle number.

$$E^k_{th\ ind\ u} = (I^k_{RMS\ u})^2 \cdot \overline{R^k_{BMS\ u}} \cdot \left(t^k_f - t^k_0\right) \tag{4.15}$$

$$k = 1...11,\ \ u = 1...4$$

Figure 4.8 (c) depicts the thermal energy released by each cell over each cycling test converges. Hence, the convergence of temperature in the short-term, together with the convergence of the thermal energy in the long-term, support the convergence of SoH_E and SoH_P illustrated in Figure 4.2 (c) and (d). As an overview, Table 4.2 gives a summary of

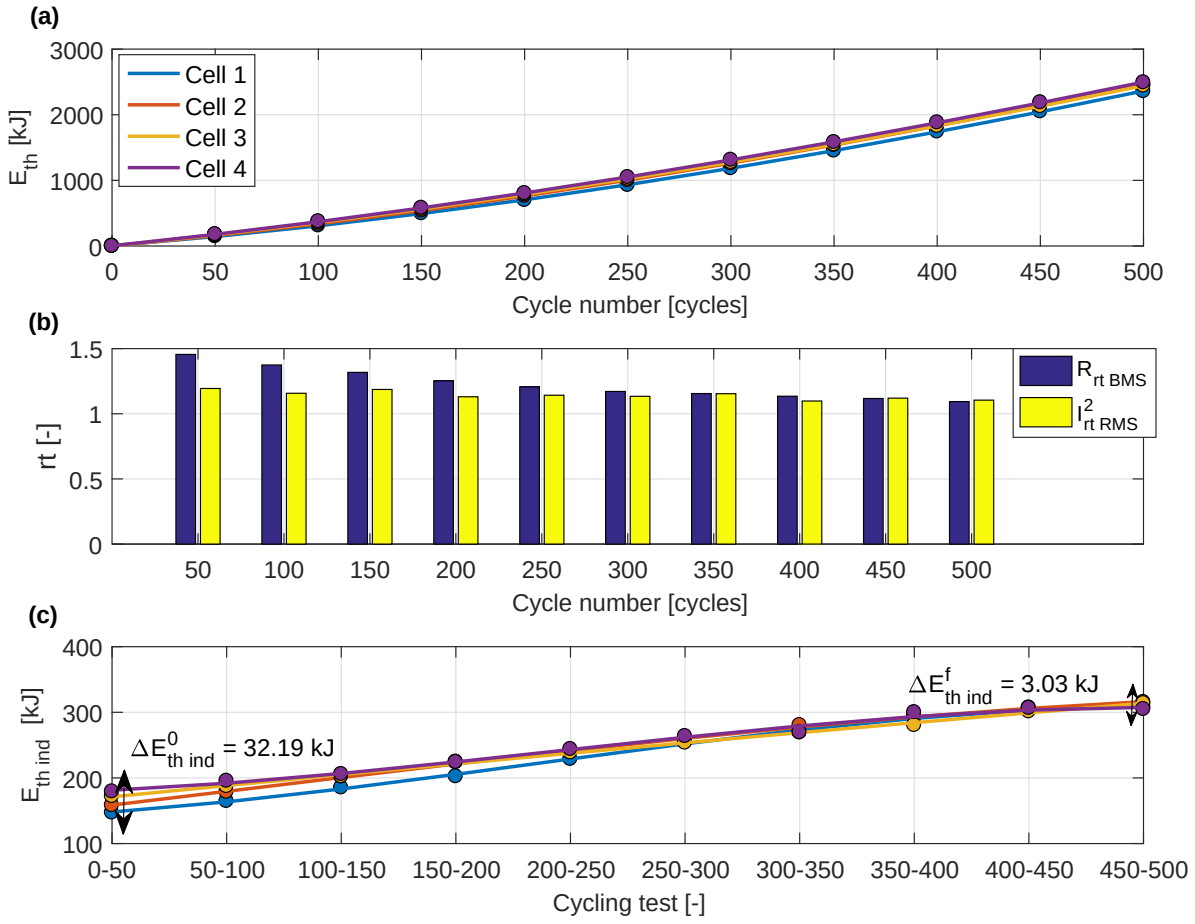

Figure 4.8: (a) Total thermal energy released by each cell over cycle number, (b) comparison between $R^k_{rt\ BMS}$ and $I^k_{rt\ RMS}$ over cycle number, (c) total thermal energy released by each cell over each cycling test.

the results evaluated in this section, highlighting the values at the beginning and the end of the experiment. It is observed that the capacity and R_{BMS} of the cells before being connected in parallel differ with respect to the values reported in [35]. Since the cells were stored over half a year between the previous and this study, this difference is attributed to calendar ageing effects.

[1] Based on 1 C capacity test.

[2] R_{BMS} measured at mid SoC.

Table 4.2: Test results for the cells before and after being connected in parallel.

	Test start						Test finish					
Cell	C^1 [Ah]	R^2_{BMS} [mΩ]	AhT [kAh]	E_{th} [kJ]	SoH_E [%]	SoH_P [%]	C^1 [Ah]	R^2_{BMS} [mΩ]	AhT [kAh]	E_{th} [kJ]	SoH_E [%]	SoH_P [%]
1	2.88	50.72	0.00	0.00	73.68	96.54	2.54	120.00	2.55	2357.80	7.89	-50.87
2	2.79	59.04	0.00	0.00	58.88	86.58	2.50	132.04	2.50	2454.30	2.96	-76.13
3	2.71	66.66	0.00	0.00	42.81	79.30	2.47	131.37	2.45	2443.30	-1.30	-68.44
4	2.66	72.15	0.00	0.00	34.64	70.94	2.48	134.85	2.40	2493.00	-1.30	-81.94

4.5 Simplified approach for SoH diagnosis and prognosis for cells connected in parallel at different ageing states

Figure 4.9 shows a correlation between capacity and ohmic resistance R_o (a)-(d); and between capacity and R_{BMS} (e)-(h) for this test scenario. In both cases, this correlation can be approximated by a first-order polynomial fit and therefore, this correlation follows an approximately linear trend. This approximation is evaluated based on the goodness of fit and the Pearson correlation coefficient.

The goodness of fit measures the discrepancy between the observed original and the fitted values [129]. This discrepancy is measured using the R-square value. The R-square can vary between 0 and 1, where 0% indicates that the model describes none of the variability of the response data with respect to its mean, and 100% indicates that the model relates all the variability of the response data concerning its mean [58]. The minimum adjusted R-square value for the C vs. R_o case is 0.6943 and 0.8831 for the C vs. R_{BMS} case. This result implies the data of C vs. R_o is less correlated than the data of C vs. R_{BMS}. Calculating the difference between the estimated and the true value in percentage, the maximum curve fit error is 5.55% for C, 5.40% for R_o and 11.1% for R_{BMS}. Apart from the fitting error, this approach needs to consider the experimental error in the measurement of C, Ro and R_{BMS}. Following on from the analysis conducted in Section 3.2.4 of Submission 1 [31], the experimental error was 3.5% for capacity and 2.5% for

R_o and R_{BMS}. As the experimental errors lie within the fitting errors, the experimental error is not significant with respect to the fitting error. However, according to internal communications with Jaguar Land Rover [20], the author states that the obtained fitting errors are not admissible for automotive applications because they fall beyond the limits to meet the requirements defined in automotive OEMs. Inaccurate estimation of the SoH would have negative implications for the vehicle, the driver and the OEM. An example of possible consequences are listed below:

- Vehicle: the BMS can trigger inappropriate control actions due to the inaccuracy of the SoH estimation. An example of an inappropriate control action would be an incorrect control of the current for particular driving conditions.
- Driver: the driver could receive an incorrect estimation of the range, leading him to drive for longer than the vehicle is capable of. The range is calculated based on the remaining capacity at a particular point of the life of the battery.
- Automotive OEM: the mentioned problems for the vehicle and the customer might lead to an increase in the warranty recalls.

Following on from internal conversations with Jaguar Land Rover [20], the maximum admissible fitting error for this approach would be 2.5%. Therefore, the fitting error needs to be reduced in further work so that this approach can be used in the real-world automotive context.

The Pearson correlation coefficient quantifies the grade of correlation between two variables which are related, e.g., through a fitting process. In this case the Pearson correlation coefficient is calculated for the correlation between C and R_o, and between C and R_{BMS} [58]. The Pearson correlation coefficient is chosen because it is commonly used in descriptive statistics to illustrate the correlation of variables of a two-dimensional data set [58]. In addition, Schuster et al. [58] employed the Pearson correlation coefficient to quantify the correlation of C and R_o, and between C and R_{BMS} as explained in Section 2.2.2. Therefore, choosing the Pearson correlation coefficient enables to compare the

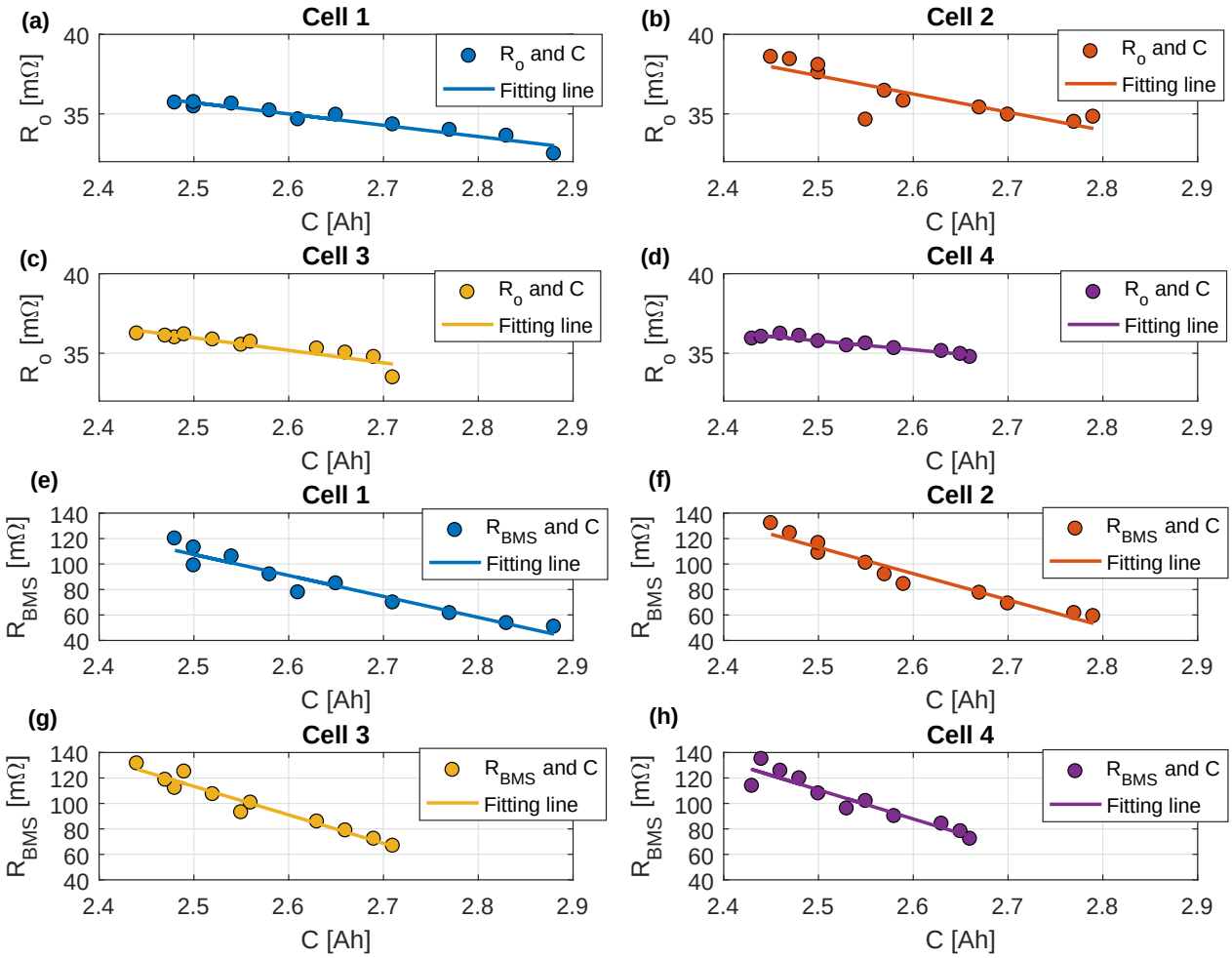

Figure 4.9: Linear correlation between capacity and R_o at mid SoC for (a) cell 1, (b) cell 2, (c) cell 3 and (d) cell 4. Linear correlation between capacity and R_{BMS} at mid SoC for (e) cell 1, (f) cell 2, (g) cell 3 and (h) cell 4.

results directly with the ones published by Schuster et al. [58]. The Pearson correlation coefficients, r, are computed as the covariance, cov, divided by the standard deviations, σ of each parameter using Equation 6.5 and Equation 4.17.

$$r_{R_o,C} = \frac{cov_{R_o,C}}{\sigma_{R_o} \cdot \sigma_C} \tag{4.16}$$

$$r_{R_{BMS},C} = \frac{cov_{R_{BMS},C}}{\sigma_{R_{BMS}} \cdot \sigma_C} \tag{4.17}$$

The Pearson correlation coefficient varies between -1 and +1, depending if the correlation is weak or strong. Employing the command *corrcoef* in MATLAB [108], the minimum PPMC value for the C vs R_o case is 0.8514 and 0.9459 for the C vs R_{BMS} case.

It is concluded that this linear correlation provides further justification for calculating capacity or resistance based on the knowledge of the other. Secondly, this linear correlation allows the BMS to estimate in the short-term, diagnosis, and in the long-term, prognosis, the capacity based on the resistance in a simple way for the case of cells with different ageing level.

4.6 Limitations and further work

The experimental investigation conducted for Study 2 comprised of a single capacity and resistance measurement for each cell and ageing state. According to the theory of Design of Experiments [129], it is recommended to measure more than one sample to ensure the measurements are representative. Thus, measuring a greater sample size is necessary to increase confidence in the findings of this study.

The results of this study are only valid for the described experimental conditions. In cases where the testing conditions change, e.g., ambient temperature or C-rate; or, the number of cells connected in parallel is different than four; or, the conditions at which the cells were initially aged are different; then, the convergence may not be reached or may be reached earlier. For instance, if the C-rate is higher than 1.5C, then the least aged cell could release or receive more current than the maximum current specified by the cell's manufacturer. Therefore, the same study at different experimental conditions needs to be investigated in the future.

Similarly, the correlation between the capacity and resistance could also be non-linear for other test conditions, for instance, when cycling and storage conditions are combined.

Hence, the applicability of this correlation should be tested against other testing conditions, cell chemistries and modules/pack topologies. From an application perspective, the accuracy of this estimation should be improved to OEM automotive standards and compared with the accuracy provided of other methods such as Coulomb-counting [6].

4.7 Conclusions

To address the research objective number 1 defined in Section 4.2, this work analysed the cell-to-cell SoH variation of four commercial 3 Ah 18650 Li-ion cells connected in parallel. The cells were charged and discharged until their EoL value, which corresponds to 500 cycles. In reality, this test is representative of 100,000 miles / 10 years BEV service. For an initial SoH_E difference of 40% at the beginning of the test, the cells SoH_E converge to 10% at the end of the test. For the case of the SoH_P, for an initial difference of 45% the cells converge to within 30% at the end of the test. These results revealed that the BMS would track an incorrect value of the SoH until the SoH of each cell converges.

To understand the reasons behind the SoH convergence, the distribution of the SoC, current, temperature, charge-throughput and thermal energy were studied. The distribution of the cell currents does not entirely depend on the initial ageing state of each cell as it is commonly assumed. The variation depends on the OCV-SoC relationship and the change of cell impedance with respect to SoC. This non-linearity in the variation of the current may cause uneven heat generation within a pack, which may require a higher specification thermal management system [35].

In comparison with the current distribution, the variation of the SoC and the temperature is less dynamic. Although these parameters change differently, all of them tend to converge over time, driving the convergence of SoH. The charge-throughput and the thermal energy of each cell over 500 cycles were also studied to analyse the variation of the current and the temperature in the long-term. Similarly as for the current and the

temperature, the charge-throughput and the thermal energy tend to converge over time.

To meet the second research objective, this work suggests a simple approach for SoH diagnosis and prognosis within the BMS. This approach, previously introduced in [58,61,62], suggests calculating the capacity based on the ohmic or polarisation resistance through a linear correlation. This correlation was proved in this study for the case when cells forming a module have different ageing states. This result is relevant for two main reasons. Firstly, it is only necessary to measure the ohmic or BMS resistance to calculate the capacity. This approach is advantageous because measuring the ohmic or BMS resistance is quicker than measuring the capacity. Secondly, this correlation could be further used to estimate the EoL of the battery.

5. Study 3 - Critical review of non-invasive diagnosis techniques for quantification of degradation modes (DMs)

5.1 Introduction

Understanding the root causes of Lithium-ion battery degradation is a challenging task due to the complexity of the different mechanisms involved [38]. To simplify this, previous studies [64, 66–68] suggest categorising the different ageing mechanisms into three DMs called CL, LLI, and LAM. As discussed in Chapter 4, the BMS quantifies SoH based on the decrease in capacity and increase in resistance. This definition of SoH does not provide a measurement of the ageing mechanisms causing the degradation. In Section 2.3.1 it is argued that understanding the reasons for battery ageing under real-world operating conditions is critical to improve lifetime control strategies within the BMS and to develop the design of new batteries and manufacturing processes. Section 2.3.1 also outlines that pOCV, IC-DV, EIS, DTV and a combination of pOCV and EIS are the most common non-invasive diagnostic techniques suitable to quantify DMs. According to Section 2.2.2, the pulse-power test is quite advantageous to measure the resistance in real-world scenarios due to their low hardware requirements and its short duration, i.e., in the order of seconds without considering a prior relaxation period. This method is not considered in this review because, in comparison to the other methods, it cannot infer the full set

of DMs. In particular, the pulse power method is applied at high and mid frequencies and so, degradation processes characteristic of low frequencies such as LAM cannot be deciphered. Before selecting a particular technique, a comparison among them highlighting their relative strengths and drawbacks in a real application context is needed. To the best of our knowledge, none of the reviews available in the literature focuses on evaluating non-invasive diagnostic techniques to quantify DMs. To fill this gap in knowledge, this Chapter reviews the non-invasive diagnostic methods employed to quantify DMs. This review is conducted based on the requirements that these techniques need to fulfill to be applied in real-world scenarios.

The structure of this work is divided as follows: Section 5.2 describes the main objective of this study. Section 5.3 summarises the most common ageing mechanisms in LIBs. Ageing mechanisms are grouped into DMs, and their occurrence is further related to the upper and lower levels of factors that can be monitored by a BMS, e.g., temperature, C-rate, SoC, ΔDoD and cycle number. The principle of each diagnostic technique is subsequently introduced in Section 5.4. These techniques are reviewed in Section 5.6 according to the criteria defined in Section 5.5. The limitations of this study and further work are stated in Section 5.7. Finally, Section 5.8 presents the main conclusions of this study.

5.2 Objective of this study

According to Table 2.1, the main objective of Study 3 is to review the most recent literature regarding non-invasive diagnostic techniques to quantify DMs in real-world applications.

5.3 Degradation mechanisms in Lithium-ion batteries

Figure 5.1 provides a graphical illustration of the DMs and ageing mechanisms in LIBs. Each DM can lead to an increase in resistance, a reduction in current density, capacity or/and power in a partly reversible, e.g., lithium plating, or irreversible manner, e.g., SEI formation [65]. Uddin et al. [65] suggested a general relationship between battery ageing extrinsic factors and the affected component with the corresponding ageing mechanism and potential effects for LIBs. Table 5.1 extends the relationship derived by Uddin et al. [65] adding the most pertinent DM, mechanism type and observed effects. Mechanism type is defined as gradual or overstress. Gradual stands for progressive degradation whereas overstress for abrupt degradation. The observed effects are defined as capacity fade (CF) and power fade (PF). Previous studies that have examined the ageing mechanisms within LIBs [38, 130] were also considered.

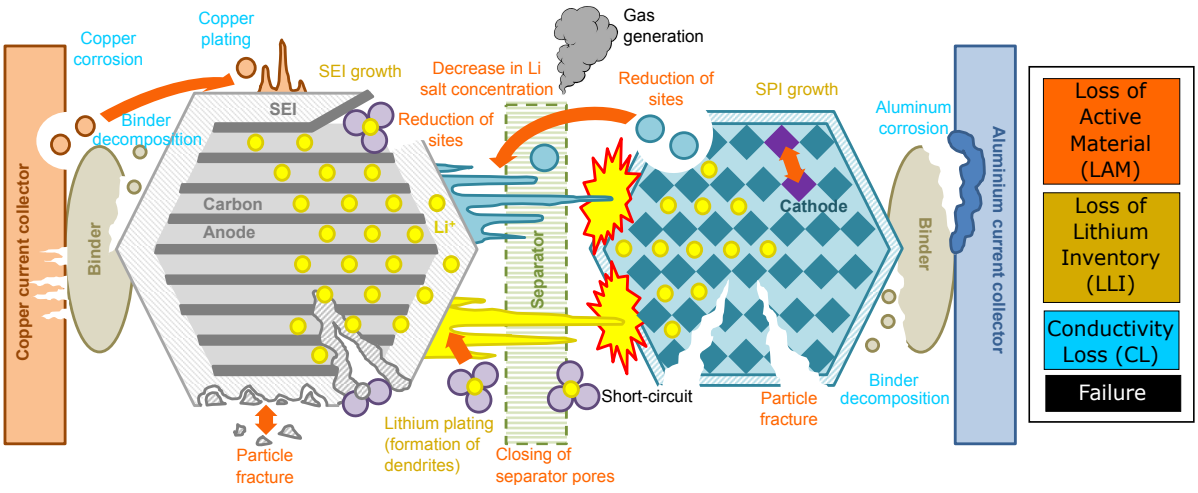

Figure 5.1: Graphical illustration of the DMs and ageing mechanisms in LIBs, adapted from [64, 65, 131].

It is noteworthy that some ageing mechanisms are driven when two or more extrinsic factors co-occur. For instance, according to Vetter et al. [38], lithium plating is pertinent when the battery is cycled with high C-rates at low temperatures. As explained in Section 1.4 it is beyond the scope of this thesis to understand and explain these ageing mechanisms at material and chemical level. Further explanation regarding these degra-

dation mechanisms can be found in a number of research articles such as [38, 132, 133] and a basic introduction to them is given in Submission 3 [33]. The general ageing mechanisms presented in Table 5.1 hold true for most LIBs [64]. Nonetheless, there might be pronounced differences for each particular LIB when taking into account the effect of having different cathode electrode materials or form factors such as cylindrical, pouch or prismatic. The reader is referred to previous publications [132, 134] where the degradation mechanisms are explained more in detail according to the type of cathode material and form factor.

Table 5.1: Relationship of the battery ageing extrinsic factors with the affected component, ageing mechanism, potential ageing effects, most pertinent DM, mechanism type and most pertinent observed effects [38, 65].

Extrinsic factor	Level	Affected component	Ageing mechanism	Most pertinent DM	Mechanism type	Most pertinent observed effects
T	High (>35 °C)	NE - Anode (Active material).	SEI growth.	LLI	Gradual.	CF&PF
			Particle fracture (with cycling).	LAM	Overstress.	CF&PF
		PE - Cathode (Active Material).	SPI growth.	LLI	Gradual.	CF&PF
			Gas generation.	LAM	Overstress.	CF
			Particle fracture with cycling).	LAM	Overstress.	CF&PF
		Current collectors.	Binder decomposition.	CL	Gradual.	PF
		Separator.	Closing of separator pores.	LAM	Overstress.	CF&PF
		Electrolyte (salts).	Decrease in lithium salt concentration.	LAM	Gradual.	PF
		Electrolyte (organic solvents).	Gas generation.	LAM	Overstress.	PF
T	Low (<5 °C)	NE - Anode (Active Material).	Lithium plating and dendrite growth on anode surface.	LLI	Gradual.	CF&PF
C-rate	High (>2C)	NE - Anode (Active Material).	Lithium plating and dendrite growth on anode surface.	LLI	Gradual.	CF&PF
			Particle fracture (with cycling).	LAM	Overstress.	CF&PF
			SEI growth.	LLI	Gradual.	CF&PF
		PE - Cathode (Active Material).	Particle fracture (with cycling).	LAM	Overstress.	CF&PF
SoC	High (>95%)	NE - Anode (Active material).	SEI growth.	LLI	Gradual.	CF&PF
			Particle fracture (with cycling).	LAM	Overstress.	CF&PF
		PE - Cathode (Active Material).	Gas generation.	LAM	Overstress.	CF.
		Current collector (PE-Cathode).	Pitting corrosion of aluminum.	CL	Gradual.	PF
		Current collectors.	Binder decomposition.	CL	Gradual.	PF
		Electrolyte (organic solvents).	Gas generation.	LAM	Overstress.	PF
SoC	Low (<5%)	PE - Cathode (Active Material), mostly in LCO and LMO.	Reduction of sites.	LAM	Gradual.	CF&PF
		Current collector (NE-Anode).	Free copper particles of copper plating.	CL	Gradual.	CF&PF
ΔDoD	Large (>80%)	NE - Anode and PE - Cathode (both active material).	Particle fracture.	LAM	Overstress.	CF&PF
			Reduction of sites.	LAM	Gradual.	CF&PF
Cycle number	Continuous	NE - Anode and PE - Cathode (both active material).	Particle fracture.	LAM	Overstress.	CF&PF
			Reduction of sites.	LAM	Gradual.	CF&PF

5.4 Description of diagnostic models to identify and quantify DMs

Figure 5.2 illustrates the relationships between the required measurements for each of the diagnostic methods reviewed in this study. Next subsections describe the working principle of each of these methods briefly. Additional explanations are beyond of the scope of this thesis because they can be found in the corresponding citations or Submission 3 [33].

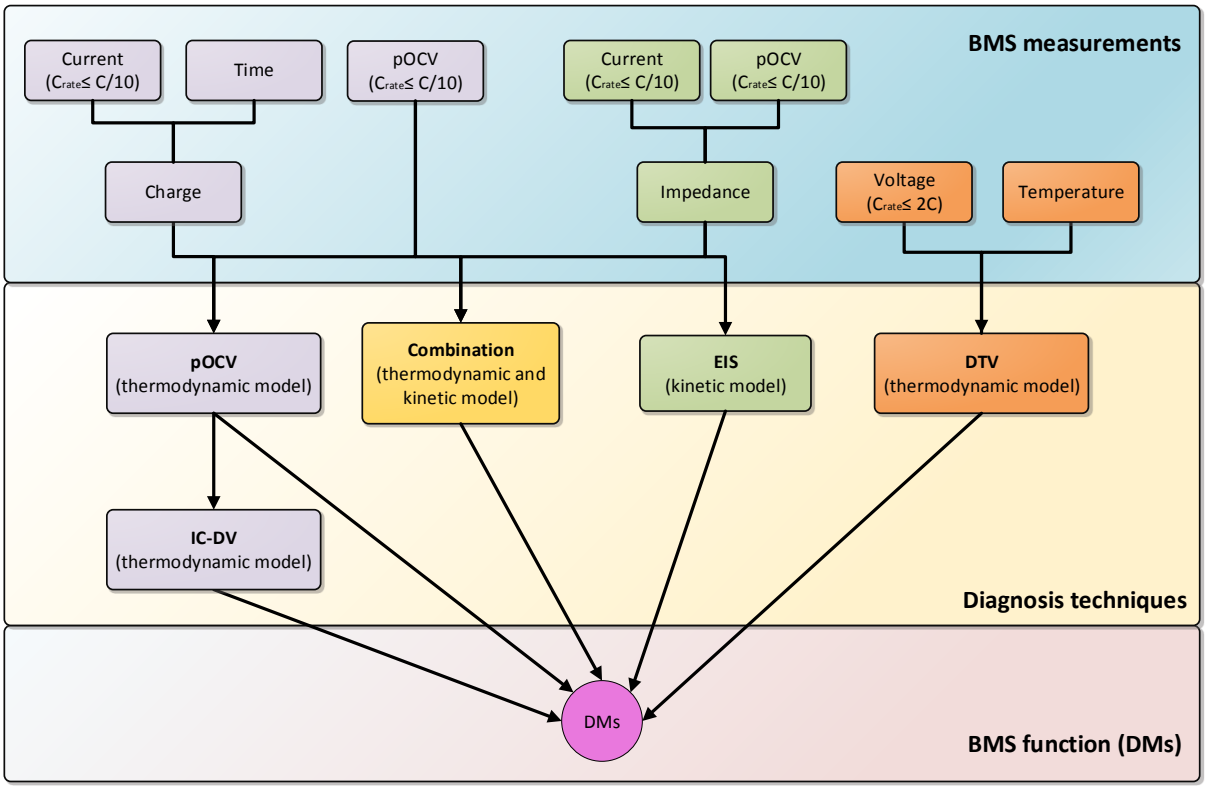

Figure 5.2: Relationship between BMS measurements and DMs diagnostic techniques reviewed in this study.

5.4.1 Pseudo-OCV

The pOCV based methods identify and quantify DMs based on the changes of pristine half-cell pOCV curves. These half-cell pOCV measurements need to be performed only once at laboratory conditions for a particular cell, and then the method can be applied repeatedly [64,68]. This feature makes possible to consider this method as non-invasive. As

explained in Section 3.4.4, pOCV measurements emulate equilibrium conditions so that two or more phases with different lithium concentrations at the same chemical potential coexist.

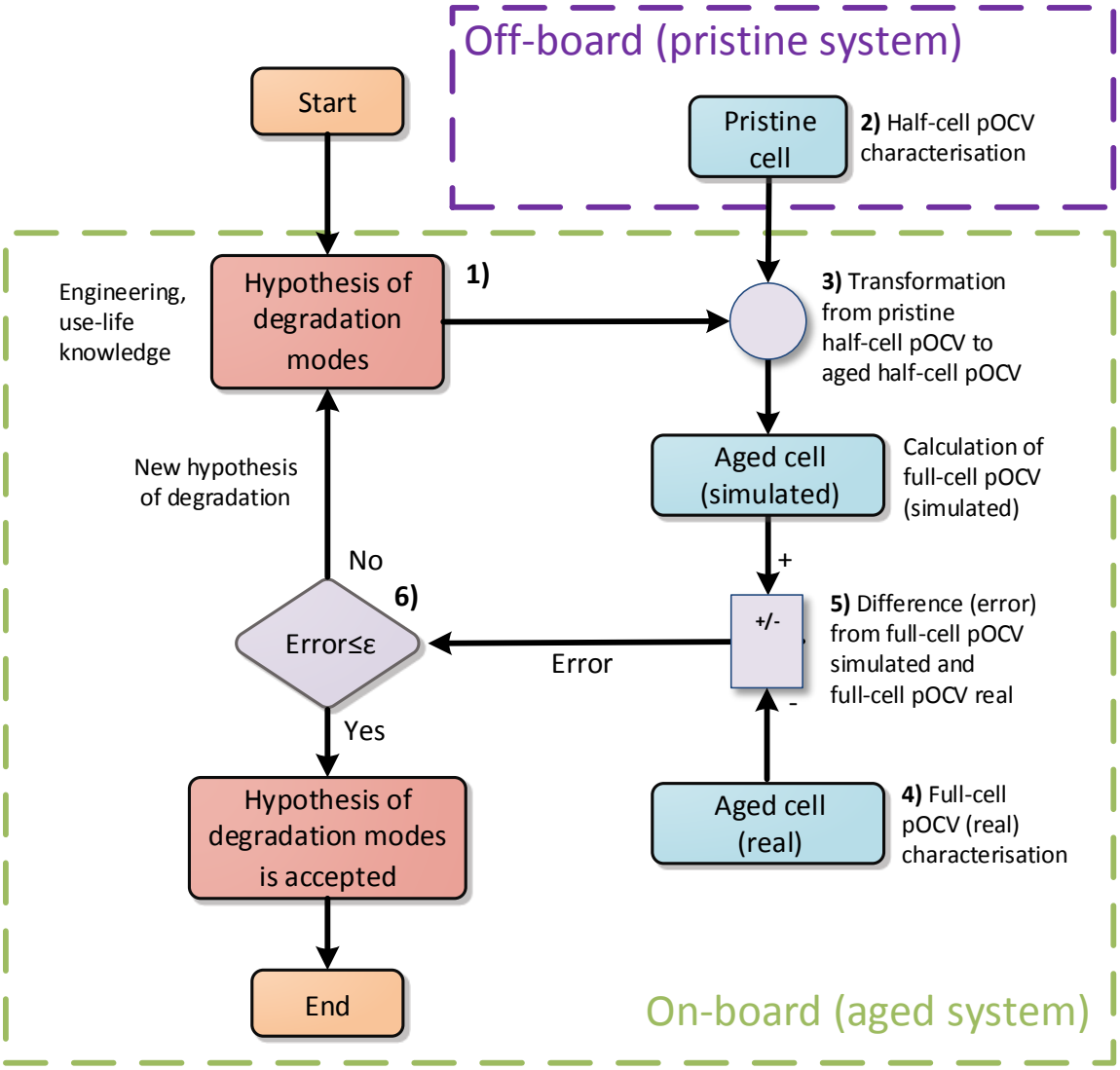

Figure 5.3: Generic framework of pOCV based methods.

The pOCV method operates on a backward basis, i.e., firstly the degradation is hypothesized and once this is proved, the hypothetical degradation is accepted as the true degradation. This process is divided into the following steps:

- **Step 1:** the expected DMs are hypothesized based on engineering rules as shown in Table 5.1 or use-life knowledge. The LAM can take place in the delithiated,

LAM_{de}, or lithiated phase, LAM_{li}, if the electrode is empty or full of lithium ions, respectively.

- **Step 2:** half-cell pOCV measurements are performed when the cell is new.
- **Step 3:** pristine half-cell pOCV measurements are transformed into aged half-cell pOCV measurements through simulation by using the hypothesized DMs from step 1.
- **Step 4:** the full-cell pOCV at C-rates lower than C/25 is measured if the battery is charging (parking mode) or the full-cell pOCV is estimated if the battery is discharging (driving mode).
- **Step 5:** the difference between the simulated and the measured full-cell pOCV is calculated.
- **Step 6:** the difference obtained in step 5 is compared with a pre-defined threshold error (ϵ). The estimated error can be expressed as the absolute error or the RMSE. The value of ϵ is defined on an individual basis according to the requirements of each particular application. If this error is lower or equal than the pre-defined threshold, the hypothesized degradation is accepted. Otherwise, the hypothesized degradation is rejected. In this case, a new hypothesis needs to be made and steps 3 to 5 are repeated until the error is lower or equal than ϵ. The value of ϵ is defined on an individual basis according to the requirements of each particular application. As an example, Marongiu et al. [68] obtains a maximum ϵ of 1.10% for the pOCV discharge and 0.98% for the pOCV charge process. A limitation of this method is that more than one hypothesis within the same iteration can be true and hence, the degradation modes may not be estimated correctly. In mathematics, this problem is known as local error [135]. A simple solution for this would be to compare the result of the estimation with historical battery operating parameters. This comparison would enable to evaluate whether the estimation provided is plausible with respect to the theory of battery degradation shown in Table 5.1.

Though pOCV based methods follow the process depicted in Figure 5.4, this review has categorised the pOCV methods into three different groups.

- **Group 1:** includes studies in which the relationship between half-cell pOCV curves and DMs are determined according to the change of the charge-throughput and loading ratio, defined in Section 2.3.2. This method corresponds to the 'Alawa diagnostic tool proposed by Dubarry et al. [67] and further applied in [64,68,83]. It is noteworthy Group 1 articles differentiate for each electrode if LAM takes place in delithiated, LAM_{de}, or lithiated phase, LAM_{li}. Delithiated phase is said when an electrode is empty of Li-ions and lithiated when an electrode is full of Li-ions.

- **Group 2:** includes studies in which the relationship between half-cell pOCV curves and DMs is determined according to the change in SoC. SoC and loading ratio from Group 1 have both the same physical meaning, only the notation used is different. This notation was used by the research group from Tsinghua University and therefore, the reviewed articles related to this group are classified separately. In particular, the SoC representation was suggested by Han et al. [111], extended by Ouyang et al. [136] and applied in [116, 137, 138].

- **Group 3:** includes studies in which the relationship between half-cell pOCV curves and DMs are determined according to the change in SoC. In contrast to Group 2, the studies of Group 3 introduce two parameters, m, equivalent to LAM, and δ, equivalent to LLI. This method was initially presented by Honkura et al. [139, 140] and further applied in [141, 142].

Figure 5.4 provides an overview of the principle, required measurements, computation and output for each pOCV group. The principle of quantifying the DMs based on the shifts of half-cell pOCV is common in each Group. The main difference between them is how they relate the DMs with the shifts of half-cell pOCV. Table 5.2 summarises other differences between them. The characteristics which are not included in this table are the same for each Group.

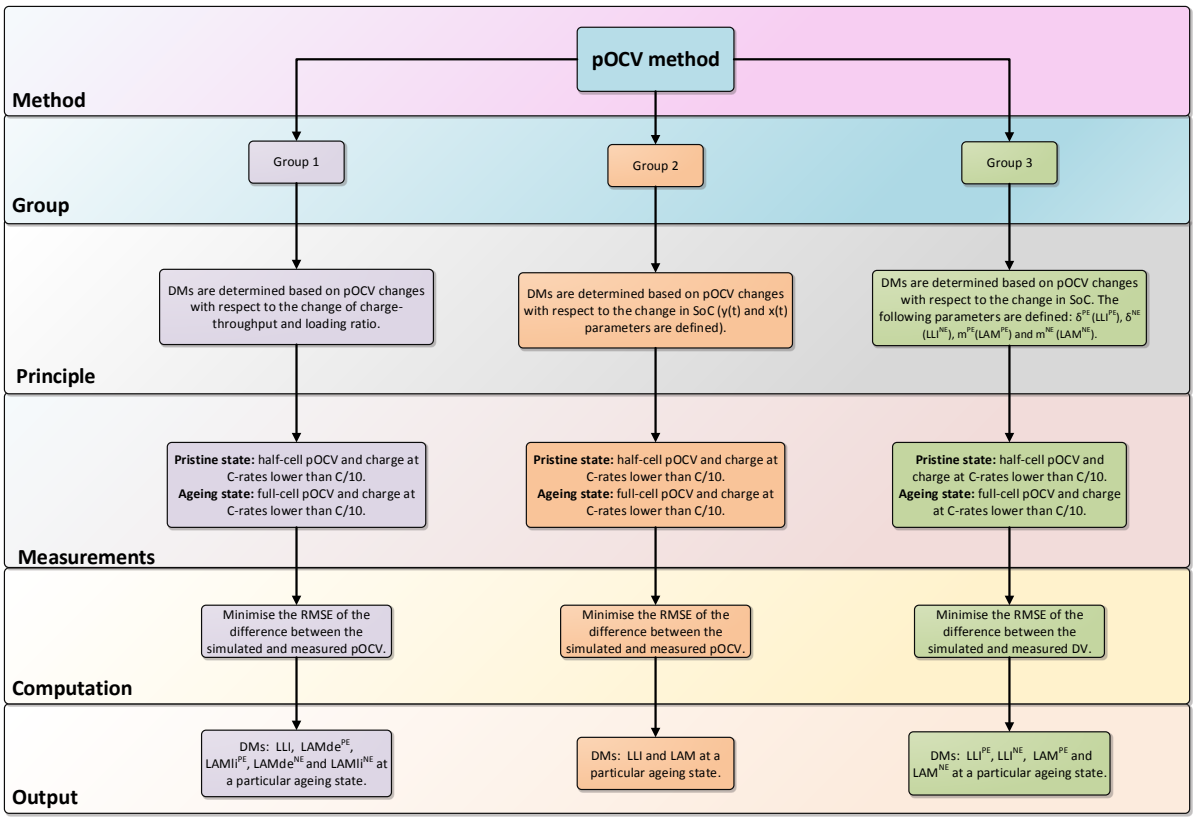

Figure 5.4: Principle, required measurements, computation and output of each group of the pOCV technique.

Table 5.2: Differences between methods of Group 1, Group 2 and Group 3.

Characteristic	Group 1	Group 2	Group 3
DMs	LLI, $\mathrm{LAM}_{de}^{\mathrm{PE}}$, $\mathrm{LAM}_{li}^{\mathrm{PE}}$, $\mathrm{LAM}_{de}^{\mathrm{NE}}$ and $\mathrm{LAM}_{li}^{\mathrm{NE}}$	LLI, LAM and R	$\mathrm{LLI}^{\mathrm{PE}}$, $\mathrm{LLI}^{\mathrm{NE}}$, $\mathrm{LAM}^{\mathrm{PE}}$ and $\mathrm{LAM}^{\mathrm{NE}}$
Parameters to relate DMs	LLI, $\mathrm{LAM}_{de}^{\mathrm{PE}}$, $\mathrm{LAM}_{li}^{\mathrm{PE}}$, $\mathrm{LAM}_{de}^{\mathrm{NE}}$ and $\mathrm{LAM}_{li}^{\mathrm{NE}}$	x_0 and y_0	δ^{PE} ($\mathrm{LLI}^{\mathrm{PE}}$), δ^{NE} ($\mathrm{LLI}^{\mathrm{NE}}$) m^{PE} ($\mathrm{LAM}^{\mathrm{PE}}$) and m^{NE} ($\mathrm{LAM}^{\mathrm{NE}}$)
Measurement of the resistance	No	Yes	No
Kinetics effects (e.g temperature)	No	Yes (in [136])	No
Error calculation	Difference between $pOCV_{sim}^{\mathrm{FC}}$ and $pOCV_{meas}^{\mathrm{FC}}$	Difference between $pOCV_{sim}^{\mathrm{FC}}$ and $pOCV_{meas}^{\mathrm{FC}}$	Difference between $dpOCV_{sim}^{\mathrm{FC}}/dQ_{sim}^{\mathrm{FC}}$ and $dpOCV_{meas}^{\mathrm{FC}}/dQ_{meas}^{\mathrm{FC}}$

5.4.2 Incremental Capacity - Differential Voltage

Some of the pOCV based methods use IC and DV curves to corroborate the DMs quantified using half-cell pOCV measurements and thus, to identify DMs. According to the different possibilities to identify and quantify DMs using IC and DV curves, the IC-DV methods are classified into two groups.

- **Group 1:** includes the studies which use the IC-DV curves derived from the Group 1 pOCV based methods. This approach was introduced by Dubarry et al. [67] and further applied in [143, 144]. There are other studies [111, 116, 136, 138, 145–147] in which DMs are identified by making assumptions. As these studies do not follow an automated process, they are beyond of the scope of this review.

- **Group 2:** constitutes the studies which relate the change of the peak area of the IC curves with DMs. This approach was firstly presented in Dubarry et al. [148] to confirm the DMs quantified using the 'Alawa model [67]. This approach has been mainly developed by the researchers of Dubarry's group [148–150] and [151].

Figure 5.5 provides an overview of the principle, required measurements, computation and output for each IC-DV group. In both groups, the DMs are derived using the same steps as in pOCV based techniques (refer to Figure 5.3) with an additional step. This further step calculates the IC and DV curves from the simulated pOCV curves once the hypothesized DMs are accepted. Then either the changes of the IC-DV curves (Group 1) or the changes of the peak area of the IC curves (Group 2) are related to the changes in DMs.

To keep consistency with the previous section, Table 5.3 summarises the main differences between the Group 1 and Group 2 methods. The characteristics which are not included in this table are the same for each Group.

Table 5.3: Differences between the methods to quantify DMs using IC-DV*.

Characteristic	**Group 1**	**Group 2**
DMs	LLI, LAM_{de}^{PE}, LAM_{li}^{PE} LAM_{de}^{NE} and LAM_{li}^{NE}	LLI, LAM_{de}^{PE}, LAM_{li}^{PE}, LAM_{de}^{NE} and LAM_{li}^{NE}
Parameters to relate DMs	Changes in IC and DV curves	Peaks of IC curves
Method to determine DMs	DMs are not quantified, only identified	Calculation of integral area determined by the inflection points of the IC peaks

*In contrast to Table 5.2, measurement of the resistance and kinetics effects are not considered for any of these methods. Thus, resistance measurements are not included here.

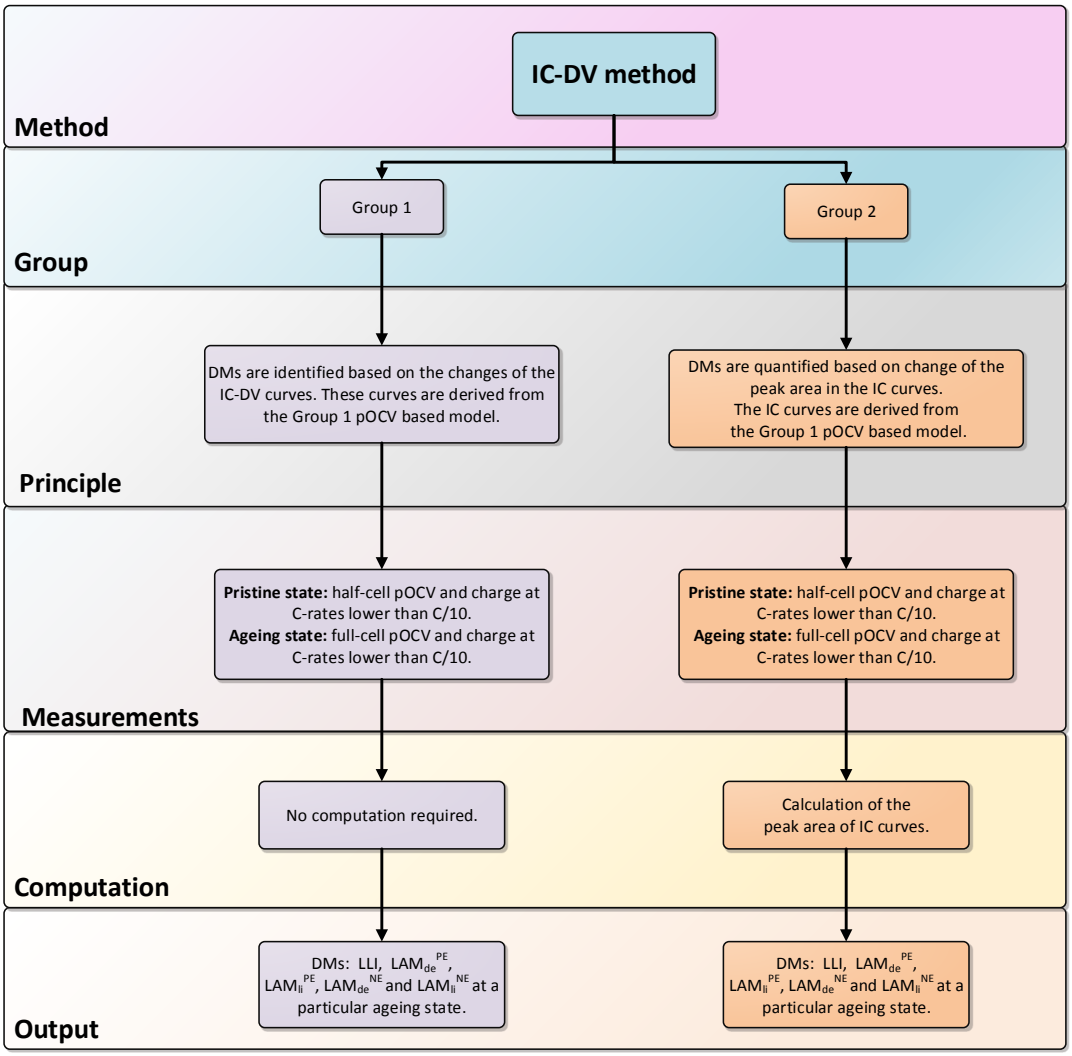

Figure 5.5: Principle, required measurements, computation and output of each group of the IC-DV technique.

5.4.3 Electrochemical Impedance Spectroscopy

The majority of the studies identified in the literature [66, 82, 152–154] use EIS as a characterisation technique to infer ageing mechanisms without following an automated approach. In addition, some authors [155–157] study the on-board implementation of EIS through novel power electronic, e.g., switched-inductor ladder topology, and control, e.g., digital proportional integral - PI, systems. These studies are relevant because they consider EIS as an on-board diagnostic technique. Only the model from Schindler et al. [83] relates specifically to the changes of the EIS resistances with the DMs. Aside from EIS, this model also employs pOCV measurements, and hence, the explanation of this

model is included in Section 5.4.4.

5.4.4 Combination of pOCV and EIS methods

Schindler et al. [83] proposed an automated method to couple thermodynamics and kinetics. The model is composed of a pOCV submodel to quantify LAM and LLI, and an EIS based model to quantify the overpotential due to Li-ion kinetics. The steps of the pOCV model are the same as in Group 1 pOCV based techniques with two main differences. Firstly, the transformation of pristine half-cell pOCV into aged half-cell pOCV measurements, as shown in step 3 of Figure 5.3, considers a gradual change of the NE pOCV shrinkage instead of a constant change. Schindler et al. [83] established this gradual change because the active material loss across the SoC window is not uniform. Secondly, following on from the studies of pOCV Group 3 [139–142], Schindler et al. [83] use a RMSE cost function based on DV curves to determine the DMs. The DV data is better amplified than the pOCV data, and hence, solving the RMSE cost function using DV data leads to a more reliable result than using pOCV data [83].

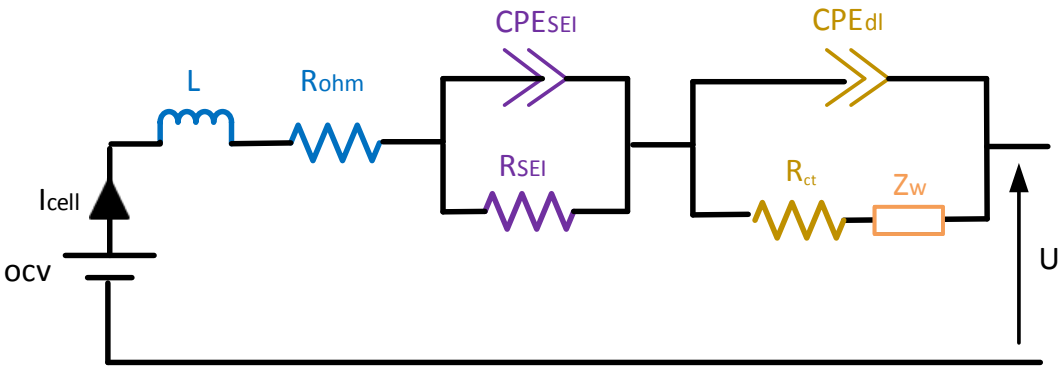

Figure 5.6: Adapted Randles ECM.

The EIS model is based on an Adapted Randles ECM, illustrated in Figure 5.6. The voltage drop due to R_o is added to the pOCV caused by LLI and the voltage drop due to $R_{ct}+R_W$ is added to the pOCV caused by LAM [83]. R_W is the real part of the Warburg impedance, Z_W. Relating the different resistances of the Adapted Randles ECM with CL, LLI and LAM involve several risks and can be misleading. For example, the

contribution to power fade due to increase in R_{ct} and R_W is consistent with the theory of battery degradation showed through Table 5.1. However, within the LLI, LAM and CL framework there is no obvious way to express that resistance rise and power fade are the principal modes and effects of degradation. Similarly, within this framework the main degradation mode for SEI is LLI as listed in Table 5.1. This is controversial with respect to previous literature [38, 158], which state that power fade is the main result of SEI growth and not LLI. In summary therefore, attributing ECM to specific DMs as suggested in [66, 82, 152–154] and corroborated in this study is limited and in some cases can be misleading. To quantify such inaccuracy and validate the results obtained alternative ex-situ post-mortem analysis such as Scanning Electron Microscopy, Energy Dispersive Spectrometry or X-Ray Diffractometry [69] should be used. Additional descriptions regarding the Adapted Randles ECM are provided in Section 6.4.1.

5.4.5 Differential Thermal Voltammetry

Initial studies of Reyner et al. [159] and Maher et al. [160] demonstrate that changes in the entropy profiles can be used as a measure to indicate ageing mechanisms that were occurring in either the PE or NE. Later, Wu et al. [161] and Merla et al. [162,163] propose the DTV technique to obtain information of the entropic behaviour of the cell by taking the temperature profile of the cell surface during galvanostatic charge and discharge. These authors in [161–163] infer ageing mechanisms by applying the DTV technique, but they do not prove its capability to identify and quantify DMs. Thus, following the systematic approach specified in Section 5.6.2, this technique could be excluded from this review because their corresponding studies neither identify nor quantify DMs directly. However, the ageing mechanisms are directly related to the DMs, and thus, for completeness, this technique has been considered as a part of this review.

5.5 Requirements on battery monitoring algorithms

In the process of designing a diagnostic function, a minimum amount of requirements need to be fulfilled. The articles are then reviewed according to the requirements characteristic of automotive applications, and previously agreed with the sponsoring company. The results of this review would ultimately support the implementation of these techniques in real-world applications. It is noteworthy that this list is not exhaustive and more requirements can be added based on the particularities of each system design. The requirements considered are listed below.

- **Universality:** according to automotive standards such as MISRA [164], there is a need to adapt diagnostic algorithms to the different cell technologies without modifying the algorithms significantly.
- **Real application capability:** the framework defined for the methods reviewed should be implementable in real applications. In general, a diagnostic method is implementable when it has the potential to fulfill commercially viable software and hardware requirements [71, 74]. Hardware and software requirements are defined in detail below.
  - **Hardware requirements:** an algorithm needs to consider the characteristics of the target hardware where it is executed. Following on from Ungurean et al. [74], hardware requirements are divided into data processing mode and processing time.

    Data processing mode denotes how the DMs are being quantified. Data processing can be done offline and online as described in Table 1.1.

    Processing time is related to the time needed by the diagnostic algorithm to produce the estimation of the DMs. This time depends mainly on the complexity of the method and the power of the microcontroller used.

  - **Software requirements:** an algorithm needs to consider the requirements of the target software where it is programmed [71, 74]. According to [165], these requirements include functionality, reliability, usability, efficiency, maintainability, portability and traceability. It is beyond the scope of this study to define and discuss each of these requirements in detail; they are however described fully in a number of standards and guidelines such as ISO 9126 [165] or MISRA [164, 166].

- **Consideration of main ageing factors:** ageing related parameters such as temperature or SoC are considered by testing the diagnostic function with real-world data such as non-repetitive driving cycle input data [78].

- **Accuracy and precision:** since LIBs are non-linear and time-varying systems, estimating the DMs with a low level of uncertainty is a challenge [6, 71, 74]. The level of uncertainty is measured with the accuracy and the precision. Accuracy quantifies the difference between a DM value estimated and the true value of the same type of DM. Precision quantifies the difference between two estimations of the same DM at the same state. Accuracy and precision levels are difficult to calculate in this context because the true DM value cannot be easily derived, even if more complex electrochemical techniques such as Scanning Electron Microscopy or X-Ray Diffractometry are used. Thus, accuracy and precision are determined indirectly by calculating the error of the parameter used to quantify the DMs. For instance, Marongiu et al. [68] use the difference in pOCV to estimate the accuracy.

- **Robustness:** the reviewed methods should ensure optimal performance for different operating conditions [71, 74]. This means a method needs to be tested with different type of input data, considering typical scenarios of vehicle operation such as driving or parking.

- **Scalability from cell to module and battery pack:** although the majority of methods are developed for cell level, they should be scalable to module and pack level in view of a real application [92].

5.6 Systematic and critical review of methods to identify and quantify DMs

5.6.1 Introduction to systematic literature reviews

In the context of BMS applications, Ungurean et al. [74] reviews systematically the most relevant state of the art models, algorithms and commercial devices employed in the estimation of the battery SoH and remaining useful life. The remaining useful life is the number of charge and discharge cycles or the time left until the battery reaches SoH equals to 0% [74]. The systematic review conducted in this study enables to draw reliable and accurate conclusions due to a generalised and consistent analysis of the literature [167]. According to Tranfield et al. [167], systematic reviews differ from traditional narrative reviews by adopting a replicable, scientific and transparent process that aims to minimise bias through exhaustive literature searches of published and unpublished studies. The main limitation of systematic reviews is the lack of flexibility. For instance, following a consistent analysis could lead to the loss of relevant information which is not seen within the specified review criterion [168]. Other related problems are the inappropriate subgroup analysis to fulfill the review criterion, or the conflict with new experimental data which cannot be categorised within the review criterion [168]. These problems were mitigated by considering some flexibility in the criterion used. The level of flexibility was argued in each case. An example of this is given in Section 5.4.5 for the DTV technique. Further information concerning the steps to conduct a systematic review can be found in [168]. It is beyond the scope of this study to describe in detail these steps.

5.6.2 Evaluation criterion

For this study, 14 metrics were used to review the method described in each article systematically as shown Table 5.4. The first three metrics (automated, identification and quantification) are intrinsically related to the type of techniques evaluated in this study. The remainder (4) to (14) are derived from the requirements defined in Section 5.5.

The following metrics were included as a part of the review to have a better understanding of the research groups involved in the field and the impact of their publications:

- Main author of the article.
- Research group.
- Country of the research group.
- Month and year when the article was available online.
- Conference proceedings or journal in which the article was published. The following proceedings or journal were used in this review: Journal of Power Sources (JPS), Applied Energy (AE), Journal of Electrochemical Society (ECS), Journal of Cleaner Production (JCP), American Society of Mechanical Engineers (ASME) and the Institute of Electrical and Electronics Engineers (IEEE).
- # of cits: number of citations of each reviewed article by 8th July 2018 according to Google Scholar [169].

Following on from this criterion, tables are included to review the articles systematically in Section 5.6.3, Section 5.6.4, Section 5.6.6 and Section 5.6.8 for pOCV, IC-DV, EIS and DTV technique, respectively. It is beyond the scope of this study to describe the particularities of each article reviewed. For this, it is recommended to refer to the corresponding citations or Submission 3 [33].

Table 5.4: Metrics used to conduct the literature review.

Metric	Description
(1) Automated	An article is related to Y (Yes) if the diagnostic method is automated; or to N (No), if not. A diagnostic method is automated if it follows a step-by-step process to identify or/and quantify the DMs. Automated processes are desired for a further hardware and software implementation of a diagnostic technique [74].
(2) Identification	An article is related to Y if the diagnostic method identifies the DMs; or to N, if not.
(3) Quantification	An article is related to Y if the diagnostic method quantifies the DMs; or to N, if not.
(4) Universality	An article is related to Y if the diagnostic method is universal; or to N, if not.
(5) On-board capability	An article is related to Y if the method can be implemented on-board; or to N, if not.
(6) Method	Describes the method or group of methods used (pOCV, IC-DV, EIS or DTV) in an article.
(7) Cell chemistry type	Describes the cell chemistry type or types to which the method was applied, e.g., NCA, NMC or LFP.
(8) Input data form	Input data form can be repetitive real drive cycles (RDC), repetitive artificial cycles (RS), or calendar (CAL).
(9) Data processing mode	Denotes when the acquired battery parameters are being processed: offline (Off) and online (On).
(10) Processing time	An article is related to SH if the processing time to produce the first estimation is less than 30min; or to M if the processing time is in between 30min and 60min; or to L if the processing time is longer than 60min; or to n.a. if the processing time is not available. As none of the reviewed studies attempt to implement the diagnostic methods into a real-time hardware environment, the processing time is related to software based simulations, e.g., MATLAB based simulations.
(11) Accuracy level	Provides the degree to which the result obtained by applying the method is closer to the true result. The accuracy in the determination of the DMs cannot be directly calculated as explained in Section 5.5. The accuracy in the estimation of DMs is determined indirectly by calculating the error of the estimation of the pOCV or capacity (C), which are parameters related to the DMs. Different metrics such as the absolute error or the RMSE are used to express the estimation error. In case the accuracy level is not indicated, then the accuracy level of a particular diagnostic approach is related to not evaluated (NEV).
(12) Robustness	A method is robust if given different input data the accuracy of the estimation keeps at the same level. Each article is related to Y if a method is robust; or to N if not; or to NEV if robustness is not evaluated.
(13) Scalability	An article is related to Y if the method is scalable from cell to module and pack; or to N if not; or to NEV if scalability is not evaluated.
(14) Hardware implementation	An article is related to Y if the hardware implementation of a method is studied; or to N if not; or to NEV if it is not evaluated.

Note that the studies reviewed do not consider software requirements and thus, this metric is not considered in this criterion.

5.6.3 Pseudo-OCV

Group 1

Table 5.5 evaluates the articles of Group 1 according to the criteria specified in Section 5.6.2.

Table 5.5: Systematic and critical evaluation of the articles of Group 1 (pOCV) according to the criteria specified in Section 5.6.2.

Article	Main author	Research group	Country	Available online	Journal	# cits.	Evaluation criteria 1	2	3	4	5	6	7	8	9	10	11	12	13	14
[67]	Dubarry	HNEI	USA	Jul-12	JPS	206	Y	Y	Y	Y	NEV	pOCV &IC-DV	LFP	CAL	Off	n.a.	NEV	Y	NEV	NEV
[68]	Marongiu	RWTH	Germany	May-16	JPS	8	Y	Y	Y	Y	Y	pOCV	LFP	RDC	Off&On	n.a.	1.10% in C	Y for C_{test}	NEV	NEV
[64]	Birkl	Oxford Univ.	UK	Dec-16	JPS	46	Y	Y	Y	Y	N	pOCV	LCO&NCO	RS	Off&On	n.a.	<3mV pOCV & 8% DMs	NEV	NEV	NEV
[170]	Ma	Beijing Institute	China	May-18	JPS	0	Y	Y	Y	Y	Y	pOCV&IC-DV	NMC	RS	Off	n.a.	<7mV & RMSE pOCV	NEV	NEV	NEV

(1-5) and (11-14) see Section 5.6.2 for the definition: Y (Yes), N (No), NEV (Not Evaluated) and n.a. (not available).

(8) Type of input data: C (Calendaric data), RS (Repetitive Synthetic data) and RDC (repetitive Real Drive Cycle data).

(9) Data processing mode: Off (Offline) and On (Online).

(10) Processing time: SH (Short, SH<30min), M (Mid, 30min≤M≤60min), L (Long, L>60min) and n.a. (not available).

The 'Alawa model proposed by Dubarry et al. in [67] quantifies LLI, LAM and CL and two additional DMs: faraidic rate degradation and formation of parasitic phase.

From the same research group of Dubarry or through collaborations, their model was further applied in different scenarios in [143, 144, 148–150]. Since these studies emphasize the use of IC and DV techniques to identify [143, 144] or quantify [148–150] the DMs, their review was included in Section 5.6.4. The main drawback of the approach presented by Dubarry et al. [67] is the lack of evidence to implement it on-board. This problem is faced in the model presented by Marongiu et al. [68]. The authors adapted the model proposed by Dubarry et al. [67] to quantify DMs on-board of a LFP cell cycled by a repetitive dynamic profile at 25℃. This model is composed of an offline and online part as described in Figure 5.3. This study stands out with respect to the literature because of the capability to quantify DMs on-board using input data from parking and driving

scenarios. Although this method was tested for LFP cells, it can also be applied to other cell chemistries. As pointed out in Section 5.4.1, the main drawback of this approach, which has not resolved up to date, is that the DMs may not be estimated uniquely as more than one hypothesis of DMs within the same iteration may be true.

Following on from [67], Birkl et al. [64] also proposed a parametric model to identify and quantify LLI and LAM by estimating the shifts of half-cell and full-cell pOCV curves. The contribution of this study is the derivation of the DMs as a manifestation of a host of different physical and chemical mechanisms. However, previous studies [67,68,143,149] determined the DMs using a less detailed electrochemical formulation making these models more suitable for BMS on-board applications.

Based on Dubarry's et al. model [67], Ma et al. [170] apply PSO to parametrise the half-cell model considering the individual electrode behavior and battery OCV at different ageing levels. Following on from this model, the corresponding DMs are quantified and the conclusions agree with the results obtained via IC and DV analyses. The main limitation of this study is the lack of guidelines to implement this methodology in real-world scenarios.

Group 2

Table 5.6 evaluates the articles of Group 2 according to the criteria specified in Section 5.6.2.

See definition of numeration (1) to (14) in Table 5.5.

Han et al. [111] presented an approach to quantify DMs using the shifts of half-cell and full-cell pOCV curves. Similarly to [67], IC curves were calculated to identify the DMs qualitatively. These qualitative insights corroborated the quantification of the DMs determined by pOCV curves. In addition, Han et al. [111] explain clearly the on-board capability of the IC curves using the point counting method. The simplicity and low computation requirements of this method make it suitable for BMS on-board applications.

Table 5.6: Systematic and critical evaluation of the articles of Group 2 (pOCV) according to the criteria specified in Section 5.6.2.

Article	Main author	Research group	Country	Available online	Journal	# cits.	Evaluation criteria 1	2	3	4	5	6	7	8	9	10	11	12	13	14
[111]	Han	Tsinghua Univ.	China	Nov-13	JCP	187	Y	Y	Y	Y only IC	n.a.	pOCV &IC	LTO, LFP & LMO	RS	Off&On	S	<5mV (full-cell pOCV)	NEV	NEV	NEV
[137]	Feng	Tsinghua Univ.	China	Sep-14	JPS	40	Y	Y	N	Y	NEV	pOCV &IC	NMC	RS	Off&On	n.a.	NEV	NEV	NEV	NEV
[116]	Ouyang	Tsinghua Univ.	China	Mar-15	JPS	53	Y	Y	Y	Y	NEV	pOCV &IC	LFP	RS	Off&On	n.a.	NEV	NEV	NEV	NEV
[136]	Ouyang	Tsinghua Univ.	China	Dec-15	AE	35	Y	Y	Y	Y	NEV	pOCV &IC	LFP, LMO+NMC	RS	Off&On	15min /1000 cycles	8% pOCV	Y	Y	NEV
[138]	Yan	Tsinghua Univ.	China	Jul-16	AE	9	Y	Y	Y	Y	NEV	pOCV &IC	LTO+NMC, LMO	RDC	Off&On	15min /1000 cycles	8% pOCV	Y	Y	NEV
[146]	Lu	Harbin Institute of Technology	China	Feb-17	ECS	1	Y	Y	N	Y	N	pOCV &IC-DV	NMC	CAL	Off&On	n.a.	NEV	NEV	NEV	NEV

As a disadvantage, the point counting method may not be appropriate to calculate the IC curves for the cases when noise corrupts the charging data. Further work includes testing this method using real BMS measurements.

Han's et al. degradation model was applied to quantify the DMs in different scenarios in [116, 137, 138] by authors of the same research group. Feng et al. [137] analysed the DMs of a 25Ah NMC cell exposed to temperatures larger than 80 ℃ without triggering thermal runaway. Ouyang et al. [116] evaluated the influence of the charging C-rate and the cut-off voltage limit on the DMs of 11.5Ah LFP cells cycled at -10 ℃. Yan et al. [138] studied the DMs in four high-power Li-ion batteries cycled with a durability HEV profile at 30 ℃, 40 ℃ and 50 ℃. For each of these cases, the quantification of the DMs using pOCV and Han's model IC curves were corroborated with the analysis of experimental IC curves. Ouyang et al. [136] extend the automated pOCV model presented by Han et al. [111] and further applied in [116, 137, 138]. Ouyang et al. [136] consider chemical kinetic principles in the calculation of the changes in SoC, represented by $x(t)$, $y(t)$, and R. Apart from using a novel mathematical formulation, the main contribution of this study is that a degradation model was applied under realistic scenarios. These scenarios are a frequency regulation profile for storage grid applications and a dynamic BEV profile. Additionally, DMs were also studied for a battery pack cell-to-cell variability scenario. According to the authors, further work includes building a more detailed test matrix to calibrate the model's parameters more precisely.

From a different research group as [116, 136–138], Lu et al. [146] adapted the automated model of Han et al. [111] to identify and quantify DMs. In addition to the automated model, they proposed a novel empirical expression for predicting LAM. The nonlinear least squares method was used in this case to solve the RMSE equation, and hence, quantify the parameters related to the DMs. The results revealed that LLI and self-discharge predominantly caused the capacity fade during this calendaric investigation. These results were qualitatively proven through IC and DV analysis. The main drawbacks identified for this model were: 1. lack of capability to be applied on-board; 2. lack of robustness since the model was only validated for storage conditions and it may not be valid for other scenarios.

Group 3

Table 5.7 evaluates the articles of Group 3 according to the criteria specified in Section 5.6.2. In 2008 Honkura et al. [139] published the first article ever found in which DMs are quantified following an automated model. As described in Section 5.4.1, Honkura et al. [139] quantified LAM and LLI tracking over time the changes in the amount of accessible active material, m^i, and the initial difference of Q^{PE} and Q^{NE} with respect to Q^{FC} and δ^i. Honkura et al. [140] published in 2011 a similar article where apart from quantifying the DMs as in [139], the authors also predict them using the $t^{1/2}$ rule. A year later, Dahn et al. [141] implemented this technique in a software package to quantify DMs in an automated way. None of these articles attempted to evaluate the on-board capability of the pOCV+DV method until Hu et al. [142] compute m^i and δ^i in a two iteration process rather than deriving these parameters simultaneously. The advantage of the computation method suggested by Hu et al. [142] is that the electrode slippages, δ^{PE} and δ^{NE}, are easier to estimate by observing changes in the peaks of the DV curve than by comparing the estimated and measured DV data. However, the authors identified that the following issues remain to be addressed: 1. how to use full-cell DV curves measured during a partial charge cycle to estimate the degradation parameters; 2. how to remove the noise in on-board measurements of full-cell pOCV and Q, and make the parameter estimation robust.

Table 5.7: Systematic and critical evaluation of the articles of Group 3 (pOCV) according to the criteria specified in Section 5.6.2.

Article	Main author	Research group	Country	Available online	Journal	# cits.	Evaluation criteria 1	2	3	4	5	6	7	8	9	10	11	12	13	14
[139]	Honkura	Hitachi Ltd.	Japan	2008	ECS	30	Y	Y	Y	Y	N	pOCV&DV	NMC	C	Off&On	NEV	NEV	NEV	NEV	NEV
[140]	Honkura	Hitachi Ltd.	Japan	Aug-2011	JPS	56	Y	Y	Y	Y	N	pOCV&DV	NMC	CAL	Off&On	n.a.	20% C_{est}	NEV	NEV	NEV
[141]	H. Dahn	Dalhousie Uni.	Canada	Aug-2012	ECS	66	Y	N	N	Y	N	pOCV&DV	LCO	RS	Off&On	S	0.0001 V/mAh	NEV	NEV	NEV
[142]	Hu	Iowa State Uni.	USA	Aug-2016	ASME	0	Y	Y	Y	Y	Y	pOCV&DV	LCO	RS	Off&On	n.a.	NEV	N	NEV	NEV

See definition of numeration (1) to (14) in Table 5.5.

Benefits and limitations of pOCV groups

Analysing Table 5.5, Table 5.6 and Table 5.7, the articles which meet the requirements defined in Section 5.5 are shown with respect to the group they belong to. It is seen that the methods of Group 1 and 2 are the most feasible methods to quantify DMs on-board in commercial BMS applications. Group 1 has a better on-board capability than Group 2. However, Group 2 fulfills processing time and robustness in comparison to Group 1. Despite Group 3 does not fulfill (7), (8), (11), (12), (13) and (14), the method is suitable for on-board applications as shown in [142]. The recommendation would be to choose a method of Group 1. To prove the robustness requirement, the chosen method would need to be validated with different input data forms.

Table 5.8: Comparison of the benefits and limitations of the methods of Group 1, 2 and 3 according to the evaluation criteria described in Section 5.6.2.

Group	Evaluation criteria 1	2	3	4	5	6	7	8	9	10	11	12	13	14	Key articles
Group 1 [64, 67, 68]	✓ [All]	✓ [All]	✓ [All]	✓ [All]	✓ [68]	✓ [All]	✓ [64]	✓ [68]	✓ [All]	✗	✓ [64, 68]	✓ [67]	✗	✗	[67, 68]
Group 2 [111, 116, 136–138, 146]	✓ [All]	✓ [All]	✓ [All]	✓ [111, 116, 136–138]	✗	✓ [All]	✓ [111, 136, 138]	✓ [138]	✓ [All]	✓ [111, 136, 138]	✓ [136, 138]	✓ [136, 138]	✓ [116, 138]	✗	[111, 136]
Group 3 [139–142]	✓ [All]	✓ [139, 140, 142]	✓ [139, 140, 142]	✓ [141, 142]	✓ [142]	✓ [All]	✗	✗	✓ [All]	✓ [141]	✗	✗	✗	✗	[142]

See definition of numeration (1) to (14) in Table 5.5.

5.6.4 Incremental Capacity - Differential Voltage

Group 1

Table 5.9 evaluates the articles of Group 1 according to the criteria specified in Section 5.6.2.
See definition of numeration (1) to (14) in Table 5.5.

Table 5.9: Systematic and critical evaluation of the articles of Group 1 (IC-DV) according to the criteria specified in Section 5.6.2.

Group 1																				
Article	Main author	Research group	Country	Available online	Journal	# cits.	Evaluation criteria 1	2	3	4	5	6	7	8	9	10	11	12	13	14
[67]	Dubarry	HNEI	USA	Jul-12	JPS	206	Y	Y	Y	Y	Y	pOCV &IC-DV	LFP	CAL	Off&On	n.a.	NEV	Y	NEV	NEV
[143]	Devie	HNEI	USA	Mar-15	ECS	21	Y	Y	Y	Y	NEV	pOCV &IC-DV	LTO&NMC	RS	Off&On	n.a.	NEV	Y	NEV	NEV
[144]	Berecibar	IKERLAN	Spain	Dec-16	IEEE	1	N	Y	N	N	N	IC	NMC	RS	Off&On	n.a.	NEV	NEV	NEV	NEV
[63]	Dubarry	HNEI	USA	May-17	JPS	10	Y	Y	Y	Y	Y	pOCV	LTO, NMC & LFP	RS	Off&On	n.a.	NEV	Y	NEV	NEV

Aside from quantifying the DMs using half-cell pOCV measurements as described in Section 5.6.3, Dubarry et al. [67] introduces the theory to relate the changes of IC and DV curves with DMs. This theory can be used as a guideline to identify DMs in an automated way as suggested in [23, 24]. Devie et al. [143] study the most pertinent DMs involved with and without overcharging a LTO and a NMC pouch cell. For the DMs that were initially hypothesized, IC-DV curves were used to identify DMs. Further work includes achieving a better understanding of the electrochemical processes that lead to the DMs. Since the same model and type of data was used as in [67], the contributions and drawbacks of this article are the same as in [67]. Berecibar et al. [144] used IC curves generated with the Dubarry et al. [67] model to highlight the differences in terms of DMs between NMC high power and NMC high energy cells. The DMs were in this case identified by visual inspection of the changes in the IC curves without following any automated procedure.

Dubarry et al. [63] present an approach that can cover all the possible voltage curves upon degradation to fit the voltage response during constant current steps to decipher DMs. The voltage curves are derived from simulations using the model proposed in [67]. These curves are stored in form of a look-up table that can be easily implemented in real-world applications. The authors also define FOI from IC curves with the aim of relating the change of FOIs with degradation paths. The main limitations of this approach are that chemistries with large voltage plateaus might be challenging to diagnose, the computation effort is high, and some FOIs could disappear with ageing providing an erroneous diagnosis.

Group 2

Table 5.10 evaluates the articles of Group 2 according to the criteria specified in Section 5.6.2. Dubarry et al. [148] introduce the peak area methodology in high energy and high power commercial LFP cells. In more depth, Anseán et al. [149] use peak area analysis of IC curves and Dubarry's et al. model [67] to identify and quantify the DMs for a standard charging event and a 4C fast charging event of a high power LFP cell.

Table 5.10: Systematic and critical evaluation of the articles of Group 2 (IC-DV) according to the criteria specified in Section 5.6.2.

Article	Main author	Research group	Country	Available online	Journal	# cits.	Evaluation criteria													
							1	2	3	4	5	6	7	8	9	10	11	12	13	14
[148]	Dubarry	HNEI	USA	Feb-14	JPS	73	Y	Y	Y	Y	NEV	pOCV &PA	LFP	CAL	Off&On	S	NEV	Y	NEV	NEV
[149]	Anseán	Univ. of Oviedo	Spain	May-2016	JPS	32	Y	Y	Y	Y	NEV	pOCV &PA	LFP	RS	Off&On	n.a.	NEV	Y	NEV	NEV
[150]	Anseán	Univ. of Oviedo	Spain	Apr-2017	JPS	15	Y	Y	Y	Y	NEV	pOCV &PA	LFP	RDC	Off&On	n.a.	NEV	Y	NEV	NEV
[151]	Gao	Beijing Jiaotong Univ.	China	Apr-2017	JPS	17	Y	Y	Y	Y	NEV	pOCV &PA	LCO	RS	Off	n.a.	NEV	Y	NEV	NEV

See definition of numeration (1) to (14) in Table 5.5.

Since the same model was used, the drawbacks of the peak area analysis of IC curves for this study are the same as the ones described previously for [67]. Similarly as in [149], Anseán et al. [150] quantify the reversible and irreversible part of lithium plating in commercial LFP cell cycled at 23℃.

Gao et al. [151] reveal the influence of different charging current rates and cut-off voltages on the ageing mechanisms by using peak area IC analysis. In comparison to the rest of the studies of this group [148–150], Gao et al. [151] do not use Dubarry's et al. model [67] to quantify DMs based on the changes of half-cell pOCV curves. Instead, the authors relate the changes of the IC peaks with DMs by visual inspection and then, the area of each peak is calculated. The main contribution of this study is that DMs were quantified based on peak area IC analysis without using half-cell pOCV measurements. The main limitation of this approach is the amount of subjectivity involved when DMs are detected

through visual inspection. Further work includes developing an automated process to reduce the subjectivity in the interpretation of the IC peaks.

Benefits and limitations of IC-DV techniques

Analysing Table 5.9 and Table 5.10, the articles which meet the requirements defined in Section 5.5 are shown with respect to the group they belong to. Table 5.9 shows the methods of each group have approximately the same advantages and limitations. Both groups fulfill aspects (1-3) and (6), highlighting that they are automated, universal and suitable for identification of DMs. Group 2 also can quantify the DMs. However, as the main disadvantage, both groups lack an on-board implementation capability (5). Also, they do not fulfill aspects 11, 13 and 14. Apart from these, Group 1 fulfills aspects number 9 and 12, and Group 2 aspects 8, 9, 10 and 12. Hence, between the different groups, number 2 is the one which concentrates more advantages.

Table 5.11: Comparison of the benefits and limitations of the Group 1, 2 and 3 IC-DV methods according to the evaluation criterion described in Section 5.6.2.

Group	Evaluation criterion														Key
	1	2	3	4	5	6	7	8	9	10	11	12	13	14	articles
Group 1 [67,143,144]	✓ [67,143]	✓ [All]	✓ [67]	✓ [67,143]	✗	✓ [All]	✓ [143]	✗	✓ [All]	✗	✗	✓ [67,143]	✗	✗	[67]
Group 2 [148–151]	✓ [All]	✓ [All]	✓ [All]	✓ [All]	✗	✓ [148–150]	✗	✓ [150]	✓ [148–150]	✓ [148]	✗	✓ [All]	✗	✗	[148]

See definition of numeration (1) to (14) in Table 5.5.

5.6.5 pOCV and IC-DV studies focus on on-board implementation and battery pack scalability

There is a number of studies which applies pOCV and IC-DV techniques for SoH estimation rather than for quantification of DMs. Although they do not identify neither quantify DMs, it is noteworthy to mention them because some of their aspects can add value to the techniques described in Section 5.6.3 and Section 5.6.4. These complementary studies have been classified into two groups depending on the aspect that add value:

- **Group 1:** these studies [117, 147, 171, 172] support the capability of pOCV and IC-DV methods to be implemented on-board within a commercially viable BMS.
- **Group 2:** these articles [110, 173] contribute to scale pOCV and IC-DV techniques from cell to module and battery pack.

Table 5.12: Systematic and critical evaluation of the articles focus on on-board implementation according to the criteria specified in Section 5.6.2.

Group 1

Article	Main author	Research group	Country	Available online	Journal	# cits.	Evaluation criteria 1	2	3	4	5	6	7	8	9	10	11	12	13	14
[147]	Feng	Tsinghua Uni.	China	Jan-13	JPS	63	N	N	N	N	Y	IC&DV	LFP&LMO	RS	On	n.a.	2% SoH_{est}	N	N	NEV
[117]	Weng	Uni. of Michigan	USA	Feb-13	JPS	120	N	N	N	N	Y	pOCV&IC	LFP	RS	Off&On	S (187s)	1% 1C	Y	NEV	NEV
[171]	Riviere	EVE System	France	Dec-15	IEEE	9	N	N	N	N	Y	IC	LFP	RS	Off&On	n.a.	2% SoH_{est}	NEV	NEV	NEV
[172]	Wang	Jiangsu & Shandong Uni.	China	Feb-16	AE	25	N	N	N	Y	Y	DV	LFP	RS	Off&On	S (17ms)	2.5% SoH_{est}	Y	Y	NEV

Group 2

Article	Main author	Research group	Country	Available online	Journal	# cits.	Evaluation criteria 1	2	3	4	5	6	7	8	9	10	11	12	13	14
[173]	Zheng	Tsinghua Uni.	China	Dec-14	JPS	27	Y	Y	N	Y	NEV	ECDS	LFP	RS	Off&On	n.a.	0.03Ah in C	NEV	Y	NEV
[110]	Weng	Michigan & Tsinghua Uni.	China	Aug-16	AE	31	N	N	N	Y	Y	pOCV &IC	LFP	RS	Off&On	n.a	1.62% SoH_{est}	Y	Y	NEV

See definition of numeration (1) to (14) in Table 5.5.

From this classification, the specific contribution of the articles of each group is summarised in Table 5.12. As these articles are not aimed to identify nor quantify DMs, it is beyond the scope of this study to review them in detail.

5.6.6 Electrochemical Impedance Spectroscopy

Table 5.13 summarises the EIS articles according to the criterion specified in Section 5.6.2. The majority of the studies identified in the literature [66, 82, 152–154] use EIS as a characterisation technique to infer ageing mechanisms without following an automated approach. The authors in [66, 82, 152, 153] fitted the EIS measurements with an Adapted Randles ECM. Based on the change of the lumped elements of the Adapted Randles ECM, the authors infer the most obvious ageing mechanisms, such as SEI growth or lithium plating. The Adapted Randles ECM used by these authors is further explained in Chapter 6, as part of the approach proposed to quantify DMs using EIS. The common drawback of [66, 82, 152–154] is the inability to quantify the DMs following an automated process.

Table 5.13: Systematic and critical evaluation of the EIS related articles according to the criterion specified in Section 5.6.2.

Article	Main author	Research group	Country	Available online	Journal	# cits.	Evaluation criterion (BMS requirements)												
							1	2	3	4	5	6	7	8	9	10	11	12	13	14
[66]	Zhang	Pennsylvania State University	USA	May-2009	ECS	204	N	Y	N	NE	NE	EIS	LNO	RS	Off	SH	NE	NE	NE	NE
[82]	Aurora	Nissan	USA	2013	ECS	2	N	Y	N	NE	NE	EIS	NMC	RS	Off	SH	NE	NE	NE	NE
[152]	Liu	HRL Labs	USA	2010	ECS	252	N	Y	N	NE	NE	EIS	LFP	RS	Off	SH	NE	NE	NE	NE
[153]	Stiaszny	Bosch	Germany	2014	JPS	61	N	Y	N	NE	NE	EIS	NMC	RS	Off	SH	NE	NE	NE	NE
[154]	Schindler	Helmholtz-Institut Ulm (HIU)	Germany	2016	JPS	39	N	Y	N	NE	NE	EIS	LFP	RS	Off	SH	NE	NE	NE	NE

See definition of numeration in Table 5.5.

5.6.7 Combination of pOCV and EIS methods

Only the research presented by Schindler et al. [83] combines a thermodynamic (pOCV) and a kinetic (EIS) method to identify and quantify DMs following an automated process. Table 5.14 evaluates this study according to the criteria specified in Section 5.6.2. Schindler et al. [83] identify and quantify the DMs based on the fusion of an overpotential

(pOCV) and a kinetic (EIS) model. The results of the overpotential model show a linear dependency between relative the ohmic resistance and LLI values, and the polarisation resistance and LAM values. Further experimental work involving different cell chemistry types and testing conditions such as C-rate, SoC and temperature, needs to be performed to validate this linear relationship.

Table 5.14: Systematic and critical evaluation of the combination article (pOCV+EIS) according to the criteria specified in Section 5.6.2.

Article	Main author	Research group	Country	Available online	Journal	# cits.	Evaluation criteria													
							1	2	3	4	5	6	7	8	9	10	11	12	13	14
[83]	Schindler	ZSW	Germany	Jan-17	JPS	5	Y	Y	Y	Y	NEV	pOCV & EIS	LFP	RS	Off&On	n.a.	1% in pOCV	NEV	NEV	NEV

See definition of numeration (1) to (14) in Table 5.5.

5.6.8 Differential Thermal Voltammetry

Table 5.15 evaluates the DTV articles found in the literature according to the criteria specified in Section 5.6.2.

Table 5.15: Systematic and critical evaluation of the DTV articles according to the criteria specified in Section 5.6.2.

Article	Main author	Research group	Country	Available online	Journal	# cits.	Evaluation criteria													
							1	2	3	4	5	6	7	8	9	10	11	12	13	14
[161]	Wu	Imperial College London (ICL)	UK	Sep-14	JPS	29	N	N	N	Y	NEV	SRCV, IC EIS & DTV	NMC	RS	Off	n.a.	NEV	Y	NEV	NEV
[162]	Merla	ICL	UK	Jan-16	JPS	22	N	N	N	Y	NEV	SRCV, IC EIS & DTV	NMC	RS	Off	n.a.	NEV	Y	NEV	NEV
[163]	Merla	ICL	UK	Sep-16	JPS	8	N	N	N	Y	NEV	SRCV, IC EIS & DTV	NMC	RS	Off	n.a.	NEV	Y	Y	NEV
[174]	Offer	ICL	UK	Nov-17	JPS	1	N	N	N	Y	NEV	DTV	LFP	RS	Off	n.a.	NEV	Y	Y	NEV

See definition of numeration (1) to (14) in Table 5.5.

Wu et al. [161] present the DTV as a diagnostic technique to identify ageing mechanisms using voltage and temperature measurements in galvanostatic mode. The main limitation of this study is that the identification of the ageing mechanisms does not follow an automated approach and therefore, they are subject to different interpretations. To avoid this, Merla et al. [162] proposed peak position, peak width and peak height as FOIs of DTV curves to analyse the ageing mechanisms in an automated way. The results showed that it is challenging to predict the ageing mechanisms involved through individual peak parameter observation. Although the peak and changes of the DTV curves can be used

to infer DMs, this result shows clearly in practice is not possible. Another common limitation of [161, 162] is that the DTV was validated on individual cells under natural convection thermal boundary conditions. Merla et al. [163] used DTV to identify the ageing mechanisms of four commercial NMC connected in parallel placed under forced air surface cooling to emulate a BEV application. One of the cells was aged on purpose to demonstrate the diagnosis capability of the DTV. Under this scenario, the DTV results obtained for the four cells in parallel were comparable to the results obtained for the single cell test under natural convection [162].

Despite this result, DTV is not capable of identifying and quantifying DMs based on an automated approach and for this purpose DTV has not the potential of EIS and IC yet. In addition, the limitations highlighted by the authors for EIS and IC techniques can be overcome as suggested in [156, 157] for EIS (refer to Section 5.4.3), and as suggested in [67, 68, 83] for IC (refer to Section 5.4.2). From the same research group as [161–163], the last DTV study was published by Shibagaki et al. [174]. Following on from the same model as in [161–163], Shibagaki et al. [174] correlate peak DTV curve parameters with capacity fade, resistance increase and inhomogeneous electrode performance suggesting that the technique could be used for SoH estimation in real applications.

5.6.9 Comparison, benefits and limitations of diagnostic techniques

According to the criterion specified in Section 5.6.2, 14 different metrics were used to review the articles of each diagnostic technique. In addition to these metrics, other figures were evaluated to have a better understanding of the research groups involved in this field and the impact of their publications. This "soft" data and the 14 evaluation metrics are here treated separately. Figure 5.7 illustrates the level and the spread of the activity of different groups in this research area.

From analysing Figure 5.7 the following conclusions have been derived:

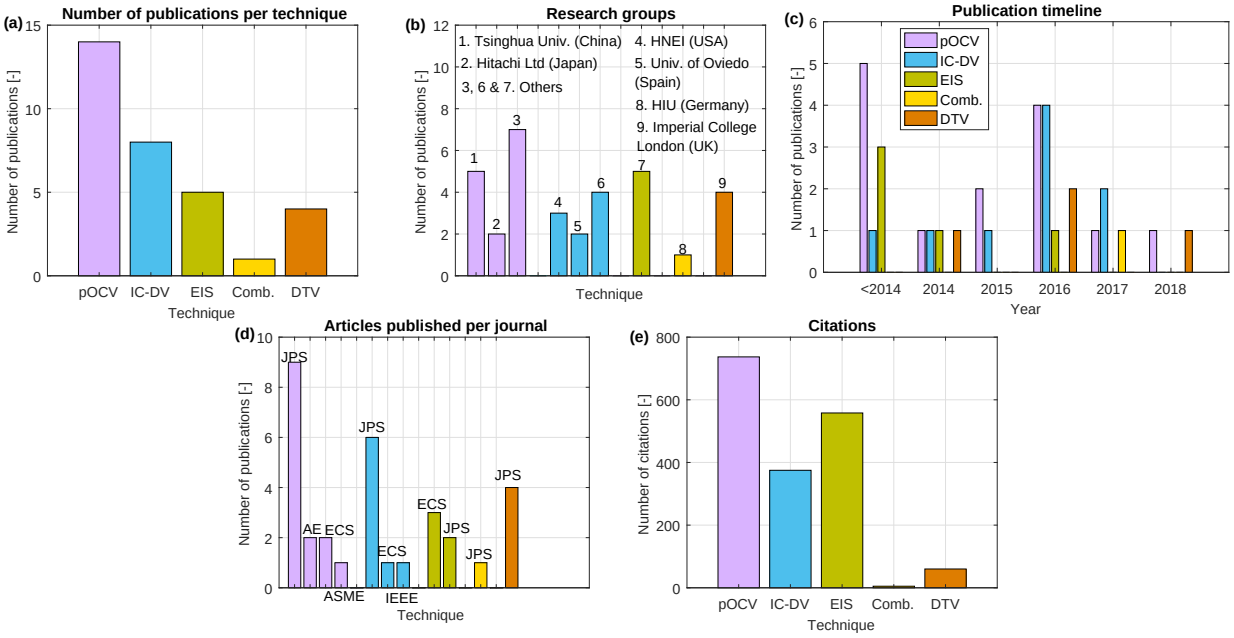

Figure 5.7: Comparison of the soft metrics for each reviewed diagnostic technique.

- **Figure 5.7 (a):** the techniques with a larger number of articles published are pOCV with 13 publications, followed by IC-DV with 9, DTV with 3, EIS with 2 and Comb with 1.

- **Figure 5.7 (b):** considering the affiliation of the first author in each publication, the most relevant research groups in the field are Tsinghua University (China) for pOCV, HNEI (USA) and University of Oviedo (Spain) for IC-DV, WMG (UK) for EIS, ZSW (Germany) for Comb. and Imperial College London (UK) for DTV.

- **Figure 5.7 (c):** from 2016 onwards the topic of this study has acquired more importance in the literature for each of the techniques evaluated.

- **Figure 5.7 (d):** JPS is the journal which has published more articles related to these diagnostic techniques. JPS is followed by AE, ECS, ASME, and IEEE.

- **Figure 5.7 (e):** the articles related to the pOCV technique have been cited 737 times followed by the IC-DV articles with 375 citations. EIS related articles have been cited 558 times, but none of them suggests an approach to quantify DMs. In

general, the articles related to the rest of the techniques (Comb. and DTV) are quite new, and hence, they have been cited 65 times.

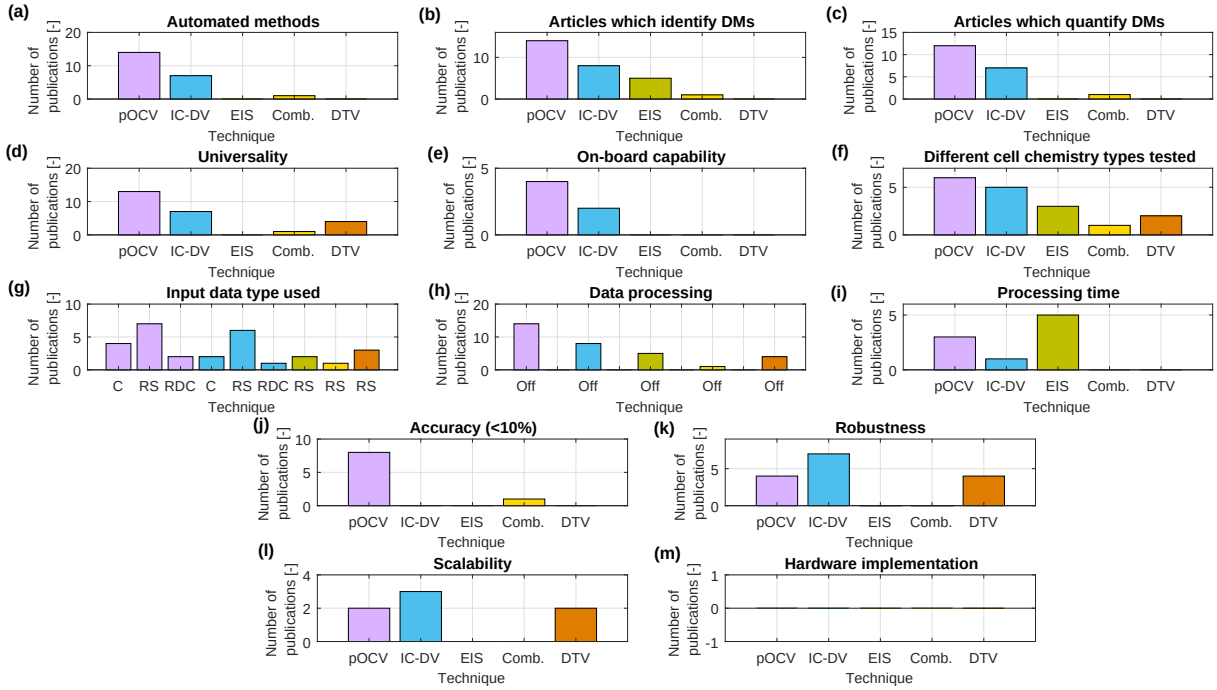

Figure 5.8: Comparison of the 14 metrics for each reviewed diagnostic technique.

According to Table 5.5, Table 5.9, Table 5.13, Table 5.14 and Table 5.15, the 14 metrics defined in Section 5.6.2 were analysed with respect to the diagnostic techniques. The results are illustrated in the form of bar plots in Figure 5.8. From the analysis of each plot the following conclusions were derived:

- **Figure 5.8 (a)-(e):** for the analysis of the automation, identification, quantification, universality and on-board capability of each of the techniques there is a superior trend in the number of pOCV articles with respect to the IC-DV ones. Only the IC-DV technique seems to be advantageous regarding on-board implementation. In comparison to the pOCV and IC-DV techniques, the rest of the techniques play a less significant role in these metrics. However, as a relative measure, all the EIS and Comb. reviewed articles fulfill the automation, identification and quantifica-

tion metrics. In contrast, the DTV technique only fulfills universality and on-board capability metrics.

- **Figure 5.8 (f):** the number of different cell chemistry types tested is larger for the pOCV (LFP, LCO, NCO, LTO, LMO and NMC) and IC-DV (LFP, LTO, NMC, LCO and NCA) techniques than for the EIS (NCA), Comb. (LFP) and DTV (NMC).

- **Figure 5.8 (g):** RS is the most common type of data used in all the techniques because it is easy to generate at laboratory conditions. The main disadvantage of this is that this type of data does not emulate real driving conditions, e.g., different C-rates, SoC, ΔDoD and temperatures. Since the number of articles published is larger for pOCV and IC-DV techniques, they are also tested with C and RDC data.

- **Figure 5.8 (h):** all the reviewed articles process the data offline.

- **Figure 5.8 (i):** only a few articles of the pOCV and IC-DV related techniques provides a measure of the processing time. This result is explained because none of the reviewed studies attempt to implement the diagnostic methods into a real-time hardware environment. The reported processing time is related to software based simulations, e.g., MATLAB based simulations.

- **Figure 5.8 (j):** a measure of the accuracy is given in terms of error of pOCV estimation for the pOCV and Comb. based methods. Therefore, the level of uncertainty is larger for the rest of the reviewed techniques.

- **Figure 5.8 (k)-(m):** robustness and scalability are mainly proved for IC-DV and pOCV related articles, followed by the DTV ones. For both cases, the number of articles which fulfill these metrics is not more than 14 articles. According to Figure 5.8 (m), the hardware implementation of the evaluated techniques has not been considered in the literature yet. This is because the research of these techniques is still in an early stage, and further work with this respect needs to be considered.

Though hardware implementation has not been studied yet, it is still valuable to analyse hardware related metrics such as offline and online processing or processing time. The availability of this information provides an indication of the stage of this research with respect to hardware implementation.

From this comparison and the individual review of each article conducted, the main benefits and limitations of each technique are shown in Table 5.16. Taking into consideration the results illustrated in Figure 5.8 and the advantages and disadvantages listed in Table 5.16, it is seen that pOCV and IC-DV are the more advantageous techniques. However, these also lack in some aspects such as the necessity of acquiring accurate half-cell measurements and the long duration of the required experiment (>10h), or the necessity of storing ageing historical data to discard the estimation of wrong DMs. Alternative techniques consider other ageing related parameters such as impedance in EIS or temperature in DTV, or the combination of them in Comb., which provide additional information to understand the DMs involved. These alternative techniques are not mature enough as they lack in aspects such as on-board capability in EIS, robustness and scalability in EIS and Comb., and capability to identify and quantify DMs in DTV. It is recommended therefore to use pOCV and IC-DV as reliable diagnostic techniques to identify and quantify DMs. At the same time, further developments in the EIS, Comb. and DTV diagnostic techniques need to be considered so that they can contribute to understanding better the diagnosis of DMs.

As suggested our work described in Section 6.6, it is recommended to apply these techniques in an off-board environment, e.g., service station, rather than on-board. Two reasons support this recommendation:

1. Hardware implementation of these techniques is less limited off-board than on-board. In an off-board application, there may be better access to more sophisticated equipment in terms, e.g., speed, accuracy or precision, than in an on-board environment, where the characteristics of the hardware components are more limited.

2. Under normal operation, degradation of LIBs is a slow process where significant changes can be noted after months or years. This low frequent check makes suitable to diagnose DMs using external equipment.

Table 5.16: Advantages and disadvantages of the reviewed diagnostic techniques.

Technique	Advantages	Disadvantages
pOCV	(a) Automated. (b) Identifies DMs. (c) Quantifies DMs. (d) Universal. (e) On-board capability. (f) Tested with RDC. (g) Accuracy is lower than 10%. (h) Robust. (i) Scalable.	(a) Pristine half-cell-pOCV measurements are required at laboratory conditions. (b) pOCV test duration is longer than 10h. (c) Ageing history measurements are required to discard the estimation of wrong DMs.
IC-DV	(a) Automated. (b) Identifies DMs. (c) Quantifies DMs. (d) Universal. (e) On-board capability. (f) Tested with RDC. (g) Robust. (h) Scalable.	(a) Pristine half-cell-pOCV measurements are required at laboratory conditions. (b) pOCV test duration is longer than 10h. (c) Ageing history measurements are required to discard the estimation of wrong DMs. (d) Level of accuracy lower than 10% is not proved. (e) DMs can be neglected from the analysis of the IC-DV curves.
EIS	(a) Automated. (b) Identifies DMs. (c) Quantifies DMs. (d) Accuracy is lower than 10%.	(a) Not mature technique for identification of DMs at laboratory conditions. (b) Universality is not proved. (c) On-board capability is not proved as hardware implementation is complex. (d) Not tested with RDC input data. (e) Robustness is not proven. (f) Scalability is not proved.
Comb.	(a) Automated. (b) Identifies DMs. (c) Quantifies DMs. (d) Universal (thermodynamic model). (e) Accuracy is lower than 10%.	(a) Pristine half-cell-pOCV measurements are required at laboratory conditions for the thermodynamic model. (b) Test duration is longer than 10h for pOCV test for the thermodynamic model. (c) Ageing history measurements are required to discard the estimation of wrong DMs. (d) Universality for the kinetic model is not proved. (e) On-board capability is not proved as hardware implementation of the kinetic model is complex. (f) Not tested with RDC input data. (g) Robustness is not proved. (h) Scalability is not proved.
DTV	(a) Universal. (b) On-board capability. (c) Robust. (d) Scalable. (e) Entropic influence (temperature) is considered. (f) Voltage can be measure up to 2C.	(a) Not automated. (b) Does not identify DMs. Only infers some ageing mechanisms. (d) Level of accuracy lower than 10% is not proved. (e) Not tested with RDC input data.

5.7 Limitations and further work

The main limitation of reviewing articles systematically is the lack of flexibility in the analysis. For instance, to keep consistency, the analysis of each article is limited to the metrics defined in Section 5.5. This type of analysis does not enable to infer additional aspects that may be of interest. Further work with this respect includes to conduct the same type of literature review using other methodologies, e.g., meta-analysis or meta-synthesis, and compare their results with the ones obtained in this study. These results could differ and hence, they can complement the outcomes of this review.

Table 5.1 relates the operation limits of the temperature, C-rate, SoC, ΔDoD and cycle number with the DMs. This relationship is derived based on different articles which tested lithium-ion cells of chemistry types and form factors at different operating conditions. Combining the conclusions from different studies may lead to inaccuracies in the analysis as a whole since the investigations described in each of these articles are not consistent one to another. A solution to avoid this problem would be to test all the different chemistry types at all the possible operating conditions consistently, i.e., same method or same input data. As this involves a large amount of work, such as experiment is unrealistic to conduct within the context of an EngD programme. Thus, researchers usually make conclusions acknowledging this source of error.

Each diagnostic technique has its drawbacks. The following points outline the most common limitations:

- The conditions at which the techniques are tested, e.g., C-rate, SoC, ΔDoD or temperature, are repetitive following synthetic profiles. Thus, future work involves proving the robustness of the diagnostic methods when the cells are aged based on more realistic scenarios such as cycling with dynamic profiles at non-repetitive SoC, ΔDoD and temperatures.

- Lack of on-board capability.
- Lack of scalability.
- Lack of hardware implementation.

According to Table 5.16, EIS, DTV and Comb. require also improvements regarding robustness. Overall, DTV is the technique which needs more attention in the future since DTV does not fulfill the majority of the defined metrics. It is also seen that none of the diagnostic techniques proposed in the literature have been tested in real-world conditions within a vehicle. Such a study is also necessary to study the gap between the requirements of the diagnostic techniques such as scalability or hardware implementation, and the current functionalities of a commercial diagnostic function. Further work includes testing these techniques in real-world conditions to evaluate the level of accuracy and robustness required, e.g., sample rate or level of noise, so that reliable results can be achieved.

5.8 Conclusions

In summary, this study comprises a critical review of the different techniques employed in the literature to quantify DMs. The outcomes of this study provide a guideline to select the most appropriate diagnostic techniques to identify and quantify DMs within BMS applications.

The reviewed diagnostic methods are classified into thermodynamics based techniques (pOCV, IC-DV, and DTV), kinetics based (EIS) and a combination of them (pOCV+EIS). After an extensive review of the literature, these techniques were evaluated following the systematic criterion described in Section 5.6.2. This criterion includes requirements characteristic of automotive applications, which were previously agreed with the sponsoring company. The results revealed that none of these techniques were tested in the vehicle in

real-world conditions and thus, their hardware implementation needs to be further studied. This study has also evaluated the feasibility of implementing the reviewed diagnostic techniques on-board and off-board. From this review can be inferred that a practical application of these approaches may be more feasible off-board than on-board. Further details with this respect are given in Chapter 7.

By comparing the different diagnostic techniques, pOCV and IC-DV seem to be more advantageous than EIS, DTV and Comb. techniques because they fulfill a more significant number of requirements. Despite this, EIS, DTV and Comb. techniques employ different ageing indicators such as the impedance for EIS, charge and impedance for Comb., and temperature for DTV. This result motivates the further evaluation of these techniques so that they can be implemented in real-world automotive applications in the future.

6. Study 4 - An approach to quantify degradation modes using non-invasive full-cell measurements

6.1 Introduction

Chapter 5 shows that pOCV and IC-DV techniques followed by EIS, Comb. and DTV are the most advanced non-invasive diagnostic techniques to quantify DMs. Chapter 5 explains that pOCV and IC-DV techniques require half-cell pOCV measurements. According to Section 2.3.2, half-cell voltage measurements are difficult and costly to perform in real-world applications. Therefore, diagnostic techniques based on full-cell measurements need to be sought. In line with this challenge, this Chapter proposes a step-by-step methodology to identify and quantify DMs based on full-cell measurements. This methodology uses IC-DV and EIS as diagnostic techniques because they employ different ageing indicators, capacity/voltage for IC-DV and resistance for EIS. Figure 6.1 illustrates the steps taken for this methodology. Each step is further explained in Section 6.3 for EIS, and Section 6.4 for IC-DV. Step 4 is described in Section 6.5.3. To analyse these techniques close to a real application, this study considers the experimental data set gathered in Study 2, described in Chapter 4.

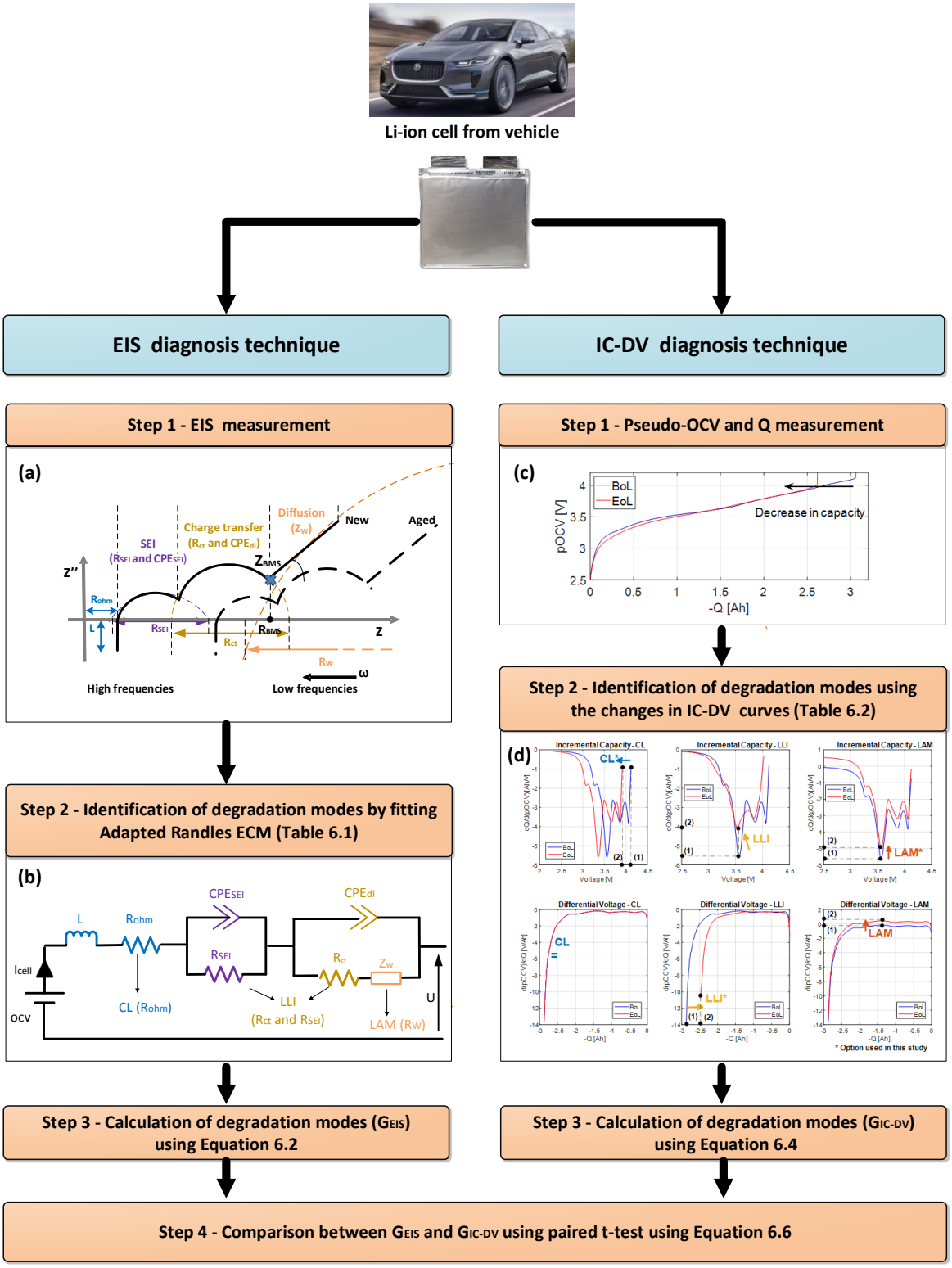

Figure 6.1: Framework of the methodology employed in this study. (a) EIS spectrum, (b) relationship of Adapted Randles ECM components with DMs, (c) pOCV curve, (d) relationship of changes in IC and DV curves with the DMs.

The structure of this work is divided as follows: Section 6.2 defines the main objective of this study. Section 6.3 and Section 6.4 describe the proposed methodology using EIS and IC-DV, respectively. Section 6.5 presents the experimental results. Following on from the approach described in Section 6.3 and Section 6.4, the DMs are calculated. Then, the DMs obtained with each technique are compared to evaluate whether there is a correlation between the results obtained with each technique. Furthermore, the quantified DMs are discussed in Section 6.5 concerning the SoC and initial level of ageing. The implications to implement these techniques in real-world applications are evaluated in Section 6.6. The limitations of this study and further work are outlined in Section 6.7. Finally, Section 6.8 presents the main conclusions of this study.

6.2 Objective of this study

The main objective of this study is to derive an a automated methodology to quantify the most pertinent DMs based on non-invasive full-cell measurements.

6.3 Electrochemical Impedance Spectroscopy

6.3.1 Theoretical background

As explained in Section 4.3.2, EIS is represented by a Nyquist plot. Fitting the Nyquist plot to a LIB ECM allows the SEI, charge-transfer, and diffusion processes to be modeled. The Adapted Randles ECM depicted in Figure 6.1 (b) is employed in this study. The Adapted Randles ECM is composed of a voltage source connected in series with a resistor; an inductor and resistor; and, Constant Phase Elements (CPEs) parallel branches. CPEs are employed to represent the porosity and tortuosity characteristics of the electrodes [175]. Porosity represents a measure of the number of sites available in the electrode morphology for Li-ion intercalation and de-intercalation [176]. Tortuosity describes the influence of the morphology of a porous electrode on its effective transport properties,

i.e., the strengths of the pores [176]. In practical applications, CPEs are often simplified to capacitors [128]. In comparison to the Randles ECM depicted in Figure 3.1, the Adapted Randles ECM can emulate more in detail the dynamic processes of LIBs. For instance, the Adapted Randles ECM can emulate the diffusion phenomenon throughout the Warburg impedance whereas the Randles ECM does not have such capability. In contrast to the Randles ECM, the Adapted Randles ECM cannot be used for modelling the battery dynamics in real-time applications because the CPEs and Warburg elements require complicated fractional integrals to be solved [32].

6.3.2 EIS measurement (Step 1) and identification of degradation modes (Step 2)

Step 1 consists of measuring the EIS spectra following on from the experimental procedure described in Section 4.3.2. As the cells were characterised individually, the EIS was measured for each cell independently without measuring the EIS when the cells were connected in parallel. The EIS measurements are then fitted to build the Adapted Randles ECM. This work proposes to track the change of the Adapted Randles ECM resistances to identify and quantify the effects of DMs. Monitoring the resistance is beneficial as the resistance increase is an indicator of power fade. SoH_P is a measure of the power fade as explained in Section 2.2.2. Secondly, the Adapted Randles ECM resistances are related to the dynamic behaviour of the battery, which, can be further linked to key DMs [177] as Figure 6.1 (b) illustrates. It is known that one Adapted Randles ECM resistance comprises the change of more than a single DM, and theoretically, it is not possible to isolate the causality between a single ageing mechanism, DM and electrical component within an ECM representation. Table 6.1 proposes a relationship between each resistance of the Adapted Randles ECM and the most pertinent DMs and ageing mechanisms. This relationship is justified in the following paragraphs. This relationship is a first step to link each resistance of the Adapted Randles ECM with individual effects of DMs, and thus, further work is required to quantify the importance of each DM with respect to

each resistance, or another component, of an ECM.

Table 6.1: Relationship between the resistances of the Adapted Randles ECM with the most pertinent DM, potential ageing mechanisms and most pertinent observed effects [38, 65].

Adapted Randles ECM component	**Unit**	**Most pertinent DM**	**Potential ageing mechanisms**	**Most pertinent observed effects**
Increase in R_o	[Ω]	CL	Current collector corrosion.	PF
			Binder decomposition.	CF
Increase in R_{SEI} & R_{ct}	[Ω]	LLI	Electrolyte decomposition.	CF & PF
			Oxidation of electrolyte.	PF
			Lithium plating.	CF & PF
			Formation of Li grains.	CF & PF
			Solvent co-intercalation.	CF & PF
Increase in R_W	[Ω]	LAM	Electrode decomposition.	CF & PF
			Oxidation of the electrolyte.	CF & PF
			Intercalation gradient strains in the active particles.	CF & PF
			Formation of Li grains.	CF
			Crystal structure disordering.	CF & PF
			Transition metal dissolution.	PF
			Solvent co-intercalation.	CF & PF

R_o is used to model the resistance in the current collectors, connectors and electrolyte [178]. Corrosion of current collectors and connectors, as well as changes in the electrolyte composites due to side reactions, cause CL through ageing. CL is manifested as voltage drops when a current circulates through a R_o. Thus, the increase of R_o can be used as a measure of the increase in CL.

SEI formation, build-up, and decomposition is one of the most relevant ageing mechanisms in Li-ion batteries as explained by Vetter et al. [38]. SEI impedes the intercalation and de-intercalation of Li-ions between the electrolyte and the anode. This interphase leads in turn to the irreversible consumption of Li-ions, LLI, which results in pronounced capacity fade and increased resistance [38]. Hence, the increase of R_{SEI} is primarily a consequence of LLI. Apart from the SEI, there are other degradation effects such as dendrite growth or micro pore clogging that, as shown in Table 5.1, are mainly attributable to LLI. From the perspective of the dynamics of the cell's voltage response, these effects, as well as SEI, are translated into a reduction of the charge-transfer Li-ion intercalation and de-intercalation reactions [38], which is seen as an increase of the R_{ct}. Thus, the increase of R_{ct} is also a consequence of LLI. This result highlights that LLI is related to R_{SEI} and R_{ct}.

Diffusion is caused when the concentration level within a Li-ion particle is different. This leads to structural transformations in the Li-ion particle and between different Li-ion particles [38, 158, 179]. Warburg impedance, Z_W, models diffusion processes. According to [180], the Warburg impedance is calculated as a function of the current I, the frequency ω, the specific diffusion thickness L, the effective diffusion coefficient of the particle D and the phase angle between the current and the applied voltage Ph as shown Equation 6.1.

$$Z_W = R_W \cdot \frac{\tanh\left(\left(I\frac{L^2}{D}\omega\right)^{Ph}\right)}{I\frac{L^2}{D}\omega} \tag{6.1}$$

R_W depends on the effective diffusion path length, L^2/D term. Since diffusion processes

are related to morphological changes in the structure of the electrodes, then the increase of R_W can be attributed mostly to LAM.

6.3.3 Quantification of degradation modes (Step 3)

The growth in percentage, G_{EIS}, is the parameter proposed to quantify the effects of DMs over cycle number. The G_{EIS} is selected because its calculation is simple and fast in the context of embedded BMS applications.

$$G_{EIS} = \begin{cases} CL^{q}_{EIS,k,u}(\%) = \frac{R^{q}_{ohm,k,u} - R^{q}_{ohm,1,u}}{R^{q}_{ohm,1,u}} \cdot 100 \\ LLI^{q}_{EIS,k,u}(\%) = \frac{\left(R^{q}_{SEI,k,u} + R^{q}_{ct,k,u}\right) - \left(R^{q}_{SEI,1,u} + R^{q}_{ct,1,u}\right)}{\left(R^{q}_{SEI,1,u} + R^{q}_{ct,1,u}\right)} \cdot 100 \\ LAM^{q}_{EIS,k,u}(\%) = \frac{R^{q}_{W,k,u} - R^{q}_{W,1,u}}{R^{q}_{W,1,u}} \cdot 100 \end{cases} \tag{6.2}$$

For $k = 1...11$, $q =$ low, mid and high, and $u = 1...4$

The growth in percentage can also be computed using IC/DV, enabling us to compare the results from EIS and IC/DV. G_{EIS} is a set of metrics calculated for each characterisation test k, cell u and SoC q using Equation 6.2. The number and type of the characterisation test performed in this experiment were described in Section 4.3. These equations are used in Section 6.5.1 to quantify the effects of DMs based on the EIS technique.

6.4 Incremental Capacity and Differential Voltage

6.4.1 Theoretical background

The principle, computation and practical application of the IC-DV method were explained in Section 3.4.4 and therefore, they are not repeated here. Section 5.4.2 explains the 'Alawa model is used to quantify DMs based on IC-DV curves.

6.4.2 pOCV and capacity measurement (Step 1) and identification of degradation modes (Step 2)

Step 1 consists of measuring the pOCV as described in Section 4.3.2. Consistent with Table 6.1, Table 6.2 relates the change in the IC-DV curves with the most pertinent DMs. According to [67], shifting toward lower voltages in IC curves, and constant capacity in DV curves are related to CL. The decrease of the height of the peaks at a variable voltage in IC curves is linked to LLI. Likewise, the shifting toward lower capacities in the DV curves is related to LLI. The decrease of the height of the peaks at an approximately constant voltage in IC curves is correlated to LAM. Similarly, the decrease of the depth of the valleys at approximately constant capacity in the DV curves is correlated to LAM. These relationships are illustrated in Figure 6.2.

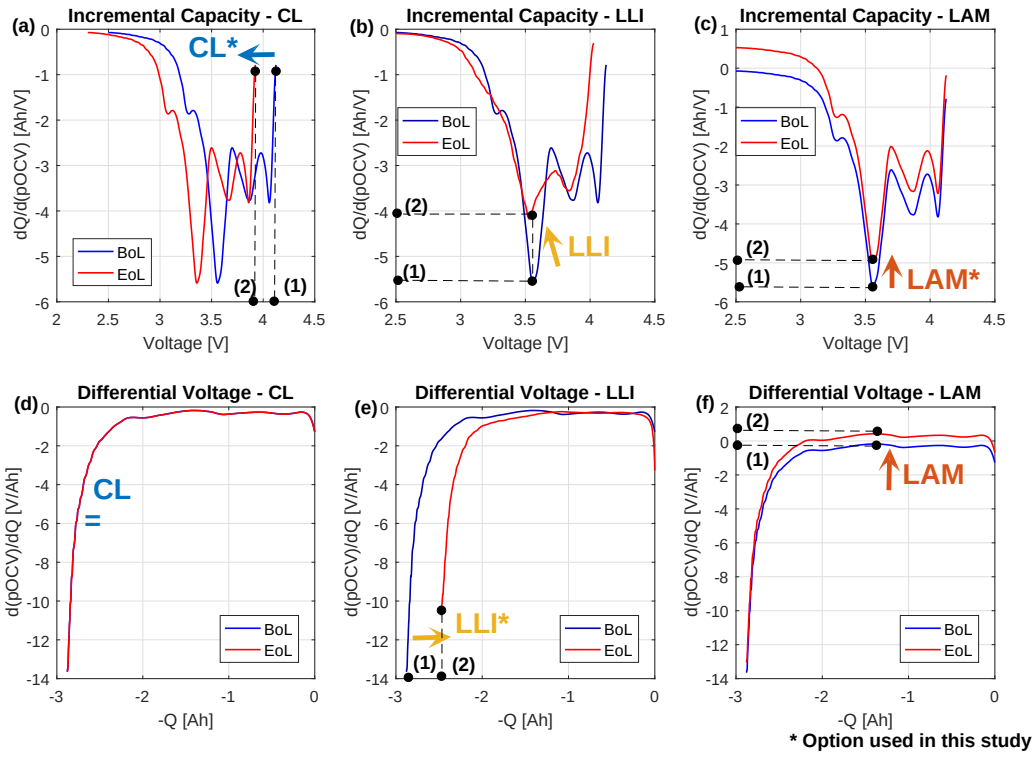

Figure 6.2: Relationship of changes in IC and DV curves with the DMs.

Subsequently, the reasons behind these relationships are explained for each case.

Neglecting the RC component of the ECM depicted in Figure 3.1, the pOCV voltage,

Table 6.2: Relationship between the changes in IC-DV curves with the most pertinent DM, potential ageing mechanisms and most pertinent observed effects.

Change in IC curve	Unit	Change in DV curve	Unit	Most pertinent DM	Potential ageing mechanisms	Most pertinent observed effects
Shifting toward lower voltages.	[V]	Lack of change.	[Ah]	CL	Current collector corrosion. Binder decomposition.	PF CF
Decrease of the height of the peaks at variable voltage.	[Ah/V]	Shifting toward lower capacities.	[Ah]	LLI	Electrolyte decomposition. Oxidation of electrolyte. Lithium plating. Formation of Li grains. Solvent co-intercalation.	CF & PF PF CF & PF CF & PF CF & PF
Decrease of the height of the peaks at approximately constant voltage.	[Ah/V]	Decrease of the depth of valleys at approximately constant capacity.	[V/Ah]	LAM	Electrode decomposition. Oxidation of the electrolyte. Intercalation gradient strains in the active particles. Formation of Li grains. Crystal structure disordering. Transition metal dissolution. Solvent co-intercalation.	CF & PF CF & PF CF & PF CF CF & PF PF CF & PF

V_{poc}, is derived as the difference between the pure OCV, V_{oc}, and the voltage drop due to the ohmic resistance, V_o.

$$V_{poc} = V_{oc} - V_o = V_{oc} - I \cdot R_o \tag{6.3}$$

Given a constant current flow and V_{oc}, an increase in R_o will cause a decrease in V_{poc}. As described in Section 6.3.2, the increase in R_o is related to CL [178]. This means that the increase in R_o only affects the cell voltage, not the capacity [67]. Therefore, without capacity fade, the effect of CL can be seen as a constant shift of the IC curve to lower voltages, and as a lack of change in the DV curves [67].

A reduction in the number of charge-transfer Li-ion intercalation and de-intercalation reactions leads to a decrease of the V_{oc} and capacity. These effects are mainly linked to LLI as described in Section 6.3.2 [38]. This does not mean that a reduction of capacity or pOCV cannot be attributed to LAM or CL. However, according to [38], the most pertinent DM when capacity or pOCV decrease is LLI. As Figure 6.2 illustrates, this is translated into a decrease of the height of the peaks at a variable voltage in IC curves, and a shift toward lower capacities in DV curves.

A decrease of the magnitude of the peaks in the IC curve represents a reduction of the charge at an approximately constant V_{poc}. Similarly, reduction of the depth of the valleys in the DV curve represents a decrease of the V_{poc} phase change at an approximately constant charge. For both cases, the V_{poc} or charge changes slightly, and so implies the system is close to equilibrium and therefore the total overpotential is approximately zero. From an electrochemical viewpoint, this scenario involves the movement of a low amount of Li-ions and therefore, these phase changes can be attributed to structure disordering of the active materials (LAM) [67, 69].

6.4.3 Quantification of degradation modes (Step 3)

As for the EIS case, the growth in percentage, G_{IC-DV}, is the metric derived to quantify the effects of DMs. Equation 6.4 is used to quantify the G_{IC-DV} for each characterisation test k and cell u. The parameters used in Equation 6.4 are:

- $max(pOCV)$: the maximum value of the pOCV is used to calculate CL.
- $max(Q)$: the absolute of the maximum value of the charge is used to calculate LLI.
- $max\left(\frac{\Delta Q}{\Delta pOCV}\right)$: the absolute of the maximum value of the phase change in charge with respect to the phase change in pOCV is used to calculate LAM.

Considering the absolute values of the $max(Q)$ and the $max\left(\frac{\Delta Q}{\Delta pOCV}\right)$ enables the use of G_{IC-DV} independently for charge or discharge pOCV measurements.

$$G_{IC-DV} = \begin{cases} CL_{IC-DV,k,u}(\%) = \frac{max(pOCV)_{1,u} - max(pOCV)_{k,u}}{max(pOCV)_{1,u}} \cdot 100 \\ LLI_{IC-DV,k,u}(\%) = \frac{abs(max(Q_1))_i - abs(max(Q_k))_u}{abs(max(Q_1))_u} \cdot 100 \\ LAM_{IC-DV,k,u}(\%) = \frac{abs\left(max\left(\frac{\Delta Q}{\Delta pOCV}_1\right)\right)_u - abs\left(max\left(\frac{\Delta Q}{\Delta pOCV}_k\right)\right)_u}{abs\left(max\left(\frac{\Delta Q}{\Delta pOCV}_1\right)\right)_i} \cdot 100 \end{cases} \tag{6.4}$$

For $k = 1...11$, $u = 1...4$

These equations are used in Section 6.5.2 to quantify the effects of DMs based on the IC-DV technique.

6.5 Results and discussion

6.5.1 EIS

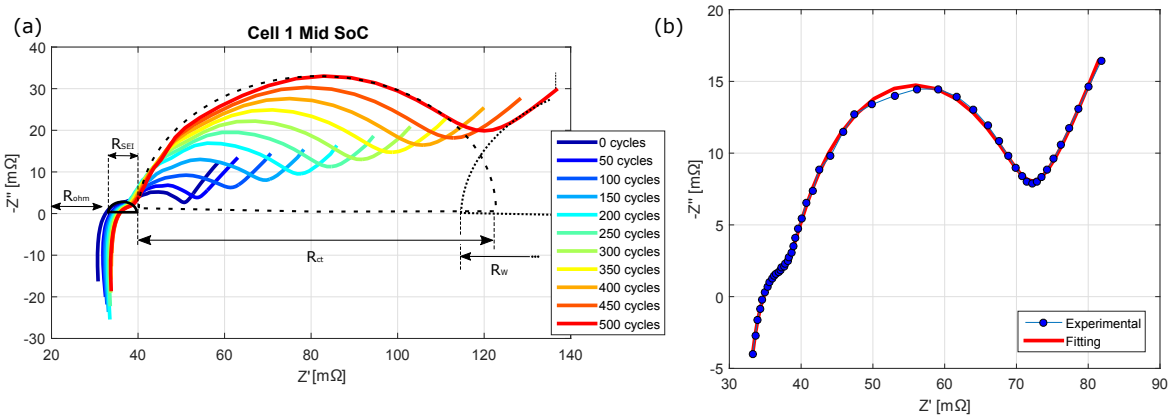

Figure 6.3: (a) EIS experimental measurements of Cell 1 at mid SoC over number of cycles; (b) Comparison of experimental and fitting of the EIS spectrum for an arbitrary measurement (characterisation test 1, Cell 4 at mid SoC).

Figure 6.3 (a) presents an example of the EIS experimental measurements obtained for Cell 1 at mid SoC (50%≤SoC≤60%) over the number of cycles. The Adapted Randles ECM was fitted to these EIS measurements using the complex non-linear least squares algorithm. The fitting routine was completed employing the Z_{view}© software package [180] that is provided with the Solatron Modulab system 2100 A. Figure 6.3 (b) compares the experimental EIS spectrum obtained from an arbitrarily selected measurement with the corresponding fitting results. The maximum difference between the fitted model response and the EIS measurements was 10%. Reducing this error would require fitting the EIS measurements to a more complex ECM including, for instance, a larger number of lumped elements. The error in the fitting may explain potential inaccuracies in the quantification of the resistances.

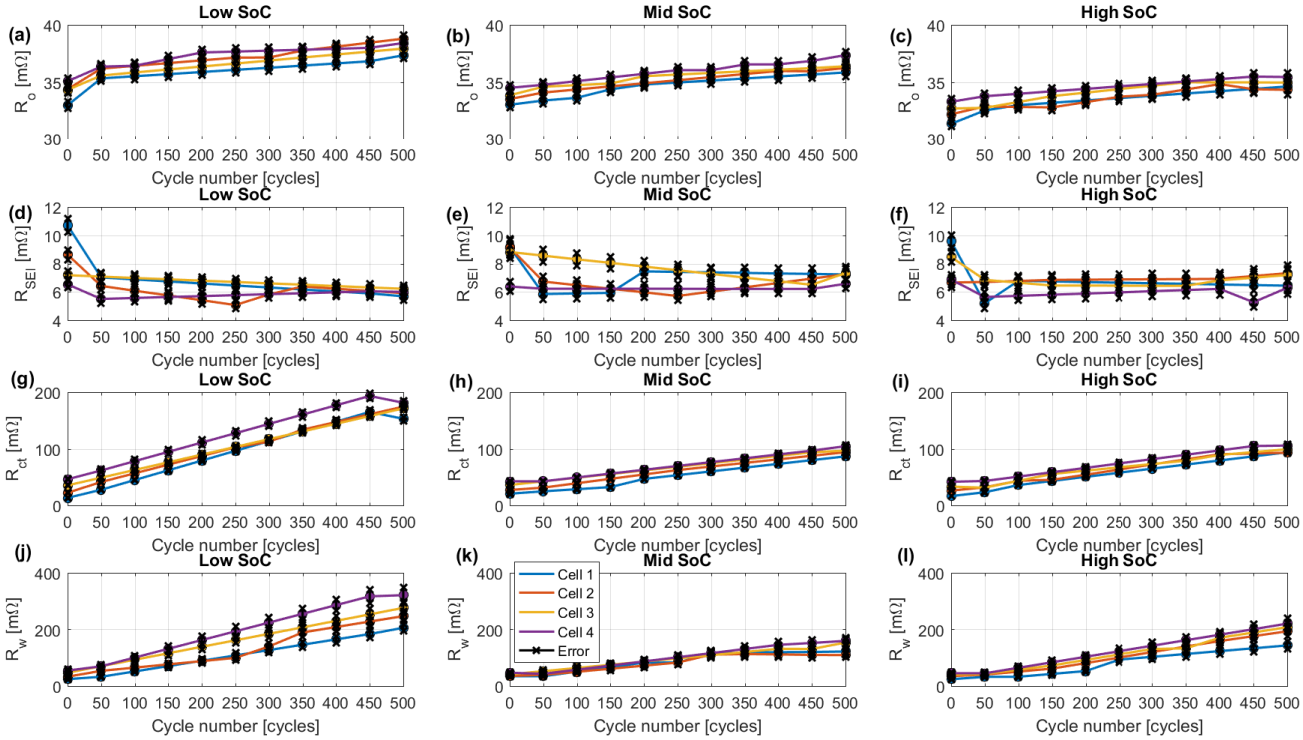

Figure 6.4: (a)-(c) R_o, (d)-(f) R_{SEI}, (g)-(i) R_{ct}, (j)-(l) R_W fitting results and error band at low SoC, mid SoC and high SoC over cycle number.

Figure 6.4 shows the values of R_o, R_{SEI}, R_{ct} and R_W obtained from the fitting process along with their error band. Figure 6.4 shows that R_o and R_{SEI} increases less than R_{ct} and R_W.

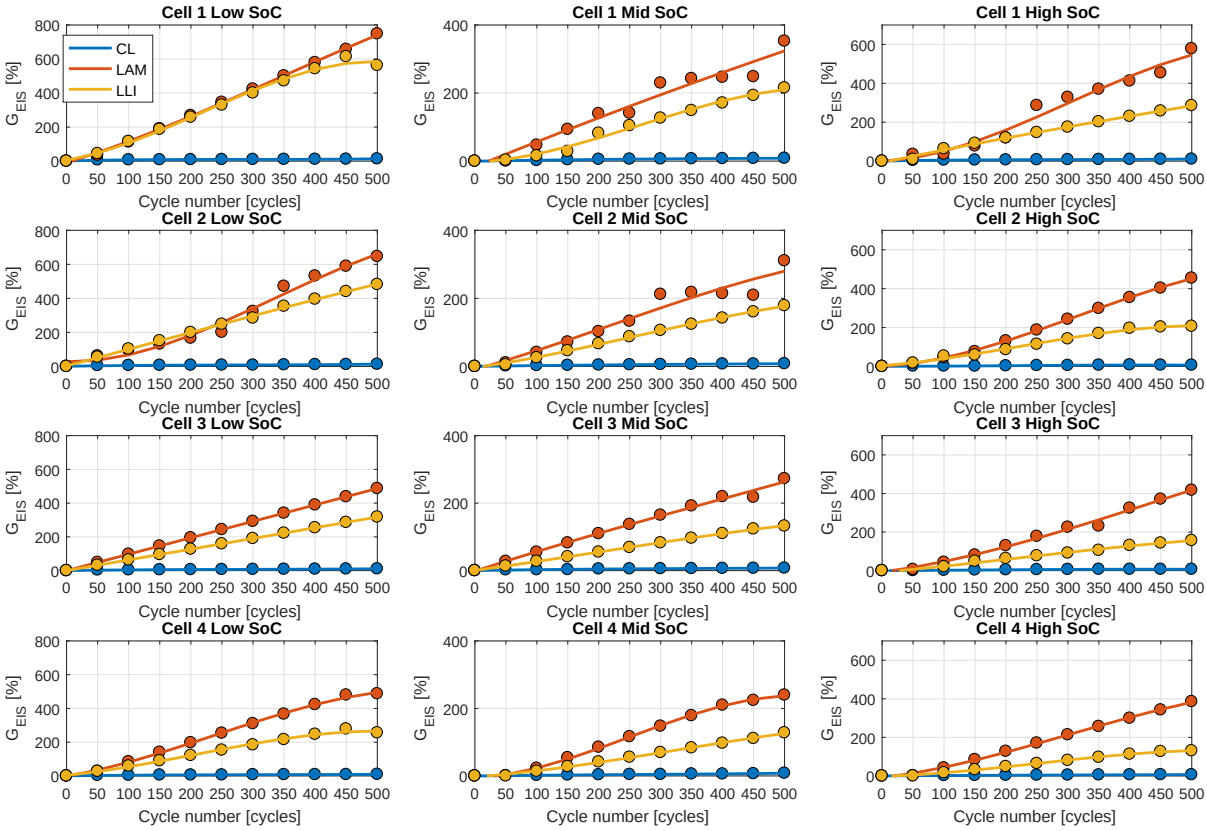

Figure 6.5: G_{EIS} for each DM for every cell at low, mid and high SoC over cycle number.

Figure 6.5 shows that the growth of LLI and LAM is larger than the growth of CL over cycle number, for each cell and SoC. This result is due to R_{ct} (LLI) and R_W (LAM) increasing more than R_o (CL) as the cell ages. Based on the operating conditions at which the cells were cycled, i.e., ΔDoD=100%, 1C discharge, C/2 discharge and 25℃, the resulting DMs are consistent with the theoretical expectations shown in Table 5.1. For other testing conditions, it is expected to obtain different amounts of DMs. Testing this assumption is part of further work as described in Section 6.7.

For most of the cells and SoCs, the growth of LLI and the growth of LAM follows an approximately linear trend over cycle number. The linear increase of the resistance observed in other studies [181, 182] supports this result.

6.5.2 IC-DV

Figure 6.6 and Figure 6.7 show the IC and DV curves for each cell. The height of the IC peaks decreases at an approximately constant V_{poc} over cycle number as a measure of the effects of LAM. This reduction of the height of the IC peaks is also manifested as a decrease in the magnitude of the depths of the valleys at an approximately constant charge in the DV curves. This study considers the reduction of the height of the peaks in the IC curves to calculate the growth of the effects of LAM because their variation is more evident than the decrease in the depths of the valleys in the DV curves.

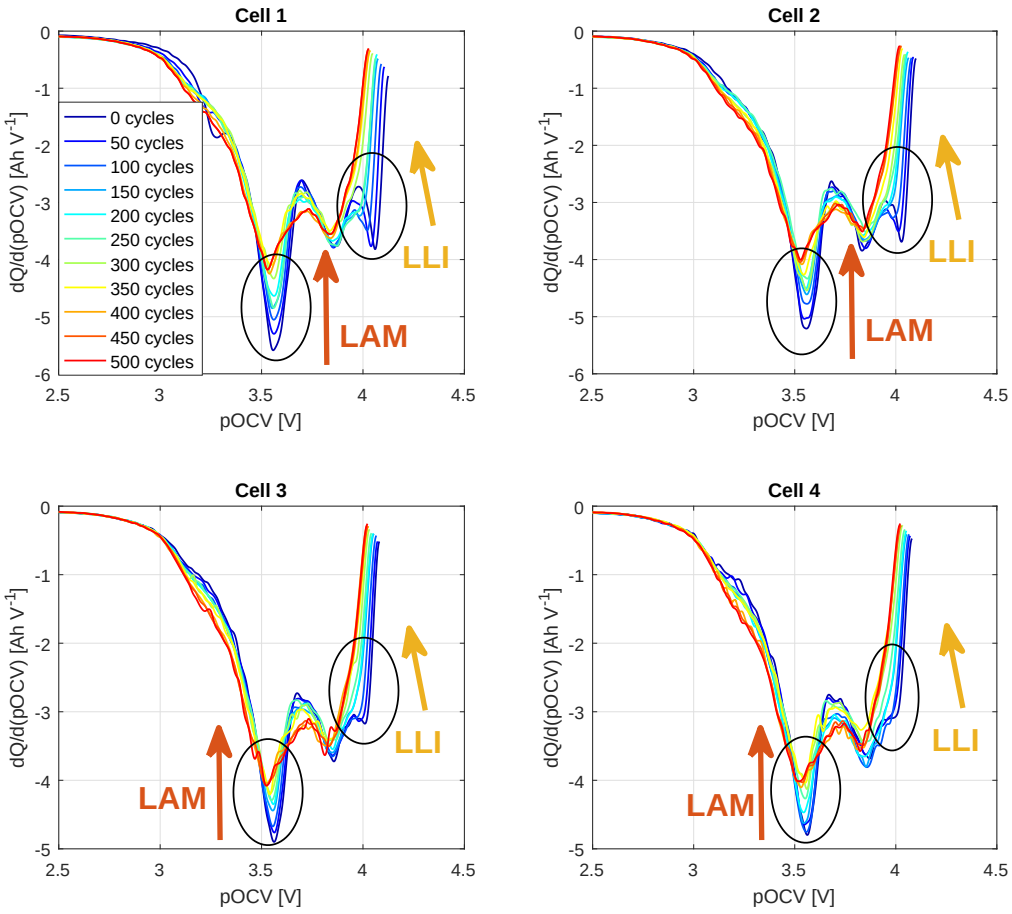

Figure 6.6: Incremental capacity results for every cell.

The shift towards lower capacities in the DV curves indicates the effect of LLI. This shift toward lower capacities is also observable as a decrease of the height of the IC

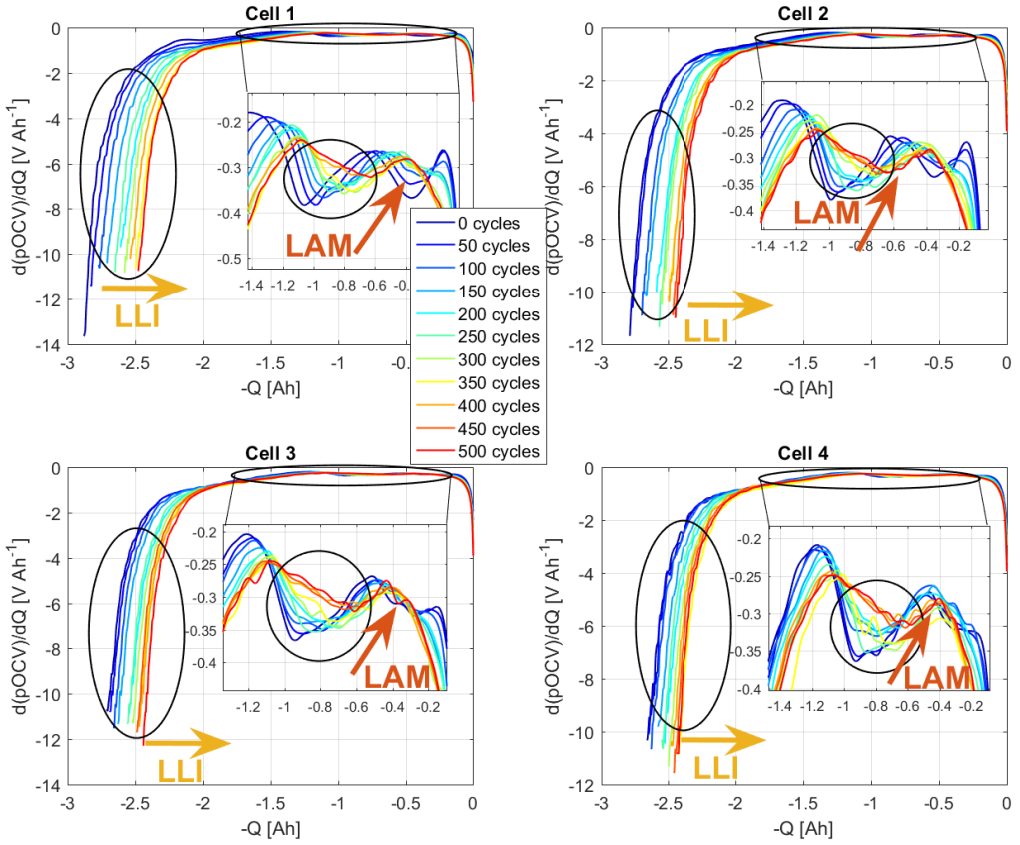

Figure 6.7: Differential voltage results for every cell.

peaks toward lower voltages as described in Section 6.4.2. Similar to LAM, this study considers the shift toward lower capacities in the DV curves to estimate the growth of the effects of LLI because their variation can be observed more apparent than the decrease of the height of the IC peaks toward lower voltages. For the case of CL, neither constant reduction of V_{poc} (IC) nor lack of change of capacity (DV) is observed and therefore, the effects of CL cannot be quantified using the IC-DV technique for this case. As explained in Section 3.4.4, the pOCV measurement required to derive the IC-DV curves emulates battery equilibrium conditions, and thus, it is difficult to capture the kinetic processes of the battery. According to Figure 6.5, this result is in agreement with the result obtained using EIS where the maximum growth of CL was 13.4%, value significantly lower in comparison to the growth obtained for LLI (614%) and LAM (748%).

The shifting of the IC and DV curves enables the quantification of the effects of the DMs

using Equation 6.4. Figure 6.8 illustrates the growth of LLI and the growth of LAM linearly increases from 0 cycles to 400 cycles and then a plateau is reached until 500 cycles. This trend is different with respect to the pattern obtained for the EIS case where the growth of the DMs increases linearly for the majority of the cases. This result relies on the fact that generally, the measures behind EIS and IC-DV change differently, i.e., resistance increases linearly and capacity decreases closer to an exponential trend with ageing as illustrated in Figure 4.2 (a) and (b).

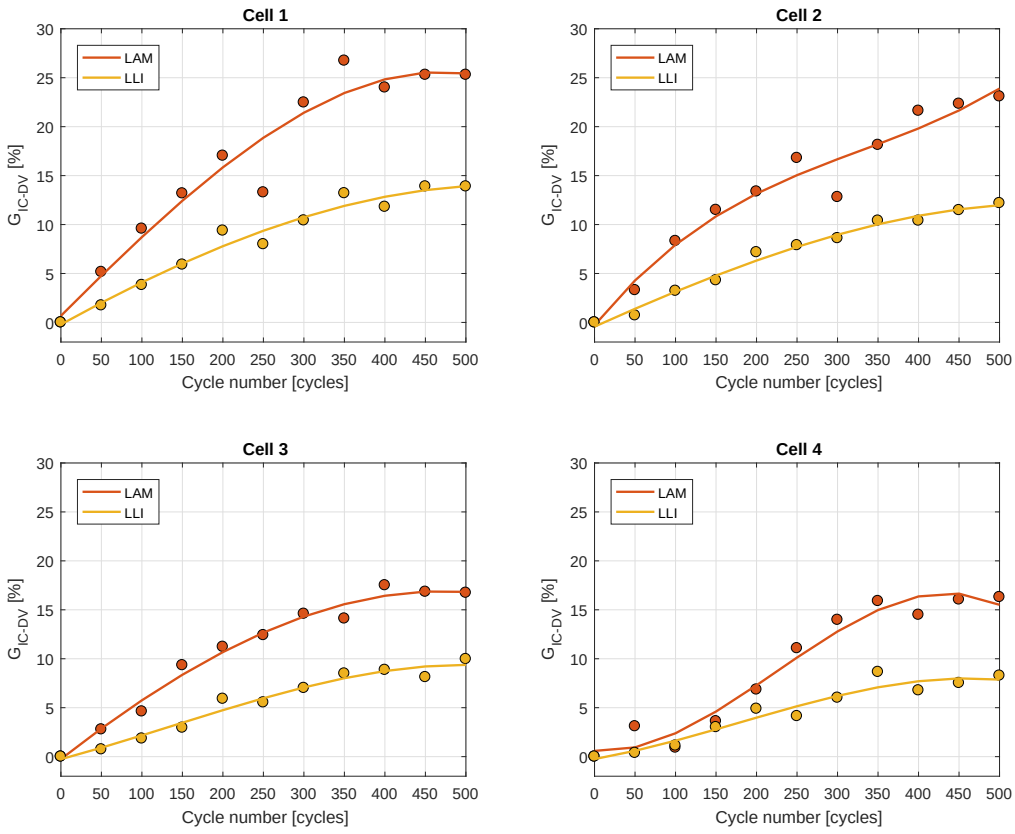

Figure 6.8: G_{IC-DV} for each DM for every cell over cycle number.

6.5.3 Comparison between the results obtained from EIS and IC-DV (Step 4)

EIS and IC-DV techniques highlight that LAM and LLI are more significant than CL. This result agrees with previous studies [37, 158, 183–186] where the related ageing mechanisms of commercial NCA-C cells were analysed for storage and cycling operation. The amplitude of each DM differs significantly between EIS (from 0% to 800%) and IC-DV (from 0% to 30%). To compare the results obtained with EIS and IC-DV each DM metric is first normalised, $G_{n\ EIS}$ and $G_{n\ IC-DV}$, and then correlated to one another. The growth due to CL has not been considered in this comparison because the IC-DV cannot quantify the CL in this case. Similarly as in Section 4.5, the Pearson correlation coefficient is chosen to quantify the degree of correlation between G_{EIS} and G_{IC-DV}. The Pearson correlation coefficients are computed as shown in Equation 6.5 [187].

$$r_{G_{n\ EIS},G_{n\ IC-DV}} = \frac{cov_{G_{n\ EIS},G_{n\ IC-DV}}}{\sigma_{G_{n\ EIS}} \cdot \sigma_{G_{n\ IC-DV}}} \tag{6.5}$$

The Pearson correlation coefficient varies between 0 and ±1, depending on whether the correlation is weak (0) or strong (±1). The paired-sample t-test is then employed to calculate the probability (p-value) that the correlation between $G_{n\ EIS}$ and $G_{n\ IC-DV}$ is significant. The paired t-value as a function of r and the sample size ss is computed using Equation 6.6.

$$t_v = \frac{r \cdot \sqrt{ss-2}}{2 \cdot \sqrt{1-r^2}} \tag{6.6}$$

This equation is the same as the one used for the one-sample t-test [187] but adapted to the paired-sample t-test. The difference between both relies on the number of degrees of freedom, i.e., ss-2 is the number of degrees of freedom for the one-sample t-test and ss-1 is the number of degrees of freedom for the paired-sample t-test.

Before applying the paired t-test, the sample data must fulfill the following requirements [187]:

- The dependent variable must be measured on a continuous scale. $G_{n\ EIS}$ and $G_{n\ IC-DV}$ are continuous measurements because they can take any value within a range between 0 and 1.
- The sample data is normally distributed. This check is performed employing the chi-square goodness of fit test, using the *chi2gof* command within MATLAB [108]. The result of this test was that the sample data $G_{n\ EIS}$ and $G_{n\ IC-DV}$ follow a normal distribution for each cell and SoC.
- The observations need to be dependent. Since the observations quantify the effect of the DMs, they are dependent.
- There should be no significant outliers. Box plots were generated for each dataset showing the absence of outliers. This check is performed using the *boxplot* command in MATLAB [108]. Figure 6.9 illustrates an example of the box plots for the case when the data of all the cells is considered. The rest of the cases were not plotted within this thesis.

As these requirements are fulfilled, the paired-sample t-test is applied to each data-set. For every cell, two DMs are defined, and for each DM there are three different data-sets since EIS includes measurements at low, mid and high SoCs. For each SoC the same $G_{n\ IC-DV}$ is considered. The Pearson correlation coefficient values and the p-values of the paired t-test are computed using *corrcoef* and *ttest* commands in MATLAB, respectively [108]. Table 6.3 shows the p-values for each cell, SoC and DM. In addition, the p-values were also computed for the case that the data of all cells is considered. For all the cases evaluated the p-value is lower than 0.05, and so $G_{n\ EIS}$ and $G_{n\ IC-DV}$ are significantly correlated. Neglecting the degradation effect due to CL which is not identifiable with the IC-DV technique, this result highlights that EIS and IC-DV identify and quantifies the same DMs at a similar level.

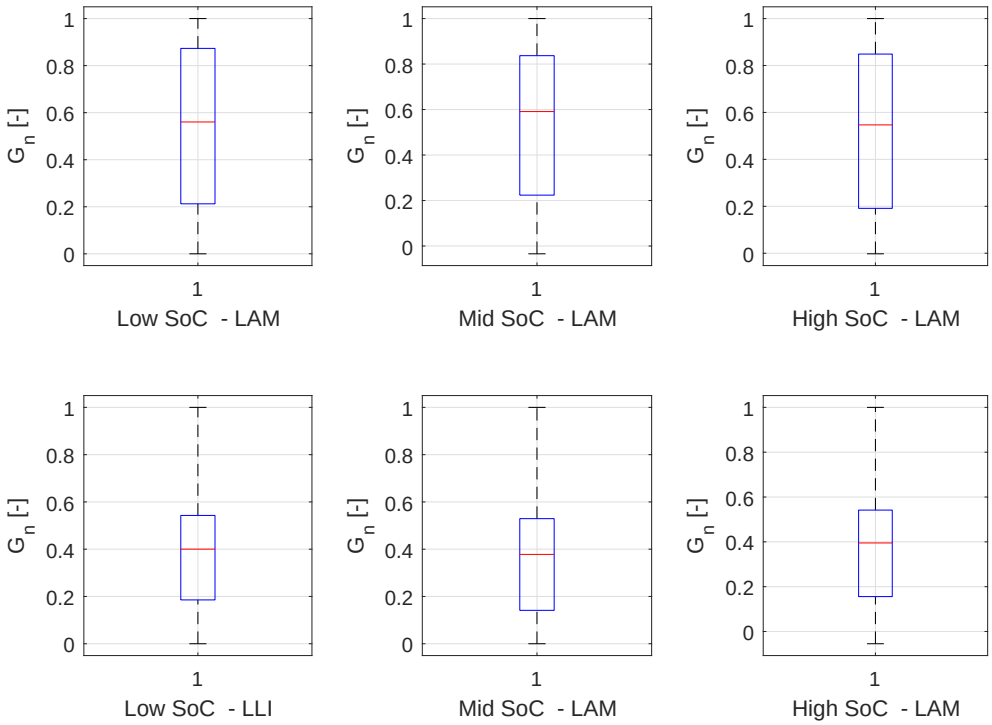

Figure 6.9: Box plots of G_n for the case when the data of all the cells is considered.

Table 6.3: p-values for each cell, SoC and DM derived from the t-test.

Cell	LLI			LAM		
	Low SoC	Mid SoC	High SoC	Low SoC	Mid SoC	High SoC
1	0.0030	0.0334	0.0034	0.0029	$4.7559 \cdot 10^{-4}$	0.0027
2	0.0011	0.0060	0.0013	0.0082	0.0064	0.0024
3	0.0014	0.0011	0.0083	0.0026	0.0015	$8.4366 \cdot 10^{-4}$
4	$6.7165 \cdot 10^{-4}$	0.0123	0.0053	0.0148	0.0236	0.0123
All	$3.9748 \cdot 10^{-13}$	$1.7939 \cdot 10^{-11}$	$4.8669 \cdot 10^{-12}$	$7.1977 \cdot 10^{-12}$	$1.1047 \cdot 10^{-11}$	$2.0279 \cdot 10^{-10}$

6.5.4 SoC dependency

Figure 6.10 shows the effect of LLI and LAM over cycle number is more significant for low SoC than for mid and high SoC. These results are generated using the EIS approach as the IC-DV methodology does not quantify the DMs with respect to the SoC.

This result means that charge-transfer and Warburg resistances increase more for low SoC than for mid and high SoC through ageing. This result is corroborated by Huang

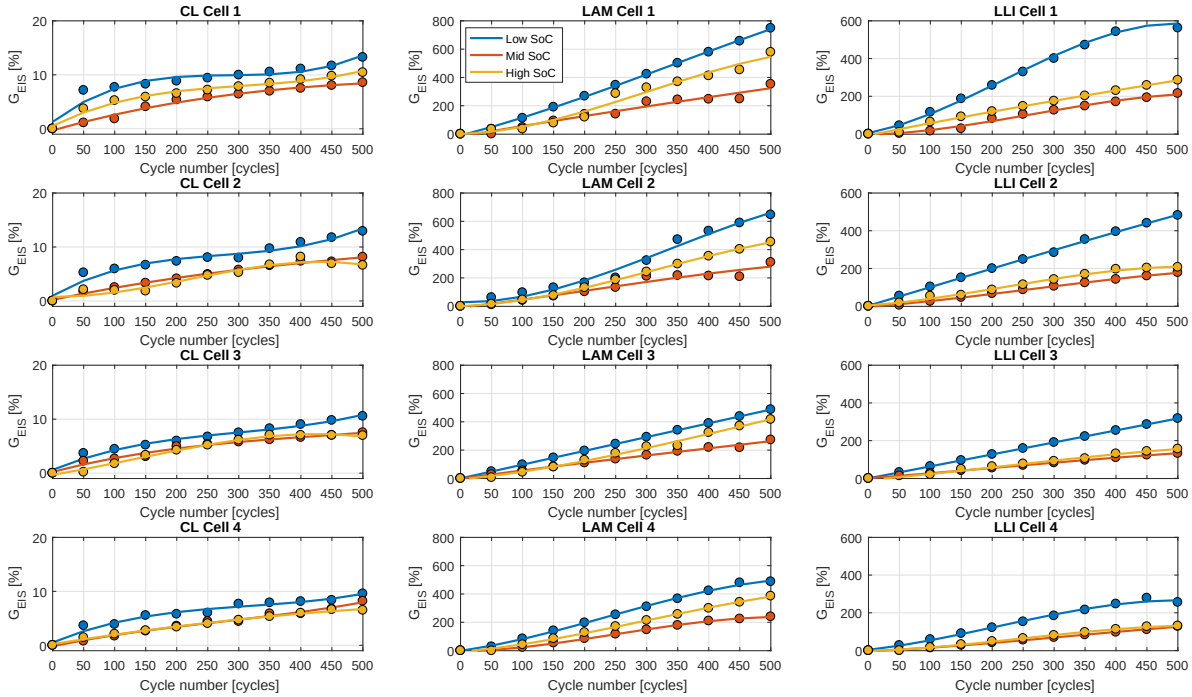

Figure 6.10: Dependency of G_{EIS} with respect to SoC for each cell over cycle number.

et al. [188] for the case of NMC chemistry when the cells are new. Pietsch et al. [189] observed that lithiation kinetics within graphite electrodes are limited by ionic diffusion and conductivity rather than by electric conductivity. In addition, Huang et al. [188] suggest that the increase of the Warburg resistance can be explained based on the diffusion coefficient and the concentration of the reactants for both positive and negative electrodes. Thus, the variation of the ionic diffusion and conductivity would need to be measured through ageing concerning the level of lithiation (SoC) for the positive and negative electrodes. Such a measurement may highlight the reasons for the larger increase in charge-transfer and diffusion resistances at low SoC. Measurement of these parameters is beyond of the scope of this study.

6.5.5 Evaluation of DMs with respect to cell-to-cell dependency

From Chapter 4 it is concluded that for an initial 40% SoH difference between the least aged and the most aged cell, the SoH tend to converge at the end of the test within 10% for SoH_E and 30% for SoH_P. This result suggests that there is a cell-to-cell interaction when the cells are connected in parallel which results in the SoH of the individual cells to converge.

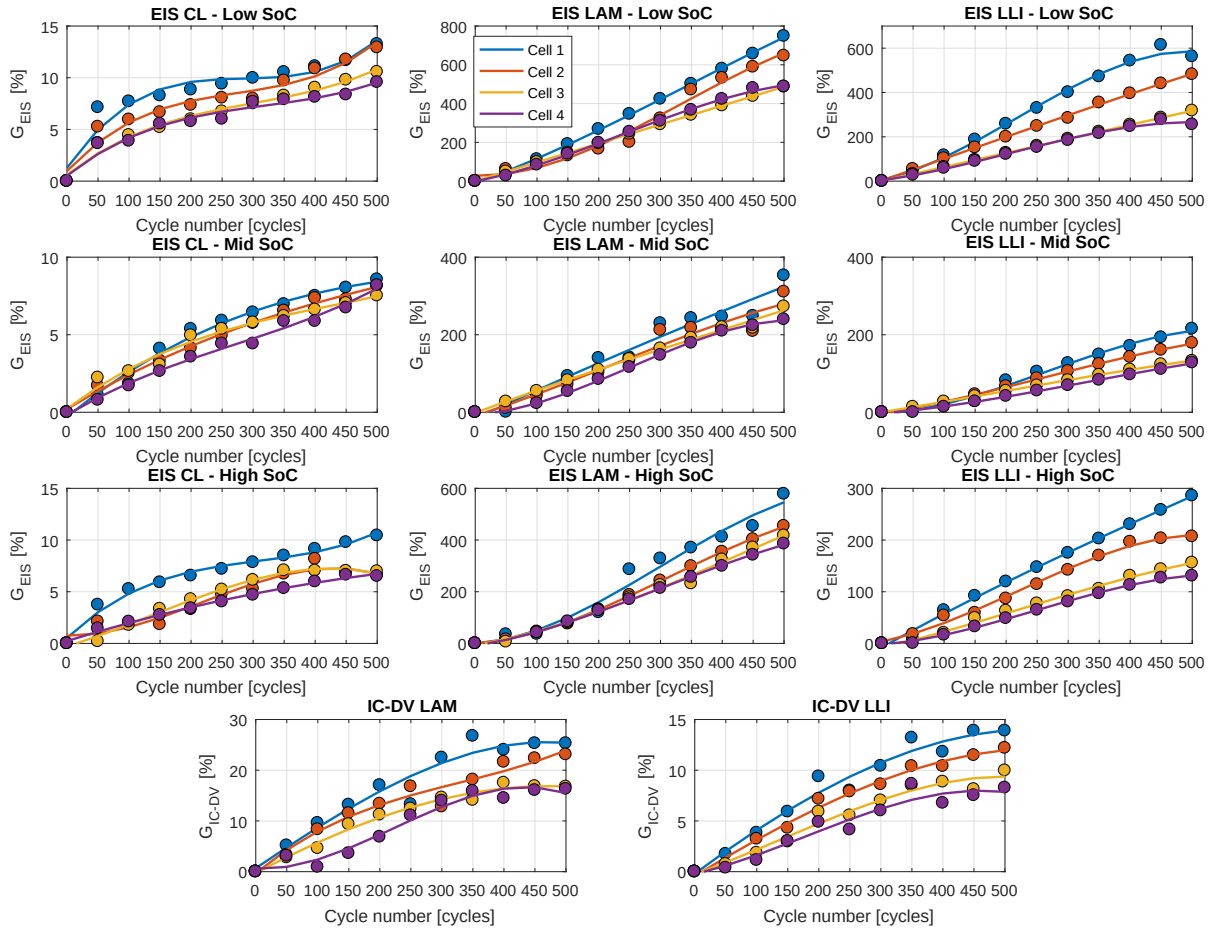

Figure 6.11: Cell-to-cell dependency of the DMs over cycle number.

For the same data set, Figure 6.11 shows the effects of the DMs obtained with EIS and IC-DV follow a relationship with respect to the initial level of ageing of each cell. As expected, the growth of the effects of each DM is more pertinent for the less aged cells

than for the more aged cells. The cells that initially have aged less degrade faster than the cells that initially have aged more. The reasons behind this result are explained in detail in Chapter 4.

6.6 Implications for future battery pack designs

The requirements to implement EIS and IC-DV in real-world applications are different. EIS measurements are performed using low amplitude voltage or current signals to avoid exciting the non-linear impedance characteristics of the cell and to maintain a constant SoC. However, these low amplitude signals can be easily perturbed by noise and so the corresponding impedance measurement may not be accurate. Thus, achieving an appropriate signal to noise ratio is a challenge [155]. Another aspect to consider is the requirement for a time invariance. Achieving time invariance involves exciting the battery with a low amplitude signal so that the SoC is kept constant along the measurement [155].
The EIS spectrum typically covers a frequency range from 0.1mHz to 400kHz as Figure 4.1 (c) illustrates. This broad frequency range is prohibitive for the capability of a low-cost BMS microcontroller as they typically support from 100MHz to 100Hz [128]. This means that a low-cost BMS is not capable to consider the dynamics at lower frequencies than 100Hz. Li-ion dynamic processes pertinent at frequencies lower than 100Hz are for instance diffusion processes. According to Equation 6.1, diffusion processes are related to morphological changes in the structure of the electrodes and hence, LAM is pertinent during diffusion. Therefore, the EIS spectra measured with a low-cost BMS is not capable to infer degradation modes characteristic at frequencies lower than 100Hz such as LAM. To overcome this, some authors [155, 156] have proposed a low-cost impedance measurement system using the current signal of the DC converter to excite the battery across a wide range of frequencies.

As explained in Section 3.6.3, the implementation of the IC-DV technique in real-world

scenarios require to discharge or charge the cells at a C-rate lower than C/10. Such a test can be performed during charging the vehicle overnight. Alternatively, the driver can set the departure time allowing at least 10 hours of charging [190] or the vehicle can be checked in a service station.

Apart from measuring the EIS or pOCV data, the fitting procedure applied in EIS, and filtering and differentiation techniques used to smooth the IC-DV curves do not require excessive computational demand and memory [68, 191]. Therefore, both techniques could be implemented in a low-cost microcontroller without incurring a significant penalty of requiring additional hardware resources.

The decision of which technique to implement within a BMS depends on a number of factors. Table 6.4 summarises the advantages and disadvantages of each technique so that it is possible to asses quickly which technique would be better for a particular case. Computationally, IC-DV is more straightforward to perform than EIS. This is because IC-DV filtering and differentiation procedure is less computationally intensive than the EIS fitting procedure. However, the full-cell charge or discharge required to acquire the data for the IC-DV curves takes at least 10h. The application of the IC-DV requires first to charge or discharge the cells from the current state to 0% or to 100% SoC and then, charge or discharge the battery following the IC-DV test procedure. Similarly, the application of the EIS involves a pre-condition testing. Prior applying the EIS test the cells need to be relaxed. According to Barai et al. [127], it is recommended to allow a relaxation time of 4h. Once the pre-conditioned test is completed, the EIS test lasts for a maximum of 25 min. This means that in overall, performing the IC-DV requires more time than the EIS. In addition, EIS enables quantification of the effects of the DMs at a particular SoC while IC-DV curves are determined along the whole SoC window. In line with this, EIS seems to provide a better resolution of the DMs than the IC-DV curves. For instance, in this case, EIS enables the identification of the effect of CL while IC-DV

not. However, applying EIS at battery pack level involves challenges in terms of noise propagation. For instance, the EIS spectra measured at pack level is disturbed significantly due to the effect of the interconnection resistances between each cell and module. Therefore, the EIS approach is only suitable to be applied in individual cells. In view of performing the EIS test in a real battery pack, the battery pack would need to be designed with instrumented cells so that the EIS test can be applied at cell level. In conclusion, it is recommended to analyse for each specific case which technique is more beneficial to use. It is noteworthy that each technique considers a different degradation parameter, capacity and resistance, and thus, each technique may also infer different DMs.

Table 6.4: Advantages and disadvantages of EIS and IC-DV.

Technique	Advantages	Disadvantages
EIS	(a) Quick test duration (25 min/cell). without considering relaxation time. (b) Possible for on-board implementation subject to signal to noise ratio and time invariance. (c) Enable measurements at particular frequencies and SoC.	(a) Accuracy dependent on different sources: measurements and model. (b) Not universal, ECM dependent.
IC-DV	(a) Accuracy dependent mostly on the C-rate used. (b) Possible for on-board implementation subject to charge/discharge C-rate. (c) Simple calculation. (d) Universal, model independent.	(a) Long test duration (10 h/cell). (b) Does not enable measurements at particular frequencies and SoC. (c) The equilibrium conditions at which the IC-DV are generated makes difficult to infer CL.

6.7 Limitations and further work

Although the results of this study are valid for the experimental conditions described in Section 4.3, the authors postulate that the underlying framework, tools and reasoning presented is transferable to other cell technologies and testing conditions. However, the applicability of the EIS and IC-DV should be investigated over a broader range of conditions, cell chemistries, formats and manufacturers. Such investigations will confirm the relationship between extrinsic factors, DMs and ageing mechanisms summarised in

Table 5.1.

Grouping the ageing mechanisms into DMs can be misleading. For example, Figure 6.4 shows that the predominant contribution to power fade occurs due to increase in R_{ct} and R_W. This result is consistent with the theory of battery degradation shown in Table 5.1. However, CL, LLI and LAM can lead to power fade, and, unless R_o, R_{SEI}, R_{ct} and R_W are quantified, it is difficult to decipher from which DM the power fade is due to. In summary, categorising DMs as suggested in [64,67,68,131] and corroborated in this study is limited and in some cases can be misleading. To quantify such inaccuracy and validate the results obtained alternative in-situ diagnostic techniques such as DTV [162, 163] and ex-situ post-mortem analysis such as Scanning Electron Microscopy, Energy Dispersive Spectrometry or X-Ray Diffractometry [69] should be applied. In line with this, simplifying the diagnostic methods from half-cell to full-cell measurements involve inaccuracies since the DMs are not the same in each electrode. Further work includes quantifying these inaccuracies so that the DMs can be quantified more precisely.

In addition, the growth of DMs changes with respect to the SoC through ageing. The measurement of the ionic conductivity and diffusion in the positive and negative electrodes may explain the variation of the growth of DMs with respect to SoC through ageing and thus, further work is required with this respect.

This work suggests the potential implementation of EIS and IC-DV techniques off-board in a commercial BMS. However, a more detailed study is required with this respect. The accuracy and robustness of these methods in such environments need to be further evaluated.

6.8 Conclusions

This study proposes a non-invasive method to identify and quantify the effects of DMs in Li-ion batteries using EIS and IC-DV diagnostic techniques. Applying this method, LLI and LAM are identified to be the most pertinent DMs for the case study described in Chapter 4. The results obtained via each technique are significantly correlated at a confidence interval of 95%, suggesting that both techniques are suitable for identification and quantification of the effects of the DMs. However, each of these techniques has its strengths and limitations for potential implementation in a commercial BMS. It is then worth investigating both simultaneously. Additionally, each method uses a different parameter, capacity or resistance, to quantify ageing and can, therefore, be used to infer different DMs.

The change in the effect of the DMs was also studied with respect to SoC and the different amount of degradation of each cell. The growth of LAM and LLI is larger at low SoCs than at mid and high SoCs. The effect of the DMs changes as a function of the initial degradation of each cell connected in parallel, i.e., the growth of the DMs is larger for the less aged cells than for the more aged cells.

7. Reflective Review

This Chapter is a reflective review of the research undertaken. The presented research has resulted in four innovations as shown in Table 7.1. For each innovation, the contribution to academia and the impact to the sponsoring company is described. In addition, opportunities for further work of this research are outlined in Section 7.5.

7.1 Innovation 1: Development of a systematic procedure to quantify CtCV in LIB packs

7.1.1 Contribution to academia

Employing experiments or simulations and further statistical analysis, the studies reviewed in Section 2.2.1 quantify the impact of CtCV in battery packs due to differences in temperature, SoC, resistance, capacity and coulombic efficiency. However, none of these studies [42–46] suggest a systematic methodology to evaluate the amount and the cause of CtCV. To overcome this, Study 1 proposes a novel systematic procedure to quantify the amount and the origin of CtCV in battery packs. The proposed diagnostic procedure is highly flexible because this procedure has been tested in 49S1P, 1S49P, 7(1)S7P, 7S7P pack topologies, LMO, NCA, and LFP cell chemistries, and normalised and skewed input data distribution. Articles regarding the description of the battery pack model [29] and the proposed approach to quantify CtCV [30] were publisehd in the Journal of Energy Storage. It is believed that academics would benefit from this publication to underpin a

Table 7.1: Summary of innovations.

Innovation number	Innovation	Contribution to academia	Impact to industry	Chapter in IR
1	Development of a systematic procedure to quantify CtCV in LIB packs.	Published in [29, 30].	1. Capability to quantify CtCV in battery packs. 2. Ability to detect and minimise in-market warranty faults. 3. Establish contingency plan for battery pack failure. 4. Knowledge and skills in assessment of balancing strategies.	3
2	Quantification of cell-to-cell SoH for an imbalance scenario representative of 100,000 miles / 10 years BEV service.	Published in [21].	1. Access to experimental measurements regarding cell-to-cell SoH imbalance. 2. Capability to design a calibration strategy to estimate the SoH under imbalance scenarios.	4
3	Evaluation of a time efficient methodology to monitor SoH at battery module/pack level composed of cells of different ageing states.	Published in [21].	Knowledge to reduce the time to measure capacity.	4
4	Derivation of a non-invasive approach to quantify DMs.	Published in [22–24, 28].	Capability to 1. improve lifetime control strategies based on on-board and off-board diagnostics and, 2. support the development of future battery designs.	6

better understanding of CtCV in Li-ion battery packs.

7.1.2 Impact to the sponsoring company

Finding a strategy to meet the end of the warranty period of battery packs with the minimum cost represents a key research activity of Jaguar Land Rover. End of the warranty period for Jaguar Land Rover is eight years [54]. If during this end of warranty period the battery pack fails, Jaguar Land Rover will need to cover the related cost to repair the battery. A common practice to repair battery failures is to replace the failed cell/module with a new cell/module [192]. As the existent and replaced cells/modules has not exactly the same characteristics, this countermeasure may result in an inhomogeneous operation of the pack [35]. Study 1 evaluates the case where CtCV are pertinent due to variation of SoC_i, SoH_i and Q_{ri}. Study 1 proposes a methodology to quantify CtCV for different pack topologies, cell chemistries and input data distributions. This methodology provides to Jaguar Land Rover the capability to study the effect of CtCV on the overall battery performance. Also, taking into consideration the severity of the failure, materials and labour costs, simulations using the Hanalike model could recommend a contingency plan, e.g., evaluate the necessity of replacing a module or a pack. In essence, the impact of this study and the overall outcome of this EngD into Jaguar Land Rover and the broader automotive industry is to reduce over-engineering efforts in the design of Li-ion batteries, by e.g.:

- Reducing recall costs and warranty claims.
- Reducing the size of the battery pack as the battery will degrade or fail less likely.
- Adopting broader cell tolerances.
- Reducing the repairment costs of battery packs.

The benefits of this thesis align with the current strategy of Jaguar Land Rover, which has recently announced that every Jaguar and Land Rover launched from 2020 will be electrified [193]. Considering that the average price of a battery pack is as high as £10,000 [12], and the average number of vehicles sold by Jaguar Land Rover in 2017 was 614,309 [194], the financial value of the benefits provided by this research to the sponsoring company can be as follows:

Reducing recall costs and warranty claims

Following on from personal communications with the sponsoring company [195], Jaguar Land Rover estimates that this study will reduce at least 10% the likelihood of a severe battery pack failure which requires the full replacement of the battery pack. Jaguar Land Rover estimates the battery failure rate is 1%. Therefore, the financial value provided by this research with this respect can be up to:

$$\begin{aligned} &10\% \text{ (likelihood of a severe battery pack failure)} \cdot 1\% \text{ (failure rate)} \cdot \\ &\quad £10,000 \text{ (battery pack cost)} \cdot 614,309 \text{ (average number of cars)} = £6,143,090 \end{aligned} \tag{7.1}$$

This saving can be effective as soon as Jaguar Land Rover can bring the outcomes of this research into the production line of their vehicles.

Reducing the size of the battery pack

According to personal communications with the sponsoring company [195], Jaguar Land Rover estimates that this study will reduce at least 2.5% the size of a battery pack. Therefore, the financial value provided by this research with this respect can be up to:

$$\begin{aligned} &2.5\% \text{ (reduction of battery pack size)} \cdot £10,000 \text{ (battery pack cost)} \cdot \\ &\quad 614,309 \text{ (average number of cars)} = £153,577,250 \end{aligned} \tag{7.2}$$

This saving can be effective as soon as Jaguar Land Rover can bring the outcomes of this research into the design phase of their vehicles.

Adopting broader cell tolerances

Based on personal communications with the sponsoring company [195], Jaguar Land Rover estimates that this study will reduce at least to 2% the cost of the battery pack by adopting broader cell tolerances. Therefore, the financial value provided by this research with this respect can be up to:

$$2\% \text{ (reduction of battery pack cost)} \cdot £10,000 \text{ (battery pack cost)} \cdot 614,309 \text{ (average number of cars)} = £122,861,800 \tag{7.3}$$

This saving can be effective as soon as Jaguar Land Rover can bring the outcomes of this research into the design phase of their vehicles.

Reducing the repairment costs of battery packs

Following on from personal communications with the sponsoring company [195], Jaguar Land Rover estimates that this study will reduce at least 1% the repairment costs of battery packs due to non-severe battery pack failures. In addition, Jaguar Land Rover estimates that 20% of the average number of cars will require a repair of the battery pack within the warranty period [195]. Therefore, the financial value provided by this research with this respect can be up to:

$$1\% \text{ (reduction of battery pack cost)} \cdot £10,000 \text{ (battery pack cost)} \cdot 20\% \text{ (number of cars to be repaired)} \cdot 614,309 \text{ (average number of cars)} = £12,286,180 \tag{7.4}$$

This saving can be effective as soon as Jaguar Land Rover can bring the outcomes of this research into the production line of their vehicles.

IC and DV cell-to-pack curves are calculated in Section 3.6.2. These curves relate to the changes of the IC-DV curves at battery pack level with changes of the IC-DV curves at the cell level. These curves can be used to quantify changes in pack voltage signature upon ageing, e.g., analysis of degradation modes, evaluate balancing strategies and screening cell-to-cell differences throughout a pack. This new visualisation tool, as opposed to an expensive and time-consuming experimental approach, can be used by Jaguar Land Rover as a virtual analysis to identify cell failures within a battery module or pack.

7.2 Innovation 2: Quantification of cell-to-cell SoH for an imbalance scenario representative of 100,000 miles / 10 years of BEV service

7.2.1 Contribution to academia

When cells are connected in parallel, the BMS approximates the SoH as that of a single equivalent value for the whole battery stack. Previous studies [35,41,48,52,53] showed that this approximation is not true when CtCV exist due to differences in cell-to-cell current, SoC, and temperature. However, none of these studies shows the quantification of SoH over time in such an imbalance scenario. In line with this, the contribution of Study 2 is to quantify experimentally cell-to-cell SoH until battery's EoL for a scenario when each initial cell SoH is different. This experiment is representative of 100,000 miles / 10 years BEV service as Appendix A.2.3 explains. The results of this study were published in [21] in Journal of Power Sources.

7.2.2 Impact to the sponsoring company

According to the results obtained in Study 2, a balance scenario is considered when the cell-to-cell SoH does not diverge more than 4% in terms of capacity. This threshold is true for the experimental conditions described in Study 2. If this is not the case, the BMS will track an incorrect value of SoH until the convergence is reached. This result is relevant to Jaguar Land Rover as their experimental measurements concerning cell-to-cell SoH imbalance were limited. Since the BMS does not have access to individual parallel cell currents [35, 196], the implementation of a balancing system to track the correct SoH would be economically infeasible for an automotive OEM such as Jaguar Land Rover as explained in Section 2.2.2. To solve this problem, the total SoH could be calibrated according to the level of imbalance. A possibility to design this calibration would be to create a look-up table using the experimental data gathered in Study 2. This 2-D look-up table would relate the initial SoH imbalance, assuming that this is measurable, with the true value of the SoH at any ageing state. This look-up table would need to use a method of interpolation, e.g., linear or exponential, to calculate the SoH value between two experimental measurements. The results obtained in this work provide to Jaguar Land Rover the knowledge and capability to design such a calibration strategy. This calibration strategy would need to consider also the total number of cells within the battery pack. As the number of cells in parallel grows, the complexity of such calibration may also increase.

7.3 Innovation 3: Evaluation of a time efficient methodology to monitor SoH at battery module/pack level composed of cells of different ageing states

7.3.1 Contribution to academia

Previous studies [58, 61, 62] have found a linear relationship between the measurement of capacity fade and the resistance increase due to cell ageing. Takeno et al. [61] and Dong et al. [62] proved this correlation for individual cells, and Schuster et al. [58] showed it for cells disassembled from a BEV battery pack in a specific state of ageing. None of these studies demonstrates this correlation at a module/pack level at different ageing states, which is a possible scenario in real-world vehicle applications. To address this knowledge, this research proves experimentally that this correlation is still valid at different ageing states for the situation when cells connected in parallel are imbalanced due to different SoH. The data to evaluate this correlation is the same as in Innovation 2. As four cells are connected in parallel, this test emulates a 1S4P battery module/pack. The results of this study were published in [21] in Journal of Power Sources.

7.3.2 Impact to the sponsoring company

The knowledge in terms of the linear correlation between resistance and capacity measurements proposed in Study 2 is highly beneficial for Jaguar Land Rover. The main advantage of this correlation is to reduce the time in the measurement of the capacity or resistance because just one of them needs to be measured. The recommendation would be to measure DC or polarisation resistance rather than capacity using, e.g., the pulse power test because performing the pulse power is in the order of minutes whereas measuring the capacity using 1C constant charge-discharge lasts for an hour. It is noteworthy that commercial BMSs have the capability to perform any of these tests as they are standardised

in the automotive industry [55].

7.4 Innovation 4: Derivation of a non-invasive approach to quantify DMs

7.4.1 Contribution to academia

Thermodynamic based [67, 68, 161] and kinetic based [154] diagnostic techniques are employed to identify and/or quantify DMs non-invasively. Before applying any of these techniques in isolation, it is required to evaluate their benefits and drawbacks. The state-of-the-art literature has not reviewed these techniques as a whole, and therefore, it is challenging to select the most appropriate diagnostic method for a particular case. Study 3 contributes with this respect by reviewing the different non-invasive diagnostic techniques systematically to quantify DMs. To ensure the impact of this review into Jaguar Land Rover, the studies are evaluated according to the requirements characteristic of automotive applications, and previously agreed with the sponsoring company. This review has been published in the Renewable and Sustainable Energy Reviews journal [28]. It is believed that academics would benefit from this systematic review to select the most appropriate diagnostic method for a particular scenario.

From the literature review conducted in Study 3, it is seen that the most common diagnostic techniques require half-cell voltage measurements to identify or quantify the DMs. According to Section 2.3.2, half-cell voltage in LIBs is challenging to measure in real-world scenarios. With the knowledge acquired from Study 3, a contribution of this research is to formulate an automated methodology to quantify the DMs based on full-cell measurements. For this, IC-DV and EIS were employed as non-invasive diagnostic techniques. Unlike post-mortem analyses, non-invasive diagnostic techniques provide the potential to be applied in real-world applications. The EIS case was published in the IEEE Trans-

portation Electrification Conference and Expo (ITEC) [22] and the IC-DV case in the IET Hybrid and Electrical Vehicles Conference [23]. Also, the results obtained with EIS and IC-DV were compared highlighting that both techniques provide similar results. This comparison was published in Journal of Power Sources [24]. This study concludes that EIS and IC-DV techniques are suitable to quantify the DMs and are complementary since each of them uses a different ageing indicator, resistance for EIS and voltage and capacity for IC-DV.

7.4.2 Impact to the sponsoring company

Following on from the USABC standard [55] and previous studies [15, 50], the definition of SoH used by the majority of the automotive OEMs is shown in Equation 2.1 and Equation 2.2. This definition is a single scalar and does not indicate the root causes that lead to battery degradation. As described in Section 1.1, quantifying the DMs in real-world scenarios is key to understand the reasons of battery degradation. Extending the SoH definition to this level of understanding is extremely beneficial for Jaguar Land Rover because of the following reasons:

1. Future cell materials, topology, design and manufacturing processes can be appropriately selected in such a way that DMs are less pertinent. For instance, an intercalation gradient strain in the active material leads to volume change within the electrode, i.e., mechanical fracture of the electrodes [65]. A battery design improvement would be to use robust polymeric binders such as alginate binder so that volume expansion, equivalent to LAM, can be reduced during cycling [66]. Quantifying the amount of DMs in Li-ion batteries provides Jaguar Land Rover with the capability to outsource with more confidence cell technologies when they engage with cell suppliers. This knowledge and experience make Jaguar Land Rover a more "intelligent-buyer".

2. Lifetime control strategies within BMSs can be designed by taking into consideration the knowledge of the most pertinent DMs for particular operating scenarios. For instance, if it is seen that LAM is accelerated at temperatures larger than 35℃ and C-rates higher than 2C, then the BMS control strategy could limit temperature and C-rate to lower values under normal operation so that the amount of LAM can be reduced over time. This reduction in temperature and C-rate should not limit the level of performance that the customer is expected and hence, a compromise between battery lifetime and vehicle performance needs to be met by the vehicle control unit [197, 198]. Apart from temperature and C-rate, other parameters that the BMS could control are the SoC and the ΔDoD [197, 198].

7.5 Opportunities for further work

Table 7.2 summarises the scope and further work of each innovation regarding:

- **Research level:** this includes proof of concept, proof of concept at different conditions, validation and implementation. The meaning of proof of concept, validation and implementation is defined in Section 1.4.
- **Level of application:** cell, module and pack.

Table 7.2 shows the studies undertaken in this doctorate were focused on proof of concept rather than validation and implementation. This research was focused on proof of concept because this was the most convenient direction taking into account the available resources. For instance, validating proof of concept in the field of battery ageing requires long-term measurements at least in the order of months [21]. Despite there are few research areas not covered in this doctorate, this work is taken forward in current and future R&D activities by the sponsoring company as Table 7.3 illustrates [195]. Opportunities for further work for each innovation are discussed in greater detail in the following subsections.

Table 7.2: Summary of innovations and areas for further investigation.

Application level	Proof of concept	Proof of concept at different conditions	Validation	Implementation in BMS
Innovation 1: Development of a systematic procedure to quantify CtCV in LIB packs.				
Cell	✓*	✓*	✗	✗
Module	✓*	✓*	✗	✗
Pack	✓*	✓*	✗	✗
Innovation 2: Quantification of the cell-to-cell SoH for an imbalance scenario representative of 100,000 miles/10 years BEV service.				
Cell	✓**	✗	✗	✗
Module	✓**	✗	✗	✗
Pack	✗	✗	✗	✗
Innovation 3: Evaluation of a time efficient methodology to monitor SoH at battery module/pack level composed of cells of different ageing states.				
Cell	✓**	✗	✗	✗
Module	✓**	✗	✗	✗
Pack	✗	✗	✗	✗
Innovation 4: Derivation of a non-invasive approach to quantify DMs.				
Cell	✓**	✗	✗	✗
Module	✗	✗	✗	✗
Pack	✗	✗	✗	✗

* Simulation based.
** Experimental based.

Legend - Background colour
Green: work undertaken in this doctorate.
Orange: further work.

7.5.1 Proof of Concept

Innovation 1 covers proof of concept at different operating conditions for cell, module and pack. Innovation 2 and 3 tackle proof of concept at cell and module level, and Innovation 4 covers proof of concept at cell level.

Proving the concept of Innovation 2 and 3 at pack level would require a more complicated test environment to emulate battery pack conditions, e.g., control of heat dissipation or higher number of voltage/temperature readings. Battery pack measurements can be further employed to validate the Hanalike model (Innovation 1). More details regarding this are explained in Section 7.5.2. The flexibility of the Hanalike model would enable to quantify DMs based on IC-DV curves (Innovation 4) at module and pack level using the

Table 7.3: Summary of innovations and areas for further investigation including Jaguar Land Rover current and future R&D activities [195].

Application level	Proof of concept	Proof of concept at different conditions	Validation	Implementation in BMS
Innovation 1: Development of a systematic procedure to quantify CtCV in LIB packs.				
Cell	✓*	✓*	JLR R&D	JLR R&D
Module	✓*	✓*	JLR R&D	JLR R&D
Pack	✓*	✓*	JLR R&D	JLR R&D
Innovation 2: Quantification of the cell-to-cell SoH for an imbalance scenario representative of 100,000 miles/10 years BEV service.				
Cell	✓**	JLR R&D	JLR R&D	JLR R&D
Module	✓**	JLR R&D	JLR R&D	JLR R&D
Pack	JLR R&D	JLR R&D	JLR R&D	JLR R&D
Innovation 3: Evaluation of a time efficient methodology to monitor SoH at battery module/pack level composed of cells of different ageing states.				
Cell	✓**	JLR R&D	JLR R&D	JLR R&D
Module	✓**	JLR R&D	JLR R&D	JLR R&D
Pack	JLR R&D	JLR R&D	JLR R&D	JLR R&D
Innovation 4: Derivation of a non-invasive approach to quantify DMs.				
Cell	✓**	JLR R&D	JLR R&D	JLR R&D
Module	JLR R&D	JLR R&D	JLR R&D	JLR R&D
Pack	JLR R&D	JLR R&D	JLR R&D	JLR R&D

* Simulation based.
** Experimental based.

Legend - Background colour
Green: work undertaken in this doctorate.
Blue: Current JLR R&D activity.
Red: Future JLR R&D activity.

Hanalike model. According to Chapter 3, the Hanalike model is capable of discharging a battery pack slowly, e.g., C/25, so that IC-DV curves can be calculated. The Hanalike model could be then used to simulate cycling scenarios including periodic characterisation tests to determine the IC and DV curves at different ageing states.

7.5.2 Validation

Validation represents a common area of further work for each study undertaken in this thesis. The experimental data gathered as part of Innovation 2 and 3 can be employed to:

1. Validate the Hanalike model at cell and module level.

2. Validate the systematic procedure to quantify CtCV. This experimental data would validate the scenario when SoH_i causes CtCV. To validate other scenarios, e.g., CtCV due to SoC_i, the corresponding experimental data would need to be collected.

As Innovation 2 and 3 involve the analysis of experimental data, validation of these innovations consists of repeating the same test at different operating conditions, e.g., ambient temperature, C-rate, module/pack topology or cell chemistry.
Validation of Innovation 4 at cell level requires to conduct post-mortem analysis such as Scanning Electron Microscopy, Energy Dispersive Spectrometry or X-Ray Diffractometry. Post-mortem analysis will outline the most pertinent DMs, and these can be compared with the DMs estimated using non-invasive diagnostic techniques. Post-mortem analyses are conducted at a cell level because it is the minimum removable component in a battery module/pack. As the Hanalike model can quantify the DMs at module and pack level, the way to validate Innovation 4 would be against the results provided by the Hanalike model. However, the Hanalike model at module and pack level needs also to be validated against real experimental data as indicated previously.

7.5.3 BMS implementation

The potential implementation of the methods into a BMS is a common area of further work for each study undertaken in this thesis. An introduction of the requirements to implement battery health diagnostic techniques in off-board and on-board BMS applications is given in Section 5.5. According to this, the computation requirements of the Hanalike model described in Section 3.7 (Innovation 1) may be a limitation in terms of hardware and software to implement it into a commercially viable BMS. Aside from the calculations of the Hanalike model, the systematic procedure to quantify CtCV is not computationally intensive and hence, this diagnostic method should be feasible to implement in a BMS. However, according to Figure 3.25, this diagnostic method requires the battery pack to be

discharged at C/25, which means that the battery would discharge over 25h. This test is excessively long for a potential implementation and thus, the feasibility of this procedure should be tested using higher C-rates, e.g., C/10. As explained in Section 6.6, 10h of charging is a reasonable amount of time if a vehicle is parked overnight, the driver set the departure time allowing at least 10 hours of charging [190], or the vehicle is checked in a service station. In practice, this test can be scheduled as ageing processes are slow and so the effects of the DMs do not need to be quantified regularly [118]. An alternative solution to avoid a 10h charge or discharge would be to adapt this approach so that a full battery charge or discharge is not needed. Such procedure could be done by screening FOIs as mentioned in Section 3.7. The problem of determining IC-DV curves is common to Innovation 4 and hence, similar countermeasures as the ones mentioned such as increasing the C-rate or screening FOIs, need to be considered. In addition, Innovation 4 employs EIS diagnostic technique to quantify DMs. As explained in Section 6.7, the BMS implementation involves challenges in terms of signal to noise ratio, time invariance and frequency range. It is then recommended to implement EIS and IC-DV off-board because, from a hardware viewpoint, would be easier and more cost-effective than to implement them on-board.

Innovation 3 involves the measurement of the ohmic or charge-transfer resistance. If EIS is the selected method to measure the ohmic or charge-transfer resistance, the mentioned challenges in terms of signal to noise ratio, time invariance and frequency range would be pertinent to implement this approach into a BMS. A possibility to overcome this would be to measure the resistance using the pulse power test. The pulse power test is a procedure commonly used in the automotive industry to measure the ohmic resistance of LIBs [58]. In comparison to EIS, pulse power is quicker (order of seconds) and is not limited by stringent hardware requirements [58]. This comparison does not consider the time required to pre-condition both EIS and pulse power tests, which is in the order of hours. As the pulse power test is a standardised procedure in commercial BMSs, the approach

proposed in Innovation 3 should be straightforward to implement using, e.g., a look-up table to estimate the capacity based on the measurement of the resistance.

Lastly, the concept behind SoH convergence (Innovation 2) is already considered in BMSs because the BMS typically approximates the SoH as that of single equivalent value for when cells are connected in parallel. Further work would include designing a calibration strategy to estimate a correct SoH value in imbalance scenarios.

8. Conclusions

This research programme started with the objective of deriving the most appropriate definition of battery SoH and to define how, within the context of a BMS, SoH diagnosis may be meaningfully employed to improve the performance of future BEV and HEV. After reviewing the corresponding literature and understanding the challenges faced by the sponsoring company, battery health diagnosis is studied in this thesis concerning two research areas.

1. **Cell-to-cell Variabilities (CtCV) and implications for SoH.**
2. **Improvement of SoH definition.**

The first research area focuses on evaluating CtCV in LIB packs in Study 1, and their implications for the monitoring of the SoH in Study 2. According to experimental data, simulations and further statistical studies, previous investigations [42–46] quantify the impact of CtCV in battery packs due to differences in SoC, resistance, coulombic efficiency, capacity and temperature. However, none of these publications [42–46] outline a systematic procedure to quantify the amount and the cause of CtCV within battery packs. To overcome this, Study 1 proposes a systematic modeling methodology to evaluate the amount and the origin of CtCV in battery packs. This procedure extracts FOIs from IC curves to quantify the amount and the source of CtCV. The results revealed that some FOIs could be used to quantify CtCV due to SoC_i and SoH_i. This outcome proves this procedure is not universal as there are testing scenarios where no suitable FOI is found to quantify CtCV. The impact of CtCV into battery pack performance was evaluated

and the results highlight that CtCV up to (+/-)10% can reduce the capacity to 15%. This result indicates that CtCV contribute significantly to reduce battery lifetime. In addition, Study 1 proposes a new calculation of IC curves to relate changes in the pack at cell level. This new visualisation tool is useful because it enables to identify differences between cells throughout a pack. The impact of this research provides new knowledge and capabilities to Jaguar Land Rover regarding quantification of CtCV, detection of battery faults, warranty contingency plan and assessment of balancing strategies.

For the particular case when cells are connected in parallel, the BMS commonly approximates the SoH as that of a single equivalent value for the whole battery stack. Previous studies [35, 41, 48, 52, 53] showed that this approximation might not be true for the cases when CtCV exist due to differences in cell-to-cell current, SoC, and temperature. However, none of these studies shows the quantification of SoH over time in such imbalance scenario. To fill this gap, Study 2 quantifies experimentally cell-to-cell SoH until battery's EoL for a scenario when each initial cell SoH is different. This experiment is representative of 100,000 miles / 10 years BEV service as Appendix A.2.3 explains. Following on from previous investigations [58,61,62], this study proves a linear correlation between the measurement of capacity fade and the resistance rise for the test scenario when imbalanced cells are connected in parallel. The main benefit of this correlation is to simplify the calculation of the SoH since only the measurement of the ohmic or the charge-transfer resistance is needed.

The second research area was concentrated on the improvement of the definition of SoH. The definition of SoH does not indicate the underpinning ageing mechanisms causing the degradation. Study 3 critically reviewed different non-invasive diagnostic techniques used to quantify DMs. To ensure the impact of this review to Jaguar Land Rover, the studies are reviewed according to the requirements that these techniques need to fulfil as part of real-world automotive applications. This review highlights that pOCV and IC-

DV diagnostic techniques are more advantageous than EIS, DTV and Comb. techniques because they fulfil a more significant number of predefined requirements. However, EIS, DTV and Comb. techniques employ different ageing indicators, such as impedance or temperature, that motivates their development in the future. The results of this review also revealed that none of the evaluated techniques was tested in a vehicle in real-world conditions and thus, their hardware implementation need to be further studied. Following on from this review, Study 4 proposes an automated methodology to quantify the DMs based on full-cell measurements. For this, IC-DV and EIS were employed as non-invasive diagnostic techniques. Unlike post-mortem analyses, non-invasive diagnostic techniques provide the advantage to be applied in real-world applications. Applying this approach using the data gathered in Study 2, it is seen that LLI and LAM are the most pertinent DMs. In addition, the results obtained with IC-DV and EIS were compared to evaluate the differences between using one technique or the other. The results revealed that the obtained DMs with each technique are significantly correlated at a confidence interval of 95%. This outcome suggests that IC-DV and EIS techniques are suitable for identification and quantification of DMs. It is seen that each technique has its advantages and disadvantages and choosing one or the other will depend on each specific scenario. For Jaguar Land Rover, this approach can be used to improve the current definition of SoH, quantifying the root causes that lead to battery degradation. This improved definition of SoH provides the capability to Jaguar Land Rover of 1. improving lifetime control strategies based on on-board and off-board diagnostics and, 2. supporting the development of future battery designs.

In summary, the research presented in this thesis provides new knowledge, experimental data, and simulation models that allow manufacturers and researchers to comprehend battery degradation within on-board and off-board vehicle applications better. It gives a transferable procedure to quantify CtCV in LIB packs. It offers extensive ageing data for a common imbalance scenario in LIBs. It formulates a methodology to quantify ageing

root causes in the context of BMSs. This thesis further proves the significant contribution of these findings to the academia, sponsoring organisation and the broader automotive industry.

List of References

[1] Automotive Council UK, Industrial Strategy Automotive Sector Deal (2018), https://www.automotivecouncil.co.uk/wp-content/uploads/sites/13/2018/01/180110-BEIS-Automotive-Sector-Deal-FINAL.pdf, accessed April 20, 2018.

[2] European Parliament, Regulation EC 443/2009 Emission performance standards for new passenger cars as part of the Community's integrated approach to reduce CO2 emissions from light-duty vehicles. (2013), https://eur-lex.europa.eu/legal-content/EN/TXT/?uri=celex%3A32009R0443, accessed June 15, 2018.

[3] Jaguar Land Rover, Sustainability Report 2015/16 (2017), https://www.jaguarlandrover.com/2016/environmental-innovation, accessed June 25, 2018.

[4] H. Popp, J. Attia, F. Delcorso, A. Trifonova, Lifetime analysis of four different lithium ion batteries for (plug–in) electric vehicle, Transport Research Arena (TRA) 5th Conference: Transport Solutions from Research to Deployment, (2014), https://trid.trb.org/view/1327725.

[5] Union of Concerned Scientists, Electric Vehicle Battery: Materials, Cost, Lifespan (2018), https://www.ucsusa.org/clean-vehicles/electric-vehicles/electric-cars-battery-life-materials-cost, accessed May 12, 2018.

[6] A. Farmann, W. Waag, A. Marongiu, D. U. Sauer, Critical review of on-board capacity estimation techniques for lithium-ion batteries in electric and hybrid electric vehicles, Journal of Power Sources 281 (2015) 114–130. doi:10.1016/j.jpowsour.2015.01.129.

[7] M. Kane, Jaguar I-Pace – Everything We Know – Videos, Specs & Images Galore (2018), https://insideevs.com/jaguar-i-pace-everything-we-know/, accessed June 16, 2018.

[8] M.-T. Von Srbik, Advanced Lithium-ion Battery Modelling for Automotive Applications, PhD thesis, Imperial College London (2015), https://spiral.imperial.ac.uk/bitstream/10044/1/51498/1/von-Srbik-MT-2015-PhD-Thesis.pdf, accessed May 10, 2018.

[9] D. Myall, D. Ivanov, W. Larason, M. Nixon, H. Moller, Accelerated Reported Battery Capacity Loss in 30 kWh Variants of the Nissan Leaf, Preprint (March). doi:10.20944/PREPRINTS201803.0122.V1.

[10] E. Loveday, Inside EVs - Nissan Issues Statement On LEAF 30-kWh Battery Degradation (2018), https://insideevs.com/nissan-issues-statement-on-leaf-30-kwh-battery-degradation/, accessed June 22, 2018.

[11] E. Yurday, NimbleFins - A Study on Real-Life Nissan Leaf Battery Deterioration (2018), https://www.nimblefins.co.uk/nissan-leaf-battery-capacity-range, accessed June 22, 2018.

[12] L. Somerville, Post-mortem analysis of lithium-ion cells after accelerated lifetime testing, Engd (int.) thesis, The University of Warwick (2016).
URL http://wrap.warwick.ac.uk/95224/1/WRAP_Theses_Somerville_2017.pdf

[13] C. Hendricks, N. Williard, S. Mathew, M. Pecht, A failure modes, mechanisms, and effects analysis (FMMEA) of lithium-ion batteries, Journal of Power Sources 297 (2015) 113–120. doi:10.1016/j.jpowsour.2015.07.100.

[14] Reuters, A list of Tesla car fires since 2013 (2018), https://www.autoblog.com/2018/05/11/a-list-of-tesla-car-fires-since-2013/?guccounter=2, accessed June 25, 2018.

[15] D. Andre, C. Appel, T. Soczka-Guth, D. U. Sauer, Advanced mathematical methods of SOC and SOH estimation for lithium-ion batteries, Journal of Power Sources 224 (0) (2013) 20–27. doi:10.1016/j.jpowsour.2012.10.001.

[16] R. Burguess, UK car manufacturing drops 3% as industry faces "greatest challenge". (2018) Accessed: 5th March 2018, https://www.autocar.co.uk/car-news/industry/uk-car-manufacturing-drops-3-industry-faces-%E2%80%9Cgreatest-challenge%E2%80%9D, accessed March 5, 2018.

[17] Westover Group, Jaguar Land Rover is Britain's biggest car manufacturer for a second year (2017), http://www.westovergroup.co.uk/landrover/news/britains-biggest-car-manufacturer-for-a-second-year/, accessed March 5, 2018.

[18] S. Ewing, Land Rover debuts Range Rover Hybrid, not bound for US (2013), https://www.autoblog.com/2013/09/11/land-rover-range-rover-hybrid-frankfurt-2013/?guccounter=1{#}slide-997444, accessed July 3, 2018.

[19] J. Mcllroy, New 2018 Jaguar I-Pace: specs, prices, pics and video (2018), http://www.autoexpress.co.uk/jaguar/i-pace/97706/new-2018-jaguar-i-pace-specs-prices-pics-and-video, accessed July 3, 2018.

[20] P. Haney, Personal communication, Jaguar Land Rover R&D Manager (2018).

[21] C. Pastor-Fernández, T. Bruen, W. D. Widanage, M. A. Gama-Valdez, J. Marco, A Study of Cell-to-Cell Interactions and Degradation in Parallel Strings: Implications for the Battery Management System, Journal of Power Sources 329 (2016) 574–585. doi:10.1016/j.jpowsour.2016.07.121.

[22] C. Pastor-Fernández, W. D. Widanage, J. Marco, M. Gama-Valdez, G. H. Chouchelamane, Identification and quantification of ageing mechanisms in lithium-ion batteries using the eis technique, in: 2016 IEEE Transportation Electrification Conference and Expo (ITEC), 2016, pp. 1–6. doi:10.1109/ITEC.2016.7520198.

[23] C. Pastor-Fernández, W. D. Widanage, G. H. Chouchelamane, J. Marco, A SoH diagnosis and prognosis method to identify and quantify degradation modes in Li-ion batteries using the IC/DV technique, 6th Hybrid and Electric Vehicles Conference (HEVC 2016), London, pp. 1-6. (2016). doi:10.1049/cp.2016.0966.

[24] C. Pastor-Fernández, G. H. Chouchelamane, W. Widanage, J. Marco, A Comparison between Electrochemical Impedance Spectroscopy and Incremental Capacity-Differential Voltage as Li-ion Diagnostic Techniques to Identify and Quantify the Effects of Degradation Modes within Battery Management Systems, Journal of Power Sources 360 (2017) 301–318. doi:10.1016/j.jpowsour.2017.03.042.

[25] Techopedia Inc., Proof of Concept, https://www.techopedia.com/definition/4066/proof-of-concept-poc, accessed June 23, 2018.

[26] Global Harmonization Task Force, Quality Management Systems - Process Validation Guidance (GHTF/SG3/N99-10:2004 (2004), http://www.imdrf.org/docs/ghtf/final/sg3/technical-docs/ghtf-sg3-n99-10-2004-qms-process-guidance-04010.pdf, accessed June 26, 2018.

[27] Warwick Manufacturing Group, EngD student handbook (2016).

[28] C. Pastor-Fernández, T. F. Yu, W. D. Widanage, J. Marco, Critical review of non-invasive diagnosis techniques for quantification of degradation modes in lithium-ion batteries, Renewable and Sustainable Energy Reviews 109 (2019) 138 – 159. doi:https://doi.org/10.1016/j.rser.2019.03.060.

[29] M. Dubarry, G. Baure, C. Pastor-Fernández, T. F. Yu, W. D. Widanage, J. Marco, Battery energy storage system modeling: A combined comprehensive approach, Journal of Energy Storage 21 (2019) 172 – 185. doi:https://doi.org/10.1016/j.est.2018.11.012.

[30] M. Dubarry, C. Pastor-Fernández, G. Baure, T. F. Yu, W. D. Widanage, J. Marco, Battery energy storage system modeling: Investigation of intrinsic cell-to-cell variations, Journal of Energy Storage 23 (2019) 19 – 28. doi:https://doi.org/10.1016/j.est.2019.02.016.

[31] C. Pastor-Fernández, M. Gama-Valdez, W. D. Widanalage, J. Marco, A Study of Cell-to-Cell Interactions and Degradation in Parallel Strings: Implications for the Battery Management System, EngD Submission 1, WMG, University of Warwick (2015).

[32] C. Pastor-Fernández, G. H. Chouchelamane, W. D. Widanage, J. Marco, A Comparison between Electrochemical Impedance Spectroscopy and Incremental Capacity -Differential Voltage as Li-ion Diagnostic Techniques to Identify and Quantify the Effects of Degradation Modes within Battery Management Systems, EngD Submission 2, WMG, University of Warwick (2017).

[33] C. Pastor-Fernández, W. D. Widanage, J. Marco, G. H. Chouchelamane, Critical Review of On-Board Diagnosis Techniques for Quantification of Degradation Modes in Vehicle Lithium-ion Batteries, EngD Submission 3, WMG, University of Warwick (2017).

[34] C. Pastor-Fernández, M. Dubarry, P. Haney, W. D. Widanage, J. Marco, An Approach to Diagnose Cell-to-Cell Variations in Lithium-ion Battery Packs through Incremental Capacity Analysis, EngD Submission 4, WMG, University of Warwick (2018).

[35] T. Bruen, J. Marco, Modelling and experimental evaluation of parallel connected lithium ion cells for an electric vehicle battery system, Journal of Power Sources 310 (2016) 91–101. doi:10.1016/j.jpowsour.2016.01.001.

[36] K. Rumpf, M. Naumann, A. Jossen, Experimental investigation of parametric cell-to-cell variation and correlation based on 1100 commercial lithium-ion cells, Journal of Energy Storage 14 (2017) 224–243. doi:10.1016/j.est.2017.09.010.

[37] J. W. Braithwaite, A. Gonzales, G. Nagasubramanian, S. J. Lucero, D. E. Peebles, J. A. Ohlhausen, W. R. Cieslak, Corrosion of LithiumIon Battery Current Collectors, Journal of The Electrochemical Society 146 (2) (1999) 448–456. doi:10.1149/1.1391627.

[38] J. Vetter, P. Novák, M. R. Wagner, C. Veit, K. C. Möller, J. O. Besenhard, M. Winter, M. Wohlfahrt-Mehrens, C. Vogler, A. Hammouche, Ageing mechanisms in lithium-ion batteries, Journal of Power Sources 147 (1–2) (2005) 269–281. doi:10.1016/j.jpowsour.2005.01.006.

[39] D. Worwood, Q. Kellner, M. Wojtala, W. D. Widanage, R. MGlen, D. Greenwood, J. Marco, A new approach to the internal thermal management of cylindrical battery cells for automotive applications, Journal of Power Sources 346 (2017) 151–166. doi:10.1016/j.jpowsour.2017.02.023.

[40] B. Kenney, K. Darcovich, D. D. MacNeil, I. J. Davidson, Modelling the impact of variations in electrode manufacturing on lithium-ion battery modules, Journal of Power Sources 213 (2012) 391–401. doi:10.1016/j.jpowsour.2012.03.065.

[41] R. Gogoana, M. B. Pinson, M. Z. Bazant, S. E. Sarma, Internal resistance matching for parallel-connected lithium-ion cells and impacts on battery pack cycle life, Journal of Power Sources 252 (2014) 8–13. doi:10.1016/j.jpowsour.2013.11.101.

[42] Y. Jiang, J. Jiang, C. Zhang, W. Zhang, Y. Gao, Q. Guo, Recognition of battery aging variations for LiFePO4batteries in 2nd use applications combining incremental capacity analysis and statistical approaches, Journal of Power Sources 360 (2017) 180–188. doi:10.1016/j.jpowsour.2017.06.007.

[43] S. Miyatake, Y. Susuki, T. Hikihara, S. Itoh, K. Tanaka, Discharge characteristics of multicell lithium-ion battery with non uniform cells, Journal of Power Sources 241 (2013) 736–743. doi:10.1016/j.jpowsour.2013.05.179.

[44] S. Paul, C. Diegelmann, H. Kabza, W. Tillmetz, Analysis of ageing inhomogeneities in lithium-ion battery systems, Journal of Power Sources 239 (2013) 642–650. doi:10.1016/j.jpowsour.2013.01.068.

[45] C. Zhang, Y. Jiang, J. Jiang, G. Cheng, W. Diao, W. Zhang, Study on battery pack consistency evolutions and equilibrium diagnosis for serial- connected lithium-ion batteries, Applied Energydoi:10.1016/j.apenergy.2017.05.176.

[46] L. Zhou, Y. Zheng, M. Ouyang, L. Lu, A Simulation Study on Parameter Variation Effects in Battery Packs for Electric Vehicles, Energy Procedia 105 (2017) 4470–4475. doi:10.1016/j.egypro.2017.03.949.

[47] C. J. Rydh, B. A. Sandén, Energy analysis of batteries in photovoltaic systems. Part I: Performance and energy requirements, Energy Conversion and Management 46 (11) (2005) 1957–1979. doi:10.1016/j.enconman.2004.10.003.

[48] X. Gong, R. Xiong, C. Mi, Study of the Characteristics of Battery Packs in Electric Vehicles with Parallel-Connected Lithium-Ion Battery Cells, IEEE Transactions on Industry Applications, vol. 51, no. 2, pp. 1872-1879, (2014). doi:10.1109/TIA.2014.2345951.

[49] K. Bullis, Sensors Could Make Electric-Car Batteries Smaller and Cheaper (2013), https://www.technologyreview.com/s/518791/sensors-could-make-electric-car-batteries-smaller-and-cheaper/, accessed March 28, 2018.

[50] A. Nuhic, T. Terzimehic, T. Soczka-Guth, M. Buchholz, K. Dietmayer, Health diagnosis and remaining useful life prognostics of lithium-ion batteries using data-driven methods, Journal of Power Sources 239 (0) (2013) 680–688. doi:10.1016/j.jpowsour.2012.11.146.

[51] T. Bruen, J. Marco, M. Gama, Current Variation in Parallelized Energy Storage Systems, 2014 IEEE Vehicle Power and Propulsion Conference (VPPC), Coimbra, pp. 1-6 (2014). doi:10.1109/VPPC.2014.7007040.

[52] N. Yang, X. Zhang, B. Shang, G. Li, Unbalanced discharging and aging due to temperature differences among the cells in a lithium-ion battery pack with parallel combination, Journal of Power Sources 306 (2016) 733–741. doi:10.1016/j.jpowsour.2015.12.079.

[53] W. Shi, X. Hu, C. Jin, J. Jiang, Y. Zhang, T. Yip, Effects of imbalanced currents on large-format LiFePO4/graphite batteries systems connected in parallel, Journal of Power Sources 313 (2016) 198–204. doi:10.1016/j.jpowsour.2016.02.087.

[54] Jaguar Land Rover Automotive PLC, FAQ's Does the battery has a warranty? (2018), https://www.jaguar.co.uk/jaguar-range/i-pace/electric-vehicles/faqs.html, accessed June 16, 2018.

[55] U.S. Department of Energy Vehicle Technologies Program (USABC), Battery Test Manual For Electric Vehicles - Revision 3 (2015), https://inldigitallibrary.inl.gov/sites/sti/sti/6492291.pdf, accessed August 14, 2016.

[56] T. Smith, Testing and Characterisation of Lithium Ion Cells for capacity and power capability, internal CATAPULT Report, CAT_C_004A, Tech. rep. (2013).

[57] K. Uddin, M. Dubarry, M. B. Glick, The viability of vehicle-to-grid operations from a battery technology and policy perspective, Energy Policy 113 (October 2017) (2018) 342–347. doi:10.1016/j.enpol.2017.11.015.

[58] S. F. Schuster, M. J. Brand, C. Campestrini, M. Gleissenberger, A. Jossen, Correlation between capacity and impedance of lithium-ion cells during calendar and cycle life, Journal of Power Sources 305 (2016) 191–199. doi:10.1016/j.jpowsour.2015.11.096.

[59] W. Waag, S. Käbitz, D. U. Sauer, Experimental investigation of the lithium-ion battery impedance characteristic at various conditions and aging states and its influence on the application, Applied Energy 102 (2013) 885–897. doi:10.1016/j.apenergy.2012.09.030.

[60] A. Barai, G. H. Chouchelamane, Y. Guo, A. McGordon, P. Jennings, A study on the impact of lithium-ion cell relaxation on electrochemical impedance spectroscopy, Journal of Power Sources 280 (2015) 74–80. doi:10.1016/j.jpowsour.2015.01.097.

[61] K. Takeno, Quick testing of batteries in lithium-ion battery packs with impedance-measuring technology, Journal of Power Sources 128 (1) (2004) 67–75. doi:10.1016/j.jpowsour.2003.09.045.

[62] H. Dong, X. Jin, Y. Lou, C. Wang, Lithium-ion battery state of health monitoring and remaining useful life prediction based on support vector regression-particle filter, Journal of Power Sources 271 (0) (2014) 114–123. doi:10.1016/j.jpowsour.2014.07.176.

[63] M. Dubarry, M. Berecibar, A. Devie, D. Anseán, N. Omar, I. Villarreal, State of health battery estimator enabling degradation diagnosis: Model and algorithm description, Journal of Power Sources 360 (2017) 59–69. doi:10.1016/j.jpowsour.2017.05.121.

[64] C. R. Birkl, M. R. Roberts, E. Mcturk, P. G. Bruce, D. A. Howey, Degradation Diagnostics for Lithium Ion Cells, Journal of Power Sources 341 (2016) 1–35. doi:10.1016/j.jpowsour.2016.12.011.

[65] K. Uddin, S. Perera, W. Widanage, L. Somerville, J. Marco, Characterising Lithium-Ion Battery Degradation through the Identification and Tracking of Electrochemical Battery Model Parameters, Batteries 2 (2) (2016) 13. doi:10.3390/batteries2020013.

[66] Y. Zhang, C.-Y. Wang, Cycle-Life Characterization of Automotive Lithium-Ion Batteries with LiNiO2 Cathode, Journal of The Electrochemical Society 156 (7) (2009) A527–A535. doi:10.1149/1.3126385.

[67] M. Dubarry, C. Truchot, B. Y. Liaw, Synthesize battery degradation modes via a diagnostic and prognostic model, Journal of Power Sources 219 (2012) 204–216. doi:10.1016/j.jpowsour.2012.07.016.

[68] A. Marongiu, N. Nlandi, Y. Rong, D. U. Sauer, On-board capacity estimation of lithium iron phosphate batteries by means of half-cell curves, Journal of Power Sources 324 (2016) 158–169. doi:10.1016/j.jpowsour.2016.05.041.

[69] E. Sarasketa-Zabala, F. Aguesse, I. Villarreal, L. M. Rodriguez-Martinez, C. M. López, P. Kubiak, Understanding Lithium Inventory Loss and Sudden Performance Fade in Cylindrical Cells during Cycling with Deep-Discharge Steps, The Journal of Physical Chemistry C 119 (2) (2015) 896–906. doi:10.1021/jp510071d.

[70] H. Bergveld, Battery Management Systems Design by Modelling, PhD thesis, Twente University (2001), http://doc.utwente.nl/41435/1/thesis{_}bergveld.pdf, accessed April 14, 2015.

[71] W. Waag, C. Fleischer, D. U. Sauer, Critical review of the methods for monitoring of lithium-ion batteries in electric and hybrid vehicles, Journal of Power Sources 258 (0) (2014) 321–339. doi:10.1016/j.jpowsour.2014.02.064.

[72] S. M. Rezvanizaniani, Z. Liu, Y. Chen, J. Lee, Review and recent advances in battery health monitoring and prognostics technologies for electric vehicle (ev) safety and mobility, Journal of Power Sources 256 (2014) 110 – 124. doi:10.1016/j.jpowsour.2014.01.085.

[73] M. Berecibar, I. Gandiaga, I. Villarreal, N. Omar, J. Van Mierlo, P. Van den Bossche, Critical review of state of health estimation methods of Li-ion batteries for real applications, Renewable and Sustainable Energy Reviews 56 (2016) 572–587. doi:10.1016/j.rser.2015.11.042.

[74] L. Ungurean, G. Cârstoiu, M. V. Micea, V. Groza, Battery state of health estimation: a structured review of models, methods and commercial devices, International Journal of Energy Research 31 (August 2007) (2016) 135–147. arXiv:arXiv:1011.1669v3, doi:10.1002/er.3598.

[75] J. Zhang, J. Lee, A review on prognostics and health monitoring of Li-ion battery, Journal of Power Sources 196 (15) (2011) 6007–6014. doi:10.1016/j.jpowsour.2011.03.101.

[76] M. Krupa, Methods of Technical Prognosis - Review, International Scientific Journal (2013), http://mech-ing.com/journal/Archive/2013/2/45_Krupa.MTM12.pdf.

[77] N. Karami, H. El-Sheikh, N. Moubayed, Evaluation study of different useful life estimation techniques of lithium-ion battery, 2016 Third International Conference on Electrical, Electronics, Computer Engineering and their Applications (EECEA), Beirut, pp. 77-82 (2016) 77–82doi:10.1109/EECEA.2016.7470769.

[78] L. Wu, X. Fu, Y. Guan, Review of the Remaining Useful Life Prognostics of Vehicle Lithium-Ion Batteries Using Data-Driven Methodologies, Applied Sciences 6 (6) (2016) 166. doi:10.3390/app6060166.

[79] E. McTurk, C. R. Birkl, M. R. Roberts, D. A. Howey, P. G. Bruce, Minimally Invasive Insertion of Reference Electrodes into Commercial Lithium-Ion Pouch Cells, ECS Electrochemistry Letters 4 (12) (2015) A145–A147. doi:10.1149/2.0081512eel.

[80] M. Berecibar, N. Omar, M. Garmendia, M. Dubarry, I. Villarreal, P. V. den Bossche, J. V. Mierlo, Soh estimation and prediction for nmc cells based on degradation mechanism detection, in: 2015 IEEE Vehicle Power and Propulsion Conference (VPPC), 2015, pp. 1–6. doi:10.1109/VPPC.2015.7353020.

[81] E. Sarasketa-Zabala, E. Martinez-Laserna, M. Berecibar, I. Gandiaga, L. M. Rodriguez-Martinez, I. Villarreal, Realistic lifetime prediction approach for Li-ion batteries, Applied Energy 162 (2016) 839–852. doi:10.1016/j.apenergy.2015.10.115.

[82] P. Aurora, N. Ramaswamy, T. Han, K. Adjemian, Electrochemical Impedance Spectroscopic Analysis of Lithium-Ion Battery Aging Mechanisms, Meeting Abstracts MA2013-01 (2013), http://ma.ecsdl.org/content/MA2013-01/4/254.abstract.

[83] S. Schindler, M. A. Danzer, A novel mechanistic modeling framework for analysis of electrode balancing and degradation modes in commercial lithium-ion cells, Journal of Power Sources 343 (2017) 226–236. doi:10.1016/j.jpowsour.2017.01.026.

[84] M. Doyle, J. Newman, A. S. Gozdz, C. N. Schmutz, J. Tarascon, Comparison of Modeling Predictions with Experimental Data from Plastic Lithium Ion Cells, Journal of The Electrochemical Society 143 (6) (1996) 1890–1903. doi:10.1149/1.1836921.

[85] I. J. Ong, J. Newman, Double Layer Capacitance in a Dual Lithium Ion Insertion Cell, Journal of The Electrochemical Society 146 (12) (1999) 4360–4365. doi:10.1149/1.1392643.

[86] J. Christensen, J. Newman, Effect of Anode Film Resistance on the Charge/Discharge Capacity of a Lithium-Ion Battery, Journal of The Electrochemical Society 150 (11) (2003) A1416–A1420. doi:10.1149/1.1612501.

[87] C. Zhang, K. Li, S. Mcloone, Z. Yang, Battery modelling methods for electric vehicles - A review, in: 2014 European Control Conference (ECC), 2014, pp. 2673–2678. doi:10.1109/ECC.2014.6862541.

[88] L. Tao, J. Ma, Y. Cheng, A. Noktehdan, J. Chong, C. Lu, A review of stochastic battery models and health management, Renewable and Sustainable Energy Reviews 80 (2017) 716–732. doi:10.1016/j.rser.2017.05.127.

[89] G. Fan, K. Pan, G. L. Storti, M. Canova, J. Marcicki, X. G. Yang, A Reduced-Order Multi-Scale, Multi-Dimensional Model for Performance Prediction of Large-Format Li-Ion Cells, Journal of The Electrochemical Society 164 (2) (2017) A252–A264. doi:10.1149/2.0791702jes.

[90] C. Zhang, Y. Jiang, J. Jiang, G. Cheng, W. Diao, W. Zhang, Study on battery pack consistency evolutions and equilibrium diagnosis for serial- connected lithium-ion batteries, Applied Energy 207 (2017) 510–519. doi:10.1016/j.apenergy.2017.05.176.

[91] M. Dubarry, B. Y. Liaw, Development of a universal modeling tool for rechargeable lithium batteries, Journal of Power Sources 174 (2) (2007) 856–860. doi:10.1016/j.jpowsour.2007.06.157.

[92] M. Dubarry, N. Vuillaume, B. Y. Liaw, From single cell model to battery pack simulation for Li-ion batteries, Journal of Power Sources 186 (2) (2009) 500–507. doi:10.1016/j.jpowsour.2008.10.051.

[93] M. Dubarry, C. Truchot, A. Devie, B. Y. Liaw, State-of-Charge Determination in Lithium-Ion Battery Packs Based on Two-Point Measurements in Life, Journal of The Electrochemical Society 162 (6) (2015) A877–A884. doi:10.1149/2.0201506jes.

[94] M. Dubarry, A. Devie, B. Y. Liaw, Cell-balancing currents in parallel strings of a battery system, Journal of Power Sources 321 (2016) 36–46. doi:10.1016/j.jpowsour.2016.04.125.

[95] Z. Li, P. Zhang, Z. Wang, Q. Song, Y. Rong, State of Charge Estimation for Li-ion Battery Based on Extended Kalman Filter, Energy Procedia 105 (4) (2017) 3515–3520. doi:10.1016/j.egypro.2017.03.806.

[96] J. Groenewald, ABACUS project blog (2015).
URL https://blogs.warwick.ac.uk/abacus/entry/welcome{_}to{_}the/

[97] Sungrow, SD200-B storage system specifications (2017), https://en.sungrowpower.com/product_view?id=504, accessed November 12, 2017.

[98] ElectroPapa, Li-Ion-battery - 6600mAh (2.5V) black - for laptop notebook replaces BAT-1S3P (2017), https://electropapa.com/, accessed December 1, 2017.

[99] Dell, Specifications Dell Latitude E6220, https://data.technimax.cz/attach/artilky/Dell-Latitude-E6220-parametry.pdf.

[100] Sun Xtender Battery Installation & Battery Bank Configuration. (2017), http://sunxtender.com/battery_banks.php, accessed November 14, 2017.

[101] Second Life Storage, What else can we learn from Tesla battery pack design (2017), https://secondlifestorage.com/t-What-else-can-we-learn-from-Tesla-battery-pack-design, accessed June 15, 2018.

[102] M. Broussely, Battery Requirements for HEVs, PHEVs, and EVs: An Overview. Chapter 13 in Electric and Hybrid Vehicles: Power Sources, Models, Sustainability, Infrastructure and the Market, Elsevier, ISBN: 9780444535665, 2010.

[103] Automotive Council UK, Electrical Energy Storage Roadmap (2018), https://www.apcuk.co.uk/app/uploads/2018/02/EES_Full_Pack.pdf, accessed August 19, 2018.

[104] M. Kassem, J. Bernard, R. Revel, S. Pélissier, F. Duclaud, C. Delacourt, Calendar aging of a graphite/LiFePO4 cell, Journal of Power Sources 208 (2012) 296–305. doi:10.1016/j.jpowsour.2012.02.068.

[105] A. Eddahech, O. Briat, J. M. Vinassa, Performance comparison of four lithium-ion battery technologies under calendar aging, Energy 84 (2015) 542–550. doi:10.1016/j.energy.2015.03.019.

[106] Y. Zheng, M. Ouyang, L. Lu, J. Li, X. Han, L. Xu, H. Ma, T. a. Dollmeyer, V. Freyermuth, Cell state-of-charge inconsistency estimation for LiFePO4 battery pack in hybrid electric vehicles using mean-difference model, Applied Energy 111 (2013) 571–580. doi:10.1016/j.apenergy.2013.05.048.

[107] D. Shin, M. Poncino, E. Macii, N. Chang, A statistical model-based cell-to-cell variability management of Li-ion battery pack, IEEE Transactions on Computer-Aided Design of Integrated Circuits and Systems 34 (2) (2015) 252–265. doi:10.1109/TCAD.2014.2384506.

[108] The Mathworks Inc., Matlab help, https://uk.mathworks.com/help/matlab/.

[109] M. Berecibar, M. Garmendia, I. Gandiaga, J. Crego, I. Villarreal, State of health estimation algorithm of LiFePO4 battery packs based on differential voltage curves for battery management system application, Energy 103 (2016) 784–796. doi:10.1016/j.energy.2016.02.163.

[110] C. Weng, X. Feng, J. Sun, H. Peng, State-of-health monitoring of lithium-ion battery modules and packs via incremental capacity peak tracking, Applied Energy 180 (2016) 360–368. doi:10.1016/j.apenergy.2016.07.126.

[111] X. Han, M. Ouyang, L. Lu, J. Li, Y. Zheng, Z. Li, A comparative study of commercial lithium ion battery cycle life in electrical vehicle: Aging mechanism identification, Journal of Power Sources 251 (2014) 38–54. doi:10.1016/j.jpowsour.2013.11.029.

[112] A. Barai, W. D. Widanage, J. Marco, A. Mcgordon, P. Jennings, A study of the open circuit voltage characterization technique and hysteresis assessment of lithium-ion cells, Journal of Power Sources 295 (2015) 99–107. doi:10.1016/j.jpowsour.2015.06.140.

[113] M. Dubarry, G. Baure, A. Devie, Durability and Reliability of EV Batteries under Electric Utility Grid Operations: Path Dependence of Battery Degradation, Journal of The Electrochemical Society 165 (5) (2018) A773–A783. doi:10.1149/2.0421805jes.

[114] D. Cox, N. Reid, The Theory of the Design of Experiments, Chapman & Hall/CRC Monographs on Statistics & Applied Probability, ISBN: 9781420035834, 2000.

[115] Chroma, Regenerative Battery Pack Test System Model 17020, http://www.chromaate.com/product, accessed February 25, 2018.

[116] M. Ouyang, Z. Chu, L. Lu, J. Li, X. Han, X. Feng, G. Liu, Low temperature aging mechanism identification and lithium deposition in a large format lithium iron phosphate battery for different charge profiles, Journal of Power Sources 286 (2015) 309–320. doi:10.1016/j.jpowsour.2015.03.178.

[117] C. Weng, Y. Cui, J. Sun, H. Peng, On-board state of health monitoring of lithium-ion batteries using incremental capacity analysis with support vector regression, Journal of Power Sources 235 (2013) 36–44. doi:10.1016/j.jpowsour.2013.02.012.

[118] M. Steinbuch, Tesla Model S battery degradation data (2015), https://steinbuch.wordpress.com/2015/01/24/tesla-model-s-battery-degradation-data/, accessed December 8, 2016.

[119] A. Fortier, M. Tsao, D. N. Williard, Y. Xing, G. M. Pecht, Preliminary Study on Integration of Fiber Optic Bragg Grating Sensors in Li-Ion Batteries and In Situ Strain and Temperature Monitoring of Battery Cells, Energies 2017, 10(7), 838 (2017). doi:10.3390/en10070838.

[120] A. Maheshwari, M. A. Dumitrescu, M. Destro, M. Santarelli, A modelling approach to understand charge discharge differences in thermal behaviour in lithium iron phosphate – graphite battery, Electrochimica Acta 243 (2017) 129–141. doi:10.1016/j.electacta.2017.05.049.

[121] M. Farag, H. Sweity, M. Fleckenstein, S. Habibi, Combined electrochemical, heat generation, and thermal model for large prismatic lithium-ion batteries in real-time applications, Journal of Power Sources 360 (2017) 618–633. doi:10.1016/j.jpowsour.2017.06.031.

[122] P. Cicconi, D. Landi, M. Germani, Thermal analysis and simulation of a Li-ion battery pack for a lightweight commercial EV, Applied Energy 192 (2017) 159–177. doi:10.1016/j.apenergy.2017.02.008.

[123] I. Bloom, A. N. Jansen, D. P. Abraham, J. Knuth, S. a. Jones, V. S. Battaglia, G. L. Henriksen, Differential voltage analyses of high-power, lithium-ion cells, Journal of Power Sources 139 (1-2) (2005) 295–303. doi:10.1016/j.jpowsour.2004.07.021.

[124] M. Dubarry, V. Svoboda, R. Hwu, B. Yann Liaw, Incremental Capacity Analysis and Close-to-Equilibrium OCV Measurements to Quantify Capacity Fade in Commercial Rechargeable Lithium Batteries, Electrochemical and Solid-State Letters 9 (10) (2006) A454–A457. doi:10.1149/1.2221767.

[125] Voltaplex, Panasonic BD 18650 Battery, 3180mAh, 10A, 3.6V, Grade A Lithium-ion (NCR18650BD), https://voltaplex.com/panasonic-bd-18650-battery-ncr18650bd, accessed August 20, 2015.

[126] A. Jossen, Fundamentals of battery dynamics, Journal of Power Sources 154 (2) (2006) 530–538. doi:10.1016/j.jpowsour.2005.10.041.

[127] A. Barai, Test procedure: Electrochemical Impedance Spectroscopy Test Procedure for Lithium-ion Cell, Tech. rep., Internal HVM CATAPULT project (2014).

[128] P. Weicker, A systems approach to Lithium-Ion mattery management, Artech House, ISBN: 9781608076598, 2014.

[129] S. Gupta, Measurement Uncertainties. Physical parameters and calibration of instruments, Springer-Verlag, ISBN: 9783642209895, 2012.

[130] A. J. Smith, J. C. Burns, D. Xiong, J. R. Dahn, Interpreting High Precision Coulometry Results on Li-ion Cells, Journal of The Electrochemical Society 158 (10) (2011) A1136–A1142. doi:10.1149/1.3625232.

[131] M. Dubarry, A. Devie, B. Y. Liaw, The Value of Battery Diagnostics and Prognostics, Journal of Energy and Power Sources, 1 (5), 242-249 (2014), https://www.soest.hawaii.edu/HNEI/alawa/images/Resources/2014_JEPS.pdf.

[132] M. Wohlfahrt-Mehrens, C. Vogler, J. Garche, Aging mechanisms of lithium cathode materials, Journal of Power Sources 127 (1-2) (2004) 58–64. doi:10.1016/j.jpowsour.2003.09.034.

[133] V. Agubra, J. Fergus, Lithium ion battery anode aging mechanisms, Materials 6 (4) (2013) 1310–1325. doi:10.3390/ma6041310.

[134] P. Kubiak, K. Edström, M. Morcrette, Review on ageing mechanisms of different Li-ion batteries for automotive applications (2011).
URL https://trimis.ec.europa.eu/sites/default/files/project/documents/20120404_144808_53382_DELIVERABLE_2_1.pdf

[135] D. A. Pierre, Optimization problems, in: Optimization Theory with Applications, Wiley, New York, NY, ISBN: 9780486136950, 1986.

[136] M. Ouyang, X. Feng, X. Han, L. Lu, Z. Li, X. He, A dynamic capacity degradation model and its applications considering varying load for a large format Li-ion battery, Applied Energy 165 (2016) 48–59. doi:10.1016/j.apenergy.2015.12.063.

[137] X. Feng, J. Sun, M. Ouyang, X. He, L. Lu, X. Han, M. Fang, H. Peng, Characterization of large format lithium ion battery exposed to extremely high temperature, Journal of Power Sources 272 (2014) 457–467. doi:10.1016/j.jpowsour.2014.08.094.

[138] D. Yan, L. Lu, Z. Li, X. Feng, M. Ouyang, F. Jiang, Durability comparison of four different types of high-power batteries in HEV and their degradation mechanism analysis, Applied Energy 179 (2016) 1123–1130. doi:10.1016/j.apenergy.2016.07.054.

[139] K. Honkura, K. Takahashi, T. Horiba, State Analysis of Lithium-Ion Batteries Using Discharge Curves K. Honkura, ECS Transactions 13 (19) (2008) 61–73. doi:10.1149/1.3018750.

[140] K. Honkura, K. Takahashi, T. Horiba, Capacity-fading prediction of lithium-ion batteries based on discharge curves analysis, Journal of Power Sources 196 (23) (2011) 10141–10147. doi:10.1016/j.jpowsour.2011.08.020.

[141] H. M. Dahn, A. J. Smith, J. C. Burns, D. A. Stevens, J. R. Dahn, User-Friendly Differential Voltage Analysis Freeware for the Analysis of Degradation Mechanisms in Li-Ion Batteries, Journal of The Electrochemical Society 159 (9) (2012) A1405–A1409. doi:10.1149/2.013209jes.

[142] C. Hu, M. Hong, Y. Li, H.-l. Jeong, On-Board Analysis of Degradation Mechanisms of Lithium-ion Battery using Differential Voltage Analysis, Proceedings of the ASME 2016 International Design Engineering Technical Conferences and Computers and Information in Engineering Conference (2016) 1–9.doi:10.1115/DETC2016-59389.

[143] A. Devie, M. Dubarry, B. Y. Liaw, Overcharge Study in Li4Ti5O12 Based Lithium-Ion Pouch Cell: I. Quantitative Diagnosis of Degradation Modes, Journal of the Electrochemical Society 162 (6) (2015) A1033–A1040. doi:10.1149/2.0941506jes.

[144] M. Berecibar, M. Dubarry, N. Omar, I. Villarreal, J. Van Mierlo, Degradation mechanism detection for NMC batteries based on Incremental Capacity curves, World Electric Vehicle Journal 8 (2) (2016) 350–361. doi:10.3390/wevj8020350.

[145] C. Zhang, F. Yan, C. Du, J. Kang, R. Turkson, Evaluating the Degradation Mechanism and State of Health of LiFePO4 Lithium-Ion Batteries in Real-World Plug-in Hybrid Electric Vehicles Application for Different Ageing Paths, Energies 10 (1) (2017) 110. doi:10.3390/en10010110.

[146] T. Lu, Y. Luo, Y. Zhang, W. Luo, L. Yan, J. Xie, Degradation Analysis of a Lithium-Ion Battery with a Blended Electrode, Journal of The Electrochemical Society 164 (2) (2017) A295–A303. doi:10.1149/2.1051702jes.

[147] X. Feng, J. Li, M. Ouyang, L. Lu, J. Li, X. He, Using probability density function to evaluate the state of health oflithium-ion batteries, Journal of Power Sources 232 (2013) 209–218. doi:10.1016/j.jpowsour.2013.01.018.

[148] M. Dubarry, C. Truchot, B. Y. Liaw, Cell degradation in commercial LiFePO4 cells with high-power and high-energy designs, Journal of Power Sources 258 (2014) 408–419. doi:10.1016/j.jpowsour.2014.02.052.

[149] D. Anseán, M. Dubarry, A. Devie, B. Y. Liaw, V. M. García, J. C. Viera, M. González, Fast charging technique for high power LiFePO4 batteries: A mechanistic analysis of aging, Journal of Power Sources 321 (2016) 201–209. doi:10.1016/j.jpowsour.2016.04.140.

[150] D. Anseán, M. Dubarry, A. Devie, B. Y. Liaw, V. M. García, J. C. Viera, M. Gonzalez, Operando lithium plating quantification and early detection of a commercial LiFePO4 cell cycled under dynamic driving schedule, Journal of Power Sources In press (2017) 36–46. doi:10.1016/j.jpowsour.2017.04.072.

[151] Y. Gao, J. Jiang, C. Zhang, W. Zhang, Z. Ma, Y. Jiang, Lithium-ion battery aging mechanisms and life model under different charging stresses, Journal of Power Sources 356 (2017) 103–114. doi:10.1016/j.jpowsour.2017.04.084.

[152] P. Liu, J. Wang, J. Hicks-Garner, E. Sherman, S. Soukiazian, M. Verbrugge, H. Tataria, J. Musser, P. Finamore, Aging Mechanisms of LiFePO4 Batteries Deduced by Electrochemical and Structural Analyses, Journal of The Electrochemical Society 157 (4) (2010) A499–A507. doi:10.1149/1.3294790.

[153] B. Stiaszny, J. C. Ziegler, E. E. Krauß, J. P. Schmidt, E. Ivers-Tiffée, Electrochemical characterization and post-mortem analysis of aged LiMn2O4–Li(Ni0.5Mn0.3Co0.2)O2/graphite lithium ion batteries. Part I: Cycle aging, Journal of Power Sources 251 (2014) 439–450. doi:10.1016/j.jpowsour.2013.11.080.

[154] S. Schindler, M. Bauer, M. Petzl, M. A. Danzer, Voltage relaxation and impedance spectroscopy as in-operando methods for the detection of lithium plating on graphitic anodes in commercial lithium-ion cells, Journal of Power Sources 304

(2016) 170–180. doi:10.1016/j.jpowsour.2015.11.044.

[155] D. a. Howey, P. D. Mitcheson, S. Member, V. Yufit, G. J. Offer, N. P. Brandon, Online Measurement of Battery Impedance Using Motor Controller Excitation, IEEE Transactions on Vehicular Technology 63 (6) (2014) 2557–2566. doi:10.1109/TVT.2013.2293597.

[156] E. Din, C. Schaef, S. Member, K. Moffat, S. Member, J. T. Stauth, A Scalable Active Battery Management System with Embedded Real-Time Electrochemical Impedance Spectroscopy, in: IEEE Transactions on Power Electronics, Vol. 32, 2016, pp. 5688–5698. doi:10.1109/TPEL.2016.2607519.

[157] R. Mingant, J. Bernard, V. Sauvant-Moynot, Novel state-of-health diagnostic method for Li-ion battery in service, Applied Energy 183 (2016) 390–398. doi:10.1016/j.apenergy.2016.08.118.

[158] M. Broussely, P. Biensan, F. Bonhomme, P. Blanchard, S. Herreyre, K. Nechev, R. J. Staniewicz, Main aging mechanisms in Li ion batteries, Journal of Power Sources 146 (1–2) (2005) 90–96. doi:10.1016/j.jpowsour.2005.03.172.

[159] Y. F. Reynier, R. Yazami, B. Fultz, Thermodynamics of Lithium Intercalation into Graphites and Disordered Carbons, Journal of The Electrochemical Society 151 (3) (2004) A422–A426. doi:10.1149/1.1646152.

[160] K. Maher, R. Yazami, A study of lithium ion batteries cycle aging by thermodynamics techniques, Journal of Power Sources 247 (2014) 527–533. doi:10.1016/j.jpowsour.2013.08.053.

[161] B. Wu, V. Yufit, Y. Merla, R. F. Martinez-Botas, N. P. Brandon, G. J. Offer, Differential thermal voltammetry for tracking of degradation in lithium-ion batteries, Journal of Power Sources 273 (2015) 495–501. doi:10.1016/j.jpowsour.2014.09.127.

[162] Y. Merla, B. Wu, V. Yufit, N. P. Brandon, R. F. Martinez-Botas, G. J. Offer, Novel application of differential thermal voltammetry as an in-depth state-of-health diagnosis method for lithium-ion batteries, Journal of Power Sources 307 (2016) 308–319. doi:10.1016/j.jpowsour.2015.12.122.

[163] Y. Merla, B. Wu, V. Yufit, N. P. Brandon, R. F. Martinez-Botas, G. J. Offer, Extending battery life: A low-cost practical diagnostic technique for lithium-ion batteries, Journal of Power Sources 331 (2016) 224–231. doi:10.1016/j.jpowsour.2016.09.008.

[164] D. Ward, MISRA standards for automotive software, 2nd IEE Conference on Automotive Electronics (2006) 5–18doi:10.1049/ic:20060570.

[165] B. Behkamal, M. Kahani, M. K. Akbari, Customizing ISO 9126 quality model for evaluation of B2B applications, Information and Software Technology 51 (3) (2009) 599–609. doi:10.1016/j.infsof.2008.08.001.

[166] Robert Bosch GmbH, Bosch Automotive Handbook, 9th Edition, Bentley Publishers, ISBN: 9780837606149, 2014.

[167] D. Tranfield, D. Denyer, P. Smart, Towards a methodology for developing evidence-informed management knowledge by means of systematic review *, British Journal of Management 14 (2003) 207–222. arXiv:9605103, doi:10.1111/1467-8551.00375.

[168] D. Denyer, D. Tranfield, Producing a literature review, in: SAGE Handbook of Organizational Research Methods, SAGE Publications Ltd., London, ISBN: 9781446246054, 2009, Ch. 39.

[169] Google Inc., Google Scholar, https://scholar.google.co.uk/, accessed July 8, 2018.

[170] Z. Ma, Z. Wang, R. Xiong, J. Jiang, A mechanism identification model based state-of-health diagnosis of lithium-ion batteries for energy storage applications, Journal of Cleaner Production 193 (2018) 379–390. doi:10.1016/j.jclepro.2018.05.074.

[171] E. Riviere, P. Venet, A. Sari, F. Meniere, Y. Bultel, U. Claude, B. Lyon, U. D. Lyon, V. Cedex, LiFePO 4 Battery State Of Health Online Estimation Using Electric Vehicle Embedded Incremental Capacity Analysis, 2015 IEEE Vehicle Power and Propulsion Conference (VPPC), Montreal, QC, pp. 1-6.doi:10.1109/VPPC.2015.7352972.

[172] L. Wang, C. Pan, L. Liu, Y. Cheng, X. Zhao, On-board state of health estimation of LiFePO4 battery pack through differential voltage analysis, Applied Energy 168 (2016) 465–472. doi:10.1016/j.apenergy.2016.01.125.

[173] Y. Zheng, M. Ouyang, L. Lu, J. Li, Understanding aging mechanisms in lithium-ion battery packs: From cell capacity loss to pack capacity evolution, Journal of Power Sources 278 (2015) 287–295. doi:10.1016/j.jpowsour.2014.12.105.

[174] T. Shibagaki, Y. Merla, G. J. Offer, Tracking degradation in lithium iron phosphate batteries using differential thermal voltammetry, Journal of Power Sources 374 (October 2017) (2018) 188–195. doi:10.1016/j.jpowsour.2017.11.011.

[175] J. Landesfeind, J. Hattendorff, A. Ehrl, W. A. Wall, H. A. Gasteiger, Tortuosity Determination of Battery Electrodes and Separators by Impedance Spectroscopy, Journal of The Electrochemical Society 163 (7) (2016) A1373–A1387. doi:10.1149/2.1141607jes.

[176] M. Ebner, V. Wood, Tool for Tortuosity Estimation in Lithium Ion Battery Porous Electrodes, Journal of The Electrochemical Society 162 (2) (2015) A3064–A3070. doi:10.1149/2.0111502jes.

[177] Y. Zhang, C.-Y. Wang, Cycle-Life Characterization of Automotive Lithium-Ion Batteries with LiNiO[sub 2] Cathode, Journal of The Electrochemical Society 156 (2009) A527. doi:10.1149/1.3126385.

[178] D. P. Abraham, S. D. Poppen, A. N. Jansen, J. Liu, D. W. Dees, Application of a lithium–tin reference electrode to determine electrode contributions to impedance rise in high-power lithium-ion cells, Electrochimica Acta 49 (26) (2004) 4763–4775. doi:10.1016/j.electacta.2004.05.040.

[179] A. Barré, B. Deguilhem, S. Grolleau, M. Gérard, F. Suard, D. Riu, A review on lithium-ion battery ageing mechanisms and estimations for automotive applications, Journal of Power Sources 241 (2013) 680–689. doi:10.1016/j.jpowsour.2013.05.040.

[180] Scribner Associates incorporated, Help document Zview version 3.3b (2011).

[181] S. F. Schuster, T. Bach, E. Fleder, J. Müller, M. Brand, G. Sextl, A. Jossen, Nonlinear aging characteristics of lithium-ion cells under different operational conditions, Journal of Energy Storage 1 (2015) 44–53. doi:10.1016/j.est.2015.05.003.

[182] J. Groot, M. Swierczynski, A. I. Stan, S. K. Kær, On the complex ageing characteristics of high-power LiFePO4/graphite battery cells cycled with high charge and discharge currents, Journal of Power Sources 286 (2015) 475–487. doi:10.1016/j.jpowsour.2015.04.001.

[183] S. Bourlot, P. Blanchard, S. Robert, Investigation of aging mechanisms of high power Li-ion cells used for hybrid electric vehicles, Journal of Power Sources 196 (16) (2011) 6841–6846. doi:10.1016/j.jpowsour.2010.09.103.

[184] S. Watanabe, M. Kinoshita, K. Nakura, Comparison of the surface changes on cathode during long term storage testing of high energy density cylindrical lithium-ion cells, Journal of Power Sources 196 (16) (2011) 6906–6910. doi:10.1016/j.jpowsour.2010.12.028.

[185] S. Watanabe, M. Kinoshita, T. Hosokawa, K. Morigaki, K. Nakura, Capacity fade of LiAlyNi1xyCoxO2 cathode for lithium-ion batteries during accelerated calendar and cycle life tests (surface analysis of LiAlyNi1xyCoxO2 cathode after cycle tests in restricted depth of discharge ranges), Journal of Power Sources 258 (2014) 210–217. doi:10.1016/j.jpowsour.2014.02.018.

[186] S. Watanabe, M. Kinoshita, T. Hosokawa, K. Morigaki, K. Nakura, Capacity fading of LiAlyNi1xyCoxO2 cathode for lithium-ion batteries during accelerated calendar and cycle life tests (effect of depth of discharge in charge–discharge cycling on the suppression of the micro-crack generation of LiAlyNi1xyCoxO2 particl, Journal of Power Sources 260 (2014) 50–56. doi:10.1016/j.jpowsour.2014.02.103.

[187] D. C. Montgomery, G. C. Runger, Applied Statistic and Probability for Engineers, 5th Edition, John Wiley & Sons, Inc., ISBN: 9780470053041, 2011.

[188] Q.-a. Huang, Y. Shen, Y. Huang, L. Zhang, J. Zhang, Impedance Characteristics and Diagnoses of Automotive Lithium-Ion Batteries at 7 . 5 % to 93 . 0 % State of Charge, Electrochimica Acta 219 (2016) 0–52. doi:10.1016/j.electacta.2016.09.154.

[189] P. Pietsch, D. Westhoff, J. Feinauer, J. Eller, F. Marone, M. Stampanoni, V. Schmidt, V. Wood, Silicon-graphite lithium ion battery anodes, Nature Communications 7 (2016) 1–11. doi:10.1038/ncomms12909.

[190] Volkswagen, Departure Time Programming (2016), http://volkswagen-carnet.com/gb/en/start/app-overview/e-remote/e_manager_departure.html#tab/open/1ff273db-bab2-438c-b3ee-b168308e6296, accessed December 8, 2016.

[191] C. Fleischer, W. Waag, H.-M. Heyn, D. U. Sauer, On-line adaptive battery impedance parameter and state estimation considering physical principles in reduced order equivalent circuit battery models part 2. Parameter and state estimation, Journal of Power Sources 262 (2014) 457–482. doi:10.1016/j.jpowsour.2014.03.046.

[192] M. Mathew, Q. H. Kong, J. McGrory, M. Fowler, Simulation of lithium ion battery replacement in a battery pack for application in electric vehicles, Journal of Power Sources 349 (2017) 94–104. doi:10.1016/j.jpowsour.2017.03.010.

[193] Jaguar Land Rover, Every Jaguar Land Rover launched from 2020 will be electrified (2017), https://www.jaguarlandrover.com/news/2017/09/every-jaguar-and-land-rover-launched-2020-will-be-electrified, accessed February 28, 2019.

[194] Jaguar Land Rover, Jaguar Land Rover reports full-year results (2018), https://www.jaguarlandrover.com/news/2018/05/jaguar-land-rover-reports-full-year-results, accessed February 28, 2019.

[195] T. Fai Yu, Personal communication, Jaguar Land Rover R&D engineer (2019).

[196] M. J. Brand, M. H. Hofmann, M. Steinhardt, S. F. Schuster, A. Jossen, Current distribution within parallel-connected battery cells, Journal of Power Sources 334 (2016) 202–212. doi:10.1016/j.jpowsour.2016.10.010.

[197] K. B. Hatzell, A. Sharma, H. K. Fathy, A survey of long-term health modeling, estimation, and control of Lithium-ion batteries: Challenges and opportunities, 2012 American Control Conference (ACC) (June 2012) (2012) 584–591. doi:10.1109/ACC.2012.6315578.

[198] K. Mueller, D. Tittel, L. Graube, Z. Sun, F. Luo, Optimizing BMS Operating Strategy Based on Precise SOH Determination of Lithium Ion Battery Cells, Proceedings of the FISITA 2012 World Automotive Congress 201 (2013) 365–376. doi:10.1007/978-3-642-33741-3.

[199] Warwick Manufacturing Group, Equipment and capability directory (2016), https://warwick.ac.uk/fac/sci/wmg/business/capabilities/wmg_equipment_and_capability_directory_2016.pdf, accessed November 15, 2017.

[200] Technologic Vehicles, Consumption of electric cars: the top 13 in Wh/km (2012), http://www.technologicvehicles.com/en/green-transportation-news/1961/consumption-of-electric-cars-the-top-13-in-wh-km{#}.VYHkaPl{_}Okp, accessed June 17, 2015.

[201] Statistical Release, National Travel Survey: England 2013 - Statistical Release (2014), https://assets.publishing.service.gov.uk/government/uploads/system/uploads/attachment_data/file/342160/nts2013-01.pdf, accessed April 24, 2015.

[202] D. Nolan, How much will Tesla Model S battery life decrease over time? (2015), https://www.csmonitor.com/Business/In-Gear/2015/0219/How-much-will-Tesla-Model-S-battery-life-decrease-over-time, accessed June 17, 2016.

A. Appendix

A.1 Study 1 - A method to diagnose cell-to-cell variabilities in lithium-ion battery packs

A.1.1 Repeatibility of simulations

To ensure the results are representative of a particular scenario and limit the number of outliers, simulations need to be repeated N number of times. N should not be very low in order to include a complete variation of the randomness of different amount of CtCV, but neither very high so that the simulation time can be reduced. The change of a FOI, G_{FOI}, for 10 and 30 simulations was calculated. The mean value, $\overline{G}_{\mathrm{FOI}}$, and the standard error (SE), $\delta\overline{G}_{\mathrm{FOI}}$, are calculated for 10 and 30 simulations and then compared as illustrated in Figure A.1. FOI1, LMO 49S1P, normal input distribution and real scenario was the case randomly selected for this comparison. Equation A.1 calculates the difference of the $\overline{G}_{\mathrm{FOI}}$ of 30 and 10 simulations.

$$\overline{\Delta G}_{FOI} = \overline{G}^{30}_{FOI} - \overline{G}^{10}_{FOI} \tag{A.1}$$

The SE, $\overline{\delta G}_{\mathrm{FOI}}$, is calculated as the sum of the individual SE, $\overline{\delta G}^{30}_{FOI}$ and $\overline{\delta G}^{10}_{FOI}$ [129] in Equation A.2:

$$\overline{\delta G}^{N}_{FOI} = \sqrt{\frac{\frac{1}{N-1}\sum_{i=1}^{N}\left|G_{FOI} - \overline{G}_{FOI}\right|^2}{N}} \tag{A.2}$$

Figure A.1 (c) shows the results of $\overline{\Delta G}_{FOI}$ and $\overline{\delta(\Delta G)}_{FOI}$. According to this, it is possible to say that the precision in the results derived for 10 or 30 simulations is the same with a maximum difference lower than 1.5%. Having this difference in consideration, then 10 simulations is selected as the minimum repeatability number of simulations.

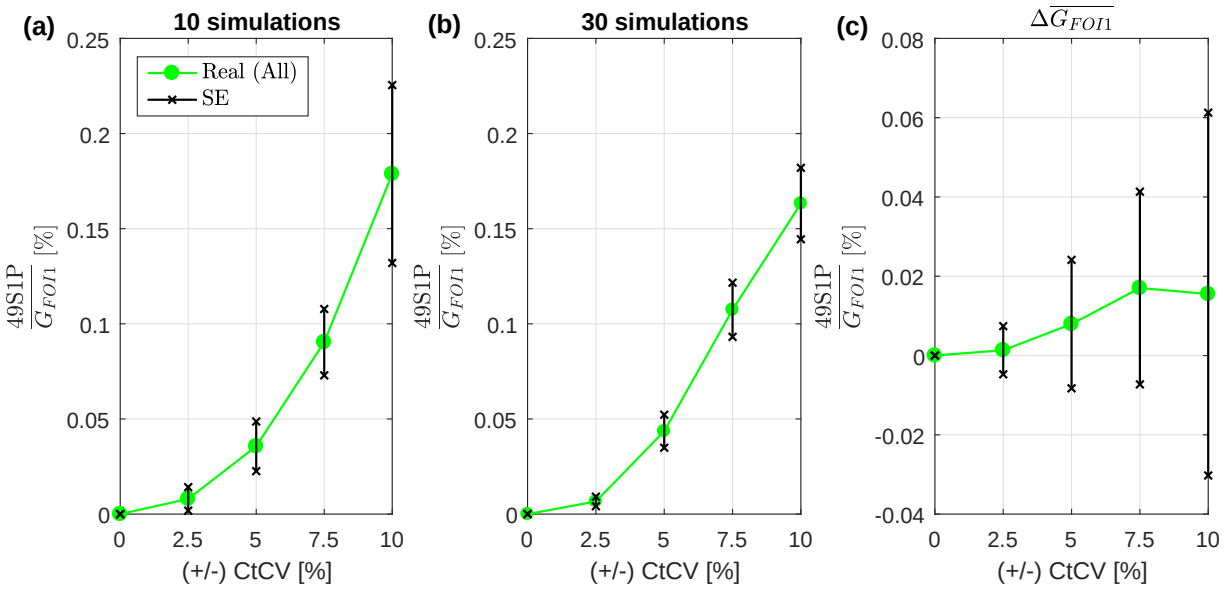

Figure A.1: Repeatability analysis for FOI 1 LMO 49S1P, real scenario, normal input distribution: (a) 10 simulations; (b) 30 simulations and (c) difference between 30 and 10 simulations.

A.1.2 Pack topology dependency

A.1.2.1 NCA

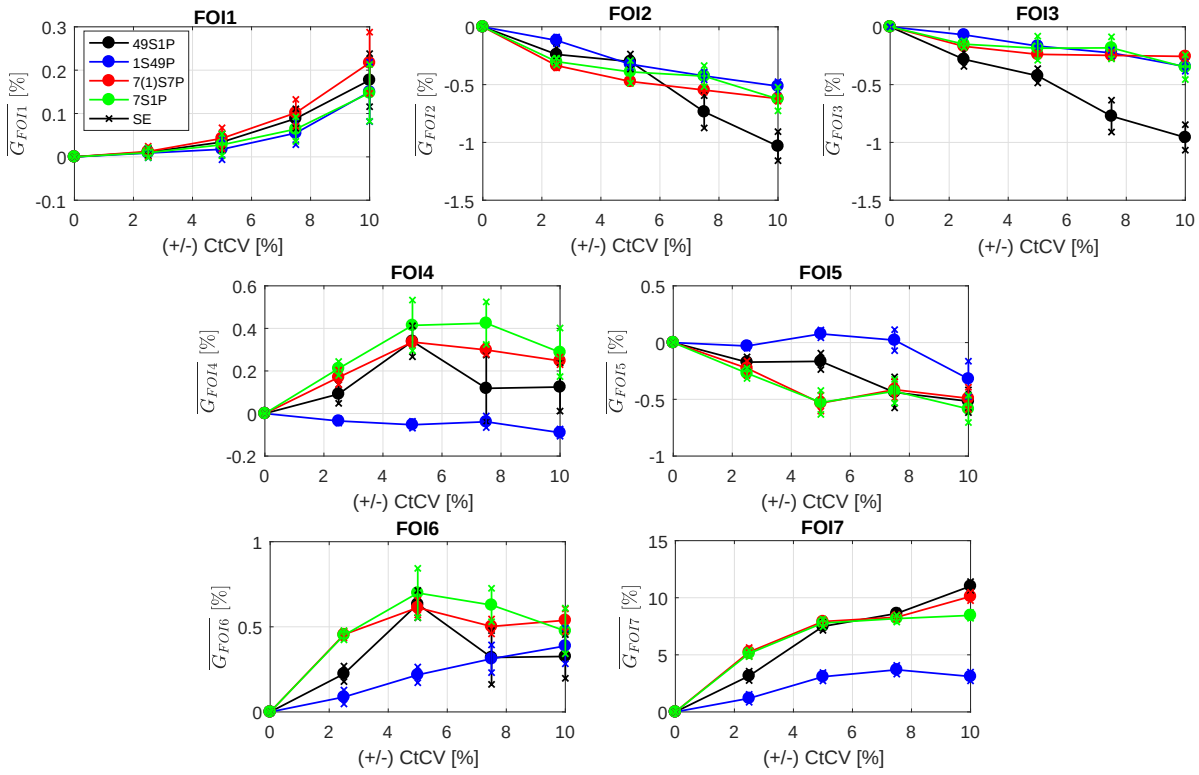

Figure A.2: Quantification of FOIs NCA normal input distribution with respect to each pack topology.

A.1.2.2 LFP

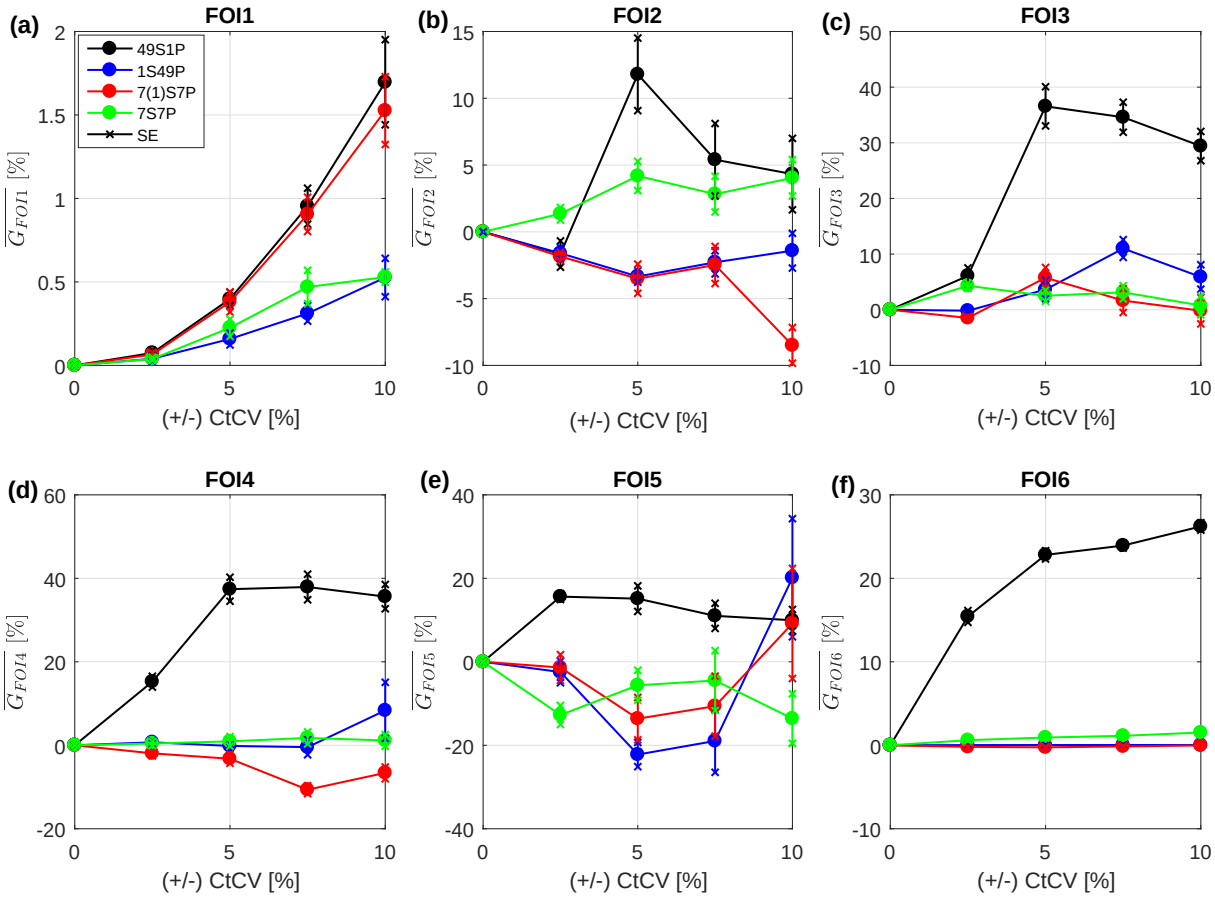

Figure A.3: Quantification of FOIs LFP normal input distribution with respect to each pack topology.

A.1.3 Analysis of the rest of simulation scenarios for normal input distribution

A.1.3.1 LMO

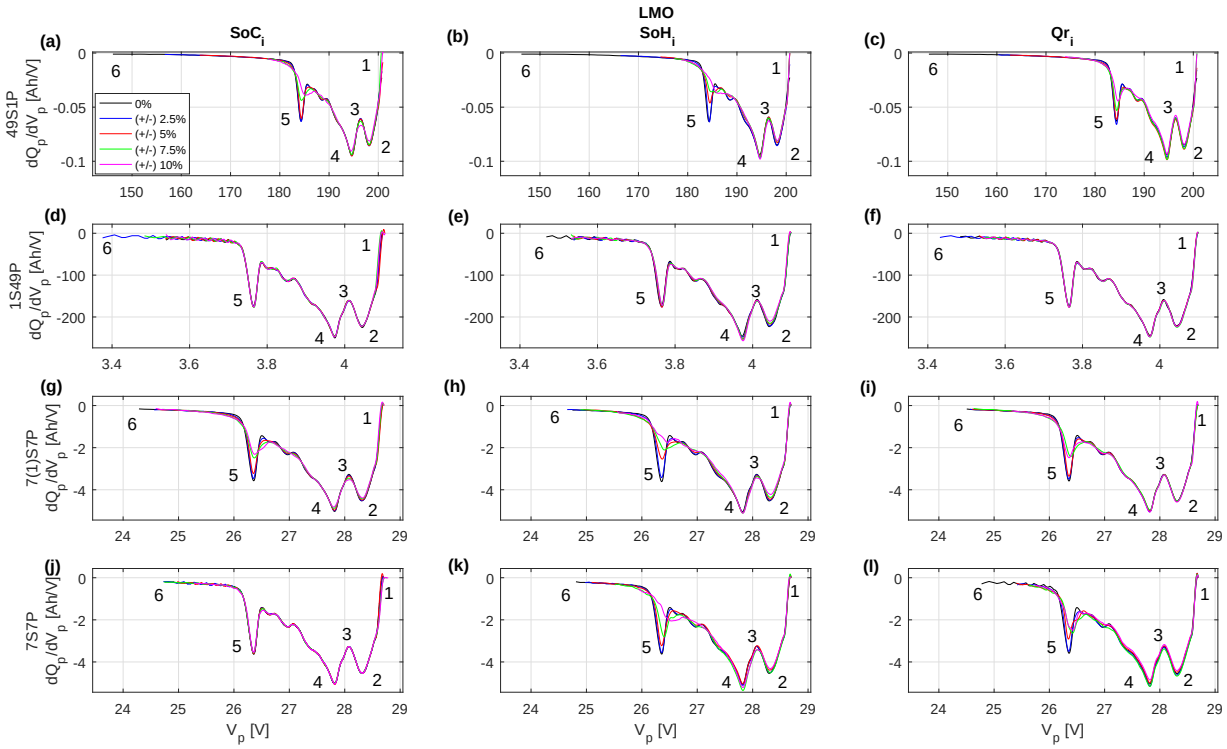

Figure A.4: IC pack curves, LMO, 49S1P, 1S49P, 7(1)S7P and 7S7P topologies, normal input distribution and theoretical CtCV.

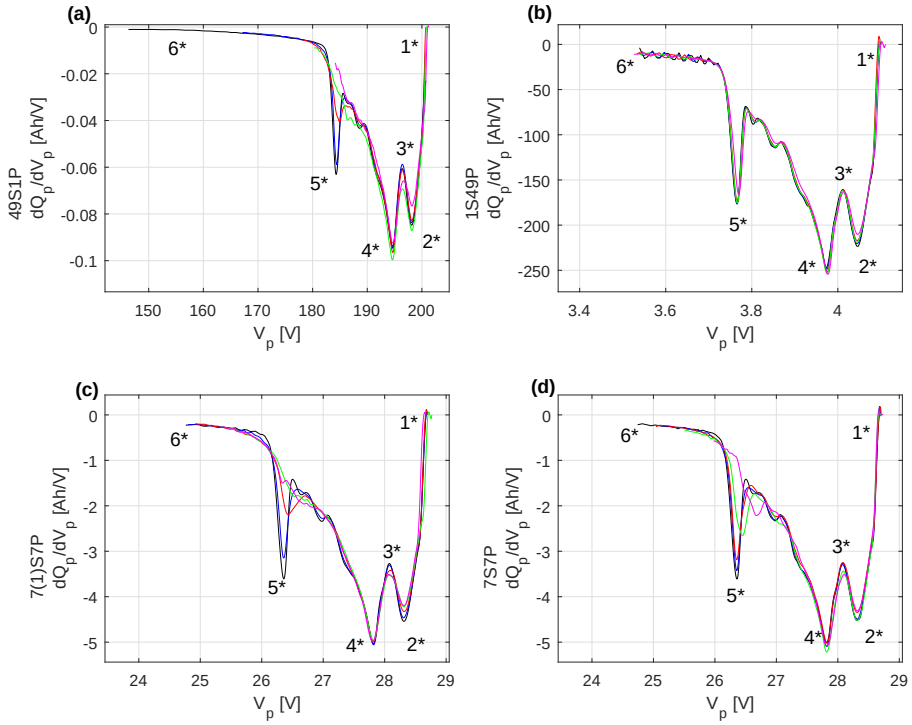

Figure A.5: IC pack curves, LMO, 49S1P, 1S49P, 7(1)S7P and 7S7P topologies, normal input distribution and real CtCV.

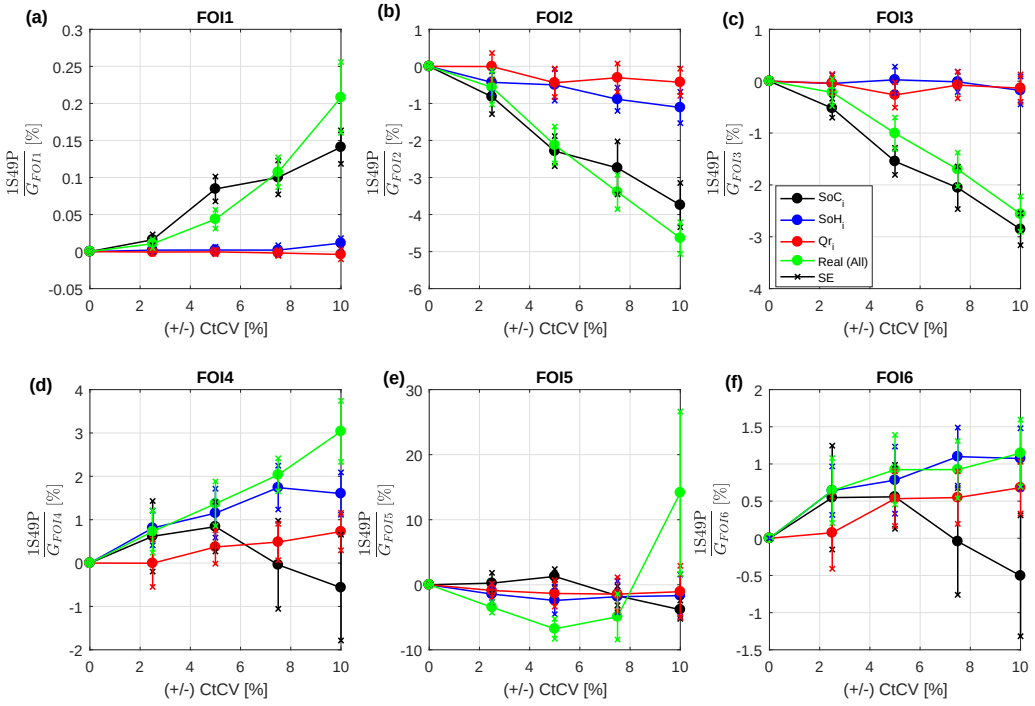

Figure A.6: LMO 1S49P normal input distribution - Quantification of each FOI for theoretical and real scenarios.

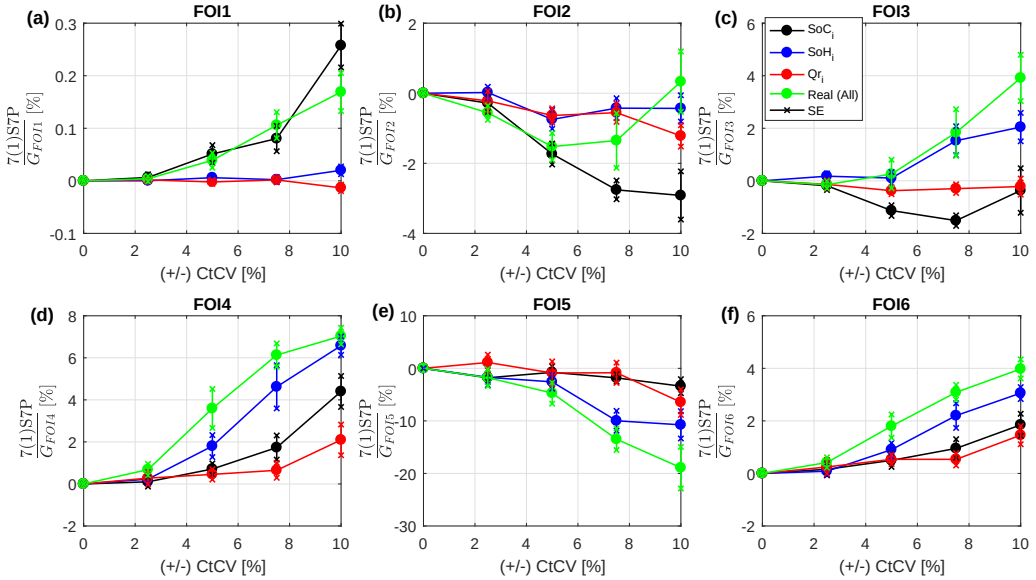

Figure A.7: LMO 7(1)S7P normal input distribution - Quantification of each FOI for theoretical and real scenarios.

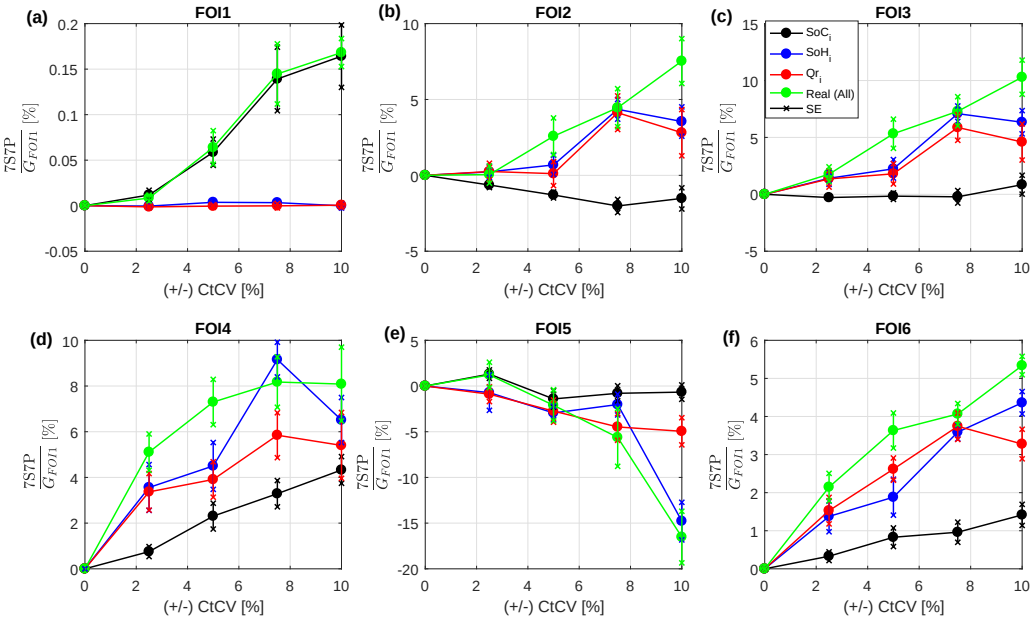

Figure A.8: LMO 7S7P normal input distribution - Quantification of each FOI for theoretical and real scenarios.

A.1.3.2 NCA

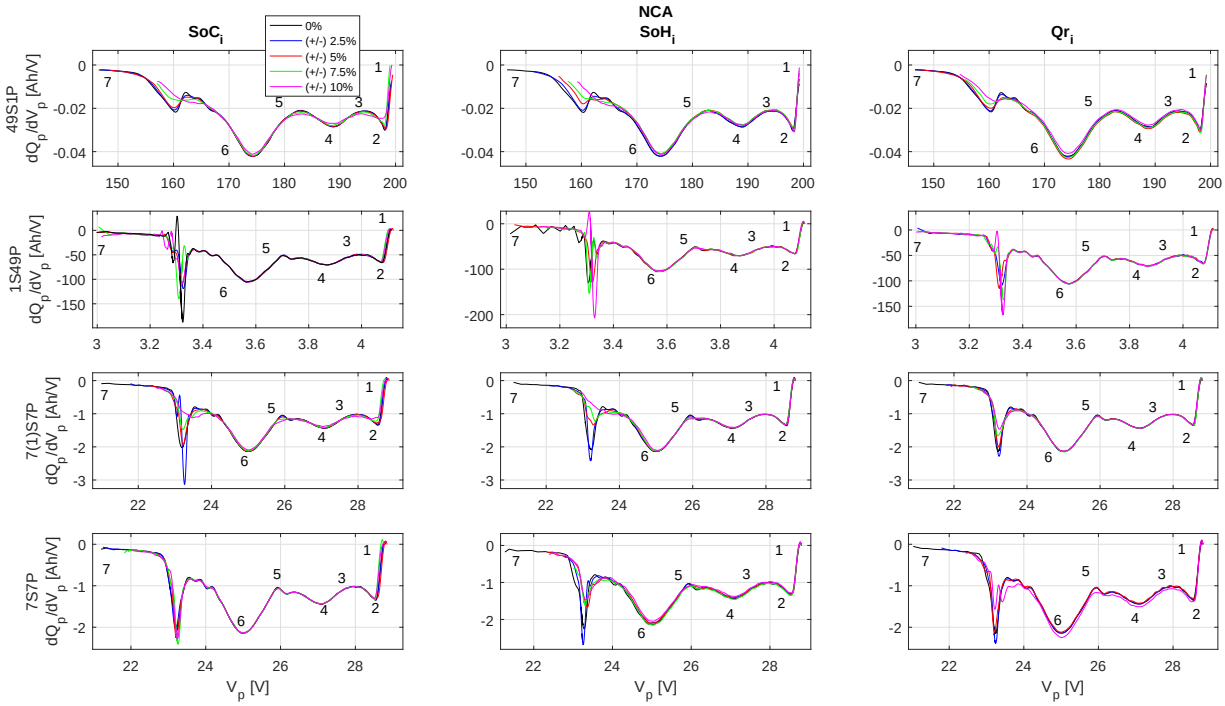

Figure A.9: IC pack curves, NCA, 49S1P, 1S49P, 7(1)S7P and 7S7P topologies, normal input distribution and theoretical CtCV.

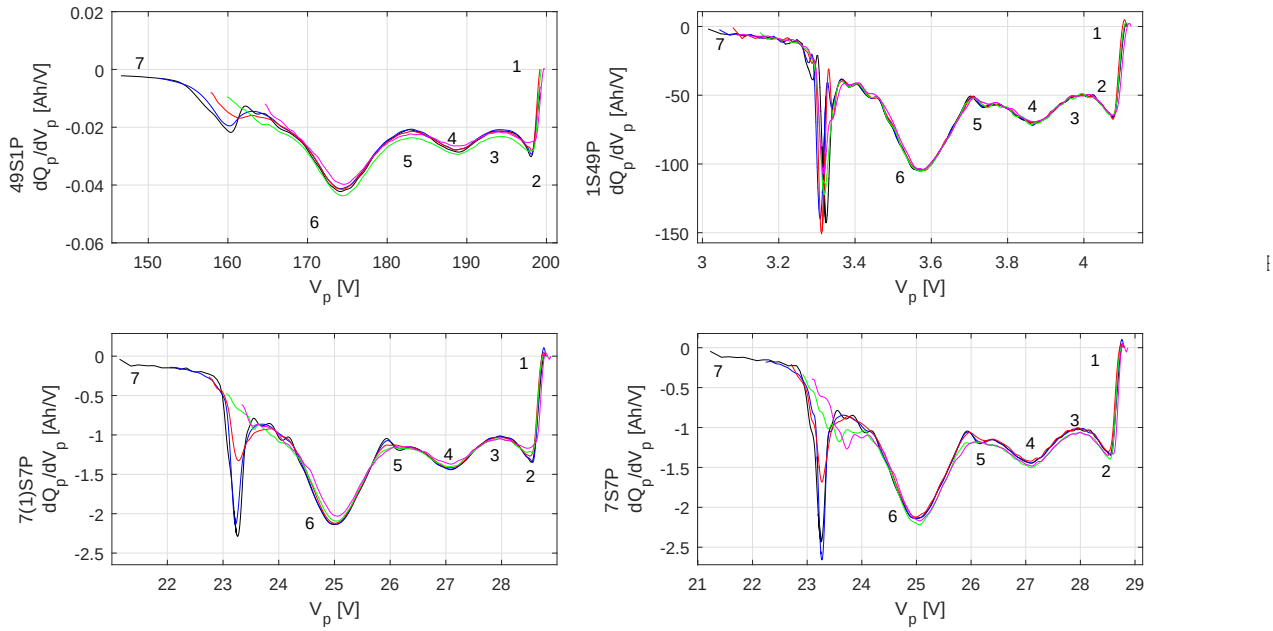

Figure A.10: IC pack curves, NCA, 49S1P, 1S49P, 7(1)S7P and 7S7P topologies, normal input distribution and real CtCV.

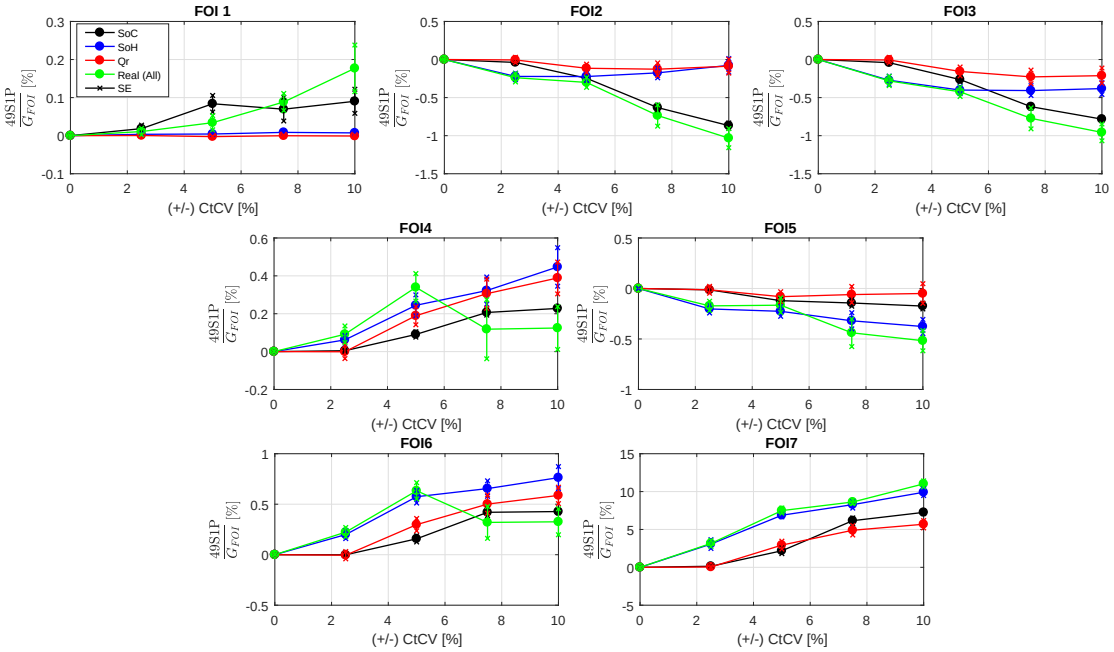

Figure A.11: NCA 49S1P normal input distribution - Quantification of each FOI for theoretical and real scenarios.

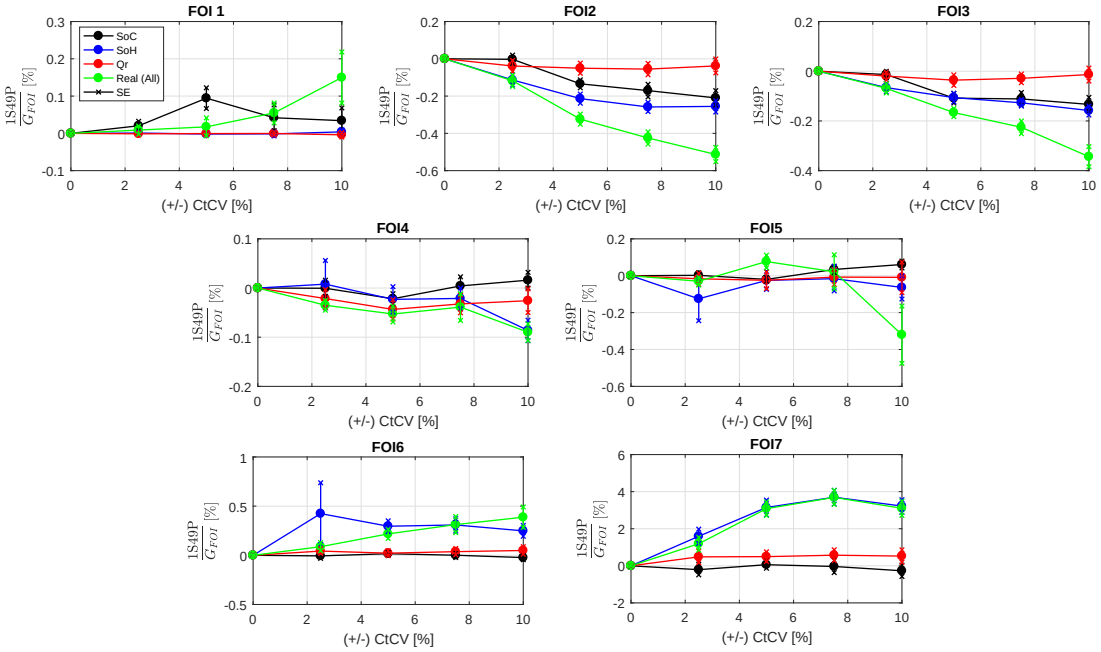

Figure A.12: NCA 1S49P, normal input distribution - Quantification of each FOI for theoretical and real scenarios.

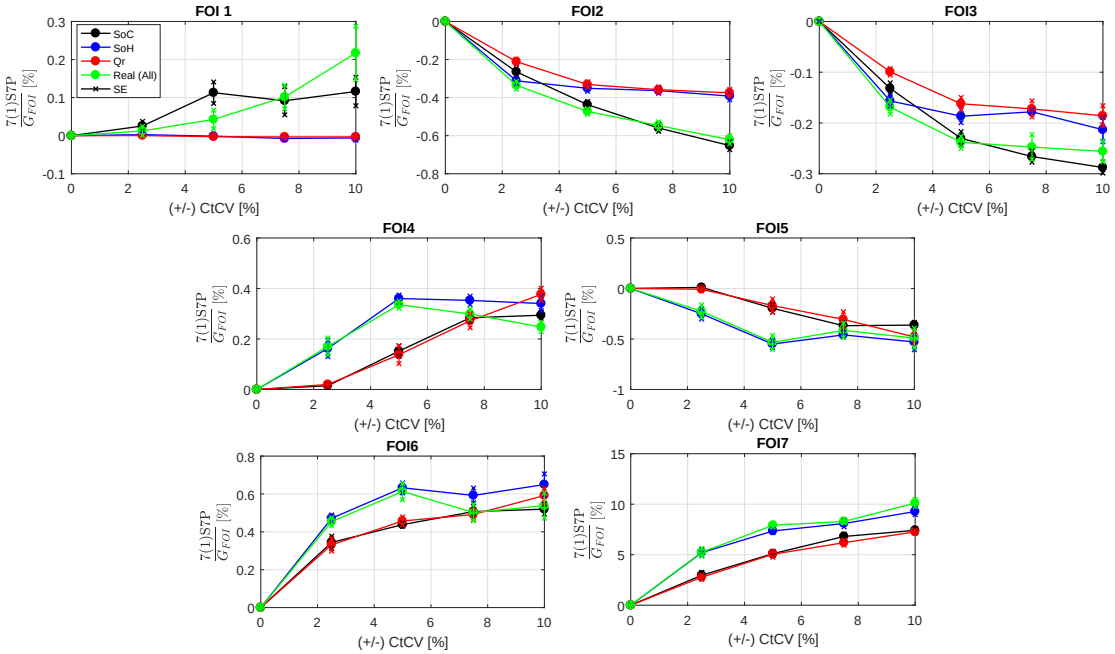

Figure A.13: NCA 7(1)S7P normal input distribution - Quantification of each FOI for theoretical and real scenarios.

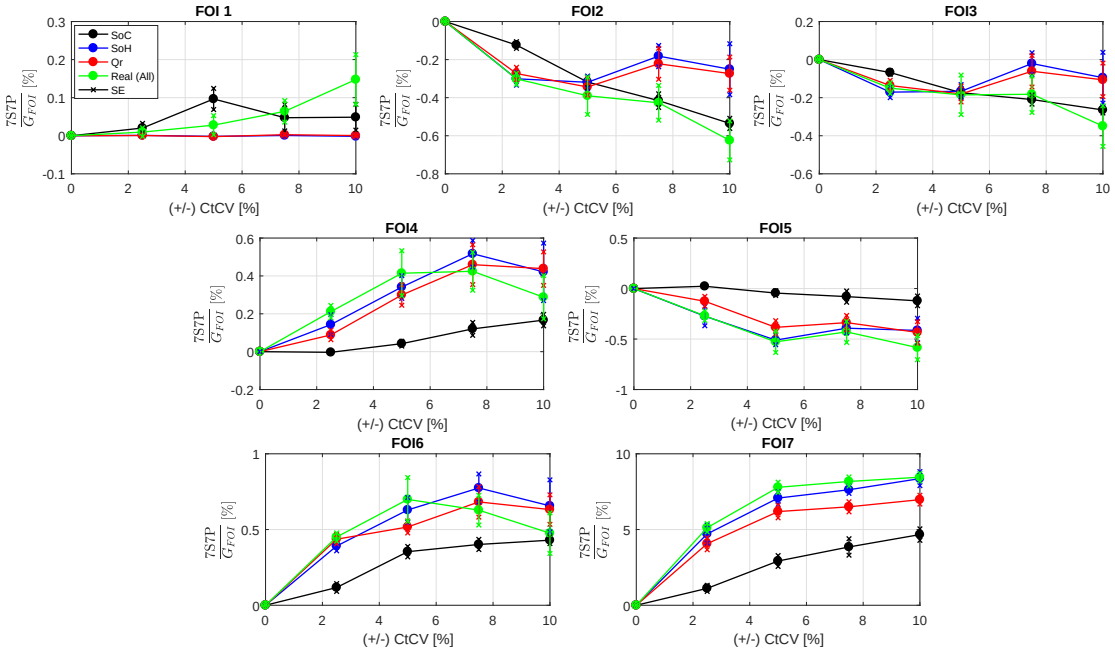

Figure A.14: NCA 7S7P normal input distribution - Quantification of each FOI for theoretical and real scenarios.

A.1.3.3 LFP

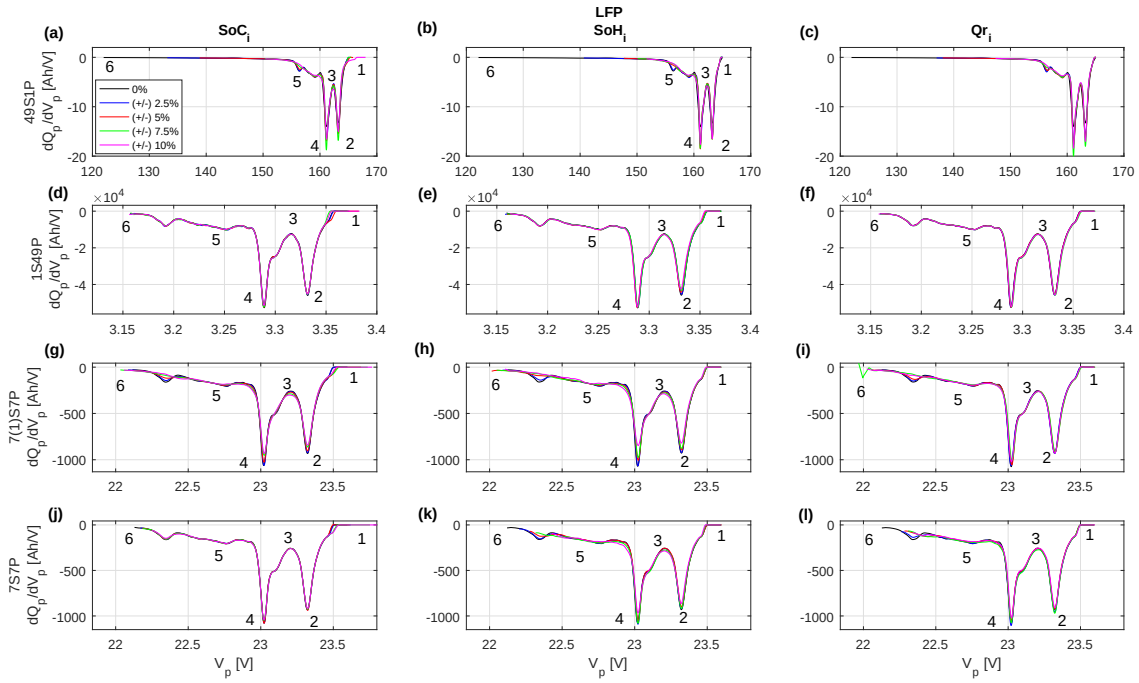

Figure A.15: IC pack curves, LFP, 49S1P, 1S49P, 7(1)S7P and 7S7P topologies, normal input distribution and theoretical CtCV.

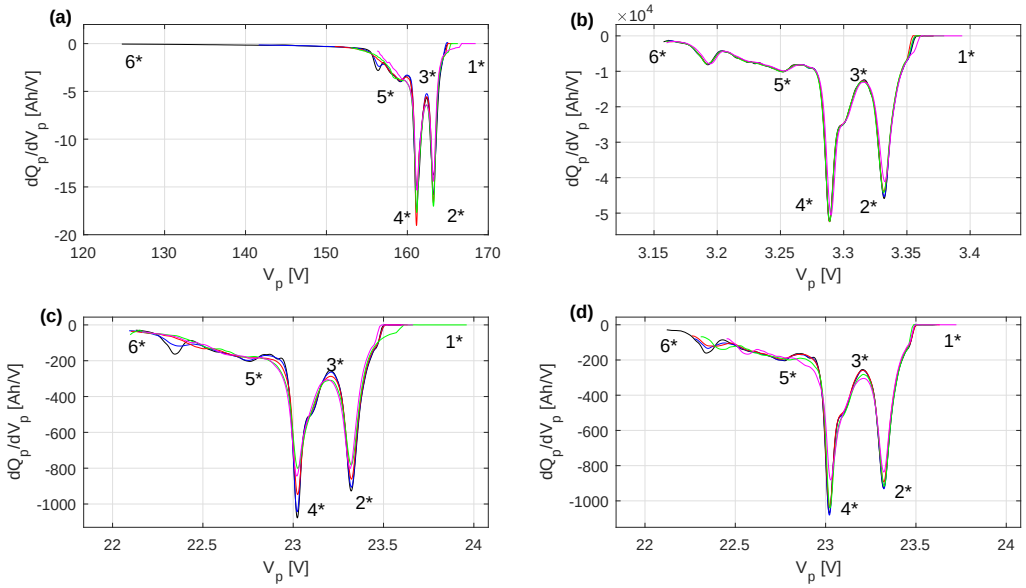

Figure A.16: IC pack curves, LFP, 49S1P, 1S49P, 7(1)S7P and 7S7P topologies, normal input distribution and real CtCV.

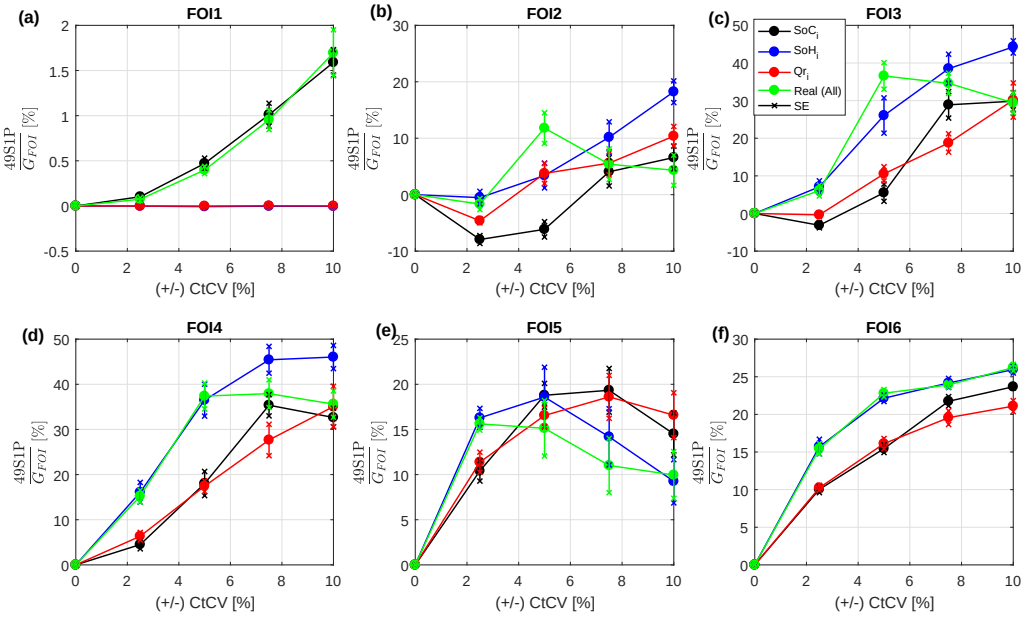

Figure A.17: LFP 49S1P normal input distribution - Quantification of each FOI for theoretical and real scenarios.

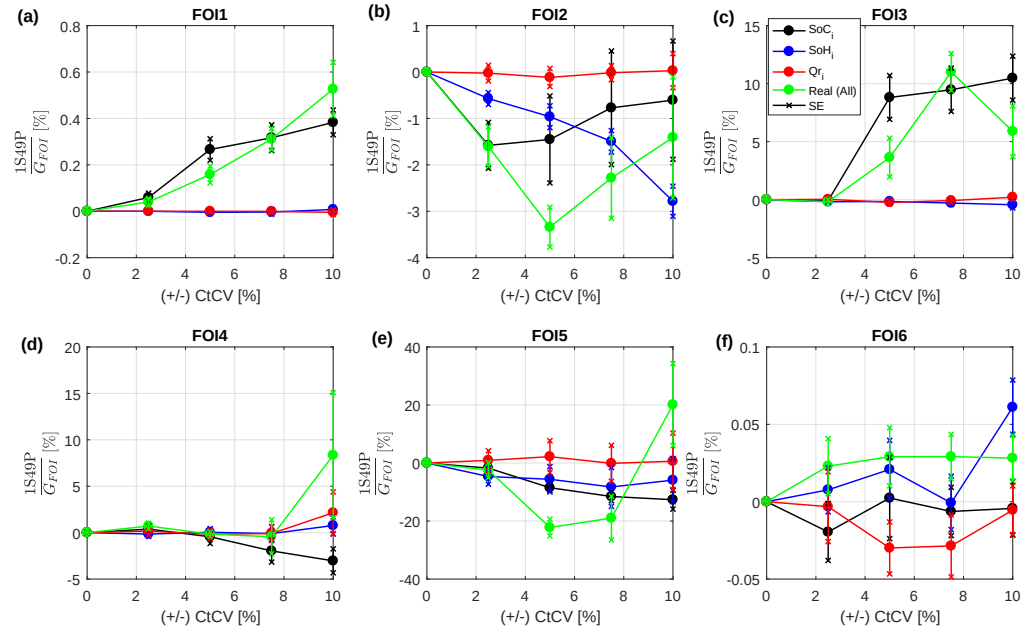

Figure A.18: LFP 1S49P normal input distribution - Quantification of each FOI for theoretical and real scenarios.

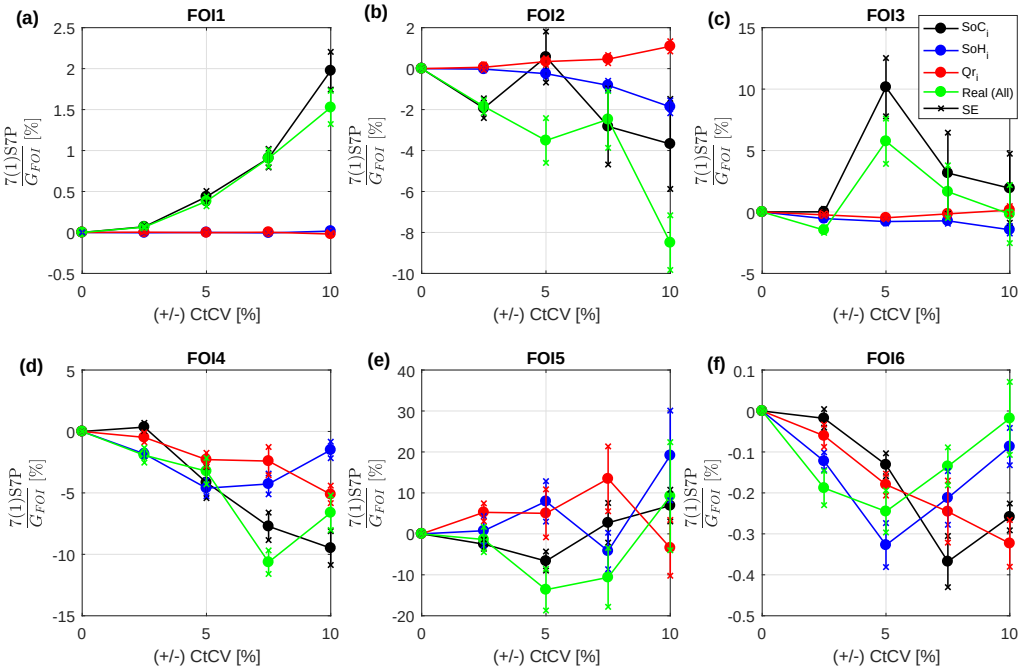

Figure A.19: LFP 7(1)S7P normal input distribution - Quantification of each FOI for theoretical and real scenarios.

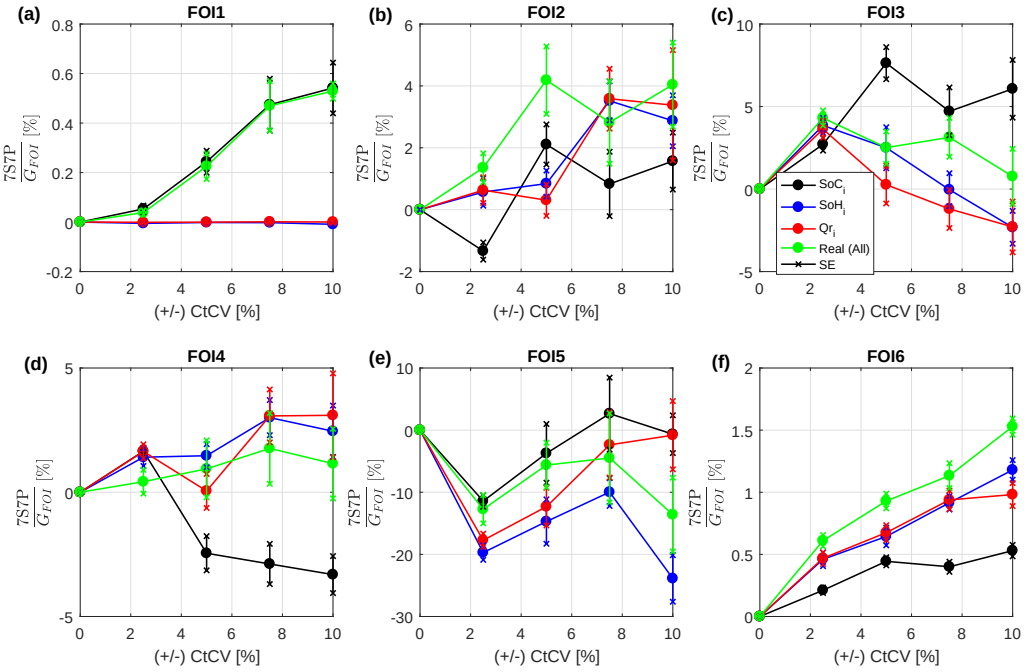

Figure A.20: LFP 7S7P normal input distribution - Quantification of each FOI for theoretical and real scenarios.

A.1.4 Battery pack performance

A.1.4.1 NCA

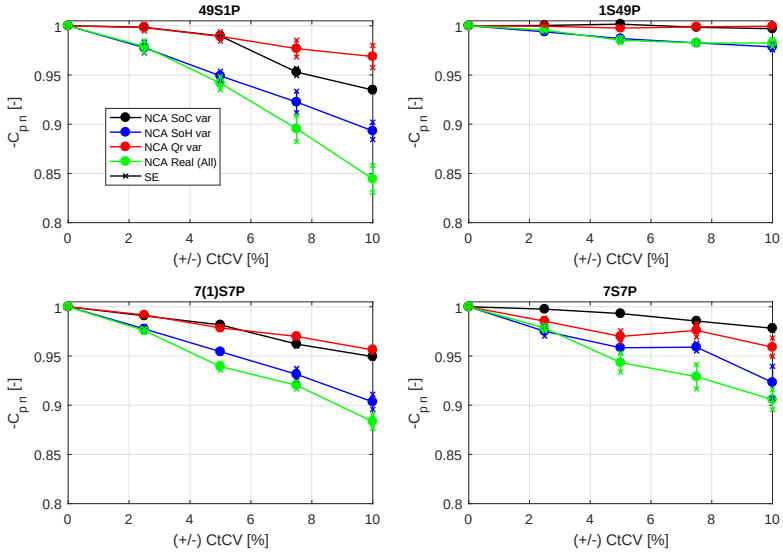

Figure A.21: NCA normalised pack capacity fade for each pack topology for theoretical and real CtCV.

A.1.4.2 LFP

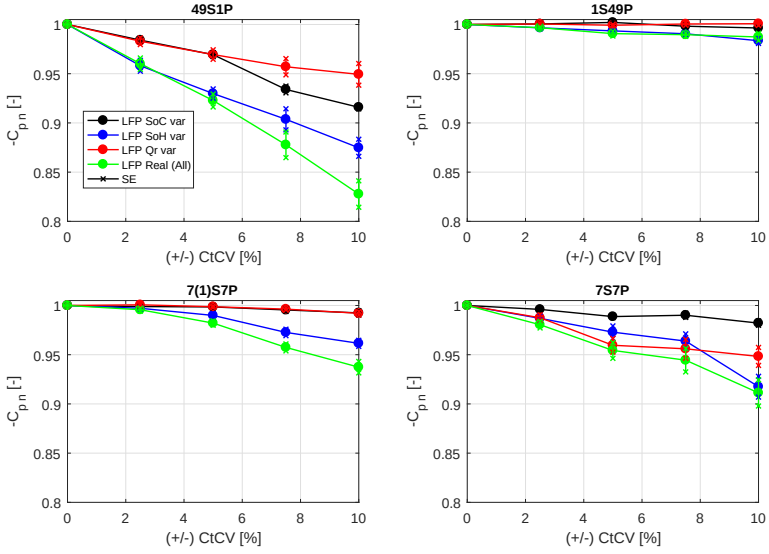

Figure A.22: LFP normalised pack capacity fade for each pack topology for theoretical and real CtCV.

A.1.5 Mathematical derivation of IC cell-to-pack curves

The mathematical derivation of IC cell-to-pack curves consists in the following steps:

1. The IC pack curve, $\frac{dQ_p}{dV_p}$, is divided into h equal increments. For the LMO_SoC_49S1P_0% and LMO_SoC_49S1P_10% scenarios, h is equal to 0.196 V. The selection of the m value is a compromise between curve smoothness and equality to the original IC cell curves.

$$\Delta\left(\frac{dQ_p}{dV_p}\right) = \frac{dQ_{p,h}}{dV_{p,h}} - \frac{dQ_{p,h-1}}{dV_{p,h-1}} \tag{A.3}$$

2. For each increment of the IC pack curve, $\Delta\left(\frac{dQ_p}{dV_p}\right)$, the dQ and the dV on each SC i (dQ_{SC_i} and dV_{SC_i}) are calculated as:

$$\begin{aligned} dQ_{SC_ip} = dQ_{SC_i} \cdot \Delta\left(\frac{dQ_p}{dV_p}\right) = dQ_{SC_i} \cdot \left(\frac{dQ_{p,h}}{dV_{p,h}} - \frac{dQ_{p,h-1}}{dV_{p,h-1}}\right) = \\ = dQ_{SC_i} \cdot \left(\frac{dQ_{p,h}}{dV_{p,h}}\right) - dQ_{SC_i} \cdot \left(\frac{dQ_{p,h-1}}{dV_{p,h-1}}\right) \end{aligned} \tag{A.4}$$

$$\begin{aligned} dV_{SC_ip} = dV_{SC_i} \cdot \Delta\left(\frac{dQ_p}{dV_p}\right) = dV_{SC_i} \cdot \left(\frac{dQ_{p,h}}{dV_{p,h}} - \frac{dQ_{p,h-1}}{dV_{p,h-1}}\right) = \\ = dV_{SC_i} \cdot \left(\frac{dQ_{p,h}}{dV_{p,h}}\right) - dV_{SC_i} \cdot \left(\frac{dQ_{p,h-1}}{dV_{p,h-1}}\right) \end{aligned} \tag{A.5}$$

3. The IC cell-to-pack, IC_{SC_ip}, is then calculated as the ratio of dQ_{SC_ip} and dV_{SC_ip}. In the plots, the x-axis is represented by the pack voltage, V_p. Depending on the number of cells connected in series (pack topology) the V_p has a different value.

$$IC_{SC_ip} = \frac{dQ_{SC_ip}}{dV_{SC_ip}} \tag{A.6}$$

4. The DV cell-to-pack, DV_{SC_ip}, is computed as the inverse of the IC cell-to-pack, IC_{SC_ip}. In the plot, the x-axis is represented by the pack capacity Q_p. Depending on the number of cells connected in parallel (pack topology) the Q_p has a different value.

$$DV_{SC_ip} = \frac{1}{IC_{SC_ip}} = \frac{dV_{SC_ip}}{dQ_{SC_ip}} \tag{A.7}$$

Relating the IC pack signature with the single cell IC curves is difficult because for each dV_{p} or dQ_{p} of the pack, each single cell could have their own dV_{SC} and dQ_{SC}. However, when cells are either connected in series or connected in parallel, i.e., nS1P or 1SmP topologies, the relationship between the pack and the single cell signatures can be deciphered. This statement is proved first for the nS1P topology, and then for the 1SmP case. It is noteworthy the subsequent notation uses p lower case as pack and P upper case as parallel.

If n cells are connected in series, the pack capacity, dQ_p, and the single cell-to-pack capacity, dQ_{SC_ip} are equal as shown in Equation A.8.

$$dQ_p = dQ_{SC_1p} = dQ_{SC_2p} = ... = dQ_{SC_np} \tag{A.8}$$

Then, the pack DV curve for a nS1P topology, DV_{pnS1P}, can be expressed as the sum of the individual cell-to-pack DV curves, $\sum_{i=1}^{i=n} DV_{SC_ip}$, as:

$$DV_{pnS1P} = \frac{dV_p}{dQ_p} = \sum_{i=1}^{i=n} DV_{SC_ip} = \frac{dV_{SC_1p}}{dQ_{SC_1p}} + \frac{dV_{SC_2p}}{dQ_{SC_1p}} + ... + \frac{dV_{SC_np}}{dQ_{SC_1p}} = \frac{\sum_{i=1}^{i=n} dV_{SC_ip}}{dQ_{SC_1p}} \tag{A.9}$$

Figure A.23 (a) proves graphically Equation A.9 by showing that the sum of the DV_{SC_ip} is equal to the DV_p for the nS1P topology. Figure A.23 illustrates small variations between the result of the sum and the pack. These variations accounts for the error in the computation, e.g., sampling, of cell-to-pack IC and DV curves. This error has not been calculated as it is not significant based on the graphical results.

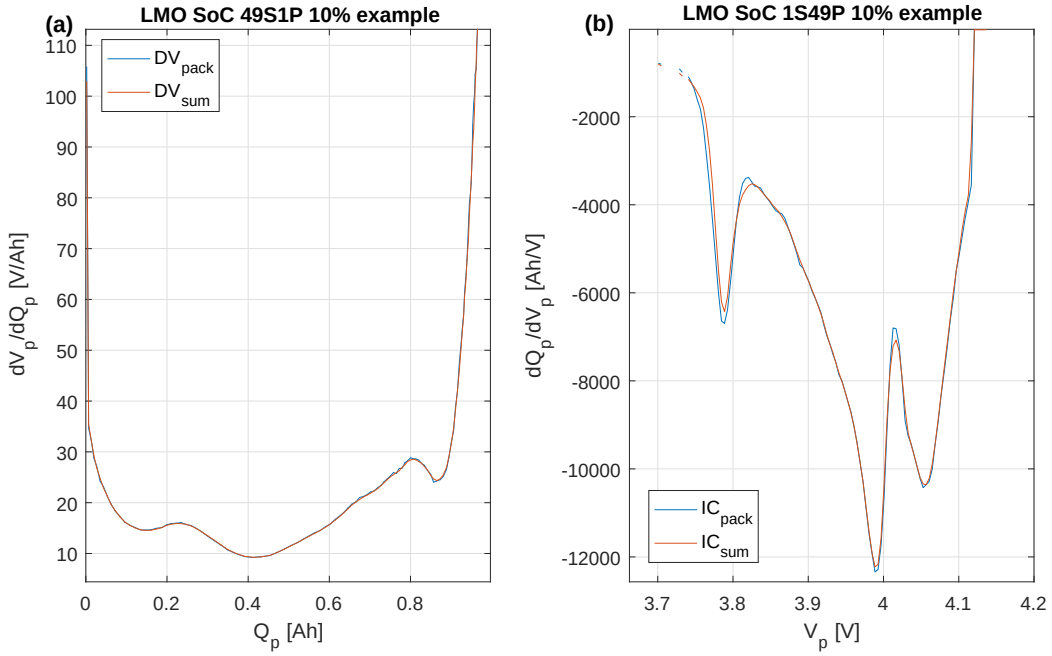

Figure A.23: Validation of the calculation of cell-to-pack IC and DV curves for (a) LMO_SoC_1S49P_10% and (b) LMO_SoC_49S1P_10%

If m cells are connected in parallel, the pack voltage, dV_p, and the single cell-to-pack voltage, dV_{SC_ip} are equal as shown in Equation A.10.

$$dV_p = dV_{SC_1p} = dV_{SC_2p} = ... = dV_{SC_mp} \tag{A.10}$$

Then, the pack IC curve for a 1SmP topology, IC_{p1SmP}, can be expressed as the sum of the individual cell-to-pack IC curves, $\sum_{i=1}^{i=n} IC_{SC_ip}$, as:

$$IC_{p1SmP} = \frac{dQ_p}{dV_p} = \sum_{i=1}^{i=m} IC_{SC_ip} = \frac{dQ_{SC_1p}}{dV_{SC_1p}} + \frac{dQ_{SC_2p}}{dV_{SC_1p}} + ... + \frac{dQ_{SC_mp}}{dV_{SC_1p}} = \frac{\sum_{i=1}^{i=m} dQ_{SC_ip}}{dV_{SC_1p}} \tag{A.11}$$

Figure A.23 (b) proves graphically Equation A.11 by showing that the sum of the IC_{SC_ip} is equal to the IC_p for the 1SmP topology.

A.2 Study 2 - A study of cell-to-cell interactions and degradation in parallel strings: implications for the Battery Management System

A.2.1 Test bench, specifications of the experimental equipment and experimental errors

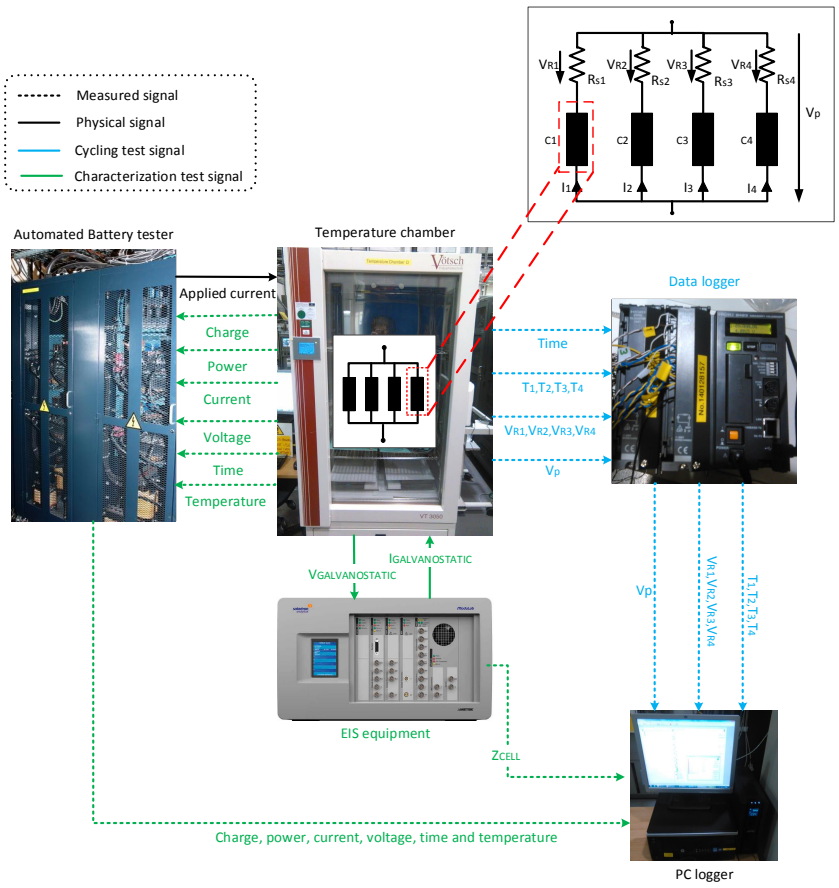

Figure A.24: Experimental test-bench

Table A.1: Technical specifications of the equipment employed [199].

Equipment	**Provider and model**	**Test procedure**	**Parameter measured**	**Measurement range**	**Accuracy**
Bitrode cycler	MCV 16-100-5	Cycling and characterisation	Applied Current	0A-100A	±0.1%[3]
			Voltage	0V-5V	±0.1%[3]
			Power	500W	-
Temperature chamber	Voetsch VT3050	Cycling and characterisation	Temperature fluctuation[1]	243.15K to 373.1K	±0.2K to ±1K
			Temperature deviation in space[2]	243.15K to 373.15K	±0.5K to ±1 K
Data logger	Hioki 8948	Cycling	Voltage shunt (V_{R1}, V_{R2}, V_{R3} and V_{R4})	-150mV to +150mV	±0.1%[3]
			Voltage parallel stack (V_P)	0-5V	±0.1%[3]
			Temperature (T_1, T_2, T_3 and T_4)	243.15K to 373.15K	±1 ℃
EIS analyser	Solartron Modulab XM	Characterisation	Galvanostatic voltage ($V_{Galvanostatic}$)	±8V	±0.2%[4]
			Galvanostatic current ($I_{Galvanostatic}$)	±300mA	
Shunt resistors	MP916	Cycling	Resistance (R_{s1}, R_{s2}, R_{s3} and R_{s4})	±0.01Ω	±5%[3]
Thermocouples	Type T	Cycling	Temperature (T_{s1}, T_{s2}, T_{s3} and T_{s4})	0 to 100 ℃	±2 ℃

[1]Measured at ambient temperature (25 ℃)
[2] In accordance with IEC 60068-3-5
[3] Accuracy with respect to full range measurement
[4] Accuracy with respect to particular measurement

A.2.2 EIS theoretical background

EIS is a widely used experimental technique that can be applied to gain a deeper insight into electrochemical processes of LIBs. EIS measurement is performed by applying a single or multiple frequency voltage known as potentiostatic, or current known as galvanostatic to the system. Then, the amplitude and phase shift (real and imaginary part) of the resulting current or voltage at that frequency is measured using Fourier transform [60]. The frequency range depends on the range of interest, the limitation of the equipment used and the duration of the test. To minimise the effect of battery non-linearities SoC variation is less than 5%, and current amplitudes is less than 250mA [60]. These amplitudes are still large enough, compared to the measurement noise and so distinguishable from it.

Considering the potentiostatic case, a small voltage signal V_t with an amplitude V_a at a frequency ω and time t is computed as shown in Equation A.12.

$$V_t = V_a \cdot sin\,(\omega t) = V_a \cdot e^{j\omega t} \tag{A.12}$$

A steady state current I_t is obtained, shifted an angle ϕ with respect to V_t:

$$I_t = I_a \cdot sin\,(\omega t - \phi) = I_a \cdot e^{(j\omega t - \phi)} \tag{A.13}$$

Using Euler relationship defined as $e^{j\phi} = cos(\phi) + j \cdot sin(\phi)$, Equation A.14 expresses the impedance Z as a function of frequency ω into complex form:

$$Z(\omega) = \frac{V_a \cdot e^{j\omega t}}{I_a \cdot e^{j\omega t - \phi}} = Z_a e^{j\phi} = Z_a\,(cos\phi + jsin\phi) \tag{A.14}$$

Where the real term Z', equivalent to the resistance, is:

$$Z' = |Z_a| \cdot \cos\phi \tag{A.15}$$

The imaginary term Z'', equivalent to the admittance, is:

$$Z'' = |Z_a| \cdot \sin\phi \tag{A.16}$$

And the modulus and the phase are:

$$|Z_a| = \sqrt{(Z')^2 + (Z'')^2} \tag{A.17}$$

$$\phi = arctan\left(\frac{Z''}{Z'}\right) \tag{A.18}$$

A.2.3 Extrapolation of the experimental investigation to Tesla Roadster model 2008 battery pack

The 18650 cells employed in this investigation are used in automotive applications. For instance, the BEV Tesla Roadster model 2008 is composed of 7104 18650 cells. To evaluate the impact of this research for commercially automotive viable applications, the time required to achieve the SoH_E and SoH_P convergence is extrapolated from cell level to the Tesla Roadster battery pack. The total energy released for each cell, u, over the whole experiment was computed in Equation A.19.

$$E_{o,u} = \int_{t_{i,dch}}^{t_{end,dch}} V_t(t)_{dch} \cdot I_t(t)_{u,dch} dt \tag{A.19}$$

$$u = [1,\ 2,\ 3,\ 4]$$

Subsequently, the average value of the four cells, $\overline{E}_o$, is calculated using Equation A.20.

$$\overline{E}_o = \frac{\sum_{u=1}^{4} E_{o,u}}{4} = 4.05 \text{ kWh} \tag{A.20}$$

$$u = [1,\ 2,\ 3,\ 4]$$

To extrapolate the energy released by a single equivalent cell to the whole battery pack, the voltage of cells connected in series and the current of cells connected in parallel are added. The Tesla Roadster battery pack includes 16 modules of 6S74P configuration summing up 7104 cells. According to Equation A.21, the equivalent energy released by the whole battery pack was computed as the product of the total number of cells of the pack, N_c, and the average value of the energy released by a single cell, $\overline{E}_o$, derived in Equation A.20.

$$\overline{E}_{o,total} = N_c \cdot \overline{E}_o = 7104 \cdot 4.05 = 28771 \text{ kWh} \tag{A.21}$$

Since the battery pack of the Tesla Roadster consumes 0.2 kWh/km [200], Equation A.22 computes the equivalent mileage as:

$$\text{Mileage} = \frac{\overline{E}_{o,total}}{\text{Consumption}} = \frac{28771}{0.2} = 143853.75 \text{ km} \tag{A.22}$$

According to a survey conducted by the Department for Transport in the UK, the average drivers annual mileage in the UK was 12700 km in 2014 [201]. Taking into consideration this figure, Equation A.23 calculates the number of years that the Tesla Roadster would be driven based on the experimental conditions of this work.

$$\text{Time} = \frac{\text{Mileage}}{\text{Annual mileage}} = \frac{143853.75}{12700} = 11.32 \text{ years} \tag{A.23}$$

According to Equation A.22 and Equation A.23, the experiment performed is equivalent to driving 143853.75 km during 11.32 years. These values are in agreement with the warranty specifications of Tesla, which defines that the total lifespan of the vehicle is 100000 miles (160934 km) [202].